



# Use of shear wave imaging to assess the mechanical and fracture behaviors of tough model gels

Heiva Le Blay

## ► To cite this version:

Heiva Le Blay. Use of shear wave imaging to assess the mechanical and fracture behaviors of tough model gels. Material chemistry. Université Paris sciences et lettres, 2021. English. NNT : 2021UP-SLS096 . tel-03962403

**HAL Id: tel-03962403**

**<https://pastel.hal.science/tel-03962403>**

Submitted on 30 Jan 2023

**HAL** is a multi-disciplinary open access archive for the deposit and dissemination of scientific research documents, whether they are published or not. The documents may come from teaching and research institutions in France or abroad, or from public or private research centers.

L'archive ouverte pluridisciplinaire **HAL**, est destinée au dépôt et à la diffusion de documents scientifiques de niveau recherche, publiés ou non, émanant des établissements d'enseignement et de recherche français ou étrangers, des laboratoires publics ou privés.



**THÈSE DE DOCTORAT**  
**DE L'UNIVERSITÉ PSL**

Préparée à l'Ecole Supérieure de Physique et de Chimie Industrielles de la ville de Paris (ESPCI Paris)

**Use of shear wave imaging to assess the mechanical and fracture behaviors of tough model gels**

**Utilisation de l'élastographie pour déterminer les propriétés mécaniques et de rupture de gels modèles**

Soutenue par

**Heiva LE BLAY**

Le 16/11/2021

École doctorale n°397

**Physique et Chimie des matériaux**

Spécialités

**Physique  
Mécanique  
Imagerie médicale**

**Composition du jury :**

Jean-François GERARD Professeur, INSA Lyon	<i>Président</i>
Sébastien MANNEVILLE Professeur, ENS Lyon	<i>Rapporteur</i>
Jian Ping GONG Professeure, Université d'Hokkaido	<i>Examinatrice</i>
Alba MARCELLAN Maître de conférences, Sorbonne Université - ESPCI	<i>Directrice</i>
Mickaël TANTER Directeur de recherche, ESPCI	<i>Co-Directeur</i>
Thomas DEFFIEUX Chargé de recherche, ESPCI	<i>Encadrant</i>

*This project has received funding from the European Union's Horizon 2020 research and innovation program under the Marie Skłodowska-Curie grant agreement No 754387.*

# Contents

<b>Remerciements</b>	<b>1</b>
<b>General Introduction</b>	<b>5</b>
<b>1 Scientific background</b>	<b>9</b>
Content	9
1.1 Hydrogels: Origin and applications	10
1.1.1 Learning from nature	10
1.1.2 Mimicking nature through synthetic hydrogels	11
1.1.3 Toward advanced gels: Active matter	14
Double network gels: The concept of toughening by bond breaking	16
Nanohybrid hydrogels with reversible bonds	16
Slide-ring hydrogels and their sliding bonds	17
1.2 Fracture mechanics	19
1.2.1 Why studying fracture?	19
1.2.2 Physical concept of fracture	20
LEFM: Linear Elastic Fracture Mechanics	20
Local crack tip plasticity - Correction to LEFM	22
Greensmith's approximation	23
1.3 Application of fracture theory on gels: design of tough gels	23
1.3.1 Fracture toughness	24
Simple network: Lake and Thomas theory	24
Complex networks: Greensmith theory	24
1.3.2 Chain scission vs disentanglement	25
1.3.3 Experimental stress field at the crack tip in single notched gels	27
<b>2 Theoretical and experimental aspects: US imaging and conventional mechanics</b>	<b>31</b>
Content	31
2.1 Mechanical wave propagation	32
2.1.1 Compression waves and Shear waves	32
2.1.2 Focus on the Ultrasound compression wave	32
2.1.3 Use of ultrasound in the medical field	34
2.2 Shear Wave Elastography	35
2.2.1 Definition of elastography	35
2.2.2 Quasi-static elastography	35
2.2.3 Dynamic elastography	36
Fibroscan	36
Acoustic radiation force	37
2.2.4 Theoretical background of elastography	38
2.2.5 Ultrafast imaging	39
2.2.6 Time of flight image reconstruction	41
2.2.7 Limitation of Shear Wave Elastography	41
2.3 Mechanics for an elastic medium	42

2.3.1	Hooke's law	42
2.3.2	Mechanics of a continuous medium: A linear analysis	42
	Stress and strain tensors	42
	Elasticity tensor in isotropic medium	43
2.3.3	Quasi-incompressibility	44
2.3.4	Wave equation	44
2.4	Acoustoelasticity: Polarized shear wave in a stressed medium	46
2.4.1	Strain energy density function used for shear wave velocity	46
2.4.2	Strain energy density function used for mechanics	49
2.5	Materials and methods	50
2.5.1	Synthesis of the model hydrogels	50
	Swelling procedure	51
2.5.2	Setups built for the project	51
	Coupled compression test between Instron and Aixplorer	51
	Coupled tensile test between Instron and Aixplorer	52
	Rheology	52
2.5.3	Imaging technique	53
	Ultrasound Elastography	53
<b>3</b>	<b>Gel behavior under homogeneous stress field: from linear to nonlinear elasticity</b>	<b>55</b>
	Content	55
3.1	Gel behavior at small strain: Linear analysis	56
3.1.1	Role of silica nanoparticles in imaging	56
	Echogenicity for elastography	56
3.1.2	Role of silica nanoparticles in mechanics	58
	Mechanical investigation of hybrid hydrogels at preparation state	58
	Frequency dependence of gels: five orders of magnitude	59
	Mechanical investigation of hybrid swollen hydrogels	60
	High frequency response of swollen gels	63
3.1.3	Nanoparticles dispersion state: Link between Bmode imaging and mechanics	64
3.1.4	Toward anisotropy at large strains	65
3.2	Coupled experiments with Shear Wave Elastography and standard mechanical tests	66
3.2.1	Tangent modulus in the nonlinear elastic region	66
3.2.2	Toward a local measure	67
3.2.3	Compression VS tensile response	68
	Impact of geometry	68
	Shear wave velocity affected by the sign of the stress	69
3.3	Large strain acoustoelasticity effects: A non linear analysis	70
3.3.1	Calculation of nonlinear Landau coefficients A and D	70
	Fitting Procedure	70
	Elastic gels: tool for calibration of large strain acoustoelasticity	70
3.3.2	Third order of non linear elasticity	72
3.4	Stress determination from the strain energy density	72
3.4.1	Stress determination from AE theory	72
3.4.2	Physical sense of Landau coefficients A and D for the studied gels	73
3.4.3	Stress determination using the Green-Lagrange Invariants	74
	Parametric study	74
	Theoretical vs. experimental study	75
3.5	Assessment of stress relaxation by Shear Wave Elastography	77
3.6	Key results	79

<b>4</b>	<b>Static gel fracture: Experimental stress field around the crack tip</b>	<b>81</b>
	Content	81
4.1	Single Edge Notched Tension (SENT) geometry	82
4.1.1	Methodology	82
4.1.2	Local shear wave velocity: pixel by pixel	83
4.1.3	From local shear wave speed to local stress	85
4.2	Temporal mapping of the stress concentration around the crack tip	86
4.2.1	Elastic gels: No temporal evolution of local stresses	86
4.2.2	Viscoelastic gels: Dynamic reorganization of the network	87
	Macroscopic relaxation processes	87
	Local relaxation processes at the crack tip	89
4.2.3	Role of swelling state	91
	Swollen elastic gels at maximum swelling degree	91
	Macroscopic relaxation behavior of swollen viscoelastic gels	92
	Local relaxation behavior of swollen viscoelastic gels	93
4.2.4	Separating macroscopic from local relaxation processes	95
	Creep test on viscoelastic gel	95
4.3	Spatial mapping of the stress concentration around the crack tip	97
4.3.1	Effect of crack tip geometry on stress field: case of elastic gels	97
	Increasing COD with fixed crack depth ratio $a/W$	97
	Effect of COD and crack depth ratio $a/W$ variations	98
	Absence of temporal evolution of the spatial mapping for elastic gels	100
4.3.2	Stress field impacted by the presence of NPs in viscoelastic gels	100
	COD and crack depth ratio $a/W$	100
	Temporal evolution of the spatial stress mapping of SP2	102
4.3.3	Influence of swelling on the local stress field	103
4.4	Finite Element Method (FEM)	104
4.4.1	Introduction to FEM	104
4.4.2	Discretization	105
4.4.3	Boundary conditions	106
4.4.4	Constitutive models	106
	Particular case of uniaxial tension	106
	Quasi-incompressible hyperelastic behavior (Rivlin)	107
	Compressible hyperelastic behavior (Mooney)	109
4.5	Stress field and comparison with simulation	110
4.5.1	Unnotched elastic gel	110
4.5.2	Crack tip stress field elaborated by Finite Element Method	110
4.6	Key results	113
<b>5</b>	<b>Dynamic Fracture Mechanics</b>	<b>117</b>
	Content	117
5.1	Fracture propagation in SENT	118
5.1.1	Methodology	118
	Ultrafast imaging	118
5.2	Physical parameters	119
5.2.1	Fracture toughness	119
5.2.2	Crack opening displacement (COD) and crack length ( $a$ )	120
5.3	Crack tip during fracture propagation: Source of shear wave	123
5.3.1	Brittle fracture of swollen elastic gel (at maximum swelling degree)	123
5.3.2	Fracture of elastic gels	127
5.3.3	Fracture propagation of viscoelastic gels	129

	First case of viscoelastic gel SP1 . . . . .	129
	Second case of viscoelastic gel with a higher amount of NPs . . . . .	132
5.4	Crack propagation analysis . . . . .	133
5.4.1	Effect of NPs on crack propagation velocity . . . . .	133
5.4.2	Multiple crack propagation in hybrid gels . . . . .	135
5.5	Key results . . . . .	137
5.6	Ultrafast imaging in double network (DN) gels . . . . .	139
5.6.1	Materials . . . . .	139
	Mechanical response of DN gels . . . . .	140
5.6.2	Fracture of DN gels dissected every millisecond . . . . .	141
	Beginning of DN gels fracture propagation . . . . .	141
	End of the DN gel fracture propagation . . . . .	144
5.6.3	Stretching of an intact DN gel . . . . .	146
5.6.4	Key results and discussion . . . . .	147
	<b>General conclusions and perspectives</b>	<b>151</b>
	<b>Annex</b>	<b>155</b>
A	Stress determination with shear wave elastography on hybrid gels . . . . .	155
A.1	Impact of strain rate on AE theory . . . . .	156
B	Local mechanical behavior of SP3.5 gels around the crack tip under tension . . . . .	158
B.1	Unusual stress field ahead of the crack tip . . . . .	158
	Spot appearing ahead of the crack tip . . . . .	159
	<b>Resumé substantiel en français</b>	<b>161</b>

# Remerciements

Parce qu'une thèse, bien que restant personnelle, ne peut être le fruit d'une personne, je dédie ces quelques lignes à toutes celles et ceux qui l'ont rendu possible et qui ont fait de ces trois années de thèse une expérience inoubliable.

Tout d'abord, je souhaite remercier mes directeurs de thèse et mon encadrant. Je vous remercie sincèrement pour la confiance que vous m'avez apportée, votre pédagogie et votre disponibilité. Alba, tu m'as transmis ta passion pour les polymères et la mécanique et c'était un réel plaisir de travailler avec toi. Tu sais fédérer en chacun de nous une envie de partir à la recherche du trésor caché sur l'île. Mickaël, ta passion et ta gentillesse font de toi un directeur de thèse très envié. Je suis honorée d'avoir pu être une de tes doctorantes et d'avoir vécu l'expérience dynamique de ton laboratoire Physmed. Thomas, j'envie tes futurs doctorants qui auront beaucoup de chance de t'avoir comme directeur de thèse. Tu as toujours les mots justes pour éclaircir nos pensées. Travailler à vos côtés est très stimulant et donne envie de donner le meilleur de soi-même.

La thèse permet des collaborations avec divers experts et j'ai eu la chance d'en faire une avec le Professeur Lucien Laiarinandrasana qui a accepté de travailler avec nous lors de ma troisième année de thèse. Cela a permis de se conforter dans la direction qui avait été prise. Merci pour le temps énorme que tu m'auras accordé et pour les résultats qui ont pu en découler. Je remercie aussi les deux rapporteurs de mon manuscrit, Professeur Jean-François Gérard et Professeur Sébastien Manneville pour avoir montré un intérêt pour ce travail, accepter de faire partie de mon jury et pour les discussions intéressantes qui en ont découlé par la suite. Je remercie Professeure Jian Ping Gong qui a accepté d'être examinatrice de mon travail et qui nous a envoyé ses fameux gels à double-réseaux. L'imagerie ultra-rapide sur ses gels a permis de montrer des résultats très intéressants durant une propagation de fracture.

Finalement, j'aimerais remercier d'autres personnes qui ont joué un rôle important avant même que cette thèse ne commence. Je pense à Barbara Lynch et Yegor Domanov qui m'ont fait confiance et m'ont engagé pour un stage de 6 mois dans le laboratoire de biophysique de la peau chez L'Oréal en Recherche Avancée. Ce stage m'a non seulement permis de comprendre que j'adorais la recherche en laboratoire, mais aussi que l'interdisciplinarité et les matériaux vivants me plaisaient énormément et me stimulaient. Si j'en suis là, Barbara y est pour beaucoup. Merci de m'avoir poussé à faire une thèse, merci d'avoir essayé d'en créer une pour moi, merci pour le suivi et le contact que nous avons su garder et merci de m'avoir engagée par la suite :) (06/12/2021). J'espère un jour être à mon tour la Barbara de quelqu'un.

J'ai eu de la chance d'appartenir à deux laboratoires très dynamiques : SIMM et Physmed, et au groupe UpToParis qui réunit 10 étudiants internationaux. Toutes ces personnes que j'ai croisées lors de ma thèse et avec qui j'ai fait un petit bout de chemin. Parmi ces groupes, il y a eu des petits groupes qui se sont créés : le groupe Tennis où j'ai pu me défouler entre deux expériences avec Baptiste, Olivier, Toto et Noémi, le groupe de girl power ou Alba's team avec Anne-charlotte, Clot, Miléna, et Julie. La team des Houches (Laura, Olivier, Marta, Vincent, Charlie...), celle de Capri (Nassim, Louis, Sandrine, Larissa, Giorgia, Yuan Yuan, Jianzhu...) ou encore celle de Sophia Antipolis avec Clot, Maxime et Camille. À la neige comme à la mer, la recherche ne s'arrête jamais.

Je vais jongler entre mes deux laboratoires pour mentionner diverses personnes qui ont contribué au bon fonctionnement de ma thèse. Je remercie Etienne Barthel, Guylaine Ducouret, et Jean-Baptiste D'Espinose de Lacaille, ça a été un plaisir d'être représentante des étudiants avec Lola et de siéger au conseil du laboratoire à vos côtés. Mathieu Pernot, tu m'as donné le spécial code de l'Aixplorer qui a permis à ma thèse de faire un bond et de passer en local, un grand merci pour ta bienveillance. Charlie Démené, merci pour tous ces échanges de clés entre le 4ème étage de l'esc. C jusqu'au sous-sol de l'esc. H, pour ton peps et ton humour. Jérôme, j'aurai presque envie de refaire une thèse si je savais que tu serais mon directeur, c'est dire à quel point je te trouve fantastique dans ta pédagogie, et ta générosité pour l'entraide.

Je remercie le workshop de l'ESPCI pour leur aide considérable dans le montage de mes expériences (Ludo, Alexandre et Amaury). Côté Physmed, c'est Hicham que je remercie, l'homme à tout faire, pièce essentielle de physmed qui nous trouve toujours une solution.

Les gestionnaires du SIMM comme de Physmed font un travail formidable qui permet à chaque laboratoire de fonctionner comme il le faut. Mention spéciale à Salima et Hinde qui forment un duo mère/fille de choc et qui apportent un vent de légèreté et d'humour dans le laboratoire.

Mon programme UpToParis qui a permis cette collaboration entre les deux laboratoires. Merci pour toutes les formations que vous nous avez apportées et pour le suivi de près auquel nous avons eu droit lors de ces trois années.

Je remercie mes nombreux co-bureaux (d'un côté Laura, Baptiste, Vincent, Toto, Blons, Anatole et de l'autre côté Cyprien, Cécile, Antoine, Valoche, Lauren, Krupal), ceux que j'ai vu partir, ou ceux que j'ai vu arriver. Dans tous les cas, ça a été un réel plaisir de partager des moments avec vous dans les bureaux. Baptiste, merci pour tes cours de tennis (et Laura pour la raquette) et ta patience que ce soit au tennis (je rêve de ce double Baptiste x2, Laura et moi) ou dans le bureau face à Laura et moi. Laura, tu étais le vrai diamant brut de ce bureau que tu n'auto-façonnais pas assez. Crois en toi comme nous croyons en toi. Je me rappellerai de tous ces fous rires dans le bureau et de ta générosité abondante. J'ai eu un rôle difficile, celui de remplacer Line qui pensait que je venais du 16, et tu m'as finalement adopté alors je voulais te remercier ma lolo. M. Poirier, un comédien et professeur brillant, qui s'est retrouvé à froter des mousses (et à tout casser dans le bureau dans ses moments durs, la thèse n'est pas que joie pour certains...). Merci d'avoir supporté mes questions incessantes et ma curiosité débordante qui m'auront valu le surnom d'inspecteur. Ce surnom n'est pas si anodin puisque une deuxième personne m'appelait aussi comme ça côté Physmed (j'ai sûrement loupé ma vocation de détective). Cette personne, c'est toto mon brillant co-bureau gémeaux doté d'un humour très fin, qui a dû supporter la tornade Laura-Heiva avant d'être secouru par Blons le roi de la focaccia, qui aura passé trop de temps en télétravail et donc pas assez avec nous dans le bureau ! #Covid. Merci à tous les deux pour votre gentillesse et pour la bonne ambiance qui émanait de notre bureau. Olivier, la première personne que j'ai croisé à Physmed, caché derrière son Aixplorer, comme moi. Chaque laboratoire a besoin d'une personne comme toi qui a la pêche, le sens de la fête et de l'accueil des nouveaux arrivants. Peut-être devrais-tu penser à une reconversion dans le social ? Non pas que les cœurs n'aient pas besoin de toi bien sûr ;). Clotilde, tu as choisi les pneus, j'ai choisi la peau, mais je suis sûre que nos chemins se croiseront à Clermont ou à Amiens, autour de jeux de société et de bonnes bières. Julie, la ptite dernière du groupe des AA (Alba's Angels et non Alcoolique Anonyme), nous serons là pour te voir soutenir et t'encourager comme tu l'as si bien fait avec chacune de nous.

J'ai beaucoup apprécié chaque moment que j'ai pu avoir avec chacun de vous. Je serai toujours ravie si nos chemins se croisent un jour. Depuis Physmed avec Sofiane, Clém, Cyprien, Noemi, Blons, Toto, David, Flora, Haritha, Sylvia, Hugues, Oscar, Hanna, Justine, Charlotte, Alexandre, Jérôme, Vincent, Hinde, Florian, Victor... au SIMM avec Julie x2, Clotilde, Cyprien, Pascal or P, Lola, Martin, Flora-Maud, Loren, Jean, Artem, Victoria, Franz, Gaëtan, Nassim, Pierre, Louis, Gaëlle, Paul, Christophe, Mélanie, Guillaume, Yuan Yuan...

Enfin, d'une manière plus personnelle, je remercie mes ami(e)s qui se reconnaîtront, qui embellissent ma vie tous les jours et qui sont un vrai pilier pour moi. J'ai une chance infinie de les avoir à mes côtés (dans la vie et pendant ce jour J de la thèse).

Ma belle-famille, avec qui je ne cesse d'apprendre tous les jours, qui m'a soutenu pour faire une thèse et qui est très présente pour moi aujourd'hui.

Ma famille, grâce à qui je suis ce que je suis aujourd'hui. Merci pour cette liberté et cette confiance qui ont permis un développement et un chemin de vie non biaisés par des pressions quelconques. Mes choix n'ont jamais été prédéterminés et c'était justement mes choix du début à la fin.

Ma future famille composée de 2 personnes aujourd'hui, mais de beaucoup plus demain.

*Ua here au ia 'oe ta'u ipo.*

*«Je me faisais du moins, tout en m'en allant, ces réflexions : Voilà un homme qui est moins sage que moi. Il est possible en effet que nous ne sachions, ni l'autre, rien de beau ni de bon. Mais lui, il croit qu'il en sait, alors qu'il n'en sait pas, tandis que moi, tout de même que, en fait, je ne sais pas, pas davantage je ne crois que je sais ! J'ai l'air, en tout cas, d'être plus sage que celui-là, au moins sur un petit point, celui-ci précisément : que ce que je ne savais pas, je ne croyais pas non plus le savoir !»*

*Apologie de Socrate, par Platon - 21d.*



# General Introduction

What do two totally different materials as a boat ship and a hydrogel (see Fig. 1) have in common? They are two objects that diverge in terms of composition, application, size, geometry, stiffness, etc. However, they are both concerned by a potential issue that arises in everyday life: fracture. Materials engineering seeks to design new alternatives to improve resistance to crack propagation.



FIGURE 1: Top: Cargo ship Ever Given stuck in the Suez Canal near Suez, Egypt, Friday, March 26, 2021<sup>1</sup>. Bottom: Gold's standard gel of Gong (Gong et al., 2003).

The mechanical fragility of materials can be caused by two intrinsic properties, the heterogeneity and the lack of dissipation mechanisms inside the material:

- Intense **stress concentrations** under deformations are often due to **heterogeneities**, as defects, present in the matrix. To take a recent example, the giant container ship stuck in the Suez Canal, the Ever Given (see Fig. 1, top), at the end of March 2021, has raised a problem of a possible fracture. With the ship blocked at both ends, the hull was vulnerable to stress and cracking. Teams of divers inspected the hull throughout to detect any damage that might have caused the hull to rupture. Local stress concentration is a key aspect in crack initiation.

<sup>1</sup><https://www.bbc.com/news/56523659>

- The lack of **dissipation mechanisms** leads to catastrophic failure when the energy stored is too high to be contained. In metals, plasticity is well-known to efficiently dissipate strain energy. Recent designs of hydrogels are capable of dissipating energy. Indeed, the energy brought into the polymer network during deformation is stored as mechanical energy in the polymer chains. The material is composed of water, i.e. with a low viscosity solvent, thus the strain energy won't be dissipated by usual mechanisms (chain friction) that can be found in elastomers. The dissipation may take place through the addition of physical dynamical bonds to relax stress or smart network topologies as double networks (see Fig. 1, bottom).

In this thesis, we focus on these new fascinating materials: hydrogels. Emblematic of soft matter, these solids, composed mainly of water, are very sensitive to their environment. They can drastically change their volume or properties via external stimuli such as temperature, pH, or humidity. The basic gel is inherently fragile as the jelly (composed of gelatin and water) for example. This brittleness can be overcome by the addition of physical interactions inside the gel matrix. The beginning of the twenty century saw the emergence of hydrogels that are almost as hard to break and stiff as rubber (Gong et al., 2003) (see Fig. 1, bottom), even though being composed of almost 90% in weight of water. Due to their large amount of water, it is easily understandable that hydrogels have become essential in tissue engineering or soft robotics. Their ability for reversible deformation is attractive for applications as artificial cartilage or ligaments. Indeed, in the past few years, macromolecular engineering has made possible the formulation of gels for use in biology to provide synthetic materials while addressing biocompatibility issues, tissue/material interface compatibility, and to be in phase with the mechanical properties that the body requires.

The model gels used in this study have already demonstrated remarkable simplicity of design and performances in terms of strength, self-repair, and adhesion (Rose et al., 2013, Rose et al., 2014, Ronsin et al., 2019). Still, fracture study on these highly deformable and viscoelastic gels has been poorly investigated experimentally. Understanding damage processes on these soft materials is essential to develop effective mechanical strengthening strategies. Yet, the exploration of the mechanisms involved, locally at the crack tip, remains very insufficient. In this PhD work, we propose to develop an ultrasound imaging tool devoted to the study of gel mechanics. Shear wave elastography (SWE) has revolutionized medical diagnosis by quantitative measurements of an elastic modulus of soft tissues. The purpose of this work is to adapt this method for the field of material science and chemistry as a new experimental tool.

A first attempt to approach the world of elastography with the one of gels has already been made by joining Physics for medicine laboratory with the SIMM (Science et Ingénierie de la Matière Molle) laboratory (Gennisson et al., 2014). Ultrasound elastographic measurements and classical rheology were compared over a frequency range spanning five orders of magnitude [0.01 to 1200 Hz] to characterize model gels at multiple scales. Shear wave elastography was validated to accurately image rheological properties of soft tissues and to differentiate soft elastic behaviors from viscoelastic responses.

In this thesis, our work aims at developing this imaging technique to probe the stress state at the vicinity of a crack. This implies large deformations, sharp stress field and fast relaxation processes. We have anticipated that water being the gel's main component like biological tissues, these materials are an excellent platform for the study of acoustic wave propagation, i.e. shear (S) or compression (P) wave. Indeed, elastography is based on mechanical waves and their difference in velocities of propagation is crucial here. Elastography is a subtle combination of these two different waves in soft solids. Through P waves (focused ultrasound), it is possible to create S waves, then image the S wave propagation (through ultrafast ultrasound plane waves). This technique could be a valuable tool in the community of materials science. It allows a local and non-invasive

approach at a high framerate to quantify in real-time and *in-situ* the mechanics of the material. By coupling this method to conventional mechanical analysis, the goal of this study is to validate the technique and demonstrate that it is possible to measure a local stress especially around a crack tip. The nature of this information is unique in the world of mechanics of materials. If this project sheds light on the fracture of soft materials, it could also provide to clinicians a real added value in the medical diagnosis to refine the description of biological tissues subjected to complex stress states.

The present manuscript is composed of 5 chapters. The first chapter presents the scientific background on hydrogels and fracture mechanics.

Chapter 2 will bring together the experimental methods (conventional mechanical tests and SWE) as well as the theoretical background needed to understand the technique. This will lead us to revisit an old analytical model of acoustoelasticity (Landau et al., 1959).

Chapter 3 will present first experimental results in the linear regime and the concordance between the conventional rheological tools (a tensile/compression testing machine and a rheometer) and elastography based on shear wave imaging. We will focus on homogeneous stress/strain field. In the nonlinear regime, at large deformations, the theoretical model of acoustoelasticity will be necessary to understand and calibrate the measure made by shear wave elastography.

Chapter 4 introduces the fracture subject with a local spatial and temporal study of the quasi-static fracture processes. For the first time, elastography will be used to probe the crack tip of hydrogels. The stress field around the crack tip will be reviewed as well as the important role of silica nanoparticles content and swelling state.

Finally, Chapter 5 will illustrate how ultrafast imaging can be used to visualize physical processes that arise during crack propagation. The material breaks because the maximum stress that it can withstand is reached. How this energy contained inside the material is released to the outside? Fracture behavior of our hybrid gels will be compared to double network (DN) gels (Gong et al., 2003), a gold standard in terms of fracture toughness.



## Chapter 1

# Scientific background

## Content

Hydrogels, being composed of almost 90% of water, are quite fragile. To resist fracture, their mechanical properties must be reinforced with the elaboration of various designs which further complicates the gel mechanics and the comprehension of fracture processes.

The main purpose of this work is the elaboration of a new technique to study the mechanical and fracture behavior in model gels. Our gel is based on the combination of a polymeric network and inorganic nanoparticles, highly swollen by water. Nowadays, abundant literature is available on gel topics, from natural gels to synthetic ones. The first part of this chapter will be dedicated to a small literature survey about hydrogels.

To start with the fracture study, the main fracture mechanisms of elastic materials must be well understood for evident progress on non elastic, and large strain processes that operate in gel fracture. That's why the second part of this chapter will be dedicated to fracture mechanics and its physical concepts usually described for brittle materials or conventional elastomers.

The third part of this chapter will present the experimental tools conventionally used to study gel fracture. It will appear that few techniques exist today to probe the local processes that arise at the crack tip and none can give the through-thickness stress.

This chapter will help to understand the importance of using a new technique to probe the fracture of gels. This technique is summarized in Fig. 1.1.

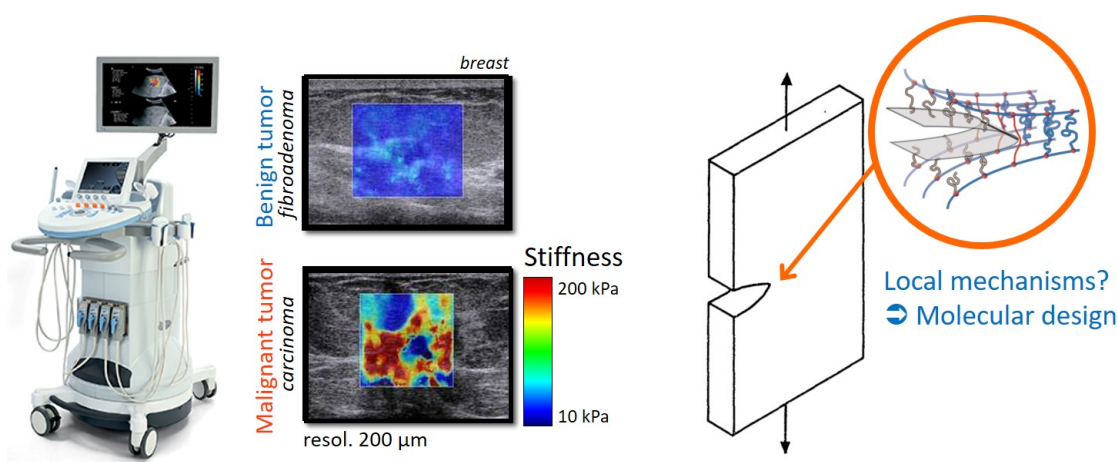


FIGURE 1.1: Left: Imaging technique used to quantify the stiffness of biological tissues. Right: Scheme of a notched gel under stress. What are the local mechanisms that arise at the crack tip?

## 1.1 Hydrogels: Origin and applications

### 1.1.1 Learning from nature

A hydrogel can be defined as a water-based soft elastic material. These simple characteristics are in fact really important and makes the hydrogel ubiquitous in a lot of fields from medicine, agriculture, food industry, cosmetics, drug delivery, and many more left since the middle of the 20th century. Before scientists discovered this highly promising material, it was already present on earth as living matter. Fig. 1.2 shows three different examples of collagenous primitive species taken from the marine environment and mainly composed of water: algae ( $\sim 76$  weight% of water, Holdt et al., 2011), jellyfish ( $\sim 95$  wt.%, Lowndes, 1942), and sea cucumber ( $\sim 80$  wt.%, Oedjoe, 2017).



FIGURE 1.2: From left to right: algae, jellyfish, sea cucumber.

Being present on earth for more than 500 million years, they adapted to their environment to survive sometimes in hostile conditions which makes them quite robust with exceptional adaptability. Nature inspires humans, and a robust and soft material being water-based is intriguing and attractive. Humans are in constant evolution where, more than ever, solutions must be found to overcome everyday life problems. Technology is beyond what we could have thought a century ago and is continuously accelerating. Dyens wrote about this subject (Dyens, 2001):

*What we are witnessing today is the very convergence of environments, systems, bodies, and ontology toward and into the intelligent matter. We can no longer speak of the human condition or even of the posthuman condition. We must now refer to the intelligent condition.*

In the aim of upgrading the human condition, the three species from Fig. 1.2 were all subjected to recent scientific researches:

- Algae have been brilliantly used for the design of water filtration system (Mihrianyan, 2011). A water filtration paper is made out of a locally grown macro-algae through their cellulose nano-fibers which can be formed into paper sheets. These paper sheets have tiny pores that are utilized for point-of-use water treatments. It has demonstrated excellent virus and bacterial removal capacity. The scientists believe that the paper filter could be an affordable and efficient remedy to prevent numerous potentially deadly water-borne infections.
- Jellyfishes mesogloea display very high tensile strength and compressive strength (0.17 MPa and 1.43 MPa respectively) even with more than 99 wt.% water (Zhu et al., 2012). This is due to its layered porous structure with pore walls consisting of nanostructured layers and fibers (Wang et al., 2011, Zhu et al., 2012). When a synthetic gel (PAAm) is incorporated into the biological jellyfish by radiation-induced polymerization and crosslinking of a hydrophilic monomer, a novel type of hybrid hydrogel with very high mechanical strength results (Wang et al., 2011). The breaking strength of the hybrid gels was about 7–30 times higher than that

of the jellyfish gel alone and 2–4 times higher than those of the corresponding PAAm gels. This study may provide gel scientists new ideas in designing and fabricating hydrogels with well-defined microstructures and unique mechanical and swelling properties.

- Sea cucumbers have collagenous tissues with a unique property: the collagen, known as mutable collagenous tissue, allows the sea cucumber to “turn to jelly” to avoid predators. They share the ability to rapidly and reversibly alter the stiffness of their connective tissue. The sea cucumber can change from its soft state into its stiff state to puzzle its enemies (see Fig. 1.3).

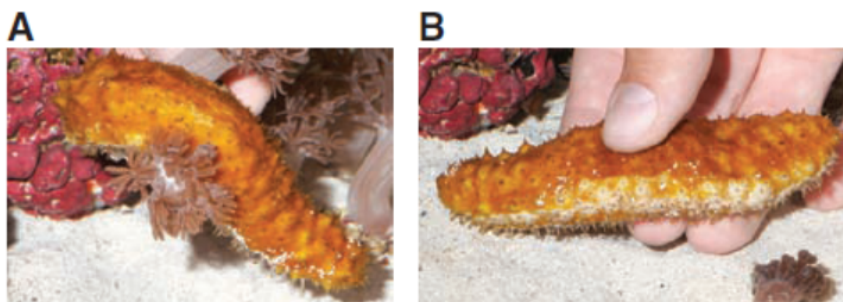


FIGURE 1.3: Sea cucumber in relaxed (A) and stiffened (B) state demonstrating the firming of dermal tissue (from Capadona et al., 2008).

This defense mechanism is enabled by a nanocomposite structure in which rigid, high-aspect ratio collagen fibrils reinforce a viscoelastic matrix of fibrillin microfibrils. The stiffness of the tissue is regulated by controlling the stress transfer between adjacent collagen fibrils through transiently established interactions (Trotter et al., 1999, Szulgit et al., 2000). These interactions are modulated by soluble macromolecules that are secreted locally by controlled effector cells. The dermis of sea cucumber species represents a compelling model of a chemo responsive material in which a tensile modulus (Young’s modulus) contrast by a factor of 10 ( $\sim 5$  to  $\sim 50$  MPa) is possible (Trotter et al., 2000). Based on this knowledge, sea cucumber was incorporated (through powder) into a synthetic dual network hydrogel formulation by using electron beam irradiation technique and was introduced as a novel crosslink agent. This study shows that these hydrogels markedly enhanced wound contraction and improved histological reorganization of the regenerating tissue (Zohdi et al., 2011). Sea cucumbers also inspired the team of Weder (Capadona et al., 2008) who created a stimuli-responsive polymer nanocomposites which have the potential for biomedical implants, like stents. This could be used to develop electrically switchable materials, such as a type of ankle or body cast that could be stiff or flexible as needed.

Given these examples, it would be desirable to provide dynamic synthetic materials that exhibit stimuli-responsive mechanical properties similar to biological tissues which interact with their environment.

### 1.1.2 Mimicking nature through synthetic hydrogels

The wet and soft nature of living organisms inspired scientists who tried to imitate nature to overcome technological difficulties. The very first reference found about hydrogel appeared in 1894 (Van Bemmelen, 1894). The hydrogel, during that period, was a colloidal gel of inorganic salts. At present, a hydrogel refers to a network of hydrophilic polymer chains, in which water is the dispersion medium. A three-dimensional material results from the polymer chains being held together by crosslinks via either covalent or physical bonds. This polymer network exhibits a characteristic mesh size of  $\xi \sim 1\text{--}100$  nm (Fig. 1.4, left).

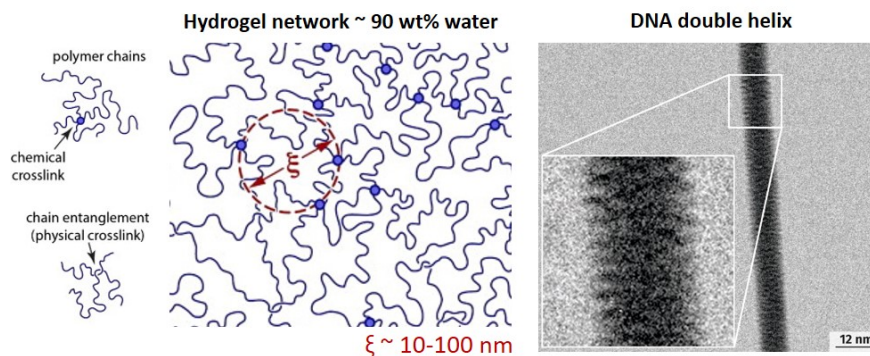


FIGURE 1.4: Left: Scheme of a synthetic polymeric network. Right: Imaging of double stranded DNA (natural polymeric network) by transmission electron microscopy (Gentile et al., 2012).

The mass fraction of water is much higher than the mass fraction of polymer. The lifetime of polymer crosslinks is long enough compared to the experimental time, which means that macroscopically, gels behave like solids, have a defined geometry, and do not flow in the corresponding timescale. At length scales lower than the mesh size, the medium behaves like a polymer solution where small molecules can diffuse.

There are two types of polymeric networks: natural, the most famous one being the DNA, or synthetic polymeric networks which are derived from synthetic chemistry (see Fig. 1.4). Even though synthetic polymers show low biodegradability and can include toxic substances, they present many great advantages as model systems: tunable mechanical properties, no batch variation, and no viruses pass by animal-derived materials.

The synthetic hydrogel of current understanding was first developed by Wichterle and Lim from the Prague Institute of Chemical Technology in 1960 (Wichterle et al., 1960). It was the first attempt to design polymers for human use with properties to fulfill the criteria of biocompatibility. Prof. Otto Wichterle had a significant impact on the ophthalmic world. He synthesized hydrogels based on a copolymer of 2-hydroxyethyl methacrylate (HEMA = ethyleneglycol monomethacrylate) with ethylene dimethacrylate (EDMA = ethyleneglycol dimethacrylate) as crosslinker. This is related to be the first biomaterial designed for medical applications. Wichterle was one of the pioneers of the modern soft contact lens industry (Fig. 1.5).

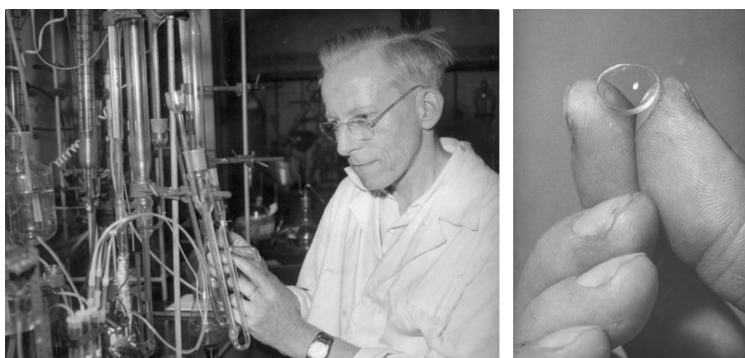


FIGURE 1.5: Left: Otto Wichterle and lens at the Academy of Sciences in 1953, Right: First contact lens created by Wichterle<sup>1</sup>.

<sup>1</sup><https://www.mua.cas.cz/en/otto-wichterle-695>

Assisted by Lim, they succeeded in preparing a crosslinking gel that absorbed up to 40% of water, exhibited suitable mechanical properties together with optical properties, oxygen permeability, etc. They patented the method in 1964<sup>1</sup>. This first contact lens was commercialized in 1971 by the society Bausch and Lomb. Later, HEMA-EDMA has been used as a suitable implant material in plastic operations for the nose (see figure 1.6) (Voldřich et al., 1975).

Since then, the number of studies about hydrogels for biomedical applications began to rise, especially from the decade of the 70's. Indeed, publications related to the keyword "hydrogel" have shown an exponential increase from 1970 to 2015 (Chirani et al., 2015).

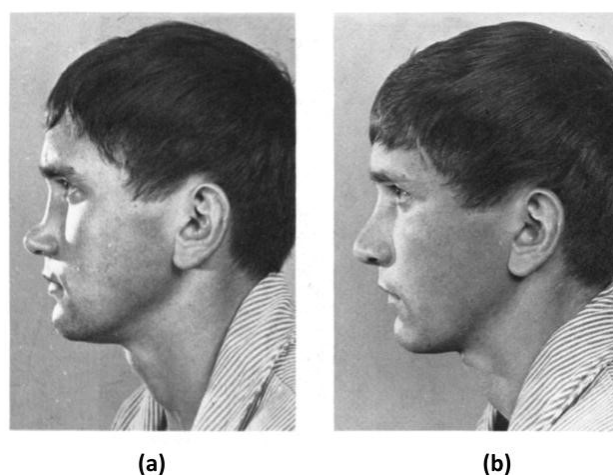


FIGURE 1.6: Hydrogel implants. Clinical use of hydrogels (copolymers of HEMA with EDMA) in rhinoplasty. a) Before surgery. b) After surgery (from Voldřich et al., 1975).

Nowadays, hydrogels are also commonly used in a wide range of applications. One of the biggest revolutions hydrogel brings is certainly in biomedical devices where the demand is tremendous. Indeed, this soft water-based material brings new solutions for the problem of biocompatibility, the tissue/material interface, and the mechanical properties the body needs. The twenty-first century opens a brand-new chapter for joints, prostheses, valves, and every tissue replacement which was so far achieved by metals and plastic. Even if these materials mimicked the function of the replaced organ, the mechanical properties are far from the one of biological tissue. A recent team at Duke University (USA) (Yang et al., 2020) designed the latest generation of a knee prosthesis for the replacement of damaged cartilage due to knee osteoarthritis. When the gel is stretched, the cellulose fibers resist pulling and help hold the material together. And when it is squeezed, the negative charges along the rigid polymer chains repel each other adhering to water, helping it spring back to its original shape.

Here are some of the revolutionary applications the hydrogel makes possible: it is a well-placed candidate for tissue engineering (review of Lee et al., 2001), optoelectronic systems for wireless optogenetics (Park et al., 2015), or bioelectronics with electrical stimulation and recording of neural activities (Yuk et al., 2019), 2D or 3D cell immobilization (Jen et al., 1996), soft robotics (Wehner et al., 2016), a lab-on-chip for malaria diagnosis (Taylor et al., 2014). Due to their swelling properties, it is also used as an ingestible hydrogel device for long-term gastric retention and physiological monitoring (Liu et al., 2019c). Other fields where absorption is of great importance is the market of disposal diapers (Peng et al., 2016) or in agriculture to reduce water consumption, improve fertilizer retention in soil and lower the death rate of plants and increase plant growth (Rudzinski et al., 2002) as well as extractions of pesticides (Jamshidi et al., 2020). The main applications are

<sup>1</sup>Patent US3496254A: "Method of manufacturing soft and flexible contact lenses."

illustrated in Fig. 1.7. Explorations are continuously being made at an accelerated cadence for their extensive usage. We understand hydrogel is a powerful material since it is present in a very large and diverse type of applications in our daily life.



FIGURE 1.7: Hydrogel applications in our daily life.

### 1.1.3 Toward advanced gels: Active matter

Being composed of a lot of water, hydrogels usually display low mechanical stiffness. In presence of water, the gel volume can change due to swelling effects. In this case, the polymer elongates by harvesting water (through hydrophilic functional groups), making the hydrogel highly absorbent (they can contain over 98% water). At first glance, hydrogels were disregarded as structural or load-bearing materials, their first applications being rather dedicated to absorption or solvent transport due to their weak mechanical properties. Nevertheless, the high content of water contributes to their biocompatibility, which is, as we saw previously, of great interest for the medical field.

To describe the behavior of polymer chains, it is important to take into account the interactions between the polymer and the solvent. A real chain conformation depends on the balance between effective repulsion energy between monomers that tends to swell the chain and the loss of entropy due to the deformation. Back in 1943, Flory and Rehner (Flory et al., 1943) showed that the maximum degree of swelling of a polymer network in contact with the pure solvent is related to the degree of cross-linking and the Flory interaction parameters  $\nu$ . The Flory theory considers a polymer chain swollen to size  $R$ , constituted of  $N$  monomers of Kuhn length  $a$ , uniformly distributed within the volume  $R^3$  without any correlation between them. Under these conditions, the end-to-end radius  $R$  becomes:

$$R = \sqrt{\langle R_N^2 \rangle} \approx aN^\nu \quad (1.1)$$

Where  $\nu$  is the Flory parameter, which varies depending on the solvent conditions. Three polymers/solvents conditions can be depicted, depending on the specific chemistry that drives the monomer-solvent interactions and on the temperature: good, poor and theta solvents. Theta solvent can be seen as an intermediate between good and bad solvent conditions which is characterized by a scaling parameter  $\nu = 1/2$  (see Fig. 1.8). The chain is at its unperturbed state.

The Flory–Rehner theory gives the change of free energy upon swelling of the polymer gel:

$$\Delta F = \Delta F_{mix} + \Delta F_{elastic} \quad (1.2)$$

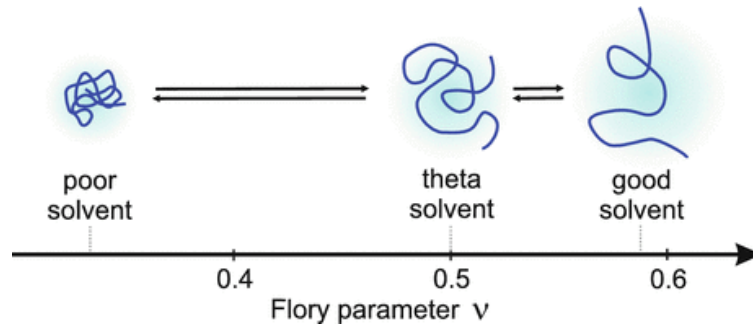


FIGURE 1.8: Interaction polymer solvent. Left to right: chain collapse, ideal chain, swollen chain or chain expansion (from Wöll, 2016).

The theory considers forces arising from three sources:

- The heat of mixing of polymer and solvent  $\Delta U_{mix}$ , which may be positive, negative, or zero so, that  $\Delta F_{mix} = \Delta U_{mix} - T\Delta S_{mix}$ .
- The entropy change  $\Delta S_{mix}$  caused by mixing of polymer and solvent.
- The entropy change caused by reduction in numbers of possible chain conformations via swelling  $\Delta F_{elastic}$ .

The swelling can also be modified according to the different interactions present in the gel. Different kinds of interactions between polymer chains in a hydrogel exist which can be classified in two categories: the physical interactions and the chemical bonds (see Fig. 1.9).

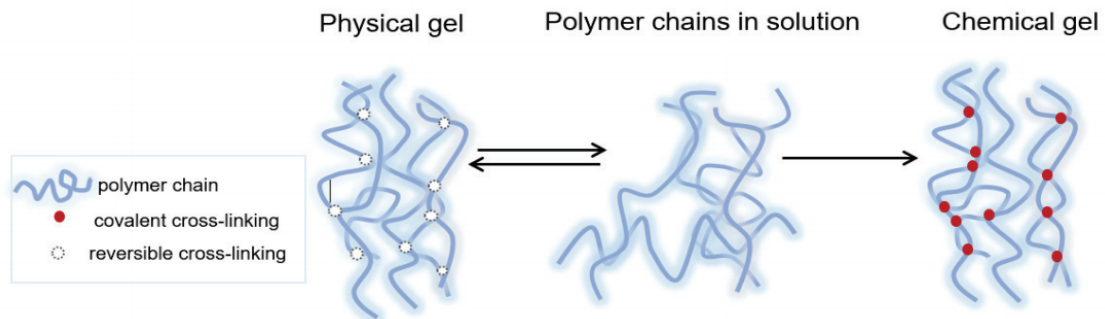


FIGURE 1.9: Polymer chains in solution. Left: schematics of physical hydrogel; Right: schematic illustration of chemical hydrogel.

The physical gel possesses reversible physical bonds which can be of many types involving: hydrogen bonds (Guo et al., 2014), ionic bonds (Sun et al., 2012), Van der Waal forces (Rubinstein et al., 1999), hydrophobic forces (Tuncaboylu et al., 2011; Mihajlovic et al., 2017), etc. These bonds, advantageously, can break and reform.

In contrast, the chemical gel possesses irreversible permanent bonds, chemical crosslinkers, which form the polymer network (monomer + crosslinker). To be more specific, the chemical interactions are represented by covalent bonds which freeze the network topology during the synthesis (phenomenon called gelation or network polymerisation). Increasing the crosslinker density generally makes materials stiffer but eventually increases the brittleness of the materials as well (Landel et al., 1993). To control these two different properties, strategies have been employed to design high-strength hydrogels. In the following, we will present three different gels that showed innovation in their reinforcement.

### Double network gels: The concept of toughening by bond breaking

The most famous example of tough gel is the double network (DN) hydrogel. The pioneers of the double network are Gong and co-workers who developed in 2003, a two-step sequential free-radical polymerization method to synthesize the first DN hydrogels consisting of poly(2-acrylamido-2-methylpropanesulfonic acid) (PAMPS) as a polyelectrolyte first network and polyacrylamide (PAAm) as a second neutral network. The two interpenetrating polymer networks are different: the first one is rigid, brittle and tightly crosslinked, while the second is soft, ductile and loosely crosslinked (Fig. 1.10).

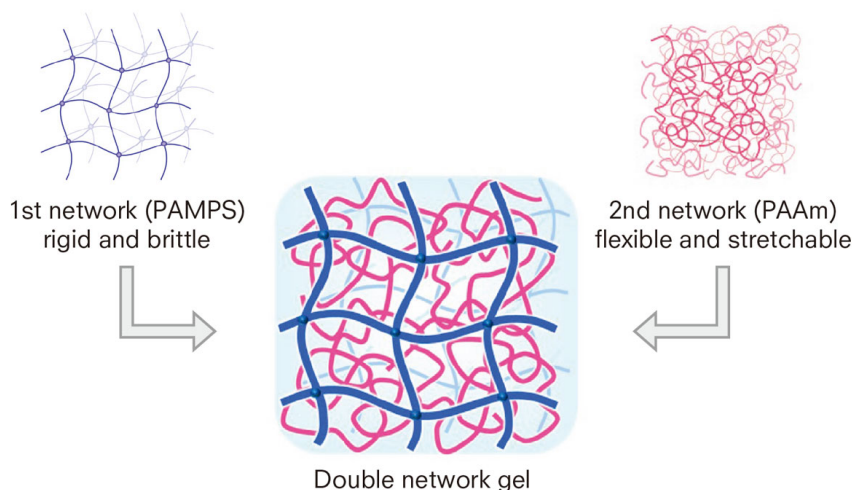


FIGURE 1.10: An illustration and a picture of a tough DN gel consisting of the first brittle network and the second ductile network (from Gong et al., 2003).

During uniaxial tensile tests, Gong's double networks revealed their strength. Indeed, in the corresponding stress (force divided by the surface) - strain curves, in Fig. 1.11.a, yielding occurs around 0.75 MPa, followed by a plateau region during the necking process. This phenomenon corresponds to an irreversible break of the first PAMPS network into plentiful small clusters throughout the volume, because of its intrinsic fragility. These formed clusters dissipate strain energy, allow an extreme fracture toughness and retard crack propagation by playing the role of physical crosslinking points for the long flexible PAAm chains, behaving as sliding crosslinker, in Fig. 1.11.b. This highlights the phenomenon of sacrificial bonds where strength raises from weakness. This mechanism has been verified by SANS (Small-angle neutron scattering) experiments under deformation (Tominaga et al., 2007).

This strategy of fracture toughening by covalent bonds breaking allows designing gels with 70% of water in weight displaying moduli of about 1 MPa and fracture energy of  $4 \text{ kJ.m}^{-2}$ , values that are in line with standard unfilled rubber. In biological tissues, cartilage contains 75 wt% of water and exhibits a large work of fracture ( $1 \text{ kJ.m}^{-2}$ ) (Simha et al., 2004). It allows the cartilage to sustain a daily compression of several MPa (Abé et al., 1996).

### Nanohybrid hydrogels with reversible bonds

The hybrid hydrogel is composed of one polymeric network maintained through chemical interactions via the crosslinks. Entangled in this network, silica nanoparticles (NPs) serve as reversible

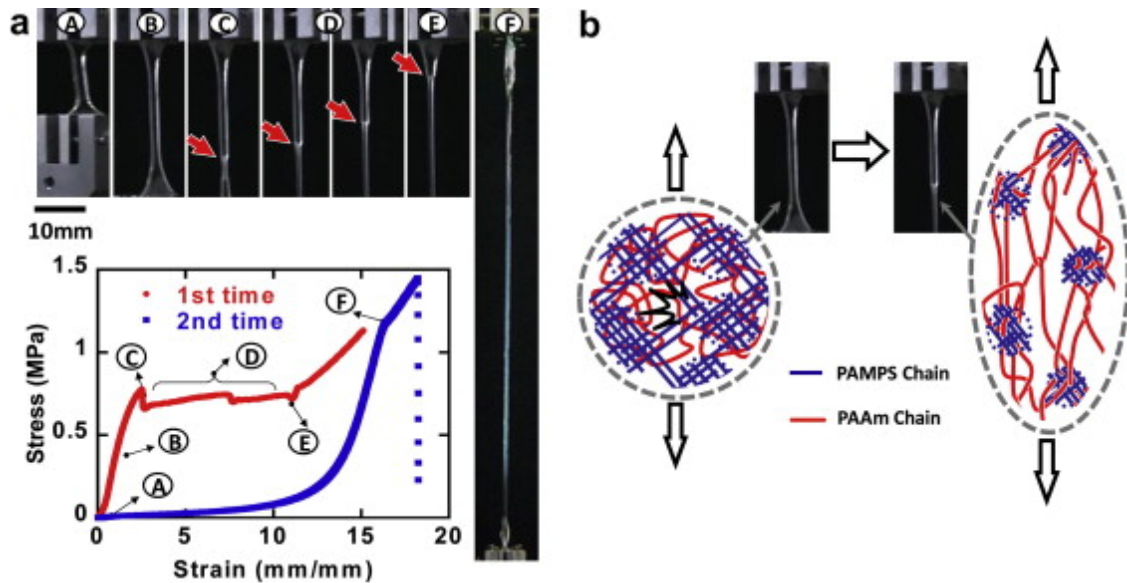


FIGURE 1.11: a) Loading curves of PAMPS/PAAm double network (DN) gel under uniaxial elongation at a rate of  $0.13 \text{ s}^{-1}$ , and images demonstrating the necking process. (b) Illustration of the network structure of the DN gel before and after necking (from Gong, 2010).

anchorage of polymer segments through simple adsorption (see Fig. 1.12a,b). In such hybrid networks, the silica NPs are well dispersed in the chemically crosslinked polymer matrix, serving as physical crosslinkers through adsorption of PDMA chains onto the silica surface, forming a transient secondary network. The presence of silica NPs increases the gel's stiffness and delays the fracture (by increasing the gel's extensibility and fracture toughness) (see Fig. 1.12c).

The adsorption abilities of polymer onto silica NPs also provide adhesion at the gel interface. Marcellan and Leibler (Rose et al., 2014) explored another way to glue hydrogels using the nanoparticle solution as adhesive, without affecting the rigidity or permeability of the assembly. This glue has also proven its efficiency with two pieces of lamb that have been stuck together (see Fig. 1.12d,e) and led to promising developments for *in vivo* applications as organ repair, hemostasis, and *in vivo* bonding (Meddahi-Pellé et al., 2014).

The hybrid hydrogel differs from the DN gel through the physical interactions: reversible in the first case and irreversible in the second case with the sacrificial bonds. This reversible feature allows for self-healing capabilities. Also, the synthesis is simpler than the one of double-network gels.

### Slide-ring hydrogels and their sliding bonds

Ito and Okumura (Okumura et al., 2001) introduced the concept of movable crosslinks: they can pass along the polymer chains freely to equalize the tension of the threaded polymer chains just like pulleys (Fig. 1.13). Their network structure is expected to be optimized automatically by relative sliding movement resulting in relieving stress concentration (Liu et al., 2019b). This is called the "pulley effect" and allows SR (slide-ring) gels to show superior extensibility ( $> 1000\%$ ) to chemical gels (Ito, 2010).

Their genuine structure provides a high swellability, about 500 times their original weight, but, this strategy does not allow to achieve high fracture resistance ( $\sim 30 \text{ J.m}^{-2}$ ).

Through these three different types of hydrogels, we understand the possibility to synthesize various kinds of materials that can be dedicated to specific applications. Indeed, a hydrogel can

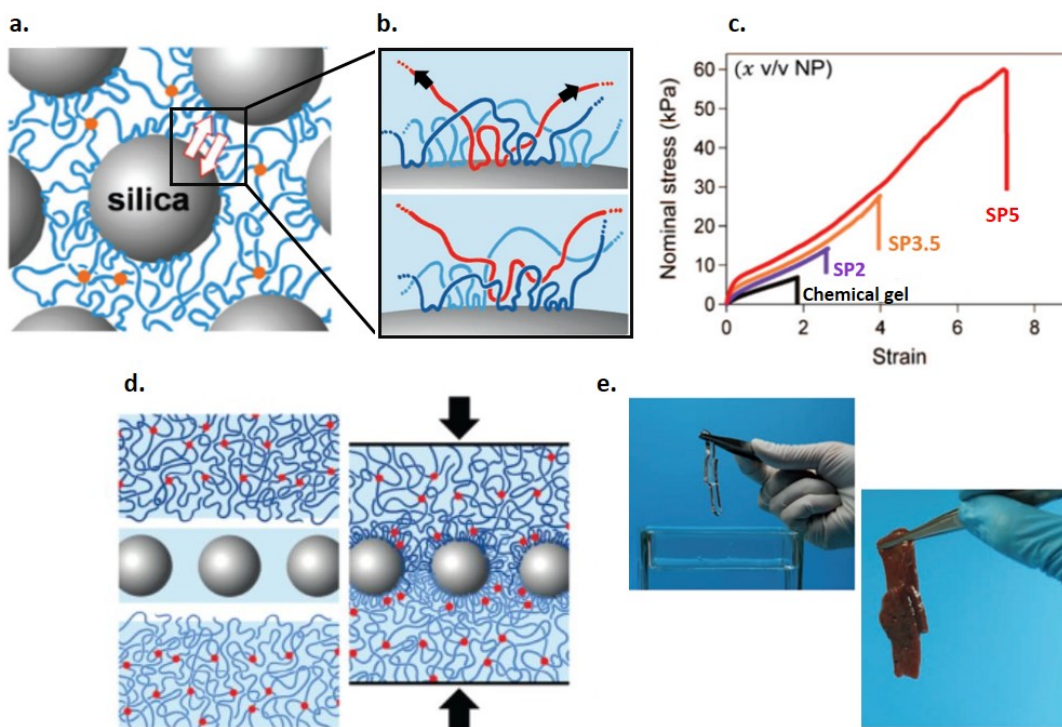


FIGURE 1.12: a) Schematics representation of hybrid hydrogels combining covalent bonds (orange dots) with physical reversible bonds (arrows). b) At adsorption equilibrium or when submitted to a tension (symbolized by the black arrows), a segment of the polymer chain detaches from the surface and can be replaced by another one. This dynamic process is at the core of the reinforcement of hybrid gels (from Rose *et al.*, 2014). c) Stress-strain curve of a tensile test until fracture for different amounts of NPs from 0 vol.% (chemical gel without silica NPs) to 20 vol.%. d) Schematic illustration of the concept of gluing swollen polymer networks together using silica NPs. e) Two pieces of gel (top) and two pieces cut from calf liver (bottom) were glued together by spreading nanosilica solution (from Rose *et al.*, 2014).

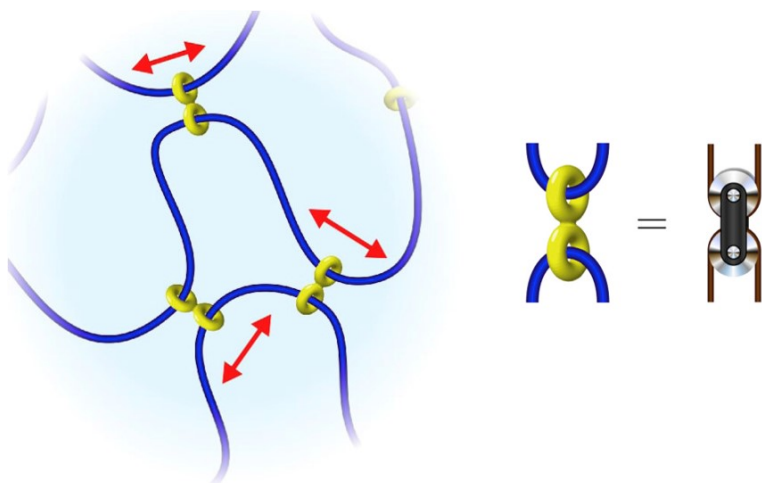


FIGURE 1.13: Schematic view of slide-ring materials with movable crosslinks. The crosslinks slide along the polymer chains acting like pulleys (from Mayumi *et al.*, 2010).

possess a wide range of mechanical properties by choosing the right amount of crosslinker and/or

different types of physical interactions. For example, their stiffness can be tunable from 0.5 kPa (PAAm) to study the stiffness dependent cell response and serve as cell substrate (Syed et al., 2015) to 1-2 MPa (DN gel of cellulose/PDMA (poly(dimethyl acrylamide)) for cartilage replacement (Azuma et al., 2007, Li et al., 2014), allowing their physical properties to be matched with different soft tissues in the human body.

The modulus and fracture energy of these materials will be compared in part. 1.3.

Getting inspired by nature is encouraging and is a great way for designing new materials that would be more suitable to our needs with a reduced impact in terms of resource consumption. Industrial applications of gels request to both enhance the mechanical properties of hydrogels and to modulate together their properties and sustainability. They need to be flexible, extensible, and mechanically resistant against stress and fracture to be easily manipulated and meet industrial applications.

## 1.2 Fracture mechanics

### 1.2.1 Why studying fracture?

Fracture is a mechanical process arising in all materials from living tissues (muscle, skin, bone...) to natural materials (wood, rubber...) or synthetic materials (nylon, acrylic, steel, polyester, carbon fiber...). Understanding fracture is significant in practical applications such as designing materials and structures. It is an important criterion in mechanics since it raises a variety of practical and fundamental physical questions. Indeed, fracture represents an extreme range of varying spatial and temporal scales where the strain energy reaches a maximum (compared to the "at rest" state) and will be ultimately released by crack propagation.

If we refer to the past, fracture caused major problems, in particular in construction. An emblematic example is the war boat engineering during World War II. As part of the government project, United States planned continuous block construction of cargo vessels ("Liberty Ship")<sup>1</sup>. About 2700 Liberty Ships were constructed from 1939 to 1945. The concepts of fracture mechanics were at their early stage at this time and 1031 damages or accidents due to brittle fracture were reported by April 1, 1946, including the "Schenectady" boat (see Fig. 1.14). The watercraft was lying at the pier when, without warning, it suddenly broke in two, with a break that was heard for at least a mile. The final report concluded that the fractures were due to the presence of cracks in steel that were sensitive to temperature (Final report of a board of investigation, United States, 1947). These accidents showed the importance of fracture toughness, and improvement in fracture mechanics has raised since then.

Fracture initiates from a defect inside the material or due to material damage under stress surrounding the cracks. Once the energy can no longer be stored in the material, it will break and the fracture will propagate allowing the energy to be released. As the Schenectady boat, hydrogels must resist fracture propagation. Once the fracture propagation has started, it is too late and the material can no longer be used. It is crucial to consider the eventuality of damage or the presence of defects, to predict the condition of crack initiation or its delay, and, finally, in the event of failure, to predict the consequences (size, velocity, and trajectory). Knowing better about fracture will also allow us to quantify the service life of hydrogels which is useful in plenty of fields.

---

<sup>1</sup><http://www.shippai.org/fkd/en/cfen/CB1011020.html>

<sup>1</sup><https://offbeatoregon.com/1606c.schenectady-cracked-ship-396.html>

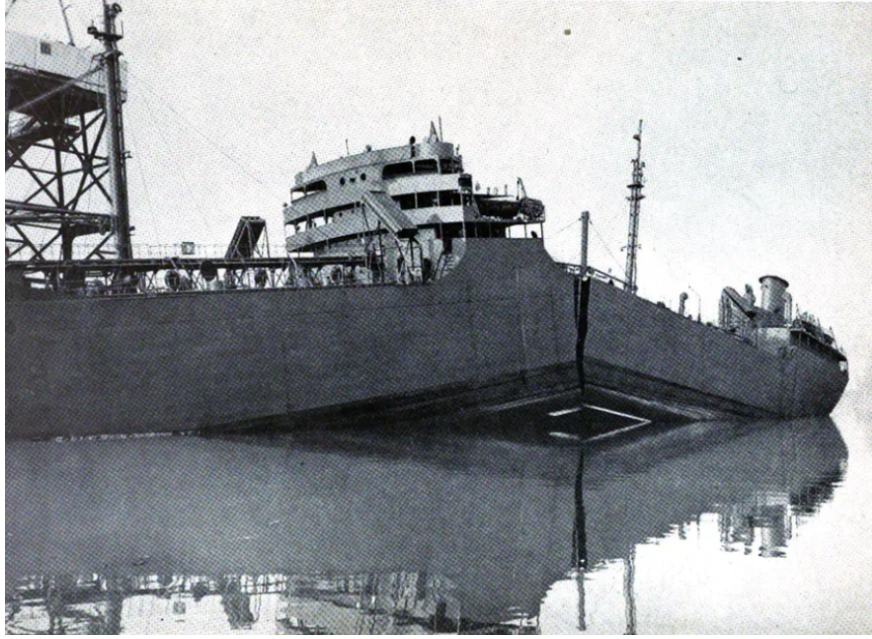


FIGURE 1.14: Schenectady boat after breaking in two on the 16th of January 1943, when it was moored at the fitting dock of Portland (Image: U.S. GPO)<sup>1</sup>.

## 1.2.2 Physical concept of fracture

### LEFM: Linear Elastic Fracture Mechanics

Fracture mechanics represents a great challenge in materials science for a century now. The fracture study started with glass on which the fracture of elastic materials is based. The foundation of fracture theory is the Linear Elastic Fracture Mechanics (LEFM) which is established on the hypothesis that the bulk material behavior remains linearly elastic everywhere except in a very small region around the crack tip. If the material is isotropic and linearly elastic, the stress field near the crack tip is calculated using the theory of elasticity.

Back in the twenties, Griffith proposed an energy-based analysis of cracks that will be considered to be the birth of the field of fracture mechanics. He postulated that a crack would grow if there is a conversion of mechanical energy (external work  $U_w$  and variations of the elastic energy  $U_{el}$ ) into a thermodynamic (reversible) energy cost per area unit to create two new surfaces. The fracture energy  $\Gamma$  is defined as the energy per unit area needed to propagate a crack:

$$\Gamma = 2\gamma_s \quad (1.3)$$

where  $\gamma_s$  is the surface energy of the material.

A strain energy release rate,  $\mathcal{G}$ , is defined (in unit of  $\text{J}/\text{m}^2$ ):

$$\mathcal{G} = \frac{\delta U_w}{\delta A} - \frac{\delta U_{el}}{\delta A} = \Gamma \quad (1.4)$$

$\mathcal{G}$  is also called the Griffith critical energy release rate and  $A$  is the surface created by crack propagation.

It turned out that Griffith neglected inelastic processes since its study applied to ideally brittle solids only. Indeed, the material Griffith used to experimentally confirm his failure criterion was glass. Glass can be considered as a model of elastic material: it is brittle, and it breaks without warning if subjected to excessive stress. Extension of Griffith's ideas for brittle solids to ductile high strength material was done by Irwin and Orowan in 1948 (Irwin, 1948, Orowan, 1949).

While the energy balance approach offers a great insight into the fracture mechanics and gives failure stress at which fracture starts, Irwin proposed a different approach where the stress intensity around the crack tip is discussed. Irwin completed Griffith's study, observing that there are three independent ways in which the two crack faces can move with respect to each other. He described the possible modes of crack behavior in the most general elastic state: crack opening, In-plane shear, and Out-of-plane shear (see Fig.1.15). In this study, we will focus on mode I, the opening mode, also called the single-edge notched specimen where displacements of crack surfaces are perpendicular to the plane of the crack.

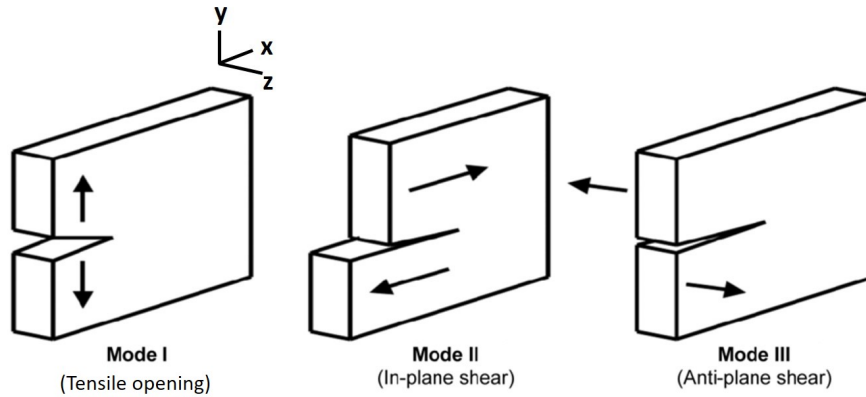


FIGURE 1.15: Three different mode of fracture.

Irwin's model is based on an infinitely large plate, subjected to an applied stress  $\sigma_\infty$ , infinitely far from the crack tip. He developed a model to describe the stress field at the crack tip induced by an external load and by the crack tip itself. The crack tip behaves as a stress concentrator. Near the crack tip, the normal stress can be approximated by:

$$\sigma_{yy}(r) = \frac{K_I}{\sqrt{2\pi r}} \quad (1.5)$$

$\sigma_{yy}$  represents the stress in the crack opening direction near the crack tip and is represented in Fig. 1.16. The K factor ( $\text{Pa} \cdot \text{m}^{1/2}$ ), here  $K_I$  for mode I, or stress intensity factor, was proposed in 1957 by Irwin to describe the spatial singularity around the crack tip and only depends on the geometry and loading conditions.  $K_I$  symbolizes the linear elastic fracture mechanics.

When the magnitude of the mode I stress intensity factor reaches a critical value,  $K_{IC}$  (when  $K_I > K_{IC}$ ), crack propagation initiates. Irwin showed that in plane stress condition, the "plane stress fracture toughness" in mode I,  $G_{IC}$ , is related to the stress intensity factor  $K_{IC}$  (Irwin, 1957):

$$G_{IC} = \frac{K_{IC}^2}{E} \quad (1.6)$$

Which is the Griffith-Irwin relationship with E, the Young's modulus. While  $K_{IC}$  defines the near-tip stress and displacement fields,  $G_{IC}$  represents the crack driving force to open that crack. For plane strain conditions,  $G_{IC}$  is multiplied by  $(1 - \nu^2)$ , with  $\nu$  the Poisson's ratio. It is worth mentioning that in most cases, materials are not perfectly elastic thus inelastic deformation such as viscoelasticity, plastic flow, void growth, microcracking and crazing can also dissipate energy in a "process zone" surrounding the crack tip. In this case, Irwin stress's approximation (Eq.1.5) needs to be corrected.

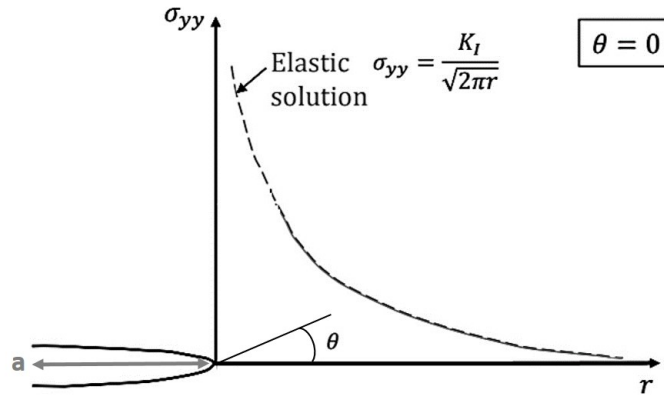


FIGURE 1.16: Stress concentration at the crack tip according to Irwin's theory. The crack depth  $a$  is defined.

### Local crack tip plasticity - Correction to LEFM

LEFM becomes increasingly inaccurate as the inelastic region at the crack tip grows, and one must take into account non linear material behavior.

If the material is non perfectly elastic, ductile fracture happens, with plastic deformation near advancing crack. This allows the crack to proceed slowly, in a more stable state because of yielding effects around the crack tip. On the contrary, the brittle fracture has little or almost no plastic deformation. Cracks spread very rapidly and are unstable because of spontaneous crack propagation (example of glass). Bringing viscoplasticity or viscosity inside the material would help to maintain, stabilize the fracture.

One can notice in Figure 1.17 the blunting effect on the stress for a non perfect elastic material.

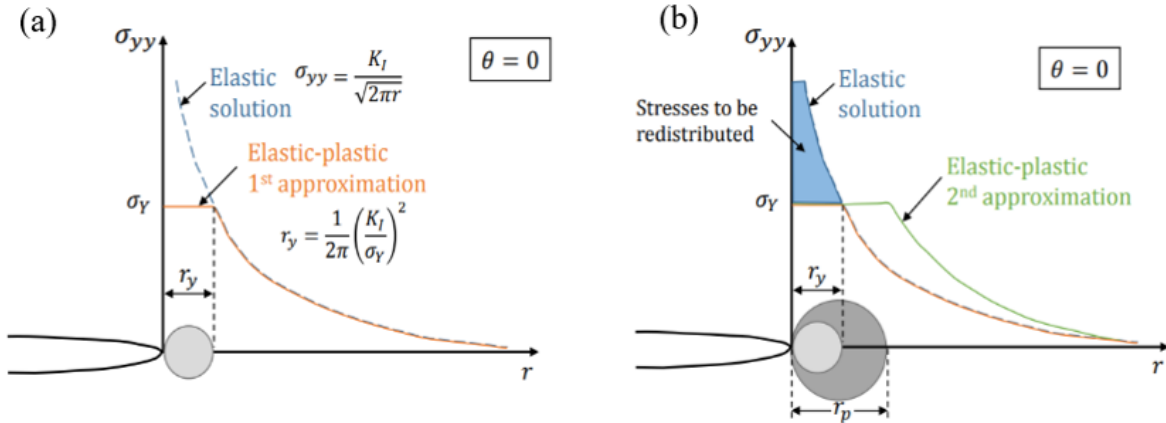


FIGURE 1.17: First order (a) and second order (b) estimation of plastic zone size ( $r_y$  and  $r_p$  respectively). The blue area in (b) represents load that must be redistributed, resulting in a larger plastic zone<sup>1</sup>.

Plasticity keeps the stress in check and hits an upper limit at yield point ( $\sigma_Y$ ). In Fig. 1.17 a, when yielding occurs, stresses need to be redistributed to satisfy equilibrium. Since the elastic stress distribution within the plastic zone is replaced by a constant yield stress  $\sigma_Y$ , the equilibrium condition along the  $y$  direction is violated. Thus, taking the second approximation, Fig. 1.17 b is obtained. Irwin's equation (Eq.1.5) is no more valid because  $\sigma$  does not decrease as  $r^{-1/2}$  but in a steeper way depending on the boundary conditions (green curve of Fig. 1.17 b). The blue

region represents forces that would be present in an elastic material but cannot be carried in the elastic-plastic material because the stress cannot exceed yield. The plastic zone must increase in size in order to accommodate these forces.

If the plastic zone size is small enough ( $r_y \ll a$ ), LEFM applies. A small plastic zone size means that  $r_y$  is roughly an order of magnitude smaller than the crack depth  $a$ .

### Greensmith's approximation

Later, the fracture energy has been investigated for non linear elastic materials like rubber. Hence, Rivlin and Thomas (Rivlin et al., 1953), then Greensmith (Greensmith, 1963), extended Griffith's work to rubber-like material. They addressed a rather simple method for the determination of the strain energy release rate or fracture energy,  $G_{IC}$  in the case of a single edge notched specimen for a long thin sample with  $a \ll e$  (where  $e$  is the sample thickness and  $a$  is the length of the cut):

$$G_{IC} = 2k(\lambda)aW_a \quad (1.7)$$

where  $W_a$  is the stored-energy density appropriate to the extension ratio  $\lambda$  (length  $L$ /initial length  $L_0$ ) in the simple extension region, and  $k(\lambda)$  is a numerical factor that varies with  $\lambda$ . It is a strain-dependent correction associated to the lateral contraction of the sample in extension. It was found experimentally by Greensmith from elastic measurements that  $k$  decreases from a value of about 3 at low extensions to a value somewhat below 2 at  $\lambda = 3$  (Greensmith, 1963). Finally, Lindley used finite element analysis to confirmed this result on a single-extension strip (Lindley, 1972) :

$$k = \frac{3}{\sqrt{\lambda}} \quad (1.8)$$

Hence, the fracture energy at the onset of crack propagation is given by:

$$G_{IC} = \frac{6aW_a}{\sqrt{\lambda}} \quad (1.9)$$

These equations account for the nonlinear elastic response of the material. When the inelastic deformations are small compared to the size of the crack, also called small-scale yielding, this equation also belongs to LEFM. In soft dissipative material, as tough gels, energy dissipation is a key aspect. Therefore, dissipative processes relax stress in a wide region in front of the crack tip but can also happen everywhere in the gel in case of large deformations. If large dissipative zones develop before the crack grows, LEFM is no longer valid and non-linearity and viscoelasticity must be taken into account.

## 1.3 Application of fracture theory on gels: design of tough gels

This part focuses on the fracture of highly deformable materials: gels. Before rupture, covalently crosslinked gels are capable of large and almost elastic deformations. Over the years, original network designs have given rise to gels tougher and more stretchable, making the quantification of fracture energy even more challenging. Indeed, gels present nonlinear elasticity and intricate coupling with dissipative mechanisms (damage, viscoelasticity, etc.)

<sup>1</sup><https://engineeringlibrary.org/reference/fracture-mechanics-plastic-yielding-at-crack-tip>

### 1.3.1 Fracture toughness

Fracture toughness is an attractive topic. It is defined in reference to the initiation and growth of a pre-existing crack under loading.

#### Simple network: Lake and Thomas theory

According to Lake and Thomas theory (Lake et al., 1967), which successfully accounts for rubber toughness, the fracture energy of a polymer network is dominated by the length of polymer strands between crosslinks and surface density that penetrate the crack plane (see Fig. 1.18).

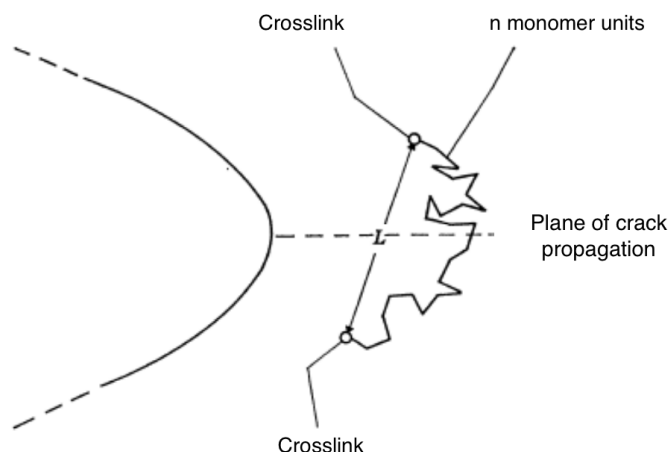


FIGURE 1.18: A macromolecular view of the strengthening mechanisms of highly elastic materials which consist of flexible long-chain molecules cross-linked at intervals. The plane of crack propagation ahead of the tip of a crack is crossed by a number of polymer chains whose cross-links lie on opposite sides of the plane. Such a chain is supposed to contain  $n$  monomer units and to have a distance  $L$  between cross-links (from Lake et al., 1967).

From the basic picture of a network formed by a collection of long and flexible chains, Lake and Thomas proposed an estimate of the threshold energy  $G_{LT}$  to propagate cracks in unfilled rubbers:

$$G_{LT} = \Sigma N_C J \quad (1.10)$$

where  $\Sigma$  is the surface density of chains crossing the fracture plane,  $N_c$  is the number of monomer units between cross-links, and  $J$  is the energy required to break one covalent bond. Such argument is based on the assumption that the transmitted load throughout the network brings each bond in a polymer strand crossing the interface close to its maximal free energy (i.e. the dissociation energy of the weakest bond in the monomer unit).

The 21st century saw the emergence of new kinds of hydrogel networks where the gel is more complex than polymer chains held together by crosslinks. Mechanisms in front of the crack tip can not be reduced to bonds crossing the fracture plane and Greensmith equation (Eq. 1.9) is generally used to calculate the gel's fracture toughness through the stress/strain curve of a fracture test.

#### Complex networks: Greensmith theory

It exists a lot of ways to enhance fracture toughness including the introduction of hybrid networks with irreversible and reversible crosslinks (Henderson et al., 2010, Sun et al., 2013), composite gels with macromolecular microspheres (Huang et al., 2007) or nanoparticles (Haraguchi et al.,

2002, Lin et al., 2010, Wang et al., 2010, Rose, 2013), slide-ring crosslinks (Imran et al., 2014), ionic crosslinks (Kong et al., 2003) and dual crosslinks (Mayumi et al., 2013) or phase-separated gels (Guo et al., 2016). The three examples presented in part. 1.1.3 are reused here to compare their fracture toughness. Their networks are illustrated in Fig. 1.19.

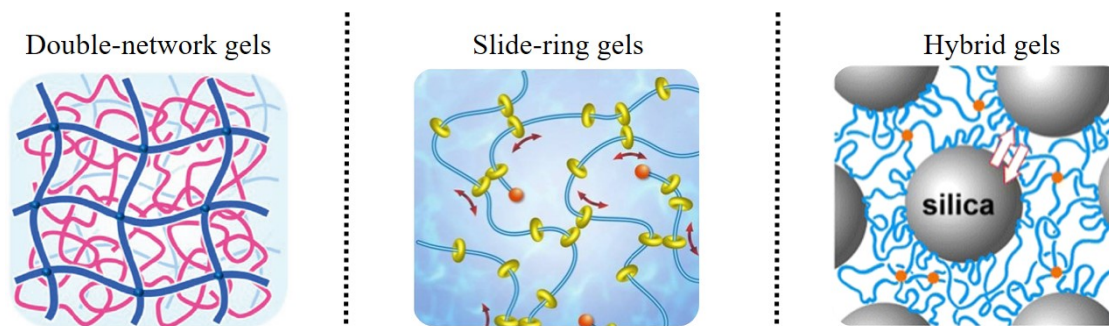


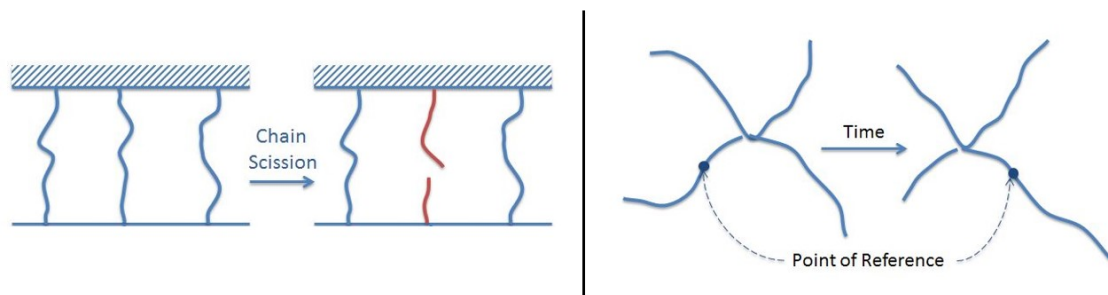
FIGURE 1.19: Dissipation mechanisms to increase fracture toughness. From left to right : Double-network gels (Gong et al., 2003), slide-ring gels (Ito, 2010), nanohybrid gels (Rose, 2013).

Based on Greensmith equation (Eq. 1.9), fracture energies of these three gels have been calculated. Gong's DN gels have tensile fracture stress and tearing fracture energy much higher than those of conventional single network hydrogels, i.e.,  $\sim 0.1$  MPa and  $\sim 10$  J.m $^{-2}$  for the single PAAm gels compared to  $\sim 8$  MPa and  $\sim 4,000$  J.m $^{-2}$  for the DN hydrogel, respectively (Gong et al., 2003). The key mechanism behind the dramatically enhanced fracture toughness is the energy dissipation due to the breakage of the sacrificial bonds near the crack tip while the other network maintains the macroscopic integrity of the gel. For slide-ring gels, two different ring coverage on axis polymer were tested (2% and 25%). Gels fracture energies were determined to be 5 and 30 J.m $^{-2}$ , respectively (Liu et al., 2019b). Gel exhibiting higher fracture toughness have less crosslinks, thus allowing a higher stress redistribution. Concerning hybrid hydrogels with silica nanoparticles (NPs), the fracture toughness appears to be 470 J.m $^{-2}$  (with 20 vol.% of SiO $_2$  NPs) compared to 10 J.m $^{-2}$  for the chemical gel (without silica NPs) (Rose, 2013). Fracture energy  $G_{LT}$  from Lake and Thomas (Lake et al., 1967), i.e in the absence of viscoelastic dissipation, has also been calculated for the chemical gel. The calculation of this fracture energy gives about 1.2 J.m $^{-2}$  and accounts for the macromolecular architecture. This value is in rather good agreement with the experimental results of Rose (10 J.m $^{-2}$ ) (Rose, 2013).

### 1.3.2 Chain scission vs disentanglement

Fracture involves material separation, which implies separating bonds (chemical or physical types). Fracture on the atomic level is called chain scission. In pure elastic gel, during stretching, the chemical interactions break due to strong stress concentration that ruptures the strand between crosslinks and this finally leads to failure. Indeed, polymer segments crossing the fracture plane are stretched until they store an elastic energy per monomer of the order of the covalent binding energy (Eq. 1.10 and Fig. 1.18 from the Lake and Thomas theory). A hydrogen-bonded network is likely to behave differently. Indeed, hydrogen bonds are considerably weaker than covalent bonds and can reform after scission.

The challenge has been to avoid fracture through smart solutions using physical bonds. Physical gels fracture is a scissionless process, also called chain disentanglement, where molecules separate from one another intact (see Fig. 1.20). This is the case for slide-ring gels but also for gelatine gels by "unzipping" process (Baumberger et al., 2006). Recently, Baumberger (Baumberger et al., 2020) wrote an exhaustive review about the control of crack propagation in polymer hydrogel by environmental conditions.

FIGURE 1.20: Chain scission and chain disentanglement<sup>1</sup>.

Anisotropy also plays a role in the fracture process. Meng and colleagues (Yang et al., 2019) worked on nanocomposite hydrogels with the use of cellulose nanofibrils (CNFs). Fibrils, being directional on the contrary to the nanoparticles (being spherical), create an alignment under strain. Indeed, the CNFs are largely oriented parallel to the loading direction to maximize the energy dissipation. This implies that the CNFs initiate deflection of crack propagation fronts and thus increase the strain energy for the continuation of the fracture. This crack bifurcation can also proceed on purely organic systems by fiber-like phase-separated domains (Guo et al., 2016).

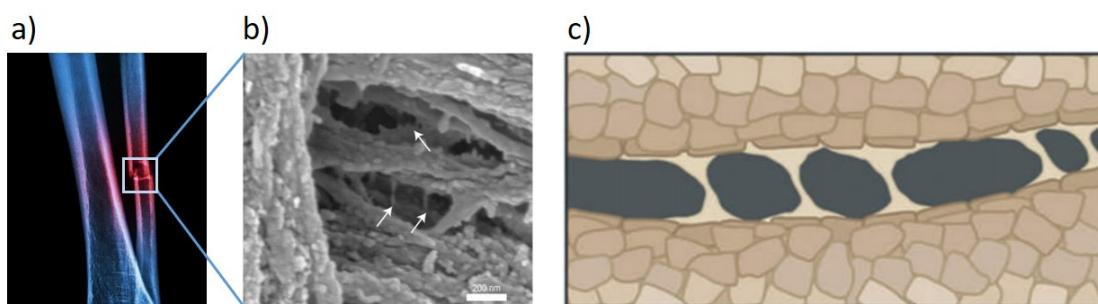


FIGURE 1.21: a) Example of a bone fracture: X-ray of the fibula (leg bone) fracture. b) Scanning electron microscope image of individual collagen fibrils together with glue filaments (arrows) (human trabecular bone). c) Schematic representation: When a force is applied, the glue resists the separation of the fibrils and filaments form between the mineralized fibrils (b) and c) from Fantner et al., 2005).

In biological tissues like bones, resistance to fracture derives from a multitude of deformation and toughening mechanisms taking place at many size scales ranging from the nanoscale structure of its protein molecules to the macroscopic physiological scale (Launey et al., 2010). In bones, the mineralized collagen fibrils that are the basic building blocks of the bone are held together by a non-fibrillar organic matrix, which acts like glue (see Fig. 1.21). When a force is applied to the bone, the glue resists the separation of the mineralized collagen fibrils, thereby counteracting the formation of cracks. When the glue is stretched, energy is dissipated through rupturing of sacrificial bonds and the stretching of hidden length (Fantner et al., 2005). This new concept of hidden length is also really important in the comprehension of energy dissipation in the process zone near the crack tip and could explain the fracture delay (see Fig. 1.22).

To conclude, these last examples show that the incorporation of physical crosslinks has positively influenced the fracture behavior of hydrogels.

<sup>1</sup><https://polymerdatabase.com>

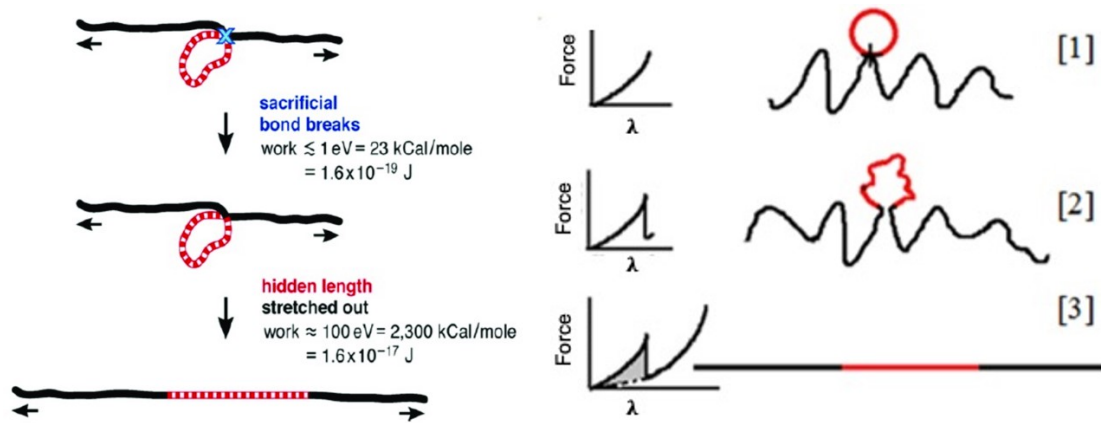


FIGURE 1.22: a) Schematic drawing of the basic principle of the sacrificial bond-hidden length (SBHL) mechanism. It takes much more work to stretch a hidden length than to break a bond (*from Fantner et al., 2005*). b) [1] Before a sacrificial bond is broken, only the black length of the molecule contributes to the entropic configurations and to the force with which the molecule resists stretching. The red length of the molecule is hidden from the force by the sacrificial bond. [2] When the bond fracture threshold is reached, the bond breaks and the whole length of the polymer (black plus red) contributes to its entropy. The force supported by the polymer molecule abruptly drops in response to this sudden increase in entropy. [3] As the polymer molecule is further stretched the force it supports increases, until the entire molecule detaches from the substrate and ruptures. The grey area represents the extra work done in stretching a polymer with SBHL system relative to a polymer of the same length but without the SBHL system (*from Elbanna et al., 2013*).

### 1.3.3 Experimental stress field at the crack tip in single notched gels

It is still challenging to predict the failure of soft tough materials due to the strongly nonlinear and dissipative deformation involved. Extensive work has been devoted to the improvement of the description of the mechanical fields near the crack tip. Gels are model systems used to explore nonlinear fracture mechanics. It is easy to tune the mechanical properties from very soft to very hard material (1 kPa to 1000 kPa) or purely elastic with  $\tan \delta = G''$  (plastic component)/ $G'$  (elastic component) = 0.01 to dissipative gel  $\tan \delta = 0.2$ . Yet, very few groups cope with gel synthesis and design and study of fracture mechanics (Long et al., 2020). There is no technique today to measure a local stress field. Therefore, a popular technique is to measure the strain caused by the opening of the notch with different COD (Crack Opening Displacement) compared to the closed state. Then, it is conventional to get a stress field indirectly through the strain field. We understand there is a lack of technique in the study of fracture and especially in the direct and local stress measurements (Marcellan et al., 2006).

Fineberg and colleagues (Livne et al., 2008) investigated fracture dynamics using polyacrylamide gels purposively chosen for their ideal elastic response. It is expected that the fracture dynamics mirrors the one of typical brittle material.

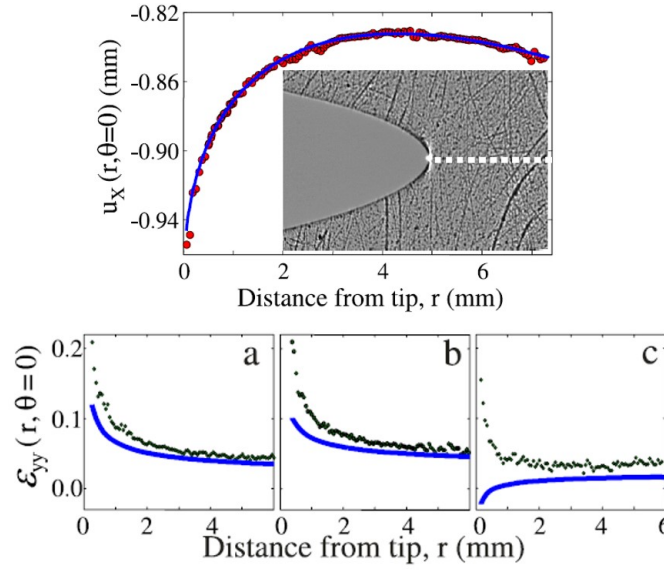


FIGURE 1.23: Top: Scratch patterns imprinted on the gels are used to measure the displacement field in the  $x$  direction surrounding the crack tip via particle tracking. The deformation is larger near the crack tip. Bottom: The measured strain  $\epsilon_{yy}$  is compared to the LEFM prediction (blue line). The prediction is not enough singular. The discrepancy between the LEFM and experiment increases with the crack velocity: (a)  $v = 0.20c_s$ , (b)  $v = 0.53c_s$ , (c)  $v = 0.78c_s$ ,  $c_s$ , being the shear wave speed of the gel. For the higher velocity (c), LEFM predicts a negative strain (compression) ahead of the crack tip. The measurements make more intuitive sense than the LEFM predictions since tensile fracture occurs under extension (from Livne et al., 2008).

To probe the crack tip, they used particle tracking. The face of one plate was randomly scratched with aluminum powder. The resulting scratch pattern was used as a "tracer field" for visualization of the displacement field and did not affect the crack dynamics. It appeared that near the tip, the measured stress intensity factor is non-unique, the crack tip deviates from its predicted parabolic form and the strains ahead of the tip are more singular than the  $r^{-1/2}$  divergence predicted by LEFM (see Fig.1.23). For high crack velocity, LEFM fails at predicting the stress ahead of the crack tip.

Lefranc and Bouchaud (Lefranc et al., 2014) shared the same conclusions: for slower cracks where the applied displacements are small, the COD is found to agree with the LEFM prediction and it has been verified by simulation (FEM) with the assumption of static crack (Long et al., 2016).

One of the most widely used methods in materials science to study material deformation is the DIC (Digital Image Correlation). DIC is a non-contact, full-field deformation measurement method. It makes measurements by recognizing patterns between images. This differs from particle tracking where particles are tracked between images based on some geometrical features that allow their unique identification and matching between images. Several researchers have applied 2D DIC to study the material response involving strain concentration of soft materials: strain closed to a notch in an agarose gel (Kwon et al., 2010), strain near a growing crack in a polyacrylamide-alginate hydrogel with an edge crack (Zhang et al., 2015), surface strain induced by a spherical tip indenter on chitosan hydrogels (Sasson et al., 2012), strain fields induced during the insertion of a needle into soft tissue phantoms (Leibinger et al., 2016) and bubble cavitation damage to a tissue surrogate (Hong et al., 2016).

Liu and colleagues (Liu et al., 2019a) used this technique on Poly(vinyl) alcohol (PVA) hydrogels. They focus on crack propagation under steady-state conditions. They have shown that the

simulation accurately predicts the crack profile under large deformation and that the calculated stress is consistent with the corresponding asymptotic field (see Fig. 1.24).

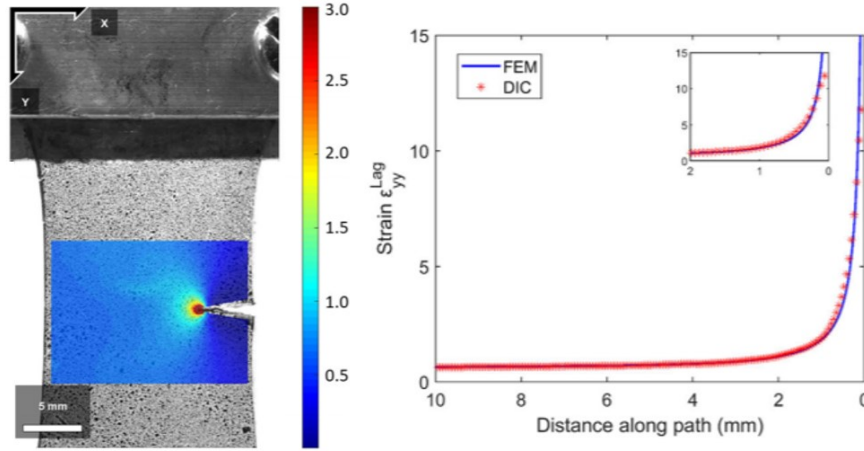


FIGURE 1.24: Results of the DIC strain measurements of an edge-notch specimen a) Distribution of  $\epsilon_{yy}$ , strain in the crack opening direction for the edge notch specimen - B) Comparison between DIC and FEM (Finite element method) along a path ahead of the crack tip (from Liu *et al.*, 2019a).

FEM was based on a 3D large deformation nonlinear viscoelastic model. The gel was assumed to be incompressible and isotropic. A numerical scheme was developed in prior works by Guo and colleagues (Guo *et al.*, 2018).

From this model, the dominant stress component near the crack tip is:

$$\sigma_{yy}(r, \theta = 0) = \frac{\mu a^2}{4r} \propto \frac{1}{r} \quad (1.11)$$

This model is in good agreement with their experimental results found through DIC (see Fig. 1.24, right). LEFM ( $\sigma \sim r^{-1/2}$ ) is not applicable since the PVA hydrogel is crosslinked by both permanent covalent bonds and reversible physical bonds making it non-elastic. As expected with the theory of crack tip plasticity (part. 1.2.2), the stress field ahead of the crack tip is steeper than the one predicted by LEFM.

In the same year, Liu and coworkers (Liu *et al.*, 2019b) analyzed the local stress/strain field of slide-ring gel using the photoelasticity principle. A high-speed polarized light camera is used to record the geometry changes of crack during fracture tests at the frame rate of 250 fps (frames per second) and to obtain the local stress/strain distribution at the crack tip. This is a coupled experience where the stress is calibrated with a conventional mechanical tool. Right before crack propagation, it appears that the stress shows a singularity at the crack tip as indicated by LEFM theory with a trend of  $x^{-1/2}$  (see Fig. 1.25, right).

The difference in the blunting effect (see Fig. 1.25, left) is due to the percentage of ring coverage on axis polymer (2% vs 25%). Compared to conventional chemical gels with fixed strand length between covalent crosslinks, one advantage of the SR network structure emerged in the modulus-independent fracture energy. The two crosslinks at opposite sides of the fracture plane tend to slide away from each other, and the strand length at the crack tip is dominated by the slidable range of crosslinks instead of the Young's modulus. It is interesting to notice that in the case of SR gels, LEFM theory applies well even near the crack tip compared to the others gel studied in this section.

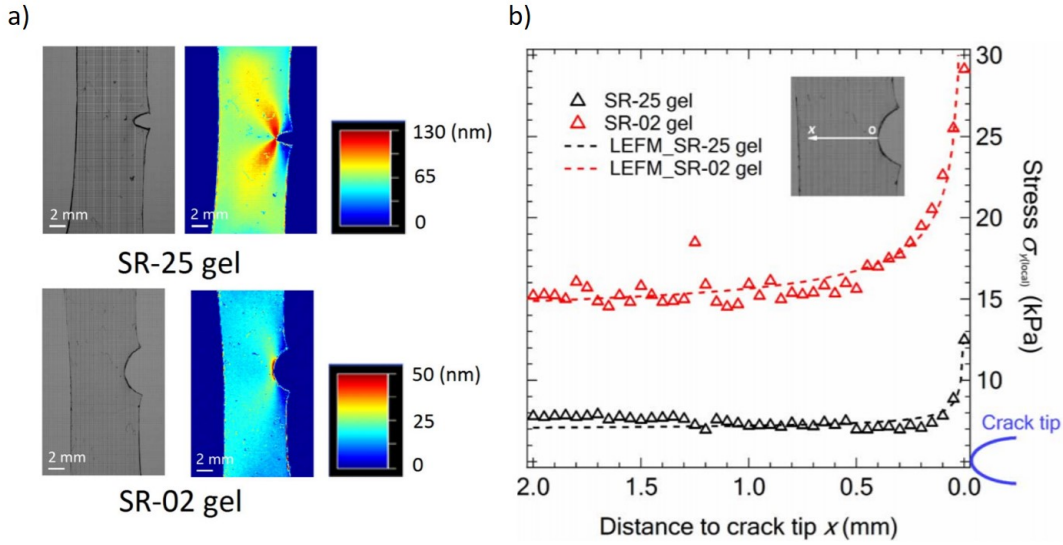


FIGURE 1.25: Gray scale and polarized-light images and retardation maps of the notched SR-25 (25% of ring coverage on axis polymer) and SR-02 (2%) gels right before crack propagation (from Liu et al., 2019b).

It has been suggested that the crack blunts before propagating when the cohesive strength (fracture stress  $\sigma_f$ ) exceeds the Young's modulus  $E$  of the gel by a factor of two (Hui et al., 2003, Luo et al., 2014). In the case of SR gels,  $\sigma_f/E$  is calculated to be 1.1 (for a percentage of ring coverage on axis polymer of 25%) and 2.8 (for a percentage of 2%). This estimation agrees well with the experimental observation: the gel with a percentage of ring coverage on axis polymer of 25% does not show obvious crack blunting, whereas the gel with 2% does (see images of Fig. 1.25). Gong and co-workers worked on polyampholyte hydrogels composed of weak and strong interactions. They also showed that the initial modulus  $E$  and the fracture stress  $\sigma_f$  of the hydrogel both increase with the stretch rate, and their ratio  $\sigma_f/E$  was found to be a key factor to determine the blunting (Luo et al., 2014). Fig. 1.26 shows the crack blunting before crack propagation.

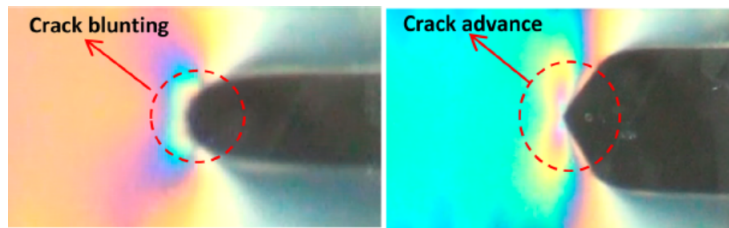


FIGURE 1.26: Isochromatic images of the polyampholyte hydrogel during the crack propagation (from Luo et al., 2014).

Fracture mechanics is a complex subject, and moreover on a complex material as hydrogels. A lot of works needs to be done since it is relatively a new material. Some aspects of fracture processes, unexplored so far, like the through-thickness stress must be elucidated by others methods. Techniques to fully study the fracture of soft matter are lacking. Shedding light on this fracture subject could be of great importance for physicians to understand organ fracture, hydrogels being close to biological tissues in terms of mechanical behavior (non linearity, anisotropy, and viscoelasticity).

## Chapter 2

# Theoretical and experimental aspects: US imaging and conventional mechanics

### Content

This work, based on the collaboration of two laboratories, is an interdisciplinary project. The aim is to bring together two different, yet complementary, methods. The conventional mechanical tests are performed by a mechanical testing tool that allows compression/tensile tests (Instron) and a rheometer for frequency sweep experiments. The other method, based on wave physics, is an imaging ultrasound (US) tool commonly used for medical diagnosis. For this thesis, the ultrasound imaging tool left the hospital for three years to dedicate its work to the study of soft materials fracture. The purpose is to come back with more knowledge on the local and real-time mechanisms involved in fracture processes and, of course, our understanding in the medical diagnosis especially when the tissue is subjected to abnormal stresses, like a tumor pushing through tissues.

The first part of this chapter will describe the theoretical background for mechanics and wave physics. Then, elastography will be presented followed by the theory of acoustoelasticity. Finally, the synthesis procedure of the hydrogels will be described as well as the different techniques used during this thesis to understand fracture in soft matter. These combined techniques, presented in Fig. 2.1, allow a large range of frequency studies.

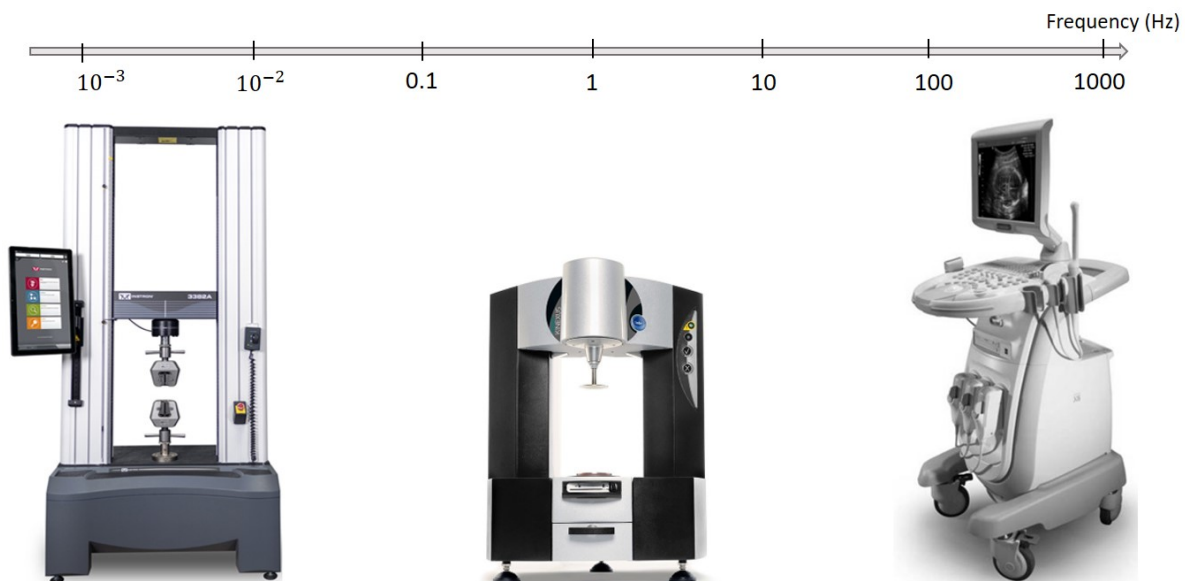


FIGURE 2.1: Bridging study: Conventional mechanical testing machines: Instron (left) and Rheometer (middle) with US imaging tool (Aixplorer).

## 2.1 Mechanical wave propagation

### 2.1.1 Compression waves and Shear waves

Mechanical waves propagate through a medium with energy transport but without material transport. They are vectors of information useful to probe the mechanical properties of a material or a biological tissue. There are plenty of waves traveling on Earth. On small scale, in our body, waves are created due to physiological vibrations as mechanical heart contraction or vibrations induced by respiration and vocal cords, and finally by external shocks in all day life. At a larger scale, earthquake creates waves that propagate through the earth's surface. Two types of mechanical waves propagate through solids: the P wave (compression or longitudinal wave) and the S wave (shear wave) (see Fig. 2.2).

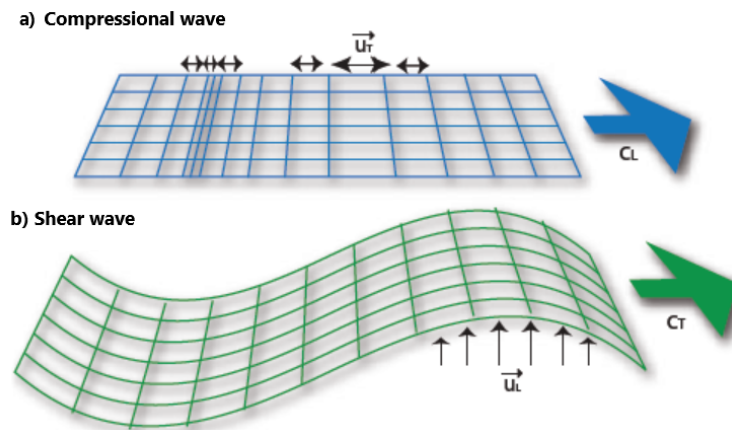


FIGURE 2.2: a) Compressional wave, also called P wave or primary wave. They leave behind a trail of compressions and rarefactions on the medium they move through. P waves are also called pressure waves for this reason. They shake the medium in the direction in which they are propagating. b) Shear wave, also called S wave or secondary wave travels much slower than P wave and can travel only through solids. They shake the medium in the direction perpendicular to which they are moving (from Deffieux, 2008)

P waves change the volume of the material through which they propagate (compression and rarefaction of the material as the wave passes through it). S waves involve shearing and rotation of the material as the wave passes through it, but not volume change. The particle motion of P plane waves is in the same direction as that of wave propagation (L stands for longitudinal). In plane S waves (secondary wave), the particle motion is perpendicular to the propagation direction (T stands for transverse) (see Fig. 2.2). In the results part, we will talk about the shear wave velocity as  $v_{ij}$ , with the index  $i$  corresponding to the direction of the shear displacement, here  $u_L$ , while the second index corresponds to the axis of propagation of the shear wave, here  $u_T$ .

### 2.1.2 Focus on the Ultrasound compression wave

The first very high-frequency sound waves above the limit of human hearing were generated by English physiologist Francis Galton in 1876 (Woo, 2002). The real breakthrough in the evolution of high frequency echo-sounding techniques came when the piezoelectric effect in certain crystals was discovered by Pierre Curie and his brother Jacques Curie at ESPCI laboratory in Paris in 1880. They observed that an electric potential would be produced when mechanical pressure was exerted on a quartz crystal: this is the direct piezoelectric effect. This is how ultrasound transducers receive the sound waves (Fig. 2.3 b). The reverse effect also happens, converting

electrical energy into kinetic or mechanical energy. This is how ultrasound transducers produce sound waves (Fig. 2.3 a).

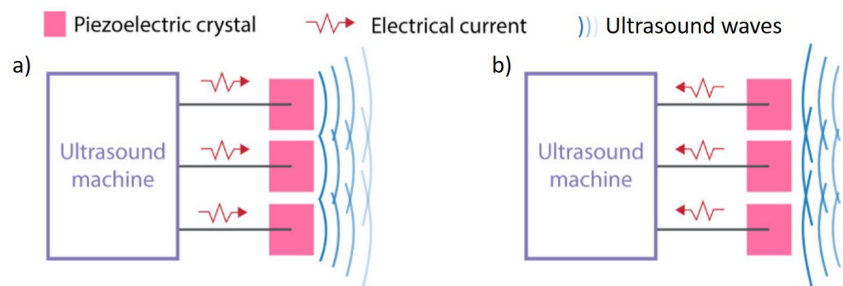


FIGURE 2.3: a) Application of an electrical current to the crystal causes it to vibrate and thus generate ultrasound waves. b) Reflected sound waves hit the crystal causing it to vibrate and generate an electrical current that is analyzed by the ultrasound machine<sup>1</sup>.

If an object is in the path of the ultrasound wave, this one bounces and returns an echo back to the transducer (see Fig. 2.4). By simply determining the time between the emission of the sound pulse and its reception, the transducer can determine the range and orientation of the object.

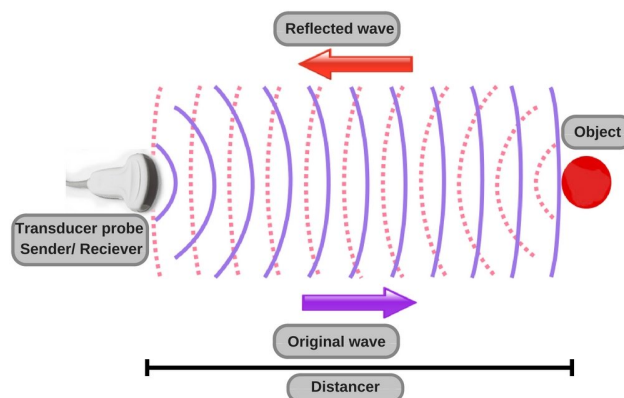


FIGURE 2.4: Scheme of how sonar (more generally ultrasounds) works: Ultrasounds are emitted from the transducer probe and come back as reflected waves after bouncing on an object.

Although animals like dolphins and bats use ultrasounds for communication and object detection for millions of years (called echolocation) (Thomas et al., 2004), humans waited until the twentieth century to explore ultrasounds. Indeed, the first ultrasound application developed for humans was the detection of submarines during the first World War. Called the sonar (Sound Navigation and Ranging) and invented by Paul Langevin, former ESPCI director, it was the first tool to map the ocean.

It started in 1916 when Langevin succeeded in obtaining echoes from a sheet of metal at a distance of 200 meters using an electrostatic projector and a carbon-button microphone. In 1917, Langevin used for the first time the piezoelectric effect combined with vacuum tube amplifiers in underwater sounding equipment. This is thought to be the first use of electronics in this manner. With this new technology, echoes were received from a submarine for the first time, in 1918, as deep as 1500 meters.

<sup>1</sup><https://ecgwaves.com/topic/the-ultrasound-transmitter-probe/>



FIGURE 2.5: Left: Paul Langevin (right) and Marcel Tournier (left) doing ultrasound experiments in ESPCI (undated)<sup>1</sup>. Right: Paul Langevin in his office at ESPCI (between 1944 and 1946) during his years as ESPCI director<sup>2</sup>.

Langevin is an eminent figure in the development of ultrasound (represented at ESPCI in Fig. 2.5). Not only, Langevin was the ESPCI director from 1944 to 1946, but he also distinguished himself for his outspoken anti-fascist views. He was imprisoned in Fresnes and later placed under house arrest in Troyes. The execution of his son-in-law and the deportation of his daughter to Auschwitz (which she survived) forced Langevin to escape to Switzerland in 1944<sup>3</sup>. He finally returned to Paris finishing his life as the head of its old school. He died in December 1946.

### 2.1.3 Use of ultrasound in the medical field

Initially used for object detection in liquid media, scientists tried to use ultrasound for medical applications. In 1942, Neurologist Karl Dussik is credited with being the first to use ultrasonic waves as a diagnostic tool<sup>4</sup>. He transmitted an ultrasound beam through the human skull in an attempt of detecting brain tumors. At this moment, it was clear that ultrasound technology will become a powerful tool for diagnosis since it is non-invasive and painless.

In our current culture, ultrasounds are best known for their use during pregnancy to produce a sonogram, to view inside the belly of a pregnant woman. The year 1958 marked the publication of the first article in obstetric ultrasound: "Investigation Of Abdominal Masses By Pulsed Ultrasound" in the Lancet Journal (Donald et al., 1958).

It is easy to probe the body and produce an image of morphological type because compression waves propagate in an almost homogeneous medium and are only partly reflected by the local interfaces at each depth during their travel. The reflections at boundaries between two different media occur because of differences in a characteristic known as the acoustic impedance  $Z$  of each substance. Impedance is defined as  $Z = \rho v$ , where  $\rho$  is the density of the medium (in  $\text{kg.m}^{-3}$ ) and  $v$  is the speed of sound through the medium (in  $\text{m.s}^{-1}$ ). At the boundary between media of different acoustic impedance, some of the wave energy is reflected and some is transmitted. The greater the difference in acoustic impedance between the two media, the greater the reflection and the smaller the transmission. The human body is composed of a lot of components of different acoustic impedance from bones to muscle, fat, or liquids. During pregnancy, the fetus develops

<sup>1</sup>[https://twitter.com/bibli\\_espci/status/1012250579496853504](https://twitter.com/bibli_espci/status/1012250579496853504)

<sup>2</sup><https://www.espci.psl.eu/fr/actualites/2020/archives-paul-langevin-un-tresor-en-ligne>

<sup>3</sup><https://www.ob-ultrasound.net/langevin.html>

<sup>4</sup><https://www.ob-ultrasound.net/dussikbio.html>

in the cavity and bathes in the amniotic fluid (see the echography in Fig. 2.6). The difference of compressibility between the liquid and the fetus bones is large, making it easy to spot.



FIGURE 2.6: Example of an echography<sup>1</sup>. The difference in the contrast is due to the impedance  $Z$ .

From the time between when the original signal is sent and when the reflections from various boundaries between media are received, the nature and position of each boundary between tissues and organs may be deduced. This is conventional ultrasound: it consists of successively focusing the ultrasounds (by applying delays to the emission) to concentrate the energy in a small area of the image. The echoes are then recorded by the device and are called the RF signals (for radio frequency). These signals are then processed in a beamforming step to reconstruct the image. Beamforming or spatial filtering is a signal processing technique used in sensor arrays for directional signal transmission or reception (Van Veen et al., 1988). The beamforming step aims at estimating the echogenicity distribution according to the echoes received. It is based on the assumption of a constant ultrasound velocity in the whole medium. The average propagation speed for sound in body tissue is  $1540 \text{ m.s}^{-1}$ . A final image is then made from all the illuminated regions.

## 2.2 Shear Wave Elastography

### 2.2.1 Definition of elastography

One of the oldest concepts in medicine had been described by Hippocrates in ancient Greece more than 2000 years ago: the principle of palpation. This method is still used by today's doctors but remains qualitative. Almost 30 years ago, Ophir and colleagues find a way to describe it quantitatively and called it: elastography, which comes from Greek: *elastos* means "ductile, flexible," and *-graphia* for "description of".

### 2.2.2 Quasi-static elastography

Elastography is an imaging technique that allows getting the tissue elasticity. It was first developed in 1991 by Cespedes and Ophir to reproduces the palpation performed by clinicians (Ophir et al., 1991). The clinician applies a gentle compression (represented by  $\sigma$  on Fig. 2.7) and the tissue response is recorded by the ultrasound transducer. The displacement and the generated strain  $\epsilon$  are then estimated using a two-dimensional correlation of ultrasound images (B-mode images) (see Fig. 2.7). The Young's modulus  $E$  is then given via Hooke's law ( $\sigma = E\epsilon$ ), which links the

<sup>1</sup><https://www.imbm-radiologie.com/>

stress ( $\sigma$ ) and the strain ( $\epsilon$ ) in a purely elastic medium (this concept will be studied in part 2.3.1, in mechanics). In practice, since the applied stress is unknown, only the strain is displayed, this strain map is sometimes called the elastogram.

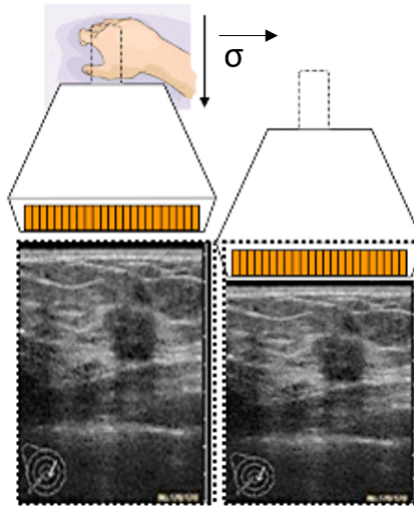


FIGURE 2.7: Illustration of quasi-static elastography: A stress  $\sigma$  is applied and the deformation  $\epsilon$  is estimated by 2D correlation of ultrasound images (from Deffieux, 2008).

In 1994, Ophir et al. (Ophir et al., 1994) published another paper where they showed that elastography can depict muscle structure at the muscle bundle level and they demonstrated differences in the elastic moduli of muscle bundles, connective tissue and fatty separations. Static elastography has also been applied to the breast *in vivo* (Cespedes et al., 1993; Krouskop et al., 1998) and to the prostate *in vitro* (Krouskop et al., 1998).

### 2.2.3 Dynamic elastography

Dynamic elastography differs from quasi-static elastography because in the first case, the sample is excited mechanically at a certain frequency while in the second case, the stress is applied manually (no frequency involved). The dynamical technique allows a quantitative result of the elasticity and a better resolution compared to the quasi-static method. It requires a more complex setup. Indeed, this method introduces the creation of shear waves to get elasticity information. The shear waves are created with a vibrational motor or by acoustic radiation force. Then, we need a detection setup to follow the shear waves which create micrometer displacements in the medium while propagating.

#### Fibroscan

In 1998, in France, Mathias Fink and his team (S. Catheline, L. Sandrin and M. Tanter) proposed to track at ultrafast frame rate the propagation of a shear wave using an ultrasonic probe. This concept called Transient Elastography was first applied to 1D measurements (Catheline, 1998). Based on this initial work, Laurent Sandrin former student of Fink's lab created the commercial device FibroScan (FS) for the estimation of liver fibrosis (Echosens, Paris, France). It was then extended to 2D imaging during J. Bercoff thesis (Bercoff, 2004).

The fibroscan is the first elastography technique developed to quantitatively and noninvasively assess soft biological tissue stiffness *in vivo*. The fibroscan uses an ultrasound probe combined with a vibrator to create the shear wave source and image with plane waves at the same time. It

is called Transient Elastography because a short mechanical impulse is used for excitation application and its transient propagation is imaged in some milliseconds (see Fig. 2.8).

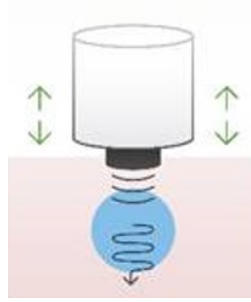


FIGURE 2.8: Fibroscan principle: ultrasound probe mounted on a vibrator creates the shear waves longitudinally to the ultrasound sent (from Sigrist et al., 2017).

This technique is widely used for fibrosis staging since it was the first time clinicians were able to determine a global elasticity score to quantify the liver fibrosis state (Sandrin et al., 2003). Shear wave velocity is determined by measuring the time the vibration wave takes to travel to a particular depth inside the liver. The shear wave carries important information since the product of the medium density,  $\rho$ , times the square of the shear wave velocity  $v$  gives rise to a parameter with the dimension of a stress (kPa) being the shear modulus  $\mu$  of the medium:

$$\rho v^2 = \mu \quad (\text{kPa}) \quad (2.1)$$

Through the assumption of a quasi-incompressible gel, it is possible to retrieve the Young's modulus which equals to  $E \approx 3\mu \approx 3\rho v^2$ , where the local density  $\rho$  is considered to be constant ( $\rho \approx 1000 \text{ kg/m}^3$  due to the high water content). As the Young's Modulus was proven to be directly linked to the liver fibrosis degree (Castera et al., 2008), this had a revolutionary impact on medicine replacing the liver biopsy, which is painful for the patient and not always trustworthy.

### Acoustic radiation force

In 1998, Sarvazyan published an article that explains the theoretical and technical aspects of the acoustic radiation force (Sarvazyan et al., 1998). The radiation force slightly displaces the tissue at the focal spot. This radiation force is created by focusing an ultrasonic beam at a given depth (Fig. 2.9) and Sarvazyan, considered as the pioneer of this technique, explains that we can have access to the elasticity if we follow the transversal shear waves created by this radiation force.

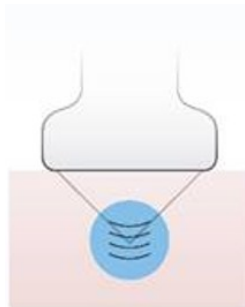


FIGURE 2.9: Acoustic radiation force principle: ultrasound probe sends focused ultrasounds to create shear waves that propagate transversely to the ultrasounds sent (from Sigrist et al., 2017).

In 2004, two fundamental ideas are developed in our laboratory to overcome the limitations of 2D elastography technique: the acoustic radiation force coupled to an ultrasound ultrafast imaging tool. These two concepts are at the heart of the Supersonic Shear Imaging technique (Bercoff et al., 2004) explained in part. 2.2.4. The concept of excitation-imaging is integrated into one probe, which became an “All-in-one” probe.

The company “Supersonic imagine” is created in 2004 by Fink, Tanter and Bercoff among others including the French physicist Georges Charpak, and Armen Sarvazyan. Supersonic imagine is the holder of about thirty patents<sup>1</sup>. The technology leveraged by Supersonic imagine is an ultrafast echographic device combined with a Shear Wave Elastography module providing quantitative maps of tissue elasticity. This device is called Aixplorer. This is the tool that will be used in this study.

### 2.2.4 Theoretical background of elastography

Ultrasound elastography has been developed as a medical imaging modality that maps the elastic properties and stiffness of soft tissue (Gennisson et al., 2013). Two types of US mechanical waves that can propagate in a medium are the compression wave (P wave) and the shear wave (S wave). Ultrasound conventional echography is based on P wave while elastography is based on S wave. Nevertheless, ultrasound elastography is a subtle combination of these two mechanical waves. As shown in Fig. 2.10, shear waves are generated within the medium by using ultrasonic radiation force as described in Bercoff *et al* (Bercoff et al., 2004).

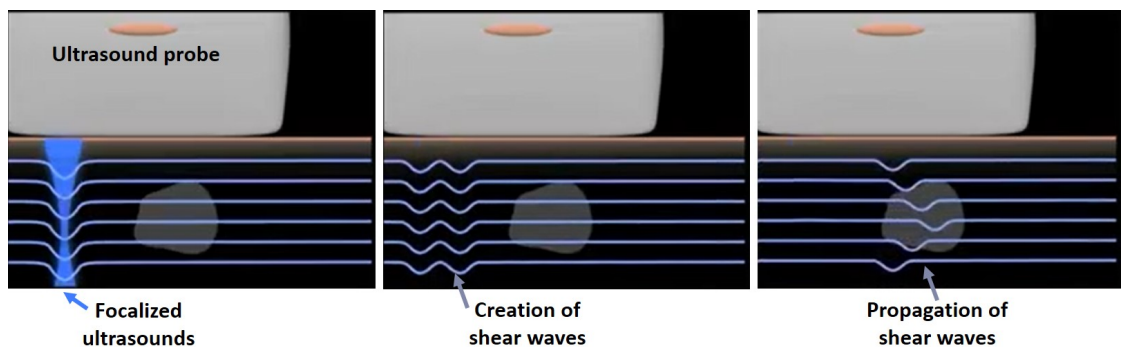


FIGURE 2.10: From left to right: The ultrasound probe sends focused ultrasounds. This creates shear waves in the medium. The shear wave propagates more or less quickly depending on the stiffness of the medium<sup>2</sup>.

An ultrasound beam (P wave) is focused at different depths (focal points) in the medium. This part is called the “push” generation and induces different mechanical effects as pressure, radiation force, temperature and shear that vary with intensity and time duration of the push. In this study, we will focus on the induced shear wave on which elastography is based. When the focused ultrasounds are stopped, matter comes back to its original state after the little deformation induced by the radiation force. This creates shear waves that propagate transversely. The combination of these shear waves forms cylindrical shear waves (as Mach Cone), with two pseudo-planar shear wave fronts going in opposite directions (see Fig. 2.11).

<sup>1</sup><https://www.supersonicimagine.fr/Portefeuille-de-brevets>

<sup>2</sup>[https://www.youtube.com/watch?v=v51DQMYw\\_Vs&t=1s](https://www.youtube.com/watch?v=v51DQMYw_Vs&t=1s)

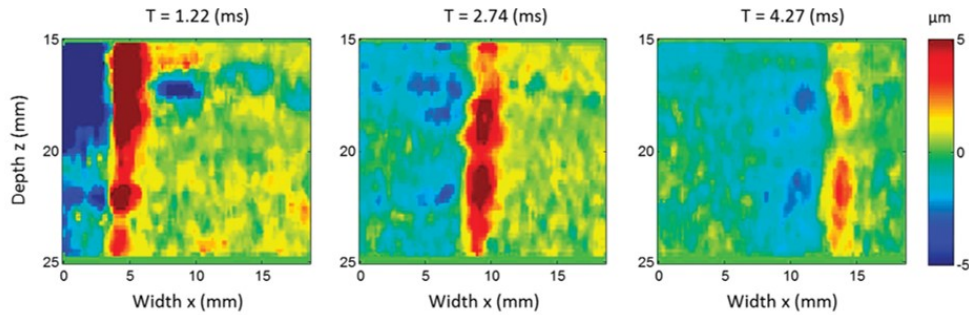


FIGURE 2.11: Shear wave propagation. By using ultrafast ultrasound imaging, a movie of the propagating shear wave is recorded in tens of milliseconds. Here, a typical experimental shear displacement field ( $z$  component) is given for an elastic gel.

Right after transmitting a transient and focused ultrasonic burst, the probe switches into an ultrafast mode by transmitting successive plane waves at ultrafast frame rates ( $>1000$  Hz) to capture the shear wave propagation in real-time ( $\sim 5000$  frames/second) and to determine the shear wave velocity (see part. 2.2.5).

### 2.2.5 Ultrafast imaging

To follow the shear wave displacement, an ultrafast scanner is needed. An ultrafast ultrasound imaging scanner sends plane waves instead of focused waves in conventional imaging. With plane-wave ultrasound imaging, the medium is insonified once (see Fig. 2.12). The image frame rate is no longer limited by sequential scanning of the focused beam but by the travel time of the pulsed plane wave to propagate through the medium and get back to the transducer array, thus the achievable frame rate is increased to thousands of hertz (approximately 30 kHz for an imaging depth of 10 mm).

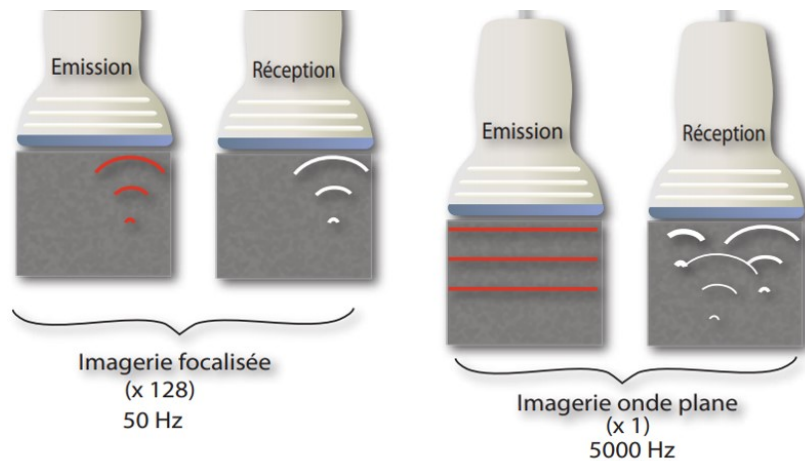


FIGURE 2.12: Conventional ultrasound imaging (focused imaging) compared to plane wave imaging. Plane wave imaging differs from the conventional scanning systems by not using a focal point for the transmission of the US signal (from Deffieux, 2008).

The plane wave transmission mode used in this thesis, allows reconstructing an ultrasound image in one single acquisition without requiring successive line per line focusing of the ultrasound beams as postulated by Shattuck *et al.* in 1984 (Shattuck *et al.*, 1984) and later demonstrated by Sandrin *et al.* and Tanter *et al.* in 2002 (Sandrin *et al.*, 2002, Tanter *et al.*, 2002). This makes it

possible to obtain imaging frequencies of several thousand images per second despite a slightly degraded resolution and imaging contrast. The acquisition time then approaches the round trip time of the ultrasound in the medium. This ultrafast imaging technique is the basis of the Super-sonic Shear Imaging technique (Fig. 2.12).

With plane waves, the acoustic energy is distributed throughout the medium and the amplitude of the recorded echoes is reduced compared to emission focusing ultrasound. In addition, the contrast is significantly reduced because echoes from different scatterers can overlap and interfere with each other. This is the counterpart of the gain in imaging rate. However, there are ways to recover contrast with this technique. Tanter *et al.* (Tanter et al., 2002) proposed to transmit plane waves at different angles, the so-called plane wave compounding approach and used it for the estimation of vectorial tissue displacement for shear wave elastography in 2002. Some years later, Montaldo (Montaldo et al., 2009) combined these compounded plane wave transmissions with a coherent synthetic summation in the receive mode in order to obtain a contrast-enhanced 2D image with coherent plane-wave compounding (see Fig. 2.13).

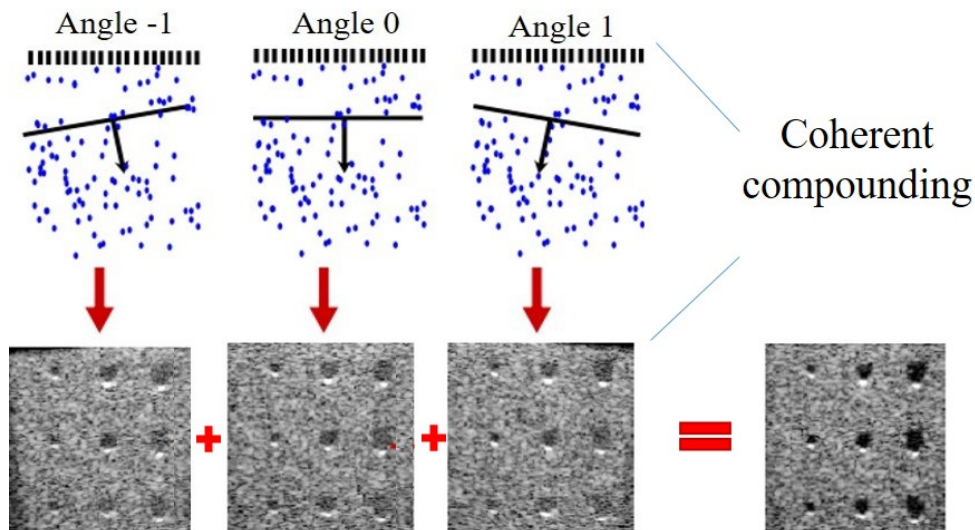


FIGURE 2.13: Schematic illustration of coherent plane wave compounding. The coherent compounding allows a great quality image at a greater framerate than the conventional imaging. This method typically increases the frame rate more than 100-fold (from Montaldo et al., 2009).

This huge increase in framerate was initially achieved through a compromise in image quality. This degradation of quality mainly affects the image contrast rather than the resolution. Indeed, Tanter and colleagues (Tanter et al., 2014) highlight the compromise between the number of angles of plane waves with the framerate. At only one angle, one can get a framerate around 20 000 frames/s while it is 1000 frames/s for 17 angles and 350 frames/s for 40 angles. The increase in the number of angles reduces the framerate. The goal of shear wave elastography is to track tissue displacement induced by shear wave propagation, thus we need a high frame rate to follow the shear wave, even more, if the tissue is stiff. We will choose to lose in resolution as an acceptable price compared with the advantages provided by ultrafast frame rates, picking three angles to follow the shear waves. Now that we are able to catch the shear wave propagation, we need a method to calculate its speed (see next part. 2.2.6).

### 2.2.6 Time of flight image reconstruction

Once the shear wave has been generated and its propagation imaged through the ultrafast scanner, the axial tissue velocity field  $U_z$  is estimated by calculating the correlation between two successive images. This yields a movie of the shear wave propagation (see Fig. 2.14 for an image shown 1 ms after the shear wave generation). A time-of-flight algorithm already described in the literature (Tanter et al., 2008) is then used. The one-dimensional time-of-flight algorithm is applied to the tissue displacement film on the pixels of interest: by calculating the temporal cross-correlation between the tissue velocity of two neighboring pixels spaced by a distance  $dx$  (correlation distance), we can estimate the time it took for the wave to propagate from one to the other, and therefore the shear wave velocity at that location. The maximum of the cross-correlation function gives the temporal shift  $dt$  and the speed of the shear wave is then simply estimated by:

$$c_T = \frac{dx}{dt} \quad (2.2)$$

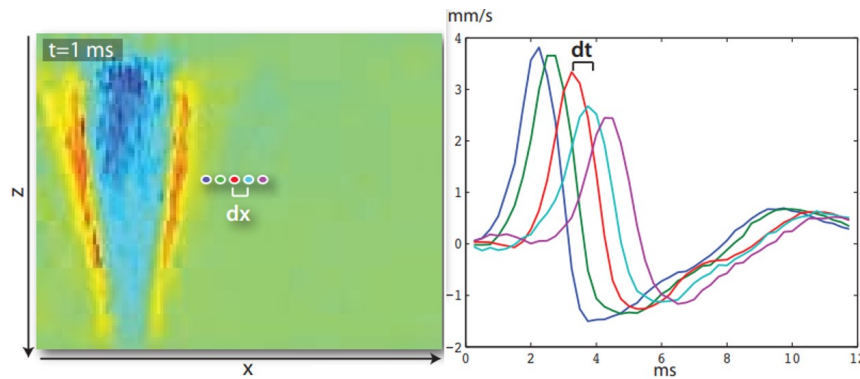


FIGURE 2.14: Principle of time-of-flight inversion. The time shift  $dt$  between two neighboring points of a distance  $dx$  is estimated by cross-correlation which allows estimating the speed of the shear wave locally between these two points (from Defieux, 2008).

The first *in vivo* experiments with this technique were conducted at Institut Curie to differentiate benign tissue from malignant tissue (in 50 patients) (Tanter et al., 2008). Time of flight method is based on signal correlation which is more robust than working on temporal or spatial derivatives. Finally, to recover the shear wave frequency, it is possible to compute the discrete Fourier transform of the signal using a fast Fourier transform algorithm on Matlab. This allows finding the maximum signal amplitude for which the frequency is reached, defined as the shear wave frequency.

### 2.2.7 Limitation of Shear Wave Elastography

Equation 2.1 is true as long as we are in the linear regime at small strains in an isotropic and elastic material. It appears that under a certain strain, in compression or tensile test, non-linear effects appear (schematically represented in fig. 2.15). We will see in part. 2.4 that this directly impacts the shear wave velocity propagating through the material.

This is a non-linear effect of the constitutive relation between mechanical stress and finite strain in a material. The commonly known relationship Hooke's Law (part. 2.3.1) is not sufficient to describe constant longitudinal and shear sound velocities when the material is subjected to a stress.

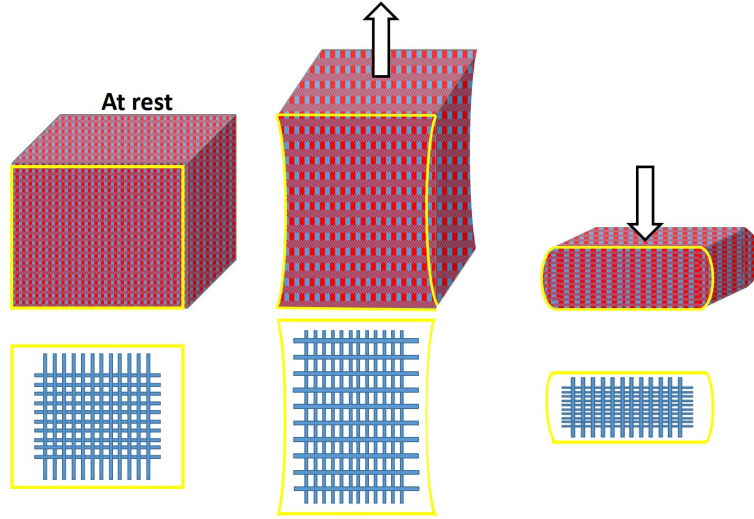


FIGURE 2.15: From isotropy (at rest) to orthotropy with nonlinear effect due to tensile (middle) and compression tests (left).

In the following part, we will review the theoretical background in mechanics and wave physics necessary to understand acoustoelasticity (interaction of acoustic waves with elastic deformation in a solid). The acoustoelastic effect includes higher order expansion of the constitutive relation between the applied stress and resulting strain, which yields longitudinal and shear sound velocities dependent on the stress state of the material.

## 2.3 Mechanics for an elastic medium

### 2.3.1 Hooke's law

Hooke's law was formulated in 1678 by Robert Hooke: "ut tensio, sic vis," meaning, "as the extension, so the force." The larger this ratio (force/deformation), the stiffer the material, and the greater its resistance to deformation. Originally developed to describe the behavior of springs, this law was then applied by physicists to soft solids in the case of weak deformations. Ultimately the elastic properties of a material are governed by the arrangement and strength of the bonds between the atoms that make up the material. Elasticity is the property of "reversible deformation". Such a medium is called linear elastic.

This linear law can be written by introducing the Young's modulus  $E$ , constant of proportionality linking the strain  $\epsilon$  with the stress  $\sigma$ :

$$\sigma = E\epsilon \quad (2.3)$$

### 2.3.2 Mechanics of a continuous medium: A linear analysis

#### Stress and strain tensors

The stress and strain tensors extend the concepts of stress and strain in the case of an elementary volume in three dimensions according to the tensor formalism. Here we depict the tensors for infinitesimal deformations of a continuum body in which the displacement gradient is small:

- The stress tensor  $\sigma_{ij}$  corresponds to the direction in which it acts but also the orientation of the surface upon which it is acting. The first index  $i$  specifies the direction in which the stress

component acts, and the second index  $j$  identifies the orientation of the surface upon which it is acting.

- The engineering strain  $\epsilon_{ij}$  is defined as

$$\epsilon_{ij} = \frac{1}{2} \left( \frac{\delta u_i}{\delta x_j} + \frac{\delta u_j}{\delta x_i} \right) \quad (2.4)$$

where  $\mathbf{u}$  is the displacement vector.

### Elasticity tensor in isotropic medium

In 1822, the French mathematician Augustin-Louis Cauchy formalized the concept of stress in the context of a generalized three-dimensional theory. He showed its properties as consisting of a  $3 \times 3$  symmetric array of numbers that transform as a tensor, derived the equations of motion for a continuum in terms of the components of stress, and developed the theory of linear elastic response for isotropic solids.

In its general form Hooke's law reads:

$$\sigma_{ij} = c_{ijkl} \epsilon_{kl} \quad \text{with } i, j, k, l = 1, 2, 3 \quad (2.5)$$

The fourth-rank tensor  $c_{ijkl}$  is called the stiffness tensor and consists of 81 entries. It can be simplified, especially in the case of isotropic media and small strains. In this particular case, each component of stress  $\sigma_{ij}$  is linearly dependent upon every component of strain  $\epsilon_{kl}$  and vice versa. Since all directional indices may assume values 1, 2, and 3, we obtain 9 relations. Each of these relations involves one component of stress and nine components of strain.

Since the stress tensor is symmetrical, i.e.  $\sigma_{ij} = \sigma_{ji}$ , only six of these equations are independent. This is also valid for the strain. Thus, only six terms of the right side of Eq. 2.5 are independent which can be rewritten as:

$$\begin{pmatrix} \sigma_{11} \\ \sigma_{22} \\ \sigma_{33} \\ \sigma_{44} \\ \sigma_{55} \\ \sigma_{66} \end{pmatrix} = \begin{pmatrix} \Lambda + 2\mu & \Lambda & \Lambda & 0 & 0 & 0 \\ \Lambda & \Lambda + 2\mu & \Lambda & 0 & 0 & 0 \\ \Lambda & \Lambda & \Lambda + 2\mu & 0 & 0 & 0 \\ 0 & 0 & 0 & 2\mu & 0 & 0 \\ 0 & 0 & 0 & 0 & 2\mu & 0 \\ 0 & 0 & 0 & 0 & 0 & 2\mu \end{pmatrix} \begin{pmatrix} \epsilon_{11} \\ \epsilon_{22} \\ \epsilon_{33} \\ \epsilon_{44} \\ \epsilon_{55} \\ \epsilon_{66} \end{pmatrix} \quad (2.6)$$

with  $\Lambda$  and  $\mu$  the Lamé coefficients.  $\Lambda$  is generally written as  $\lambda$ . Here, we use the capital Greek letter  $\Lambda$  to avoid any misunderstanding with  $\lambda$  the elongation. The Lamé coefficient  $\mu$  is generally called the shear modulus. These two coefficients are linked together by:

- The bulk modulus  $K = \Lambda + 2/3\mu$ .  $K$  represents the difficulty to modify the volume when hydrostatic pressure is applied simultaneously on its faces.
- The Poisson's ratio  $\nu = \frac{\Lambda}{2(\Lambda + \mu)}$ . This defines the ratio between uniaxial compression and resulting lateral elongation and it is equal to 0.5 for incompressible solids.
- The Young's modulus  $E = \frac{\mu(3\Lambda + 2\mu)}{\Lambda + \mu}$ .  $E$  characterizes the ability of a material to withstand changes in length when under lengthwise tension or compression.  $E$  is also equal to the longitudinal stress divided by the strain (see Eq. 2.3).

### 2.3.3 Quasi-incompressibility

In hydrogels and biological tissues, composed mainly of fluid and almost incompressible, the compression modulus  $K$  is very high (several Giga Pascal), it is thus very large compared to the shear modulus (a few tens kilo Pascal). To be convinced of this, one can try to crush a piece of meat in his hands and realize that it is almost impossible to change the volume. On the contrary, it is very easy to shear and twist it. The term of quasi-incompressibility is important because, without compressibility, there is no propagation of ultrasounds in the environment.

So we have  $K \gg \mu$  then  $K \approx \Lambda$  and  $\nu \approx 0.5$ . Finally, the Young modulus  $E$  can be simplified in:

$$E = 3\mu \quad (2.7)$$

The basis of elastography is to deduce the elasticity in a medium. In order to do that, one needs to measure the shear wave velocity. The shear wave velocity is linked to the shear modulus  $\mu$ . The development to get to these equations will be explained in part 2.3.4.

### 2.3.4 Wave equation

A disturbance in a medium is represented by a particle displacement with time dependent position  $u(x,t)$ . The general equation of motion is given by:

$$\rho \frac{\partial^2 u_i}{\partial t^2} = \frac{\partial \sigma_{ij}}{\partial x_j} \quad (2.8)$$

Where  $\rho$ ,  $\sigma$  and  $(\delta^2 u_i / \delta t^2)$  designate the density, the Cauchy stress tensor and the particle acceleration, respectively.

The density  $\rho$  of a material is defined such that the mass of an element of volume  $dV$  of the material at time  $t$  is:

$$mass = \rho dV \quad (2.9)$$

We denote the density of the material in the reference state by  $\rho_0$ . Conservation of mass of the material requires that:

$$\rho_0 dV_0 = \rho dV \quad (2.10)$$

In quasi-incompressible material, the density is constant since there is no change in volume.

The Cauchy stress tensor is given by:

$$\sigma_{ij} = \frac{\partial W}{\partial \left( \frac{\partial u_i}{\partial x_j} \right)} \quad (2.11)$$

With  $W$ , the strain energy density. In a general elastic medium, the strain energy density in a linear analysis is:

$$W = \frac{1}{2} c_{ijkl} \epsilon_{ij} \epsilon_{kl} \quad (2.12)$$

The generalized stress-strain relation for an isotropic linear elastic material is given by:

$$\sigma_{ij} = \Lambda \delta_{ij} \epsilon_{kk} + 2\mu \epsilon_{ij} \quad (2.13)$$

with  $\delta_{ij}$ , the Kronecker delta (equals 1 if the variables are equal, and 0 otherwise). Substituting the engineering strain (equation 2.4) into the stress-strain relation, we obtain the stress components in terms of the components of the displacement:

$$\sigma_{ij} = \Lambda \delta_{ij} \frac{\partial u_k}{\partial x_k} + \mu \left( \frac{\partial u_i}{\partial x_j} + \frac{\partial u_j}{\partial x_i} \right) \quad (2.14)$$

Then by substituting this expression into the equation of motion Eq. 2.8, we obtain the equation of balance of linear momentum for an isotropic linear elastic material:

$$\rho \frac{\partial^2 u_i}{\partial t^2} = (\Lambda + \mu) \frac{\partial^2 u_j}{\partial x_j \partial x_i} + \mu \frac{\partial^2 u_i}{\partial x_j^2} \quad (2.15)$$

By rewriting the previous equation in vector form and with the classical vector operators, we obtain the following general equation:

$$\rho \frac{\partial^2 \vec{u}}{\partial t^2} = (\Lambda + \mu) \text{grad}(\text{div}(\vec{u})) + \mu \Delta \vec{u} \quad (2.16)$$

The displacement field  $\vec{u}$  can be decomposed into a field with zero divergence ( $\text{div}(\vec{u}_T) = 0$ ) corresponding to the shear motion and a zero rotational field ( $\text{rot}(\vec{u}_L) = \vec{0}$ ) corresponding to the compressive motion:  $\vec{u} = \vec{u}_L + \vec{u}_T$  (Arfken et al., 1999). This allows to rewrite the previous equation by developing the laplacian  $\Delta$  in the form:  
 $\Delta \vec{u} = \text{grad}(\text{div}(\vec{u}_L)) - \text{rot}(\text{rot}(\vec{u}_T))$ :

$$\rho \left( \frac{\partial^2 \vec{u}_L}{\partial t^2} + \frac{\partial^2 \vec{u}_T}{\partial t^2} \right) = (\Lambda + 2\mu) \text{grad}(\text{div}(\vec{u}_L)) - \mu \text{rot}(\text{rot}(\vec{u}_T)) \quad (2.17)$$

We thus obtain two conventional wave equations with different velocities, the first with zero rotational field corresponds to compressional waves, the second one with zero divergence corresponds to shear waves:

$$\frac{\partial^2 \vec{u}_L}{\partial t^2} = \frac{\Lambda + 2\mu}{\rho} \Delta \vec{u}_L \quad (2.18)$$

$$\frac{\partial^2 \vec{u}_T}{\partial t^2} = \frac{\mu}{\rho} \Delta \vec{u}_T \quad (2.19)$$

By integrating, it is possible to find the wave velocities:

$$C_L = \sqrt{\frac{\Lambda + 2\mu}{\rho}} \approx \sqrt{\frac{K}{\rho}} \quad (2.20)$$

$$C_T = \sqrt{\frac{\mu}{\rho}} \quad (2.21)$$

From equation 2.21, it is possible to deduce the Young's modulus E in the case of an incompressible material:

$$E = 3\rho C_T^2 \quad (2.22)$$

It appears with this simple equation that knowing the shear wave velocity propagating inside a material allows knowing its stiffness (Young's modulus). From this brilliant idea, shear wave elastography emerged in the 21st century.

However, for large deformations, this equation is no longer valid and acoustoelasticity theory is needed.

## 2.4 Acoustoelasticity: Polarized shear wave in a stressed medium

### 2.4.1 Strain energy density function used for shear wave velocity

Many theoretical works have been devoted to the expression of the propagation velocity of elastic waves in a stretched non-linear elastic soft solid (Brillouin, 1925, Murnaghan, 1937, Hughes et al., 1953, and Landau et al., 1959). Here, the general equations are summarized.

Under mechanical loading, the shear wave velocity is affected. In contrast to a linear analysis, where we may apply a linear strain measure (engineering strain) for infinitesimal deformation, a finite strain measure is used to represent local deformations in a large deformation nonlinear analysis. In this particular case, we use the full equation of the strain (the finite strain) with nonlinear terms:

$$e_{ik} = \frac{1}{2} \left( \frac{\partial u_i}{\partial x_k} + \frac{\partial u_k}{\partial x_i} + \frac{\partial u_l}{\partial x_i} \frac{\partial u_l}{\partial x_k} \right) \quad (2.23)$$

The tensors are no longer symmetrical. Landau and Lifshitz have established the general expression for the elastic energy density of an isotropic body in the third-order approximation introducing the third-order coefficients (A, B, C) (Landau et al., 1959). From the components of a symmetrical tensor of rank two, we can form two quadratic scalars ( $e_{ik}^2$  and  $e_{ll}^2$ ) and three cubic scalars ( $e_{ll}^3, e_{ll}e_{ik}^2, e_{ik}e_{il}e_{kl}$ ). Hence, the most general scalar containing quadratic and cubic terms in  $e_{ik}$ , with scalar coefficients (since the body is isotropic), is:

$$W = \mu e_{ik}^2 + \frac{\Lambda}{2} e_{ll}^2 + \frac{1}{3} A e_{ik} e_{il} e_{kl} + B e_{ik}^2 e_{ll} + \frac{1}{3} C e_{ll}^3 \quad (2.24)$$

Catheline et al. (Catheline et al., 2003) have expressed the elastic strain energy density as a function of the invariants of the Lagrangian strain tensor and developed to the fourth-order with the fourth-order coefficients (E, F, G, H):

$$W = \mu I_2 + \frac{\Lambda}{2} I_1^2 + \frac{1}{3} A I_3 + B I_1 I_2 + \frac{1}{3} C I_1^3 + E I_1 I_3 + F I_1^2 I_2 + G I_2^2 + H I_1^4 \quad (2.25)$$

With the invariants of the Lagrangian (Green-Lagrange) strain tensor defined as follow:

$$\begin{aligned} I_1 &= \text{tr}(\mathbf{e}) \\ I_2 &= \text{tr}(\mathbf{e}^2) \\ I_3 &= \text{tr}(\mathbf{e}^3) \end{aligned} \quad (2.26)$$

From Catheline (Catheline et al., 2003), the Lamé and the Landau coefficients as a function of the elastic moduli in the Voigt's notations are :

$$\begin{aligned}
\Lambda &= c_{12} \\
\mu &= c_{66} \\
A &= 4c_{456} \\
B &= c_{144} \\
C &= c_{123}/2 \text{ etc.}
\end{aligned} \tag{2.27}$$

$c_{ij}$  is the component of the stiffness tensor described in part 2.3.2 (second order).  $c_{ijk}$  designates the component of the third-order elastic tensor.

It is possible to simplify equation 2.25, using the logarithmic strain tensor  $\bar{e}$  defined as:

$$\bar{e} = \frac{1}{2} \ln(\delta + 2e) \tag{2.28}$$

where  $\delta$  is the identity and the invariants are:

$$\begin{aligned}
i_1 &= \text{tr}(\bar{e}) \\
i_2 &= \text{tr}(\bar{e}^2) \\
i_3 &= \text{tr}(\bar{e}^3)
\end{aligned} \tag{2.29}$$

For incompressible material,  $\det(F) = 1$ . We can then define the determinant of the finite strain tensor as:  $\det(e) = 1/2 [\det(F^T F) - 1] = 0$ .

Now, using the well-known identity  $\log(\det(A)) = \text{tr}(\log(A))$ , the incompressibility condition can be easily expressed in terms of  $i_1$ :

$$i_1 = \text{tr}(\bar{e}) = \frac{1}{2} \text{tr}(\ln(\delta + 2e)) = \frac{1}{2} \ln(\det(\delta + 2e)) = \frac{1}{2} \ln(1 + 2 \det(e)) = \frac{1}{2} \ln(1) = 0 \tag{2.30}$$

For the sake of simplicity, the following calculations will be shown to the third order terms of the strain energy function. The Lagrangian strain tensor as a function of the logarithmic strain tensor can be expressed using the Taylor series of the exponential function:

$$e = \bar{e} + \bar{e}^2 + \frac{2}{3} \bar{e}^3 \tag{2.31}$$

and its invariants can be expressed as:

$$\begin{aligned}
I_1 &= i_1 + i_2 + \frac{2}{3} i_3 \\
I_2 &= i_2 + 2i_3 \\
I_3 &= i_3
\end{aligned} \tag{2.32}$$

It follows that the third-order expansion of  $W$  in terms of the invariants of the logarithmic strain  $\bar{\epsilon}$  reads:

$$W = \mu i_2 + \frac{\Lambda}{2} i_1^2 + \left( \frac{A}{3} + 2\mu \right) i_3 + (B + \Lambda) i_1 i_2 + \frac{1}{3} C i_1^3 \quad (2.33)$$

Which, if we take into account that  $i_1 = 0$ , equals to:

$$W = \mu i_2 + \left( \frac{A}{3} + 2\mu \right) i_3 \quad (2.34)$$

Or

$$W = \mu(i_2 + 2i_3) + \left( \frac{A}{3} \right) i_3 \quad (2.35)$$

$$W = \mu I_2 + \frac{A}{3} I_3 \quad (2.36)$$

If we extend this analysis to include fourth-order terms in the strain energy function, it leads us to the famous expression of Hamilton and Zabolotskaya (Hamilton et al., 2004 Zabolotskaya et al., 2004):

$$W = \mu I_2 + \frac{1}{3} A I_3 + D I_2^2 \quad (2.37)$$

With  $D = G + B + \Lambda/2$ , from equation 2.25.

According to Hamilton et al. (Hamilton et al., 2004), the  $A$  constant determines the nonlinear shear behavior while  $D$  is required to describe nonlinear distortion of shear waves in finite amplitudes.

Finally, Gennisson and colleagues (Gennisson et al., 2007) developed Eq. 2.37 using Eq. 2.8 and Eq. 2.11 to retrieve the shear wave speed when the material is subjected to a stress. The shear wave speed is first expressed as a function of the strain. To establish the connection with the stress, one need to recall that for incompressible solids:  $e = \pm \sigma / 3\mu$ . These equation were expanded to the 4th order (Destrade et al., 2010, Abiza et al., 2012):

#### Compression

$$\begin{aligned} \rho v_{21}^2 &= \mu_0 - \sigma_{22} \left( \frac{A}{12\mu_0} \right) + \sigma_{22}^2 (2\mu_0 + A + 3D) \frac{1}{9\mu_0^2} \\ \rho v_{13}^2 &= \mu_0 + \sigma_{22} \left( 1 + \frac{A}{6\mu_0} \right) + \sigma_{22}^2 (5\mu_0 + \frac{7}{4}A + 3D) \frac{1}{9\mu_0^2} \\ \rho v_{12}^2 &= \mu_0 - \sigma_{22} \left( 1 + \frac{A}{12\mu_0} \right) + \sigma_{22}^2 (5\mu_0 + \frac{7}{4}A + 3D) \frac{1}{9\mu_0^2} \end{aligned} \quad (2.38)$$

## Tensile

$$\rho v_{12}^2 = \mu_0 + \sigma_{22} \left(1 + \frac{A}{12\mu_0}\right) + \sigma_{22}^2 \left(5\mu_0 + \frac{7}{4}A + 3D\right) \frac{1}{9\mu_0^2} \quad (2.39)$$

The first index in the shear wave speed  $v_{ij}$  corresponds to the direction of the shear displacement induced by radiation force (direction of polarization of the shear wave) while the second index corresponds to the axis of propagation of the shear wave (see Fig. 3.19 of next part). One can notice when  $\sigma = 0$ , at rest, we retrieve the direct dependence of  $\mu$  on the shear wave velocity.

### 2.4.2 Strain energy density function used for mechanics

In the last part, we saw that through the strain energy density function, it was possible to express the shear wave as a function of Landau coefficients and the stress. In fact, it is also possible to use the strain energy density function by detailing the Invariants of the Green-Lagrange strain tensor as a function of  $\lambda$ , the elongation. In this particular case, it is possible to express the stress as a function of  $\lambda$  from the same equation used to find the shear wave velocity.

This time, we will use the strain tensor written as:

$$e = \frac{1}{2} (F^T F - I) \quad (2.40)$$

With  $C = F^T F$ , being the right Cauchy-Green deformation tensor which is commonly used in materials science. In purely homogeneous deformations, the deformation gradient  $F$  has a diagonal representation:  $F = \text{diag}[F_{11}, F_{22}, F_{33}] = \text{diag}[\lambda_1, \lambda_2, \lambda_3]$ .  $e$  is a measure of how much  $C$  differs from identity  $I$ .

Note that if we consider a tensile test with a stress applied in the direction 2,  $\sigma_{22}$ , with faces in axis 1 and 3 free to deform, we can write the right Cauchy-Green deformation tensor, according to the incompressibility assumption:

$$C = \begin{pmatrix} \lambda_1^2 & 0 & 0 \\ 0 & \lambda_2^2 & 0 \\ 0 & 0 & \lambda_3^2 \end{pmatrix} = \begin{pmatrix} 1/\lambda & 0 & 0 \\ 0 & \lambda^2 & 0 \\ 0 & 0 & 1/\lambda \end{pmatrix} \quad (2.41)$$

With  $\lambda = L/L_0$ ,  $L_0$ , the initial length and  $L$ , the length at the stretch state. It comes that the Green-Lagrange strain tensor invariants in tension can be written as:

$$\begin{aligned} I_1 &= \text{tr}(e) = \frac{1}{2} (\lambda^2 + \frac{2}{\lambda} - 3) \\ I_2 &= \text{tr}(e^2) = \frac{1}{4} \left[ (\lambda^2 - 1)^2 + 2 \left( \frac{1}{\lambda} - 1 \right)^2 \right] \\ I_3 &= \text{tr}(e^3) = \frac{1}{8} \left[ (\lambda^2 - 1)^3 + 2 \left( \frac{1}{\lambda} - 1 \right)^3 \right] \end{aligned} \quad (2.42)$$

From eq. 2.37, it comes that the strain energy density function can be written as:

$$\begin{aligned} W &= \mu \frac{1}{4} \left[ (\lambda^2 - 1)^2 + 2 \left( \frac{1}{\lambda} - 1 \right)^2 \right] + \frac{A}{24} \left[ (\lambda^2 - 1)^3 + 2 \left( \frac{1}{\lambda} - 1 \right)^3 \right] \\ &\quad + \frac{D}{16} \left[ (\lambda^2 - 1)^2 + 2 \left( \frac{1}{\lambda} - 1 \right)^2 \right]^2 \end{aligned} \quad (2.43)$$

From the strain energy density function and using Eq. 2.11 ( $\sigma_{22} = \delta W / \delta \lambda$ ), we can express the stress as a function of  $\lambda$ :

$$\sigma_{22} = \mu \left[ \lambda (\lambda^2 - 1) - \frac{1}{\lambda^2} \left( \frac{1}{\lambda} - 1 \right) \right] + \frac{A}{4} \left[ \lambda (\lambda^2 - 1)^2 - \frac{1}{\lambda^2} \left( \frac{1}{\lambda} - 1 \right)^2 \right] + \frac{D}{2} \left[ (\lambda^2 - 1)^2 + 2 \left( \frac{1}{\lambda} - 1 \right)^2 \right] \left[ \lambda (\lambda^2 - 1) - \frac{1}{\lambda^2} \left( \frac{1}{\lambda} - 1 \right) \right] \quad (2.44)$$

This equation can be developed to highlight the difference in the order of  $\lambda$ :

$$\begin{aligned} \sigma_{22} = & \lambda^3 \mu - \lambda \mu + \frac{\mu}{\lambda^2} - \frac{\mu}{\lambda^3} + \frac{A\lambda}{4} - \frac{A\lambda^3}{2} + \frac{A\lambda}{4} - \frac{A}{4\lambda^4} + \frac{A}{2\lambda^3} - \frac{A}{4\lambda^2} - \frac{7D}{2\lambda^3} - \frac{D}{\lambda^5} \\ & + \frac{3D}{\lambda^4} - D\lambda + \frac{3D}{2\lambda^2} + D - \frac{3D\lambda^2}{2} + \frac{5D\lambda^3}{2} - \frac{3D\lambda^5}{2} + \frac{D\lambda^7}{2} \end{aligned} \quad (2.45)$$

It appears that the maximum order is  $\lambda^7$  and the minimum order is  $\lambda^{-5}$  which represents 12 orders of difference.

## 2.5 Materials and methods

### 2.5.1 Synthesis of the model hydrogels

Nanohybrid hydrogels referenced in part. 1.1.3 will be used in this thesis. Poly(N,N-dimethylacrylamide) (PDMA) hybrid hydrogels were prepared in a nitrogen-filled and oxygen-free glove box at room temperature by *in situ* free radical polymerization of DMA using N,N'-methylenebisacrylamide (MBA) as cross-linker. After dilution of the silica suspension Ludox-TM50 (50 wt.% suspension in  $H_2O$ ) in pH 9 milliQ water, MBA (in solution) and DMA are added and the all solution is mixed and deoxygenated for at least two hours. During this process, the bottle is immersed in ice in order to slow down the polymerization process between the DMA and MBA. Then, the solution and the molds were introduced in the glove box to prevent any oxygen contamination. A solution of KPS (potassium persulfate) initially prepared and N,N,N',N'- tetramethylethylenediamine (TEMED) (two catalysts) are added under stirring. The mixture is then rapidly transferred into appropriate molds ( $\sim 30$  seconds of mixing time). The mold's geometry depends on the characterization techniques used. The polymerization is let to proceed during 24 hours.

Samples	DMA (g)	MBA (mg)	KPS (mg)	TEMED ( $\mu$ L)	SiO <sub>2</sub> Vol.%	SiO <sub>2</sub> (g)	H <sub>2</sub> O (g)
SP0	12.2	19.0	333.8	184.8	0.5	0.7	78.0
SP2	12.2	19.0	333.8	184.8	9.6	24.5	53.5
SP3.5	12.2	19.0	333.8	184.8	15.9	85.7	35.2

TABLE 2.1: Nomenclature and composition of Nano-Hybrid Hydrogels for a wanted volume of 100 mL.

This study of hybrid gels was based on a fixed weight ratio between polymer and water equals to 0.14, corresponding to a fixed polymer concentration equals to 12.2 wt%. The gels are studied in this preparation state. For all syntheses, the gel matrix hydration is well-controlled (i.e,  $\sim 88$  wt %), the (DMA)/(KPS) and (DMA)/(TEMED) molar ratios were fixed at 100. The cross-linking

density was also held constant using a cross-linker/monomer molar ratio (MBA/DMA) of 0.1 mol % (see Table 2.1 for the exact composition of a 100 mL hybrid hydrogel synthesis). Three different gels are presented according to different amounts of silica nanoparticles (NPs). It is also possible to synthesize a hybrid gel with about 20 vol.% of SiO<sub>2</sub> (SP5). This gel won't be presented in this study at preparation state due to its high stiffness but will be used in the study of swollen gels.

### Swelling procedure

To keep the silica nanoparticles (NPs) surface chemistry (fraction of silanol groups) upon swelling as controlled as possible, swelling experiments were performed in ultrapure water set at pH 9. The gel was placed in a large excess of solvent at room temperature for two months in order to reach the swelling equilibrium condition. These gels are indicated by  $Q_e$  while  $Q_0$  represents the gel at their preparation state.

To investigate different states of swelling on small samples of size of  $5 \times 2 \times 30$  (width x thickness x length) mm<sup>3</sup>, from the initial to equilibrium, the weight of the swollen gel was recorded either after 5 min, 30 min or at least 10 days to ensure that the gels were at equilibrium. Immediately after weighing, each swollen sample was stored in paraffin oil to avoid any change in gel composition. The swelling degree  $Q$ , calculated assuming volume additivity, is:

$$Q = 1 + \frac{1}{\nu_{spe}^p} x \frac{m_w}{m_p} \quad (2.46)$$

where  $\nu_{spe}^p$  is the specific volume of the dry polymer network,  $m_p$  and  $m_w$  are the mass of the dry polymer network and the mass of absorbed water, respectively.

### 2.5.2 Setups built for the project

Tests were performed on a tensile/compression testing machine (model 5565, Instron, Elancourt, France) equipped with a 10-N or 100-N load cell (with a relative uncertainty of 0.16% in the range from 0 to 0.1 N). During the test, the force ( $F$ ) and displacement ( $L$ ) are recorded in order to calculate the nominal stress  $\sigma_N$ , (also called Piola-Kirchhoff stress), and strain  $\epsilon$ :

$$\sigma_N = F/S_0 \quad \epsilon = \frac{L - L_0}{L_0} \quad (2.47)$$

with  $L_0$  and  $S_0$  the initial length and surface respectively.

It is also possible to get the true stress that we name  $\sigma$  (also called the Cauchy stress), and the true strain  $\epsilon_T$ :

$$\sigma = \sigma_N \times \lambda \quad \epsilon_T = \ln(\lambda) \quad (2.48)$$

with  $\lambda$ , the elongation:  $\lambda = 1 + \epsilon$ .

### Coupled compression test between Instron and Aixplorer

We built a set-up for compression experiments (see Fig. 2.16, left). The 70x70x70 mm<sup>3</sup> cubic gel is stuck between two plates, the bottom plate is fixed and the upper one goes down to a certain strain. To avoid dehydration during the test, the gel is covered with oil all over its faces which also makes it possible to slide between the two plates. The bottom plate has a hole of the size of the ultrasound probe, which permits to send focused ultrasound inside the gel, thus creating shear waves. After compression of 30% strain at different strain rates: 0.06 s<sup>-1</sup>, 0.01 s<sup>-1</sup> and 0.006

$s^{-1}$ , the gel was blocked for a certain time. The force applied by the upper plate and the strain imposed on the material are recorded simultaneously with the shear wave velocity every second, respectively by the Instron and the Aixplorer. Due to the symmetric axis of the cube, we get three different possible probe configurations (see Fig. 3.6 in part. 3.1.2).

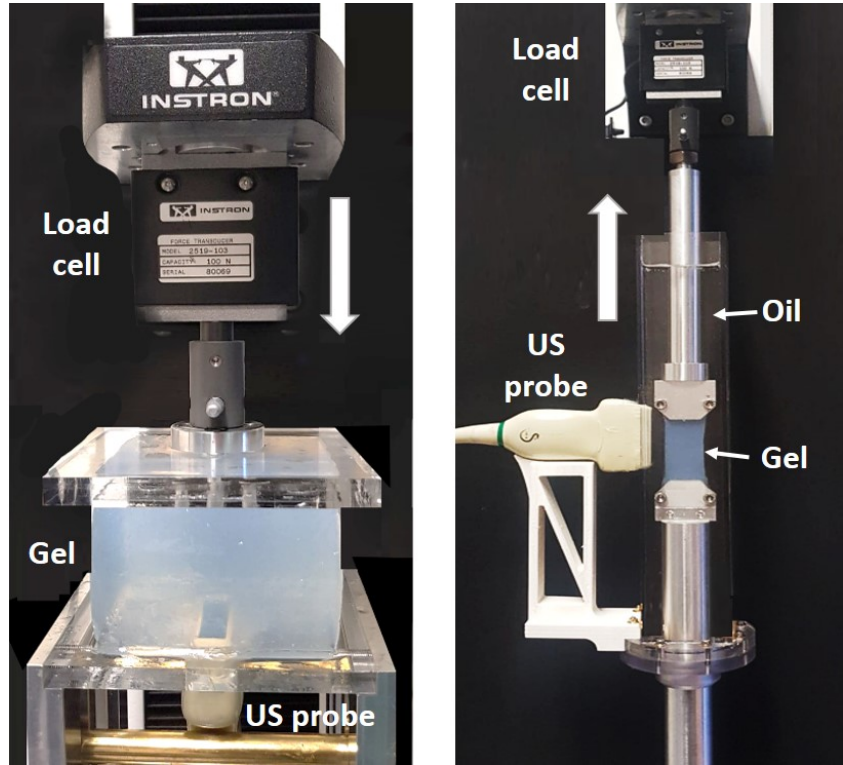


FIGURE 2.16: Experimental setup of the compression test (left) and the tensile test (right). The mechanical testing machine is linked to the imaging technique through the ultrasound probe.

### Coupled tensile test between Instron and Aixplorer

We built a set-up for a tensile experiment (see Fig. 2.16, right). Parallelepiped gels of  $e = 10$  mm thickness with widths  $W$  varying between 20 and 25 mm were synthesized. The length of the gel,  $L_0$ , was covered between 30 and 60 mm. For fracture experiments, a notch of about  $a = 5$  mm in length is made with a scalpel. The length notch has been verified on ImageJ for each test with ultrasound images. During tensile tests, samples were maintained in screw-action grips which were specifically designed for gels. No slippage effect has been detected. Tensile tests were carried out with nominal strain rates of  $0.06 s^{-1}$ ,  $0.01 s^{-1}$  and  $0.006 s^{-1}$  until a certain strain or complete fracture of the sample. The ultrasound probe faces the notch and images through the width of the gel. The whole experiment is immersed in paraffin oil to avoid gel dehydration and possible interferences or long term damage of the ultrasound beam.

### Rheology

A specific set of alumina plates has been designed by previous colleagues (Gennisson et al., 2014). Linear viscoelasticity was studied on a strain-controlled rheometer (Rheometrics RFSII, TA Instruments, Guyancourt, France), in parallel-plate geometry with a 25 mm diameter. The gels were deformed by 3% within the linear viscoelastic range, as determined using a frequency of 1 Hz.

Specific alumina plates were used to apply a stabilized normal force of 0.5 N (i.e., normal stress around 1 kPa). The frequency range investigated was comprised between 0.1 rad/s and 100 rad/s (corresponding to  $\sim 0.02$  Hz and  $\sim 15.92$  Hz respectively). Sample thickness was fixed at 2 mm.

### 2.5.3 Imaging technique

#### Ultrasound Elastography

An ultrafast ultrasound scanner (Aixplorer, Supersonic Imagine, Aix-en-Provence, France) coupled with a linear transducer array (SuperLinear 10-2; Supersonic Imagine, Aix-en-Provence, France) was used in the SWE (Shear Wave Elastography) mode. The push emission frequency was set at 2.8 MHz and the emission frequency of the plane waves was set at 6.4 MHz. The push duration was established at 300  $\mu$ s and the event duration at 350  $\mu$ s. The plane waves were sent with three different flat angles  $[-2^\circ, 0^\circ, 2^\circ]$ . The maximum framerate obtained was around 5000 Hz ( $\approx 4648$  Hz). With a time resolution of tens of milliseconds, the spatial resolution of the mapping is 200  $\mu$ m.

In coupled compression and tensile experiments, Aixplorer was driven on Matlab by a loop to take measurements approximately every second (time to create the pushes by focused ultrasounds, then to follow the shear wave propagating in the gel, and to save the data). The calculation of the shear wave speed requires post-processing on Matlab with the Time Of Flight method explained in part. 2.14. A summary of the Matlab code used is found in Fig. 2.17.

```
Beginning of the sequence at t = 0:
  For n measures:
    - Focused ultrasounds at different depths
    - Creation of shear waves at these focal spots
    - Recording of the SW propagation through US plane waves
    - Beamforming
    - Save data at t = tn
  end

Post-processing:
  - Time Of Flight method used to recover the SW speed
```

FIGURE 2.17: Matlab script used to control the measure made by Aixplorer at rest or during an uniaxial compression/tensile test.



## Chapter 3

# Gel behavior under homogeneous stress field: from linear to nonlinear elasticity

### Content

The first part of this chapter will study the gel behavior, in a linear regime, at small strain. Then, the gel will be studied under large deformations where nonlinear elasticity takes place (Fig. 3.1). The role of silica nanoparticles (NPs) on mechanics and imaging will be discussed. A five order magnitude frequency study, at rest, will be possible through the use of three techniques presented in Chapter 2: tensile/compression tests, rheology (distortion, shear), and a test based on mechanical waves (shear wave elastography). Beyond the linear regime, compression tests will highlight the gel's anisotropy which affects the shear wave velocity. By applying a theoretical approach of the strain energy in soft solid (Hamilton et al., 2004), these nonlinear effects will be carefully studied. Through acoustoelasticity, it is possible to retrieve the stress imposed on the material during a tensile or compression test. Indeed, it is closely linked to the shear wave velocity and the Landau elastic coefficients. Finally, the stress relaxation will be followed by SWE.

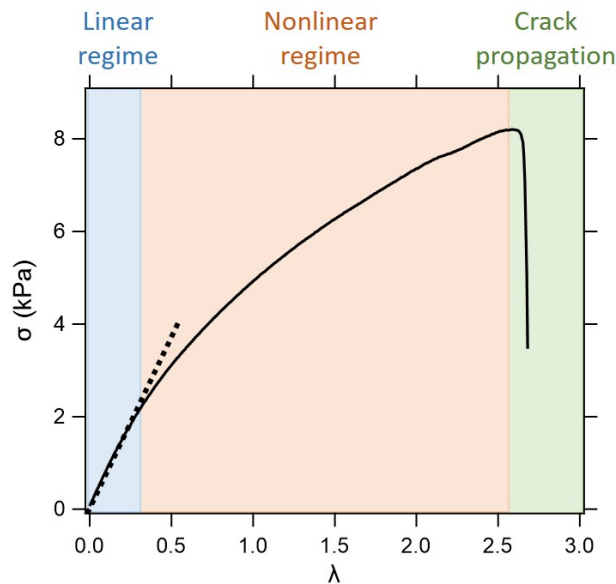


FIGURE 3.1: From at rest state to linear regime in the first part of the stress/strain curve. When the curve drops out of the linear fit, we enter into the nonlinear regime and finally the gel will break reaching its maximum deformation.

### 3.1 Gel behavior at small strain: Linear analysis

#### 3.1.1 Role of silica nanoparticles in imaging

##### Echogenicity for elastography

To propagate, a shear wave needs a medium that is rigid enough. In contrast to solids that can deform, liquids flow under the action of force. Therefore, it is not possible to create shear waves inside a liquid. Once the shear wave is created inside a solid, one needs to follow its propagation to get its velocity. In order to capture the shear wave propagation and velocity, the medium needs to contain randomly distributed Rayleigh scatterers (much smaller than the wavelength), called speckle, to reflect part of the acoustic energy and thus provide backscattered signals used to build ultrasonic images. In other words, the medium should not be transparent to ultrasonic waves. If the image is black, it means there are no echoes, no speckle (Fig. 3.2, left). The speckle is caused by the scattering of waves from the surface of small structures within a material. Speckle presence is due to interference effects between overlapping echoes and its occurrence is related to a great number of randomly distributed scattering structures. To see a shear wave propagating through an object, we need to see the displacement it creates thus the micrometric speckle displacement. Without speckle, the displacement is not visualized, thus the shear wave is not detected (Fig. 3.2, left).

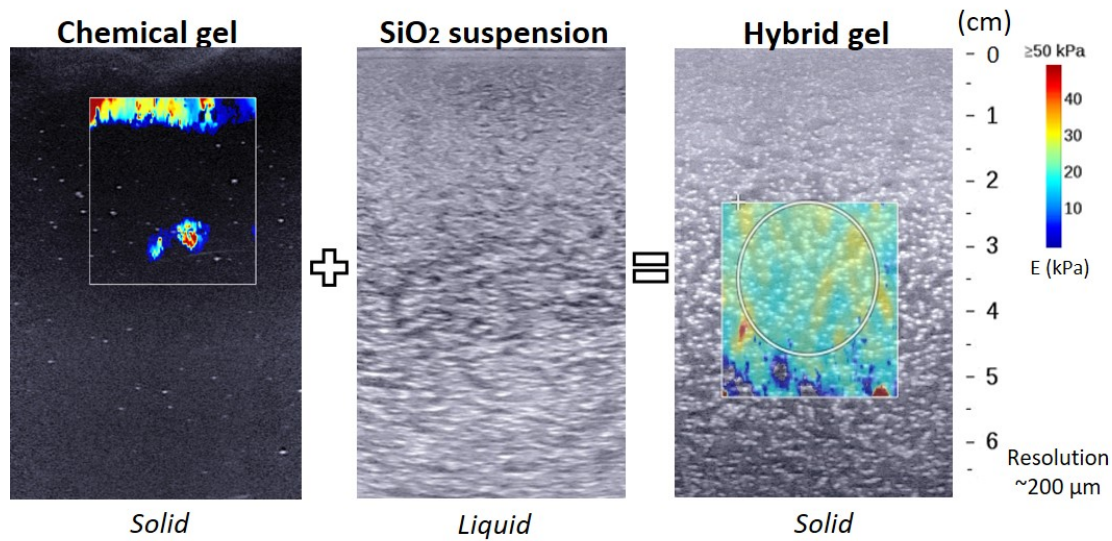


FIGURE 3.2: The chemical gel (PDMA) has a bad echogenicity due to the lack of speckle. The silica suspension Ludox TM-50 (nanoparticles) is a viscous liquid and has a good echogenicity but elastography can not be performed since it is liquid. The hybrid gel (PDMA + 10 vol.% of  $\text{SiO}_2$ ) shows a great speckle and a good signal. Tests have been performed at rest. The color bar represents the Young's modulus in kPa. The one of the hybrid gel is around 20 kPa.

In Fig. 3.2, it appears that the  $\text{SiO}_2$  NPs are essential to bring speckle inside the gel. Nevertheless, the NP diameter is around 28 nm and the spatial resolution of the imaging technique is 200  $\mu\text{m}$ . Thus, the white spots present in the image do not represent the NPs themselves but it is an indirect combination of the NPs, or probably some aggregate (local concentration fluctuations) of NPs. This assumption is confirmed by Fig. 3.3, where we see that the volume fraction of nanoparticles has no impact on the speckle. Whether it is with 1 vol.% or 20 vol.%  $\text{SiO}_2$ , we can not tell the difference between the two ultrasound images.

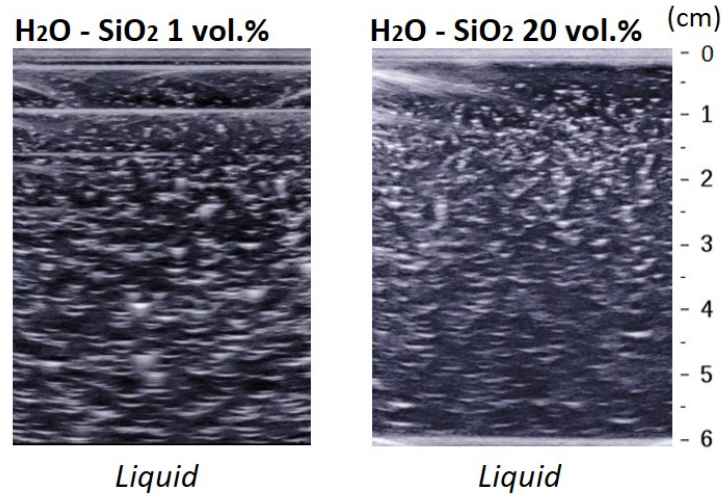


FIGURE 3.3: Silica nanoparticles are mixed with water at pH 9. The amount of NPs has no change on the speckle.

As summarized in Table 3.1, to perform elastography on the hydrogel, it is needed to add NPs inside the gel to have a good signal. This is a positive result knowing that the NPs were first added as a parameter to tune the viscoelastic properties of the hydrogel. Only a few percent of NPs induce the required echogenicity without implying strong changes in the mechanical response of the chemical gel.

	Chemical gel	SiO <sub>2</sub> susp.	Hybrid gel
State	Gel	Liquid	Gel
Chemicals	PDMA, MBA	NPs	PDMA, MBA, NPs
Diffusers	✗	✓	✓
SW created ?	✓	✗	✓
SW caught ?	✗	✗	✓

TABLE 3.1: The chemical gel (PDMA) has a bad echogenicity due to the lack of speckle. The Silica suspension (Ludox TM-50) has a good echogenicity but is a viscous liquid, therefore the shear can not happen. The hybrid gel is a good candidate for elastography.

Agar addition inside the gel is well-known to enhance the gel echogenicity ( Casciaro et al., 2010, Gennisson et al., 2014). To obtain a better ultrasonic speckle, 1 wt% agar powder was added right before molding the gel and mixed with the whole preparation for few seconds, making sure the mechanical properties were not affected (see Fig. 3.4). The chemical gels present the same Young's modulus (around 10 kPa) and the stress does not relax after having reached the desired strain (here 30% or  $\lambda = 1.3$ ).

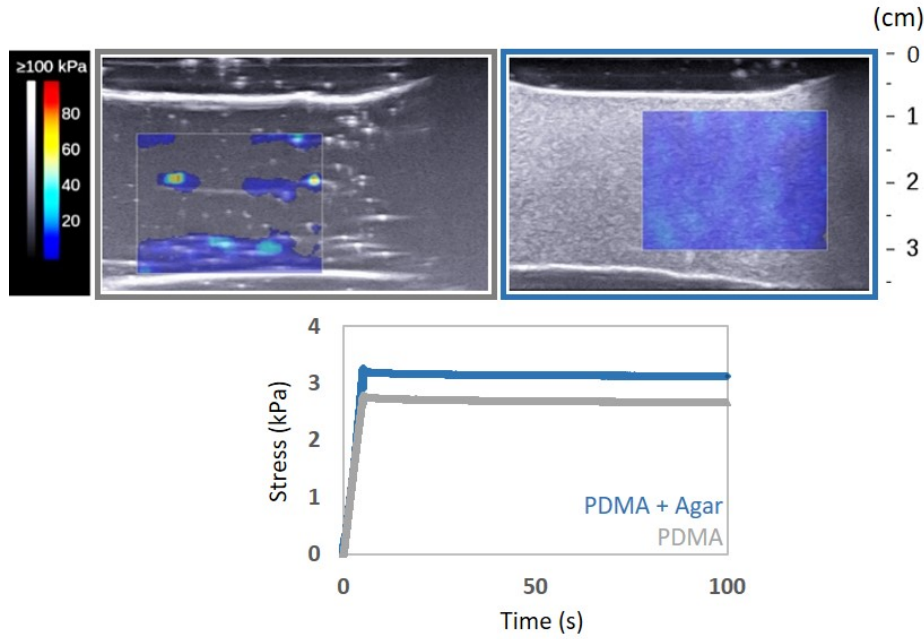


FIGURE 3.4: The chemical gel (PDMA) has a bad echogenicity due to the lack of speckle (left ultrasound image). The PDMA gel + AGAR has a good echogenicity (right ultrasound image) and the mechanical properties are unchanged.

### 3.1.2 Role of silica nanoparticles in mechanics

#### Mechanical investigation of hybrid hydrogels at preparation state

In part. 1.1.3, the mechanical properties of hybrid gels have been presented.

To sum up, the addition of silica NP inside the matrix allows physical interactions between the polymer chains that attach and detach from the NP surface. These dynamical bonds increase the stiffness of the gel, as well as its extensibility until fracture. Furthermore, the phenomenon of adsorption/desorption that occurs at the silica surface allows the matrix to rearrange under stress, thus relax. In Fig. 1.12c, the action of silica NPs is visible in a tensile test experiment. The geometry used in the study of previous colleagues (Rose, 2013) was strips of size:  $30 \times 5 \times 2 \text{ mm}^3$  (length  $\times$  width  $\times$  thickness).

In this thesis, the geometry was adapted to match shear wave elastography requirement, thus the gel's volume was considerably increased. The sizes of the samples are given in part. 2.5.2, for tensile and compression tests. The mechanical response of the gel for these new geometries are presented in figure 3.5. Compression tests are limited to a strain of  $\lambda = 0.7$  whereas tensile tests can reach a strain of about  $\lambda = 10$ . The results are similar to Fig. 1.12c. In addition, the stress relaxation is shown for the tensile and compression test with 30% strain ( $\lambda = 1.3$  or  $0.7$  respectively). One can notice that SP0, the chemical gel, shows a poor stress relaxation whereas, SP3.5 has great relaxation properties since the stress has lost 30% of its initial value (both for tensile and compression tests).

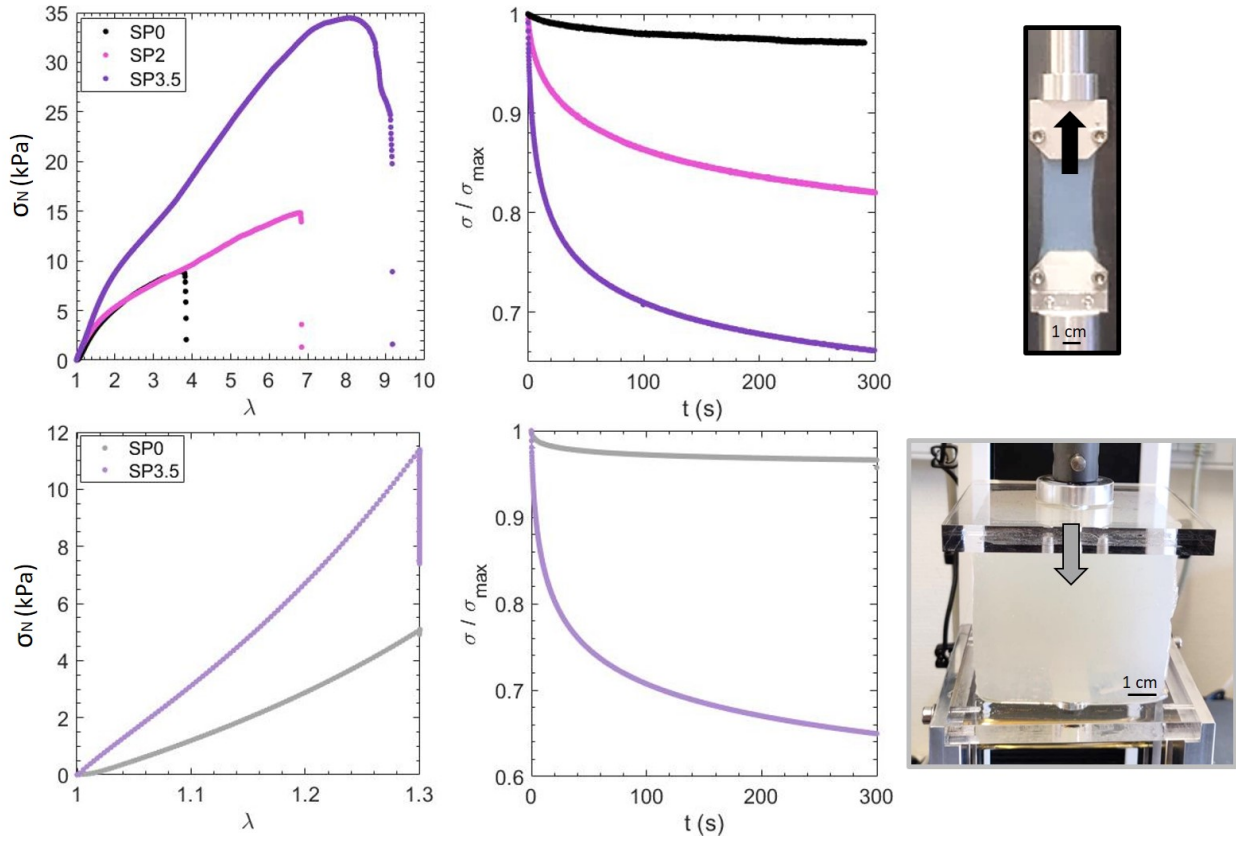


FIGURE 3.5: Top/bottom: Tensile/compression tests. Left: Nominal stress vs  $\lambda$ . Effect of SiO<sub>2</sub> NPs on the gel's stiffness and extensibility at break. Right: Effect of amount of SiO<sub>2</sub> NPs on the stress relaxation for 30% strain and a strain rate of 0.06 Hz.  $\sigma / \sigma_{max}$  is represented to compare the stress relaxation.

### Frequency dependence of gels: five orders of magnitude

Shear wave elastography allows to assess the mechanical behavior of gels over a quite large frequency range typically from 50 Hz to 300 Hz complementary to the lower frequency of rheological instruments. Thus, it enables to characterize soft materials over an enlarged frequency window. Figure 3.6 links the three different methods presented in part. 2.5.2 through the calculation of the Young's modulus at different frequencies.

In the case of Instron, at low frequency (below 1 Hz), the Young's modulus is calculated within the linear regime of the stress-strain curve (up to 5% strain).

For rheology, the Young's modulus was calculated from the storage  $G'$  and the loss modulus  $G''$ , assuming incompressibility ( $E \approx 3G$ ).

Regarding shear wave elastography, this experience is conducted at rest. The samples are measured at high frequencies (up to thousands of Hertz). These experiments were also conducted in a previous study (Gennisson et al., 2014). It is worth mentioning that in the case of shear wave elastography, the shear wave frequency cannot be chosen by the operator because it indirectly depends on the medium absorption and density and it is limited by the push frequency and push duration (Sarvazyan et al., 1998). Therefore, push frequency and push duration were changed to tune the shear wave frequency (from 2 to 10 MPa and 100 to 300  $\mu$ s respectively).

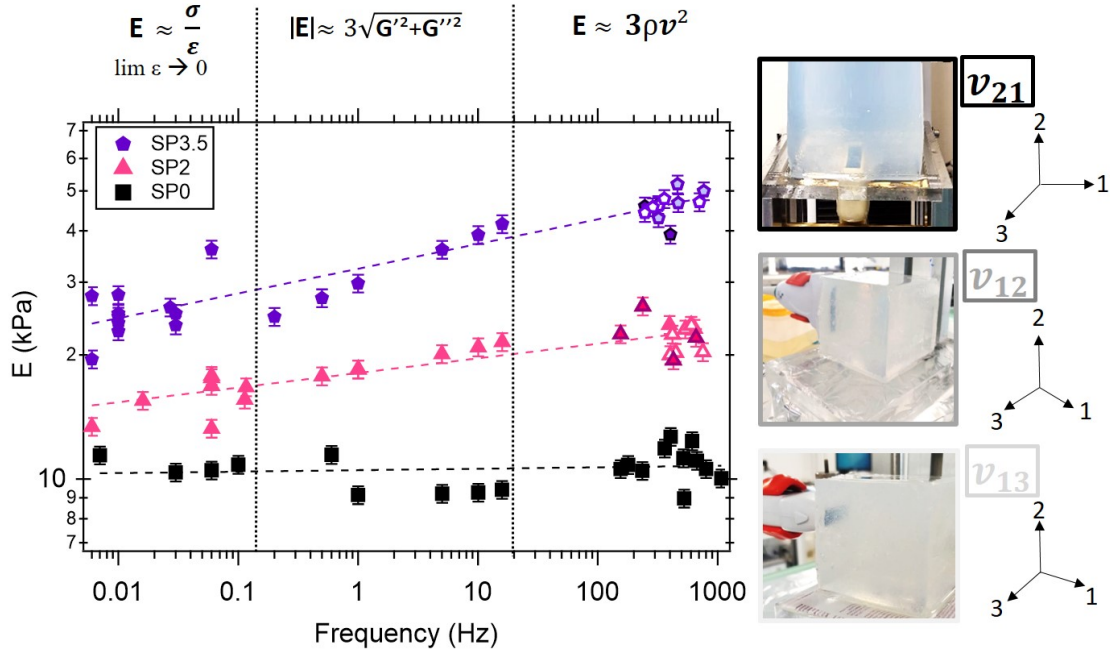


FIGURE 3.6: Frequency dependence of the Young's modulus. A logarithmic scale is used to demonstrate the power law. The Young's modulus  $E$  from shear wave elastography is obtained in three different ways corresponding to the pictures: light gray, gray and black respectively for  $v_{13}$ ,  $v_{12}$  and  $v_{21}$ .

As shown in figure 3.6, in the full frequency range, a significant increase of the initial stiffness is observed as the volume fraction of NPs gets higher. When the frequency range increases, the elastic gel, without NPs, shows no frequency dependence compared to the nanocomposite gels in which  $E$  increases strongly with a power-law as the frequency gets higher. The values of the power-law frequency are depicted in Table 3.2. A benefit of shear wave elastography is the possibility to place the probe at different positions on the sample (photos on the right of Fig. 3.6).

$E = Af^n$		
Samples	A (kPa)	n
SP0 ( $q = 20$ )	$10.5 \pm 0.3$	$0.003 \pm 0.006$
SP2 ( $q = 25$ )	$18.1 \pm 0.4$	$0.035 \pm 0.004$
SP3.5 ( $q = 29$ )	$32.4 \pm 0.7$	$0.060 \pm 0.004$

TABLE 3.2: Frequency dependence of  $E$  determined from tensile and compression tests, rheology and elastography experiments on gels at  $Q_0$ . A power law is extracted between the Young's modulus and the frequency. Mean values over all  $q$  samples were given for SP0, SP2, and SP3.5 hydrogels.

This frequency dependence is related to the dynamics of polymer adsorption/desorption at the monomer scale (Rose, 2013).

### Mechanical investigation of hybrid swollen hydrogels

For the mechanical response of swollen gels, the elastic PDMA gel and the nanocomposite gel with 20 wt% of  $\text{SiO}_2$  (SP5) are compared after having followed the directions given in part 2.5.1. In addition, different states of swelling will be studied, from the initial state  $Q_0$  to equilibrium state  $Q_e$ : gels were studied after 5 and 30 minutes immersed in water:  $t = 5$  min ( $Q_5$ ) and  $t = 30$

min ( $Q_{30}$ ). For this experiment, the gel geometry was the one of a little strip of width  $\times$  thickness  $\times$  length:  $5 \times 2 \times 30 \text{ mm}^3$ .

The gels at equilibrium state reach their maximum degree of swelling ( $Q_e$ ). They gain in weight and volume (the polymer chains stretch to accommodate water that enters into the matrix network). This swelling is less significant for nanocomposites gels since swelling equilibrium is constraint by polymer adsorption onto silica NPs, thus the extension of the polymer chains is reduced (see pre-stretch ratio induced by swelling in Table 3.3).

Swelling degree	PDMA E (kPa)	Q (v/v)	$\lambda_i$	$G_c$ (J/m <sup>2</sup> )	PDMA/Silica E (kPa)	Q (v/v)	$\lambda_i$	$G_c$ (J/m <sup>2</sup> )
Q0	$7.8 \pm 1.2$	$8.5 \pm 0$	1	$19 \pm 9$	$90.4 \pm 5.3$	$8.52 \pm 0$	1	$513.0 \pm 196.5$
Q5	$6.7 \pm 0.4$	$11.9 \pm 0.5$	1.12	$14.6 \pm 6.1$	$55.2 \pm 4.2$	$10.4 \pm 0.6$	1.07	$234.4 \pm 50.1$
Q30	$5.7 \pm 0.2$	$15.3 \pm 0.7$	1.22	$10.4 \pm 5$	$32.1 \pm 2.9$	$12.8 \pm 1.0$	1.14	$140.5 \pm 61.6$
$Q_e$	$6.8 \pm 1.5$	$41.1 \pm 3.9$	1.69	$3.8 \pm 0.9$	$13.0 \pm 1.7$	$20.1 \pm 1.4$	1.33	$35.3 \pm 12.3$

TABLE 3.3: Young's modulus E, swelling degree Q and pre-stretch ratio induced by swelling  $\lambda_i$  values for PDMA and PDMA/Silica hydrogels with 20% of SiO<sub>2</sub> depending on swelling state.

As seen in previous results, the presence of NPs clearly enhances the mechanical properties of the gel (Fig. 3.7): stress and elongation at break are drastically higher than those of the pure chemical gel. It is important to notice that even swollen at equilibrium, nanocomposite gels have a greater Young's modulus than PDMA gels at  $Q_0$  and also higher stress and strain at break (Table 3.3). This proves that silica nanoparticles play an important role even when the gel is filled with water.

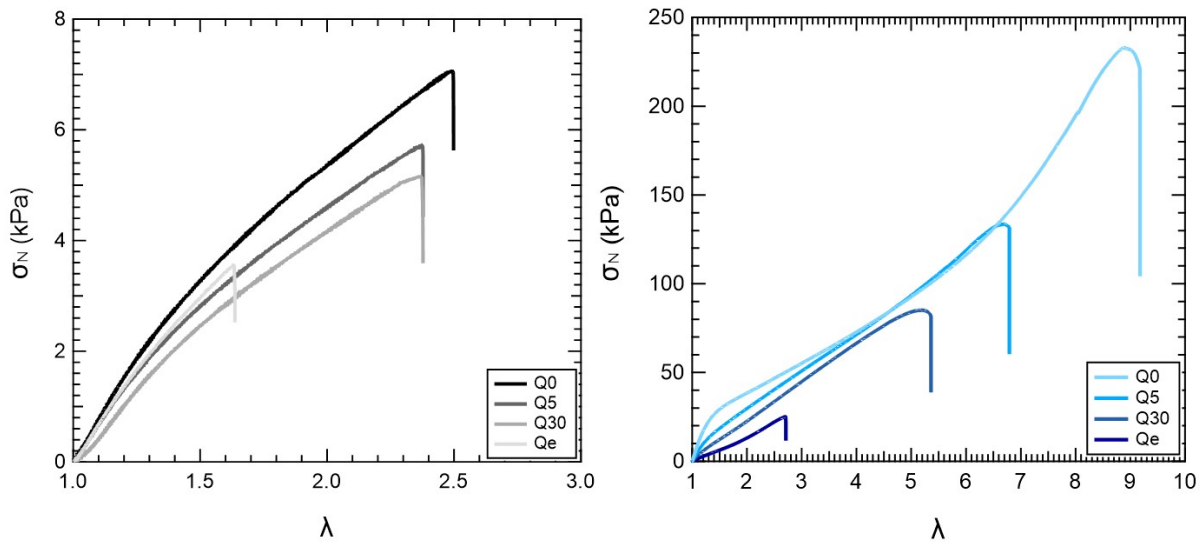


FIGURE 3.7: Stress VS strain curves of (left) PDMA samples at different swelling degrees and (right) nanocomposite PDMA/Silica samples at different swelling states. Tests were performed at a strain rate of 0.06 Hz. These experiments were carried out by Milena Lama during an internship.

Rheology under frequency sweep allows to discuss the dynamics of the hydrogels within the linear viscoelastic regime.

Figure 3.8 shows that PDMA hydrogels have an expected elastic behavior: no matter the swelling state of the sample, the storage modulus  $G'$  is independent of frequency as expected for a perfect rubbery network (Colby et al., 2003). Also,  $G'$  diminishes when the swelling increases because the density of cross-links reduces (Anseth et al., 1996). Concerning the loss modulus  $G''$ , it increases with frequency and decreases with the swelling state. This is quite surprising especially since the gels are commonly depicted as very elastic and non-dissipative systems. Since the network mesh size becomes bigger upon swelling, the length of dangling ends proportionally reduces in swollen gels, thus the relaxation through dangling chains also decreases (De Gennes et al., 1979, Curro et al., 1983). This explains why  $G''$  diminishes when swelling increases. Besides, when swollen, the entanglements in the polymer network lose the dangling polymer chains, which also decreases their relaxation time. Finally, it is also possible that some free uncross-linked chains are squeezed out of the gel and participate in the extractable content.

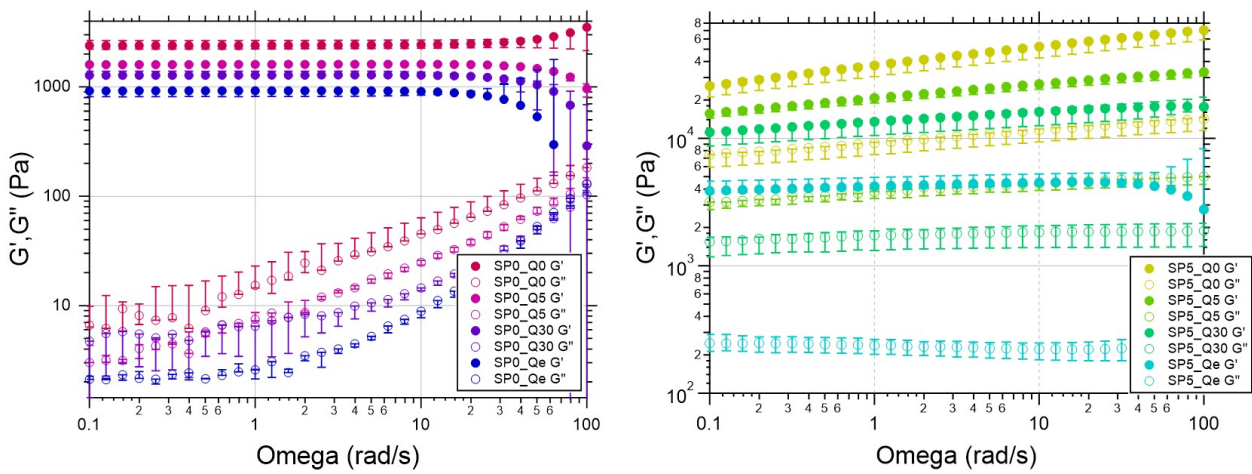


FIGURE 3.8: Storage (full circles) and loss (empty circles) moduli of (left) PDMA samples and (right) PDMA/Silica samples in different swelling states. These tests were performed by Milena Lama during an internship.

PDMA/Silica hydrogels, in figure 3.8 (right), exhibit completely different behavior. First, their storage modulus  $G'$  depends strongly on the frequency with a power-law stress relaxation in time. The more swollen the samples are, the less their storage modulus depends on frequency. When the sample reaches its equilibrium swelling state  $Q_e$ , the physical interactions (responsible here for the frequency dependency) are hindered by over-swelling the network. At a first glance, within the investigated frequency range, the nanocomposite hydrogel mechanical response resembles that of a pure chemical gel.

For both types of gels, the loss modulus  $G''$  depends on the swelling state of the sample. More remarkably, loss moduli  $G''$  evolves in a different manner if the network is purely chemical or hybrid. In the pure chemical PDMA hydrogel, only entanglements should participate to slow down the relaxation of the dangling ends while in the nanocomposite gel, these pendant chains can adsorb and desorb onto the silica nanoparticles (while relaxing to an equilibrium state). Therefore, the relaxation process in this latter case is predominant and even much more complex. Since the imaging technique is able to measure the gels at high frequency (hundreds of hertz), shear wave elastography was performed on swollen gels at rest (see next part).

### High frequency response of swollen gels

In Fig. 3.9, it appears that swelling gels show a drastic decrease in stiffness for all gels compared to the preparation state (as Fig. 3.7). For example, at low frequency and at  $Q_0$ , the Young's modulus of SP3.5 is around 25 kPa while it is around 9 kPa for  $Q_e$ .

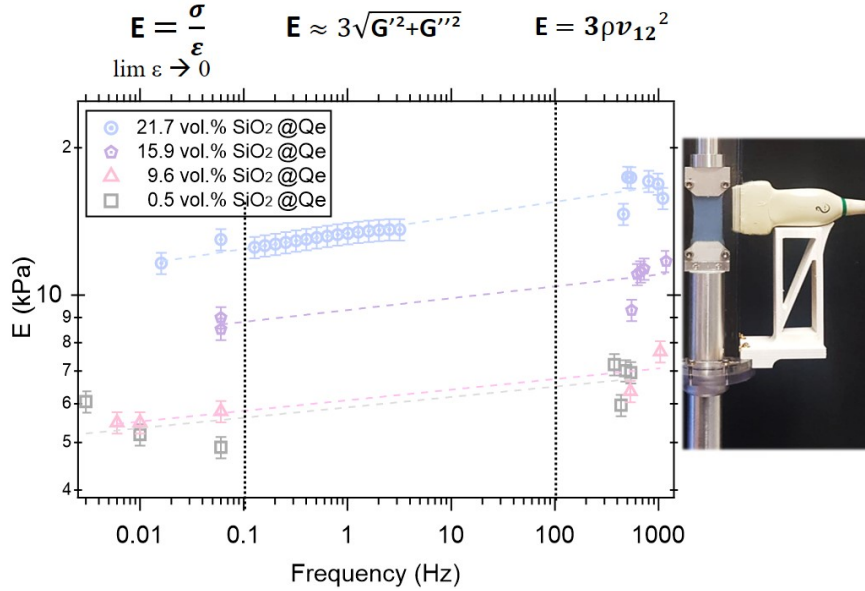


FIGURE 3.9: Frequency-dependence of the Young's modulus for gels at swollen state  $Q_e$ . A logarithmic scale is used to demonstrate the power law.

Gels are drastically mechanically weakened when they are waterlogged. Indeed, one can observe an increase of  $E$  at high frequency with an index power law  $n$  close for the four gels (between  $\approx 0.021$ - $0.032$ ) (see Table 3.4). This shows that at equilibrium state  $Q_e$  and at rest (or in the linear regime), the polymer chains govern the mechanical response of the gel over the NPs which no longer seems to act as at the preparation state.

Samples @ $Q_e$	A (kPa)	n
SP0 (q=7)	$5.9 \pm 0.6$	$0.021 \pm 0.006$
SP2 (q=5)	$6.1 \pm 0.2$	$0.022 \pm 0.007$
SP3.5 (q=7)	$9.3 \pm 0.4$	$0.021 \pm 0.008$
SP5 (q=8)	$13.4 \pm 0.1$	$0.032 \pm 0.002$

TABLE 3.4: Frequency dependence of  $E$  determined from tensile tests and elastography experiments on gels at  $Q_e$ . A power law is extracted between the Young's modulus and the frequency. Mean values over all  $q$  samples were given for SP0, SP2, SP3.5 and SP5 hydrogels.

To conclude, the mechanical tests revealed that even swollen at equilibrium, a nanocomposite gel has still higher fracture stress and strain than a chemical gel in the as-prepared state  $Q_0$  (Fig. 3.7). Nevertheless, the last result demonstrates that the dynamics of polymer segments that are adsorbed onto NPs are drastically changed by over-swelling. At rest or small strain, the amount of NPs has no significant impact on the gel's stiffness (Young's modulus) nor dynamics according to the frequency when gels are swollen compared to gels at preparation state (Fig. 3.6).

### 3.1.3 Nanoparticles dispersion state: Link between Bmode imaging and mechanics

A great advantage of elastography for mechanical engineers is the ability to link the microstructure to mechanical parameters. During the synthesis of hybrid gels with 2 vol.% of  $\text{SiO}_2$ , two different geometries have been used: one for a tensile test with strips of about  $30 \times 5 \times 2 \text{ mm}^3$  and one big cube for the ultrasound probe of  $70 \times 70 \times 70 \text{ mm}^3$ . At that time, the setup of the coupling technique did not exist. The following experiment is thus decoupled. The small samples were used for tensile tests while the big cubic samples were studied at rest by the ultrasound probe. Two different syntheses of this hybrid gel were performed (one represented in purple and the other in orange in Fig. 3.10).

The mechanical curves of Fig. 3.10 clearly show the impact of mixing on mechanical response. Two different behaviors (in purple and orange) are noticed. Yet, the same formulation has been followed. The only difference was the mixing time which was reduced for samples A and B compared to C and D (C and D curves correspond to standard preparation). By comparing ultrasound images with mechanical curves, it appears that the samples represented by the purple color show a heterogeneous distribution of the nanoparticles inside the gel. It is visible with the red spots and empty part with no signal on ultrasound images. These large heterogeneities are assigned to aggregated domains and lead to a strong mechanical stiffening together with embrittlement.

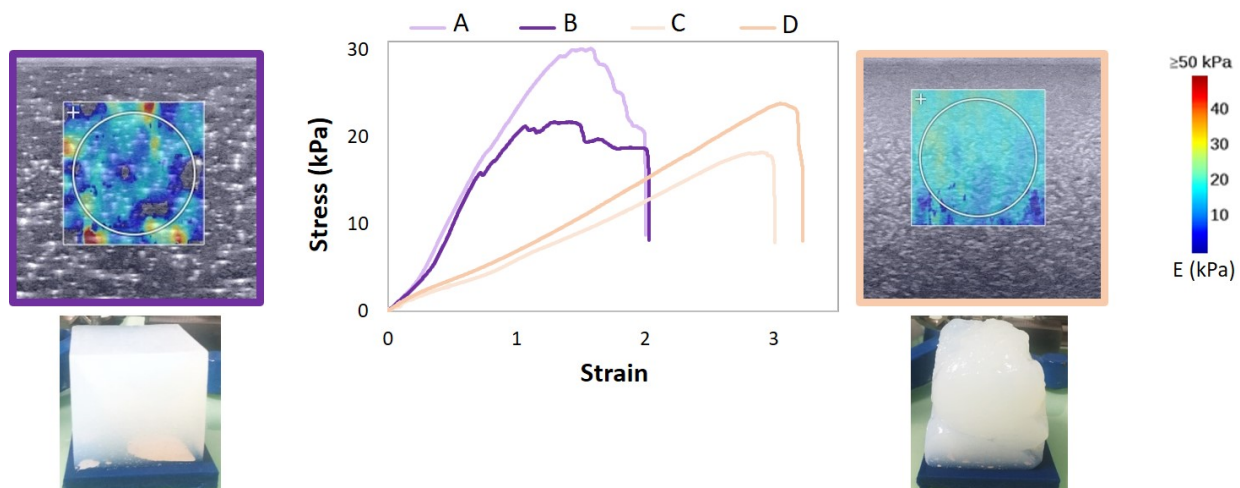


FIGURE 3.10: Link between microstructure and mechanics in hybrid gels with 2 vol.% of  $\text{SiO}_2$ : influence of the mixing time. The stress/strain curves are represented for four samples. Samples A and B come from the same synthesis while C and D come from another synthesis. The graphic and the ultrasound images (taken at rest) show evidence of aggregated silica (violet curves and image). The photography of the gels is given below the ultrasound images. For the homogeneous gel, the mixing time was too long and the gel had already started its polymerization while pouring into a mold. A good compromise must be found to have a homogeneous texture and, still a liquid gel when molding.

Heterogeneities can lead to fracture: stress concentrates at the defects which become a possible fracture propagation source. In Fig. 3.10, sample A and B have a strain to failure reduced to 200% instead of 300% in the case of a homogeneous gel (sample C and D) proving that heterogeneity must be avoided if one wants gels with better mechanical performances.

### 3.1.4 Toward anisotropy at large strains

From now, gels were studied at rest with shear wave elastography. To study the gel under deformation, a simple experiment was performed with a little homemade setup composed of two parallel plates and a screw to fix the upper plate. A compression test of 20% strain (corresponding to  $\lambda = 0.8$ ) has been performed on the elastic hydrogel SP0. The probe was set at different configurations on one side of the gel from  $0^\circ$  (horizontal probe),  $20^\circ$ ,  $45^\circ$ ,  $70^\circ$  to  $90^\circ$  (vertical probe). In the polar plot of Fig. 3.11, one can observe that when the gel is submitted to a strain, the shear wave velocity is changed (divided by 3 from the horizontal to vertical configuration).

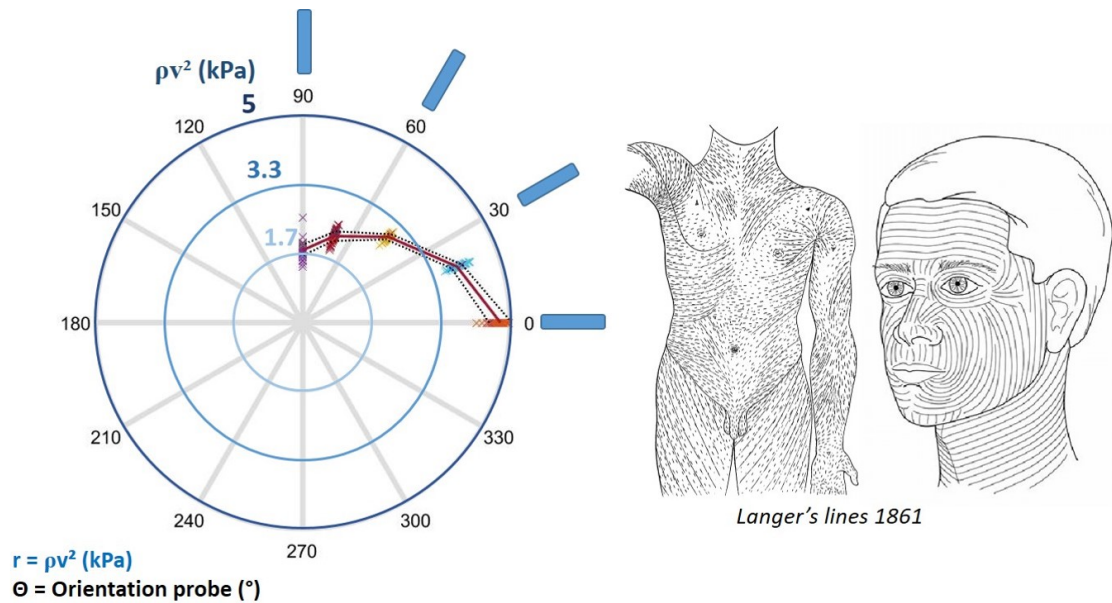


FIGURE 3.11: Left: First clues of anisotropy under stretch with a 20% compression test. The shear wave velocity appears to be different depending on the position of the probe on the gel. Right: Pre-tension in the skin is represented through Langer's lines with a clear preferred orientation depending on the body location.

This experiment reminds the one made by Langer in 1861 (Langer, 1861). He defined what he called the Langer's lines which represent the skin orientation on the body. This orientation strongly depends on the body location (Fig. 3.11, right). As a matter of fact, the skin, our biggest organ, is under tension and the collagen orientation creates the anisotropy. These lines are used nowadays to determine to best cut in surgery (to get the best healing) (Kraissl, 1951).

This simple experiment highlights the fact that elastography is able to capture the material anisotropy through the shear wave velocity that is changed under strain. The same experiment was done on an elastic gel at rest (see Fig. 3.12) and a slight change was observed between  $v_{12}$  and  $v_{21}$ ,  $v_{31}$ . This slight difference is assigned to a gravity effect under the gel's own weight (Gennisson et al., 2007).

Under large strain, the analysis is more complex and has been less investigated experimentally. The study of mechanical waves propagating in a prestressed material is called acoustoelasticity. It becomes essential from here to link mechanics and wave physics to understand the parameters estimated by shear wave elastography.

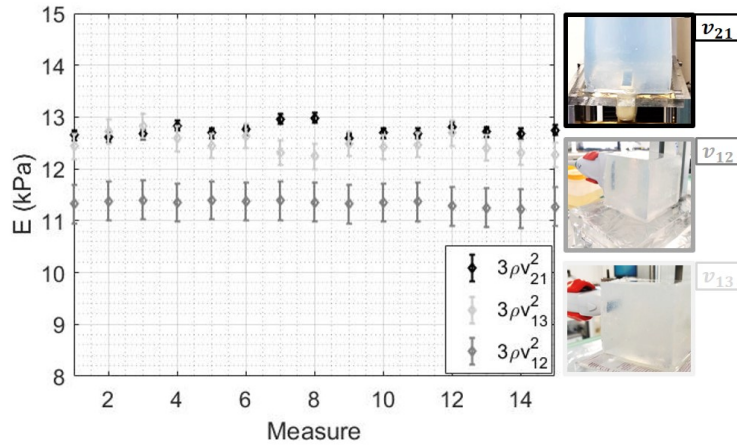


FIGURE 3.12: 15 measures are taken on the elastic gel at rest with three different probe positions.  $v_{12}$  is smaller than  $v_{21}$  and  $v_{13}$  due to the gravity effect. Error bars represent the standard deviation between the left and right shear wave velocity.

## 3.2 Coupled experiments with Shear Wave Elastography and standard mechanical tests

In this part, we will use the coupled techniques presented in part 2.5.2. This allows the simultaneous measurements of the SW velocity, the stress and the strain during mechanical tests.

### 3.2.1 Tangent modulus in the nonlinear elastic region

In part 3.1, the Young's modulus calculated by both techniques on gels at rest or at small perturbations was in good agreement for elastic gels. For the viscoelastic gels, a frequency power-law was needed between the measure from mechanical testings with the one from elastography due to the high frequency measurements by SWE. Once the linear elastic regime is passed (visible in the stress/strain curve of Fig. 3.13 for example), the tangent modulus must be used.

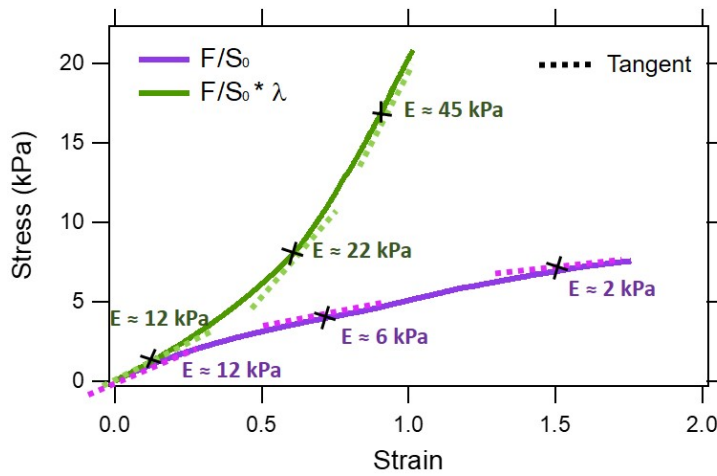


FIGURE 3.13: Tensile test until fracture for an elastic gel. Stress and strain are represented in purple as well as true stress and true strain in green (defined in 2.5.2). Three dotted lines are drawn for each curve corresponding to the tangent modulus of each point (represented by crosses).

The tangent modulus is the slope of the stress–strain curve at any specified stress or strain. In the elastic region, at the beginning of the curve, the tangent modulus is equal to the Young’s modulus. Concerning elastography, the shear wave creates a micrometric measurement that oscillates at some points in the stress/strain curve during compression or tensile test. Intuitively, this local measurement at different strains in the curve should be equal to the tangent modulus of the stress/strain curve.

The true stress and the stress versus the strain are represented in Fig. 3.13. Three tangents of each curve are depicted in dotted line. It appears that the tangents of the nominal stress/strain curve flatten out whereas the slope of the tangents increases in the case of the true stress/strain curve. The true stress/strain curve is more accurate because it takes into account the change in cross section area during the test. Elastography is a local measure into the bulk, thus does not depend on the surface (the measure is directly made inside the gel). In Figure 3.14, elastography measures an increase in the Young’s modulus during a tensile test. Therefore, the choice to work with the true stress was made.

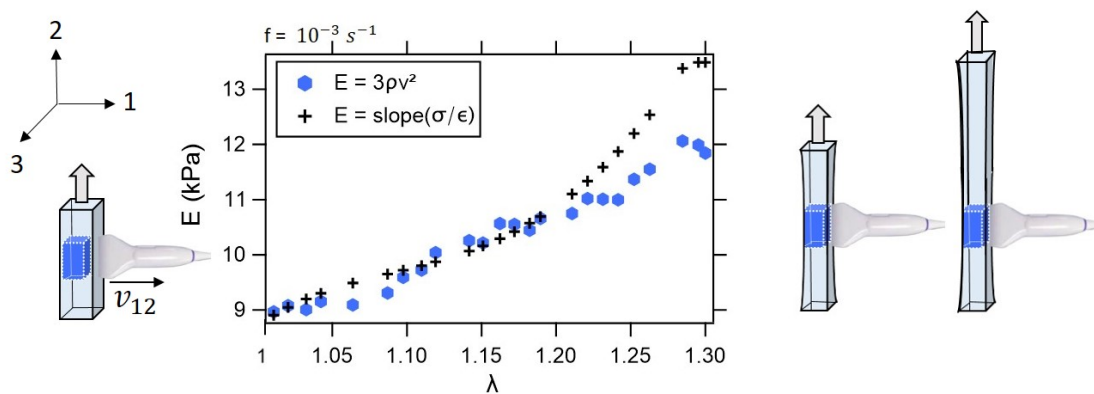


FIGURE 3.14: Tensile test until 30% strain ( $\lambda = 1.3$ ) for an elastic gel.  $E$ , the tangent modulus, is calculated through the shear wave velocity (blue) and with the tangent modulus through the true stress/strain curve (black cross).

The tangent modulus and the Young’s modulus from elastography for a tensile test until 30% strain on an elastic gel are represented in Fig. 3.14. The measure made by SWE is represented by the little blue box inside the gel on the scheme while the macroscopic measure made by mechanical testing is represented in light blue. At rest, or zero strain (elongation  $\lambda$  equals 1), the Young’s modulus calculated from elastography and from mechanics is the same as we have already seen in Fig. 3.6. Then, the two measures are in good agreement until a certain strain. From  $\lambda \approx 1.20$ , the two curves gently diverge when the strain increases. This can be explained by the sample that narrows at its middle due to lateral constraints imposed by the clamps. When deformations are large, the local measures made by SWE move away from the middle of the sample and differ from the global measure of the force. Indeed, during the tensile test, the probe does not move. Only the upper clamp moves to the top, stretching the gel (see little schemes of Fig. 3.14).

### 3.2.2 Toward a local measure

Due to sample geometry, for compression tests, the way to place the probe on the gel is more versatile. At rest, we have concluded that the probe’s position does not impact the results except a slight change when the probe was vertical due to gravity effects (see Fig. 3.12). Compression of 20% ( $\lambda = 0.8$ ) was applied to the gel (see Fig. 3.15). Note that when the probe is vertical (side  $90^\circ$ ), the maximum compression strain possible to place the ultrasound probe was around  $\approx \lambda =$

0.87. Fig. 3.15 shows that the shear wave velocity decreases when the probe is vertical instead of increasing as the other two configurations.

In compression tests, when the gel is loaded, the tangent modulus obtained by mechanical testing and the modulus calculated from the shear wave velocity are no more equal (see Fig. 3.15) whereas there is a good agreement until a certain strain for the configuration in the tensile test (see Fig. 3.14). Elastography is a local measurement: the "pushes" of the radiation force are created at 5, 10 and 15 mm from the surface of the gel. The gel has a geometry of 70 mm by side. As represented in the schemes of Fig. 3.15, we observe that both techniques are not measuring the same volume either elastography itself with the three different probe configurations. The calculation of the tangent modulus includes the stress which is the force divided by the surface ( $70 \times 70 \text{ cm}^2$ ), whereas in SWE, the modulus is measured in a small volume represented by small colored boxes depending on the probe location. The volume of these colored boxes is estimated to be around  $0.75 \text{ cm}^3$ . This result illustrates the capability of elastography to run local measures contrarily to the mechanical testing machine and that the volume sample (strip or cube) affects the results (see part 3.2.3).

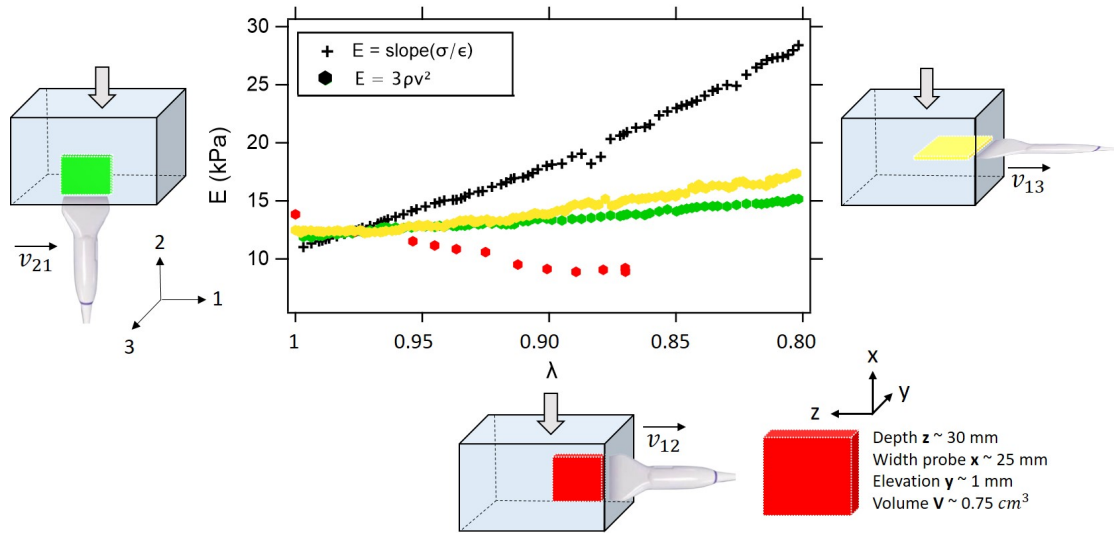


FIGURE 3.15: Compression tests for an elastic gel until  $\lambda = 0.8$  (0.87 for the red configuration) and different strain rates (0.006 Hz for the yellow and green configuration and 0.06 Hz for the red one). The schemes around the graphic show the volume of interest probed by SWE depending on the US probe location. This volume is estimated to be around  $V = 0.75 \text{ cm}^3$ .

### 3.2.3 Compression VS tensile response

In an ideal case where compression and traction could be done on the same geometry, the stress/strain curves would be identical (with a difference in the negative/positive stress).

#### Impact of geometry

For practical reasons, compression tests have been done on cubic samples of size  $70 \times 70 \times 70 \text{ mm}^3$  and tensile tests have been done on a sample size of width varying from 20 to 25 mm, thickness of 10 mm and different  $L_0$  (length between the two clamps) ranging from 30 to 60 mm.

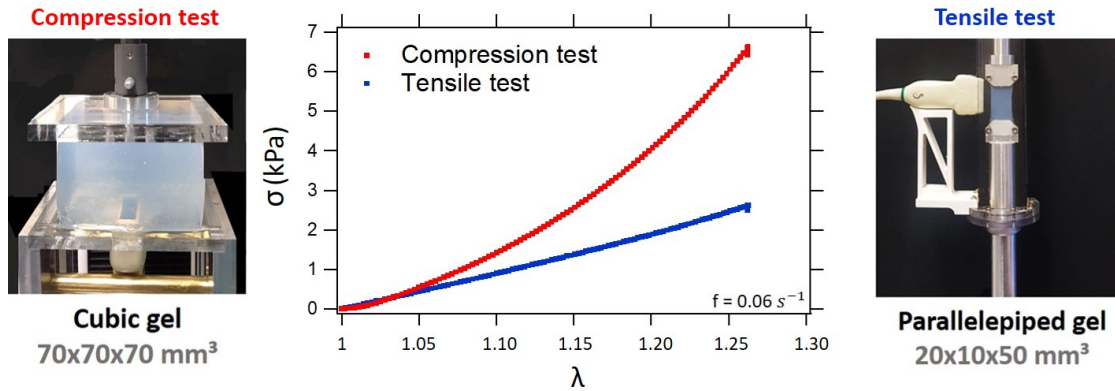


FIGURE 3.16: True stress as a function of  $\lambda$  for an elastic gel. In the linear regime, until 5%, the tangent of both curve is the same. At larger strain, the curves deviates.

Fig. 3.16 highlights geometry effects. Within the linear regime, up to 5%, the tangent of both curves is the same, thus the Young's modulus is the same. It is expected since the Young's modulus is a material property and it does not depend on the geometry. At larger strains, the curves deviate due to the geometrical effects.

### Shear wave velocity affected by the sign of the stress

If the probe is placed at the same position on the gel but in one case we stretch it and in the other case we compress it, the shear wave speed gives opposite variations upon mechanical loading (Fig. 3.14 and Fig. 3.15 reunited in Fig. 3.17).

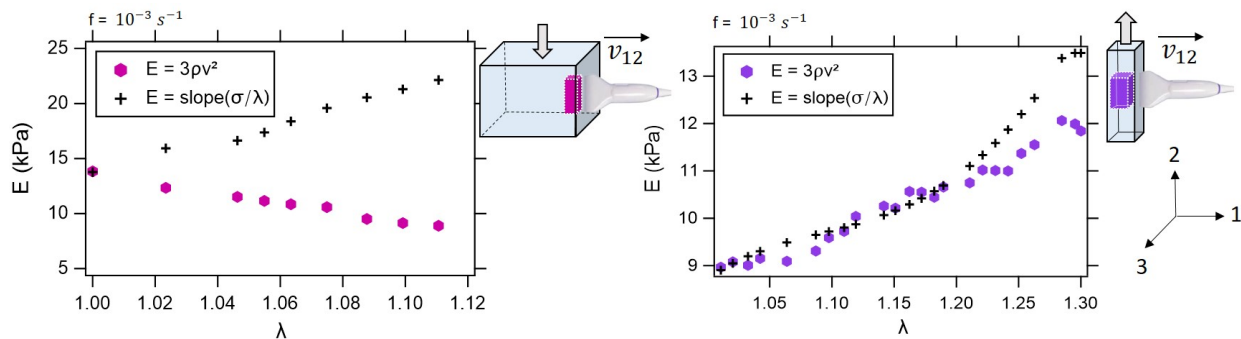


FIGURE 3.17: Tensile test vs compression test linked to the ultrasound probe. The shear wave speed is polarized and different for a tensile and a compression test.

The shear wave speed follows the stress imposed on the material. For a compression test, thus negative stress, the shear wave velocity decreases while it increases for a tensile test, thus positive stress. It appears that SWE is a powerful tool to quantify local mechanical state (in kPa) but the assumption of  $E = 3\rho v^2$  appears to be too simplistic when the material is subjected to a stress. As illustrated in Fig. 3.17, elastography and mechanical testing are no longer in agreement. More than being a bulk or geometry issue, this indicates that the measure made by SWE is more complex. The shear wave, being polarized due to the anisotropy created under strain, gives access to a lot of information and the modulus (kPa) is not enough to characterize what the shear wave velocity measures. We will see in the next part that under a stress, the shear wave velocity measures what we call an "apparent shear modulus" which is closely linked to the shear modulus at rest and the stress imposed on the material. From now, the Young's modulus won't be mentioned anymore except for the sample at rest.

### 3.3 Large strain acoustoelasticity effects: A non linear analysis

Through the strain energy density function  $W$  defined in Part 2.4.1, it is possible to retrieve two different stress functions. Firstly, by using the equation of motion, it is possible to get a formula of the shear wave velocity as a function of the stress (this is the acoustoelasticity theory) (see Eq. 2.38 and Eq. 2.39). Then, the stress can be calculated by deriving  $W$  by the elongation  $\lambda$  ( $\lambda$  being included in the Invariants  $I_2$  and  $I_3$  of the Green-Lagrange strain tensor) (see Eq. 2.44).

#### 3.3.1 Calculation of nonlinear Landau coefficients A and D

##### Fitting Procedure

By building a paired setup between the Instron (conventional mechanical tool) and the Aixplorer (SWE), the shear wave velocity, the force and the displacement were extracted during a uniaxial tensile test or compression test. The parameter that allows linking both experiments is the time since experiments are performed simultaneously. Through the use of AE theory, we can calculate the nonlinear coefficients  $A$  and  $D$  (see Fig. 3.18 for an example with a tensile test) present in Eq. 2.39 that is rewritten here:

$$\rho v_{12}^2 = \mu_0 + \sigma_{22} \left( 1 + \frac{A}{12\mu_0} \right) + \sigma_{22}^2 \left( 5\mu_0 + \frac{7}{4}A + 3D \right) \frac{1}{9\mu_0^2} \quad (3.1)$$

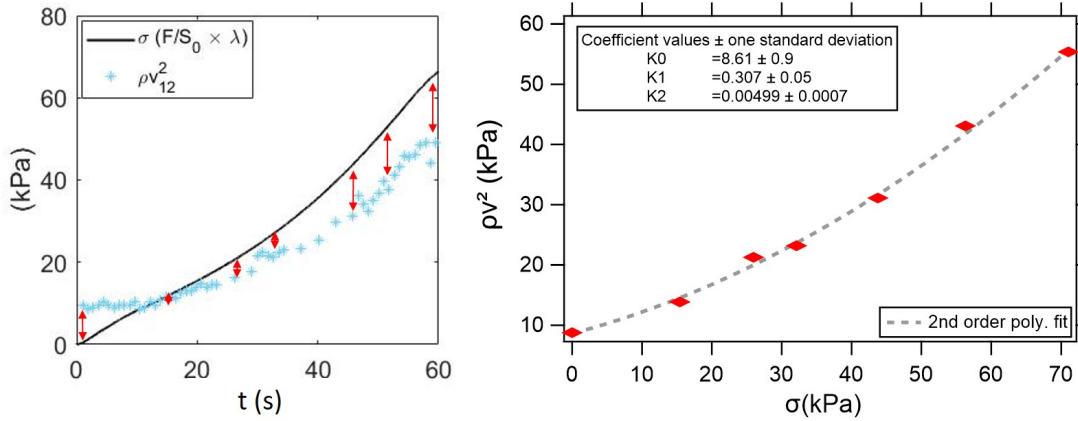


FIGURE 3.18: Fitting procedure example. Left: Experimental data of the true stress (black) and the shear wave velocity (blue) as a function of time during a tensile test. The red arrows show the matching between each measure of the SW speed with the true stress. Right: Shear wave velocity as a function of the true stress. Only a few points are represented according to the red arrows of the left graphic. The second-order polynomial fit is an interpolation and allows the calculation of the nonlinear elastic coefficients  $A$  and  $D$ :  $\rho v^2 = K_0 + K_1\sigma + K_2\sigma^2$ . Here,  $\mu_0 = 8.6$  kPa,  $A = -74.5$  kPa, and  $D = 30.0$  kPa, using eq. 3.1.

##### Elastic gels: tool for calibration of large strain acoustoelasticity

The Landau coefficients  $A$  and  $D$  have been calculated in elastic gels through four independent experiments (3 in compression test, 1 in tensile test) (Fig. 3.19). Qualitatively experimental shear wave velocities are in agreement with AE equations and the obtained fitted  $A$  and  $D$  values are of the same order of magnitude for the 4 experimental configurations (see also Table 3.5). Note that due to geometrical constraints in compression, tensile mode allows to probe drastically larger

deformation range (until rupture) and provide a more accurate identification of  $A$  and  $D$  parameters. According to Hamilton *et al.* (Hamilton *et al.*, 2004),  $A$  constant determines the nonlinear shear stress while  $D$  would required to describe nonlinear distortions of shear waves in finite amplitudes. Part (3.4.2) studies the physical sense of these two parameters. Note that as far as we know, this is the first time that AE theory is compared with large strain mechanical experiments.

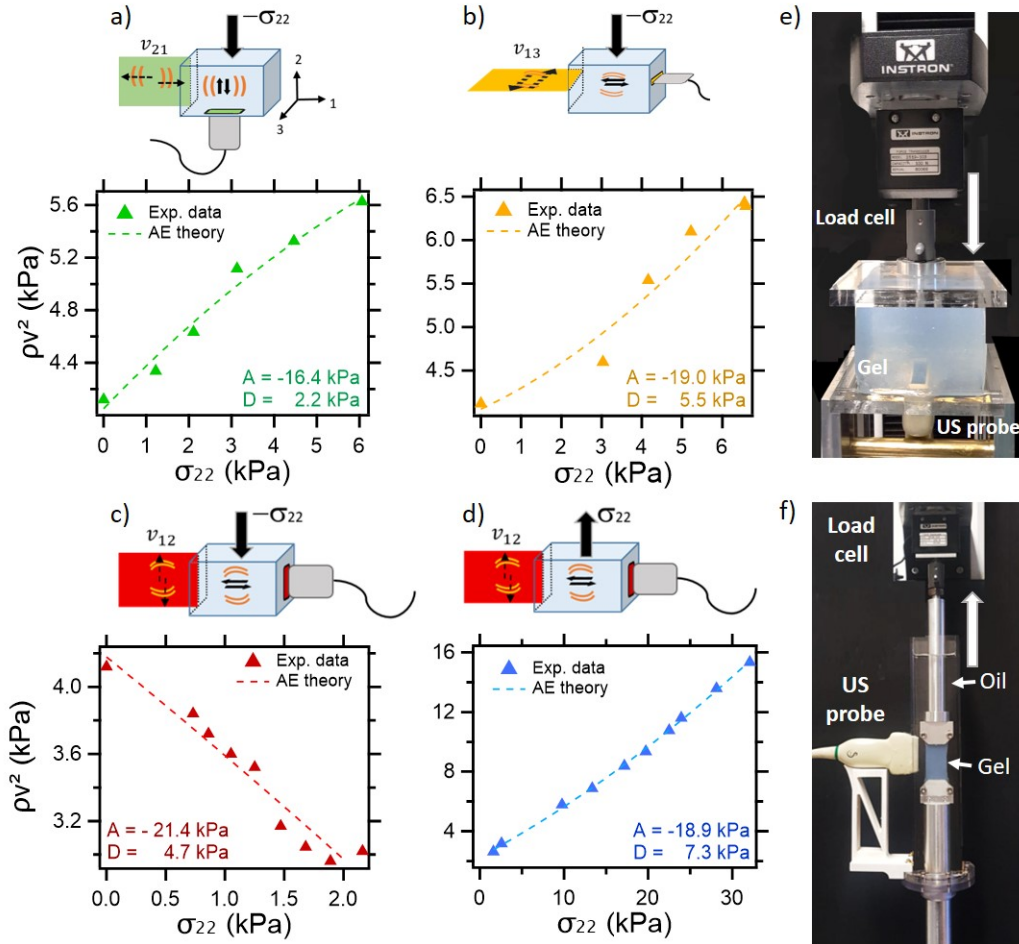


FIGURE 3.19: Coupled experimental data from shear wave elastography and conventional mechanical testing allow us to estimate  $\mu_0$  and the shear velocity while data from mechanical testing measurements give us the stress  $\sigma_{22}$  (see equations 2.38 and 2.39). This enables the calculation of the nonlinear Landau coefficients  $A$  and  $D$  with a  $2^{nd}$  degree polynomial fit. a), b), c) represent a compression test with 30% strain (except for  $v_{12}$  where the maximum possible strain was 15% due to the probe configuration) while d) is for tensile test until fracture.

(kPa)	Linear shear modulus $\mu$ Value at 0 stress	Indice of propagation 12 A / D		Indice of propagation 21 A / D		Indice of propagation 13 A / D		Mean value A / D	
		A	D	A	D	A	D	A	D
Compression test	$4.2 \pm 0.1$	-21.4	4.7	-16.4	2.2	-19.0	5.5	-18.9	4.1
Tensile test	$4.0 \pm 0.2$	-18.9	7.3	-	-	-	-	-18.9	7.3

TABLE 3.5: Table of the values of the non-linear coefficient  $A$  and  $D$  for the elastic gel calculated in compression and tensile test.

### 3.3.2 Third order of non linear elasticity

Both compression and tensile experiments conducted in-real time are illustrated in Figure 3.20. Tests are performed, consisting in a monotonic loading (compression and tension) up to a strain of about 0.30 (i.e.,  $\lambda$  comprises between 0.7 and 1.3), followed by a step of maintaining at a fixed strain level. The experimental parameter  $\rho v_{ij}^2$  (kPa) is plotted for various US probe positions. As expected from AE theory,  $v_{12}$  is sensitive to stress state (recorded from mechanical testing): it increases in tension and decreases in compression. Under fixed strain conditions, shear wave velocities remain constant since the stress relaxation is almost negligible for elastic gels.

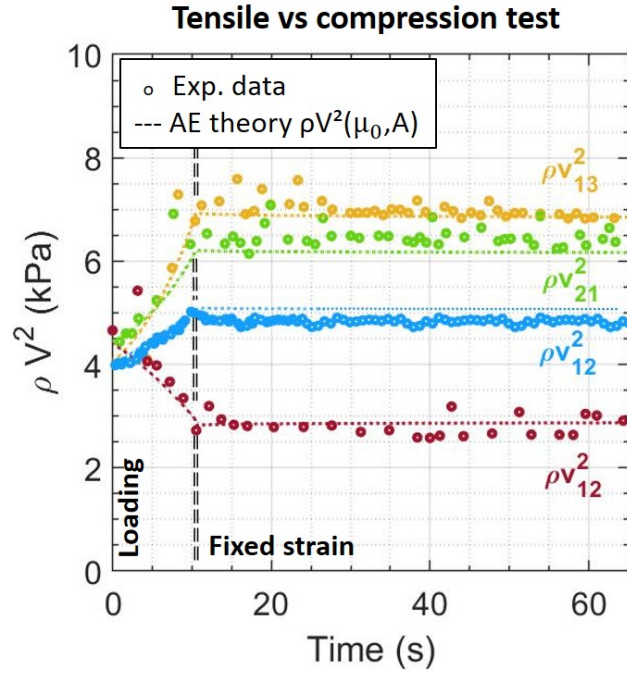


FIGURE 3.20: Validation of AE theory ( $A = -18.9$  kPa) at the third order for intermediate strains (max  $\lambda = 1.3$ ) on elastic gel with four different probe configurations (yellow, green, red are for compression tests while blue represents a tensile test). The theory (dotted line) fits well the experimental data.

AE theory is presented until the third order in Fig. 3.20 which seems to correlate rather well with experimental data up to 30% strain.

## 3.4 Stress determination from the strain energy density

### 3.4.1 Stress determination from AE theory

The non linear coefficient  $A$  and  $D$  for elastic and viscoelastic gels have been identified and are reported in Table 3.6 and 3.7 at the end of Chapter 3. Thus, the macroscopic stress can be recovered using the shear wave velocity and the nonlinear coefficients. In that purpose, the stress has been isolated from Eq. 2.39 for a tensile test:

$$\sigma_{22}^2 \left( 5\mu_0 + \frac{7}{4}A + 3D \right) \frac{1}{9\mu_0^2} + \sigma_{22} \left( 1 + \frac{A}{12\mu_0} \right) - \rho v_{12}^2 + \mu_0 = 0 \quad (3.2)$$

The solution of this second degree equation gives the stress. Fig. 3.21 compares the stress given by AE theory and the conventional true stress obtained by the force sensor. The  $\sigma_{22}$  data use the measure of the shear wave velocity and the Landau coefficients from AE theory. It appears that the 4<sup>th</sup> order ( $D$ ) is of great importance to retrieve the stress given by the load cell. Indeed, above  $\lambda \approx 2.5$  for both gels, the 3<sup>rd</sup> order diverges and the 4<sup>th</sup> order is required to fit the experimental data (black curve). This experiment underlines the fact that the 4<sup>th</sup> order needs to be used for large deformations.

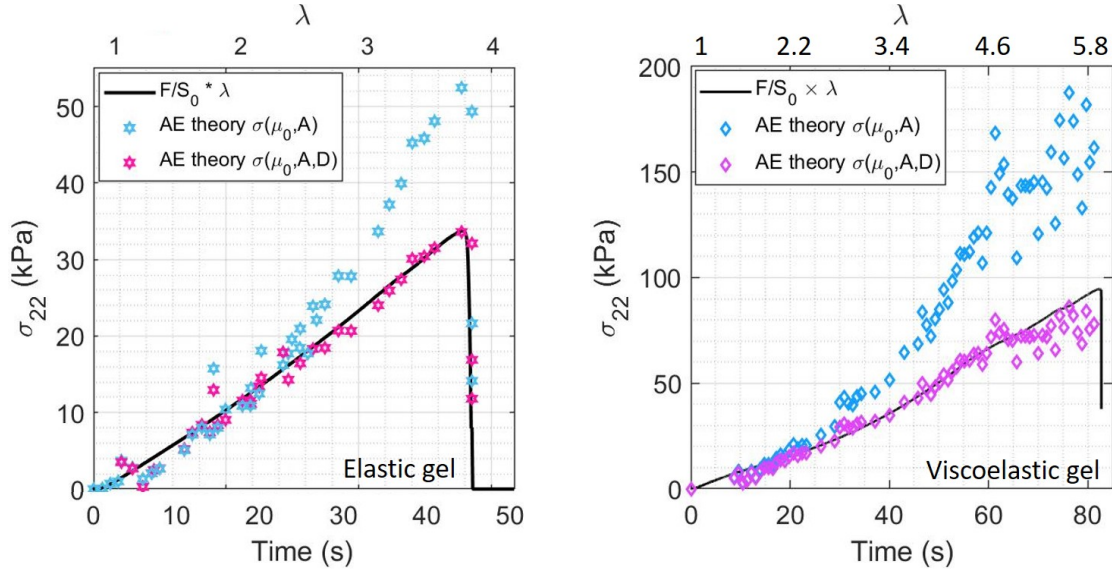


FIGURE 3.21: Tensile test until fracture for elastic (left)/viscoelastic (right) SP2 gel (10 vol.%  $\text{SiO}_2$ ). AE theory has been used in a reverse way to retrieve the macroscopic stress. It appears that the third order is no more valid when a stress of  $\sigma \approx 20 \text{ kPa}$  or  $\lambda \approx 2.5$  is reached. In this case, it is needed to use the fourth order in AE theory to retrieve the stress at larger strains.

The stress determined by AE theory has been tested on every type of gels for tensile test until fracture. These tests are available in Annex A.

### 3.4.2 Physical sense of Landau coefficients A and D for the studied gels

$A$  and  $D$  provide information on the material complexity, i.e at the third and fourth order of nonlinear elasticity. To understand their impact, we calculate these coefficients on materials that present different mechanical responses compared to the elastic gel at  $Q_0$  presented in part. 3.3.1. In Fig. 3.22, the three Landau coefficients are presented ( $\mu$ ,  $A$ ,  $D$ ) for elastic and viscoelastic gels (with 10 and 15 vol.% of  $\text{SiO}_2$ ) at  $Q_0$  (preparation state) and at  $Q_e$  (swelling equilibrium state) as a function of  $\mu_{instron}$ . Each point presented in the graphic corresponds to a specific gel. The tables of these corresponding results can be found at the end of this part (Table 3.6 and Table 3.7).

$\mu_{instron}$  corresponds to the tangent of the stress-strain curve in the linear regime divided by 3, while  $\mu_0$  is calculated at rest through the shear wave velocity  $v_{ij}$  and the density material  $\rho$  as  $\mu_0 = \rho v^2$ . The calculation of  $\mu_{instron}$  and  $\mu_0$  is independent (mechanical testing and SWE respectively). On the contrary,  $A$  and  $D$  depend on  $\mu_0$  and the true stress  $\sigma$  (which is related to  $\mu_{instron}$ ) (see equations 2.38 and 2.39).

A strong linear dependence of the coefficients  $\mu_0$ ,  $A$  and  $D$  is observed with  $\mu_{instron}$  (see the correlation coefficients between  $\mu_{Instron}$  and  $\mu_0$ ,  $A$  and  $D$ ). One can notice that when the order in the

Landau coefficient increases, the correlation with  $\mu_{instron}$  decreases which is expected since we move away from linear elasticity.

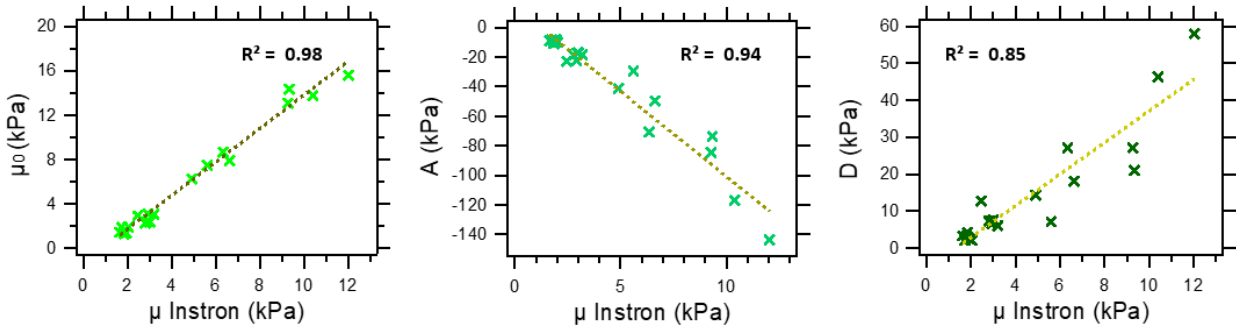


FIGURE 3.22: Elastic coefficient  $\mu_0$ ,  $A$  and  $D$  as a function of  $\mu_{instron}$  for elastic and viscoelastic gels at preparation state and equilibrium state.

The smallest  $\mu_0$ ,  $A$  and  $D$  correspond to swollen (elastic and viscoelastic) gels, i.e no matter the content of NPs from 0 to 15%, then it increases with elastic gel at  $Q_0$  and finally with viscoelastic gel at  $Q_0$  (according to the increased content of  $\text{SiO}_2$ ). As expected,  $\mu_{instron} = \mu_0$  for small shear moduli (corresponding to elastic gels), then the two moduli  $\mu$  are no more equal (viscoelastic gels) due to the different frequency used to probe the samples (refer to Fig. 3.6).

$A$  and  $D$  represent the nonlinear elastic coefficients: the closer they are to zero, the more elastic is the gel. When  $A$  and  $D$  pull away from zero, the gel non linearity increases (from  $Q_e$  to  $Q_0$ ), then the gel becomes viscoelastic (from SP0  $Q_0$  to SP2 and SP3.5 at  $Q_0$ ).

### 3.4.3 Stress determination using the Green-Lagrange Invariants

According to the strain energy function  $W$  defined in Part 2.4.1 and the Green-Lagrange Invariants (incompressibility assumption), the stress can also be rewritten as a function of  $\lambda$  (Eq. 3.3):

$$\sigma_{22} = \mu \left[ \lambda (\lambda^2 - 1) - \frac{1}{\lambda^2} \left( \frac{1}{\lambda} - 1 \right) \right] + \frac{A}{4} \left[ \lambda (\lambda^2 - 1)^2 - \frac{1}{\lambda^2} \left( \frac{1}{\lambda} - 1 \right)^2 \right] + \frac{D}{2} \left[ (\lambda^2 - 1)^2 + 2 \left( \frac{1}{\lambda} - 1 \right)^2 \right] \left[ \lambda (\lambda^2 - 1) - \frac{1}{\lambda^2} \left( \frac{1}{\lambda} - 1 \right) \right] \quad (3.3)$$

#### Parametric study

Equation 3.3 is a complex polynom where  $\lambda$  varies from  $\lambda^{-5}$  to  $\lambda^7$ . Thus, it is difficult to anticipate the role of the elastic coefficients  $A$  and  $D$  on the stress behavior. To get an idea, it is possible to perform a parametric study.

For this purpose, the elastic coefficient  $\mu$  was fixed to 1. Fig. 3.23 shows how the stress evolves with  $\lambda$  according to  $A$  and  $D$  and using eq. 3.3.

$A$  and  $D$  have approximately the same impact but  $D$  operates at smaller strain. When  $A$  and  $D$  are negatives, the stress becomes negative and diverges. From previous results, one can notice that  $A$  was found to be negative in our gels whereas  $D$  was found to be positive. In other words, when  $A$  is negative,  $D$  needs to be positive to correct the negative divergence of the stress curve (right graphic of Fig. 3.23).

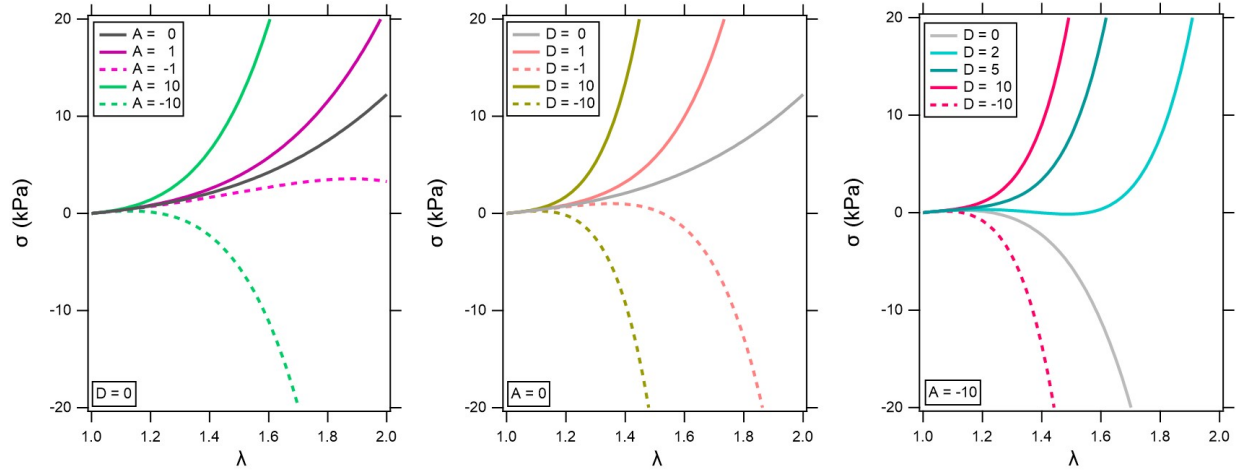


FIGURE 3.23: Parametric study of the physical parameters  $A$  and  $D$  with  $\mu = 1$ . Evolution of the true stress  $\sigma$  as a function of  $\lambda$  for different values of  $A$  and  $D$ .

### Theoretical vs. experimental study

The strain energy density function used in this thesis applies for incompressible elastic materials. The most elastic material of this study is the swollen elastic gel (SP0  $Q_e$ ) as reported in part. 3.1.2. Thus, the experimental true stress and the stress calculated from the invariants are compared for a swollen elastic gel in Figure 3.24.

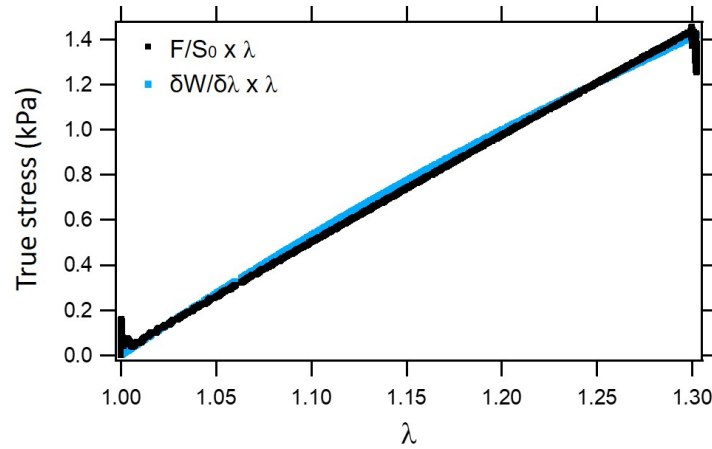


FIGURE 3.24: True stress as a function of  $\lambda$  for a swollen elastic gel at  $Q_e$ . The experimental stress calculated from the force imposed on the material divided by the area on which the force applies is represented in black. The analytical stress calculated from the strain energy function is represented in blue ( $\mu_0 = 1.45$  kPa,  $A = -8.96$  kPa and  $D = 3.25$  kPa). The curves match well for  $\lambda = 1.3$ .

The model works perfectly for a tensile test until  $\lambda \approx 1.3$ . In fig. 3.25, in a tensile test until fracture, the calculation of the above stress diverges. These calculations, based Eq. 2.37, were simplified separating effects due to compressibility and shear deformation (Hamilton et al., 2004). The three remaining terms of Eq. 2.37 are sufficient for describing shear deformation when the energy stored in compression is comparatively insignificant which is the case for the shear wave propagation. In the case of tensile tests, this assumption is not perfectly accurate since both shear and hydrostatic components take place. When a tensile test is applied, it implies a combination of

normal and shear stress. The normal stress applied creates elongation and the shear stress which is also present provides a slip condition on the material and thus helps in the breaking of material.

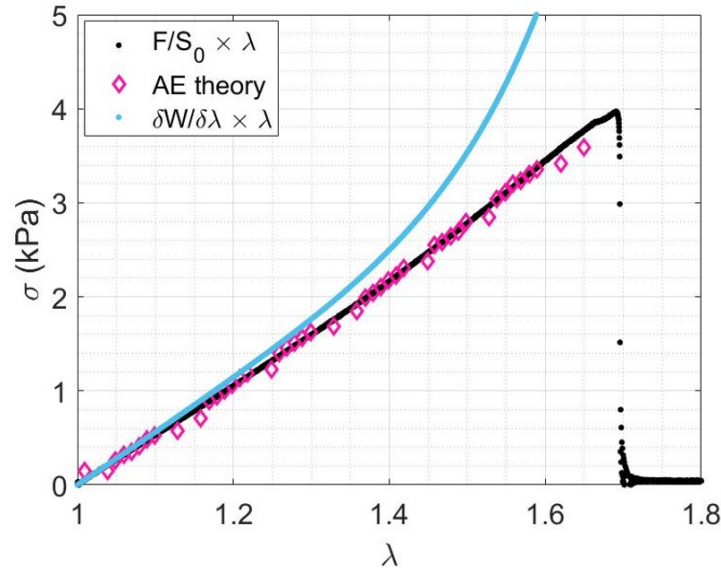


FIGURE 3.25: Tensile test until fracture at a strain rate of 0.01 Hz for an elastic gel at equilibrium state. Three different ways of calculating the stress are represented as a function of  $\lambda$ . The coefficients  $\mu_0 = 3.05$  kPa,  $A = -18.67$  kPa and  $D = 5.98$  kPa were used.

Taking into account all the terms of Eq. 2.25 with  $\nu = 0.47$  (instead of  $\nu = 0.5$  in the incompressible case), the model works better (see Fig. 3.26). Nevertheless, the parametric study is complicated since we take into account others Landau coefficients:  $A, B, C, E, F, G$  and  $H$  and the twelve orders of difference contained in Eq. 2.45.

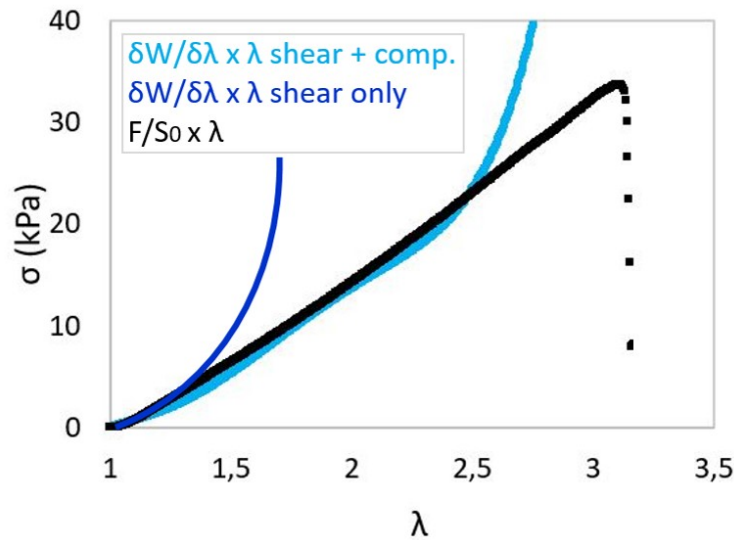


FIGURE 3.26: Tensile test until fracture at a strain rate of 0.06 Hz for an elastic gel at  $Q_0$ . Experimental data and the stress calculated by the invariants (Eq. 3.3) are represented as a function of  $\lambda$ . All Landau coefficients were used:  $\mu_0 = 2.27$ ,  $\nu = 0.47$ ,  $\Lambda = 44.8$ ,  $A = -18.88$ ,  $B = 4.12$ ,  $C = -18.01$ ,  $D = 7.29$ ,  $E = -0.01$ ,  $F = -0.01$ ,  $H = 0.03$  (kPa).

The stress determined using the Green-Lagrange Invariants has been tested on every type of gels for tensile test until fracture. These tests are available in Annex A. In this section, the focus was put on the shear wave propagation in a pre-stressed medium. It has been shown that it works well to retrieve the macroscopic stress from the load cell (see Fig. 3.21). An experimental calibration allowed determining  $A$  and  $D$  and then using SWE for an estimate of the stress imposed on the material.

### 3.5 Assessment of stress relaxation by Shear Wave Elastography

Now that we confirmed SWE is able to quantify the stress at large strains, one can wonder if the shear wave velocity can catch the stress relaxation on viscoelastic samples. For that purpose, Fig. 3.27 shows the stress relaxation of SP2 and SP3.5 under a fixed 50% strain during a tensile test.

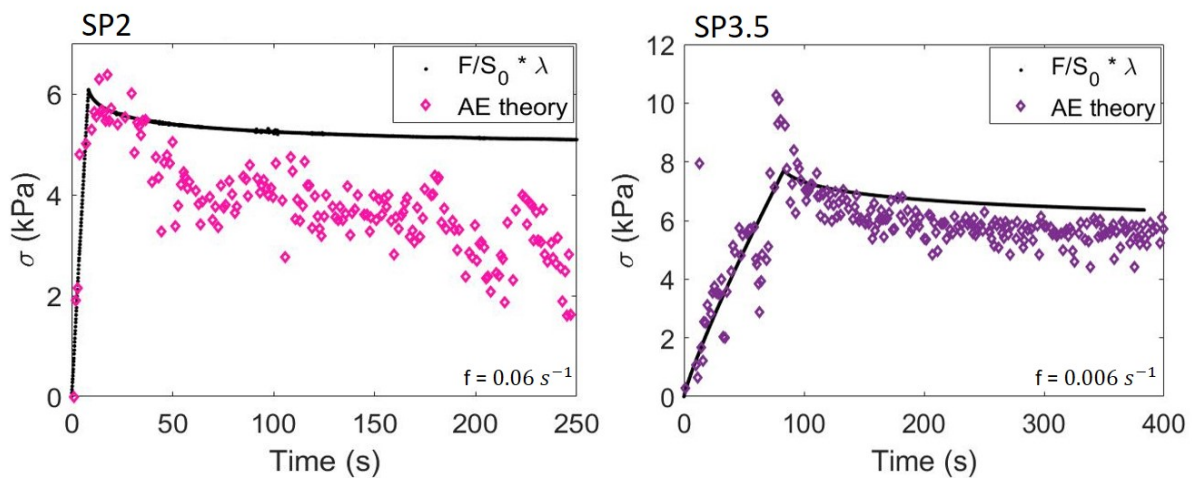


FIGURE 3.27: Relaxation processes on viscoelastic gels SP2 and SP3.5 at different strain rates for 50% strain during a tensile test.

The displacement was fixed at 50% within the regime where  $A$  and  $D$  were identified (see Table 3.6 at the end of this chapter) and the mechanical testing machine measured the force overtime. When the amount of nanoparticles increases, the relaxation increases as well (see Fig. 3.5).

In Fig. 3.27, for both SP2 and SP3.5 gel, SWE measures a larger stress relaxation than the one recorded from the mechanical testing. This might be due to the frequency range of elastography (about  $10^2$  Hz) which could capture fast events. Indeed, the load cell measures a macroscopic stress while SWE is local (as seen Fig. 3.15) and measure in one particular direction. It would be interesting to calculate the stress relaxation in the two other directions with SWE but the experiment is limited due to technical constraints on the setup. Finally, it might be possible that the push or the shear wave helps the desorption of the polymeric network onto the silica NPs.

In Tables 3.6 and 3.7, the elongation  $\lambda$  and the true stress at which the coefficients  $A$  and  $D$  were determined are indicated.

SP0.1	$\mu_{\text{INSTRON}}$	$\mu_0$	A	D	$\lambda$	True stress (kPa)
$f = 0.06 \text{ s}^{-1}$	2.79	2.27	-18.88	7.29	3.5	35
$f = 0.01 \text{ s}^{-1}$	3.19	3.05	-18.67	5.98	2.2	14
$f = 0.003 \text{ s}^{-1}$	2.91	3.13	-22.11	7.27	1.3	2.5

SP2	$\mu_{\text{INSTRON}}$	$\mu_0$	A	D	$\lambda$	True stress (kPa)
$f = 0.06 \text{ s}^{-1}$	4.90	6.23	-41.39	14.25	4.8	70
$f = 0.06 \text{ s}^{-1}$	6.33	8.66	-70.76	27.05	3	60
$f = 0.01 \text{ s}^{-1}$	6.62	7.89	-49.83	17.98	2.3	30
$f = 0.006 \text{ s}^{-1}$	5.60	7.48	-29.27	7.07	2.3	25

SP3.5	$\mu_{\text{INSTRON}}$	$\mu_0$	A	D	$\lambda$	True stress (kPa)
$f = 0.06 \text{ s}^{-1}$	10.39	13.76	-117.05	46.36	4.6	100
$f = 0.06 \text{ s}^{-1}$	12.03	15.58	-143.73	58.02	6	250
$f = 0.01 \text{ s}^{-1}$	9.33	14.32	-73.86	21.06	3.5	55
$f = 0.006 \text{ s}^{-1}$	9.27	13.06	-84.60	27.12	2	36

TABLE 3.6: Table of Landau coefficient as a function of the frequency in gels at  $Q_0$

SP0.1 $Q_e$	$\mu_{\text{INSTRON}}$	$\mu_0$	A	D	$\lambda$	True stress (kPa)
$f = 0.06 \text{ s}^{-1}$	1.63	1.45	-8.96	3.25	1.9	5.2
$f = 0.01 \text{ s}^{-1}$	1.73	1.93	-8.41	2.03	1.6	3.4
$f = 0.003 \text{ s}^{-1}$	2.02	1.90	-9.87	2.06	1.3	1.7

SP2 $Q_e$	$\mu_{\text{INSTRON}}$	$\mu_0$	A	D	$\lambda$	True stress (kPa)
$f = 0.06 \text{ s}^{-1}$	1.93	1.39	-8.39	2.48	1.5	2.5
$f = 0.01 \text{ s}^{-1}$	1.82	1.31	-9.22	3.16	2.3	7
$f = 0.006 \text{ s}^{-1}$	1.83	1.48	-11.05	4.11	1.5	2.7

SP3.5 $Q_e$	$\mu_{\text{INSTRON}}$	$\mu_0$	A	D	$\lambda$	True stress (kPa)
$f = 0.06 \text{ s}^{-1}$	2.94	2.42	-17.26	6.46	2.3	8.6
$f = 0.06 \text{ s}^{-1}$	3.00	2.37	-16.87	7.59	1.3	2.5

TABLE 3.7: Table of Landau coefficient as a function of the frequency in gels at  $Q_e$

## 3.6 Key results

---

As a summary, we have highlighted the mechanical complexity of our hybrid hydrogels:

- NPs induce viscoelastic behavior and enhance the echogenicity of the gel. The dispersion state of NPs can also be "macroscopically" controlled by US imaging.
  - Swelling state tunes the viscoelastic response at equilibrium state  $Q_e$  and reduces the dependence with the frequency. The gel is weakened: the modulus, the stress and strain at break are weaker than the gel at preparation state  $Q_0$ . Polymer chains hardly absorb to the NPs due to entropic penalty, the polymer network being stretched at its maximum. This means that the network is "frozen" and stress relaxation processes are suppressed.
  - The important role of geometry was highlighted in compression and tensile tests given different mechanical responses as the strain increases.
  - Through coupled experiments between shear wave elastography and conventional mechanical tools, the nonlinear coefficients of the 3<sup>rd</sup> and 4<sup>th</sup> order,  $A$  and  $D$  respectively, were identified and discussed. Acoustoelasticity allows the calculation of the stress from the shear wave velocity and polarisation. This stress is local, depending on where the probe is set on the material. For large deformations, the 4<sup>th</sup> order of acoustoelasticity is required. It allows to correctly assess the material's mechanics until 500 % strain and measure stresses up to 100 kPa.
-



## Chapter 4

# Static gel fracture: Experimental stress field around the crack tip

### Content

The previous chapters have allowed to better understand the measure made by elastography in a pre-stressed homogeneous medium. Fracture can now be studied on a notched specimen using our model gels. Under tension, the stress will concentrate around the notch, mimicking a pre-existing crack in the specimen. Same occurs in biological tissues (see Fig. 4.1).

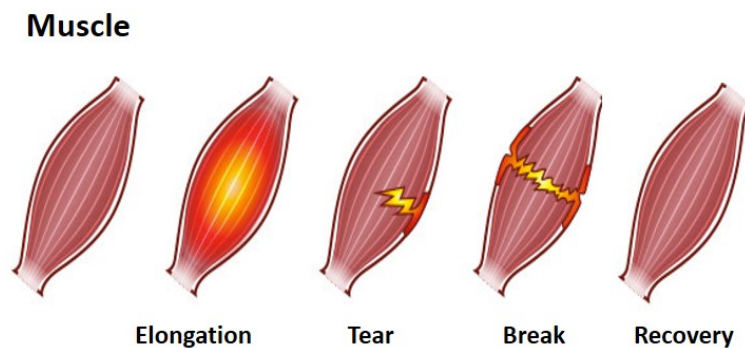


FIGURE 4.1: A cycle of muscle fracture<sup>1</sup>. During an intense effort, the muscle is first stretched, then a tear is created at a special location and finally, if the effort is extended, the fracture propagates. The strength of biological tissues is the auto-recovery of the muscle.

In this chapter, the gel fracture will be studied the same way as Figure 4.1 right before crack propagation. The fracture process will be mimicked elongating a notched gel and using shear wave elastography in parallel to probe the crack tip, the most interesting area during the fracture process. Simultaneous measurements of elastic/viscoelastic properties at both global (based on tensile experiments) and local (based on shear wave elastography) scales in our model gels will be reported. Finally, simulation with Finite Element Method (FEM) will be carried out to validate our experimental results.

<sup>1</sup><https://www.sante-sur-le-net.com/maladies/rhumatologie/dechirure-musculaire/>

## 4.1 Single Edge Notched Tension (SENT) geometry

### 4.1.1 Methodology

Tensile mode linked to shear wave elastography was used to investigate the fracture properties of hydrogels (setup of Fig. 2.16, right). Fracture tests were performed using the classical single edge notched geometry, which is known as Single Edge Notched Tensile (SENT), using the tensile test machine.

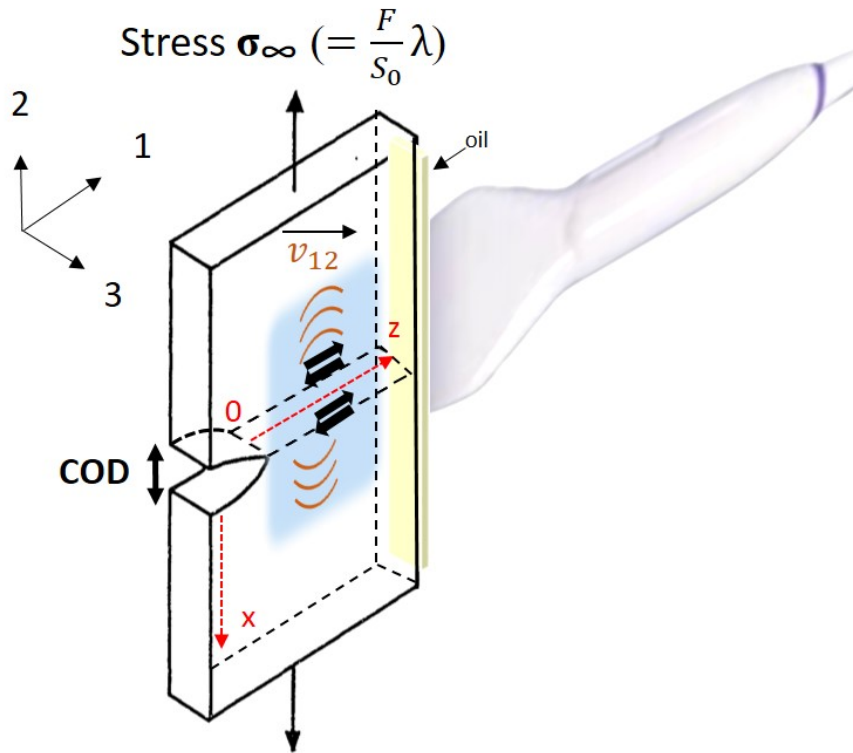


FIGURE 4.2: Scheme of the single edge notched specimen at a certain strain  $\lambda$ . The notch opens and the COD (crack opening displacement) can be extracted as a function of the force  $F$  recorded. The imaging plane is represented in blue. The dark arrows represent the shear wave polarization (index 1) and the orange demi-circles represent the shear wave propagation (index 2). Thus, the shear wave velocity in this configuration is named  $v_{12}$ . The ultrasound probe is not in contact with the gel since oil separates them.

Fig. 4.2 rationalizes the process of fracture illustrated in Fig. 4.1. The elongation produces a stress  $\sigma_\infty$  at long (virtually infinite) distances from the notch which is recorded by the load cell. The notch is incorporated into the material with a razor blade to mimic a pre-existing crack. We chose to probe the region in front of the crack tip represented by the imaging plan blue in Fig. 4.2. We define the axis  $z$ , with 0 being at the crack tip. Each notch was measured on ultrasound images and verified by ImageJ to determine its exact length  $a$ . Different crack tip ratios ( $a/W$ ,  $W$  is the width of the gel) are made from 0.1 to 0.5 approximately. In fig. 4.3, a picture of the notched gel is represented with a crack tip depth ratio  $a/W$  equal to 0.23.

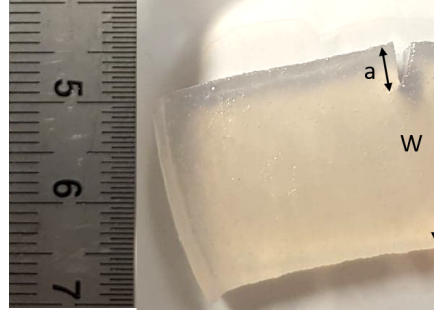


FIGURE 4.3: Picture of the notched gel with  $a = 4.7$  mm, the length of the cut and  $W = 20.7$  mm, the width of the gel. The thickness is 10 mm.

#### 4.1.2 Local shear wave velocity: pixel by pixel

The aim of this fracture study is to obtain the local mechanical state in front of the crack tip. To obtain the SW velocity at each pixel, we chose to extract the elasticity map directly from the Aixplorer (example on Fig. 4.5 a). Another method, used in the previous chapters, is the time of flight algorithm described by Tanter (Tanter et al., 2008), which gives the shear wave speed based on a phase difference algorithm. Nevertheless, this method does not compute a local map as opposed to the Aixplorer. We compared the mean velocity (through  $3\rho v^2$ ) obtained by the two approaches to be sure that the measures were consistent (Fig 4.4).

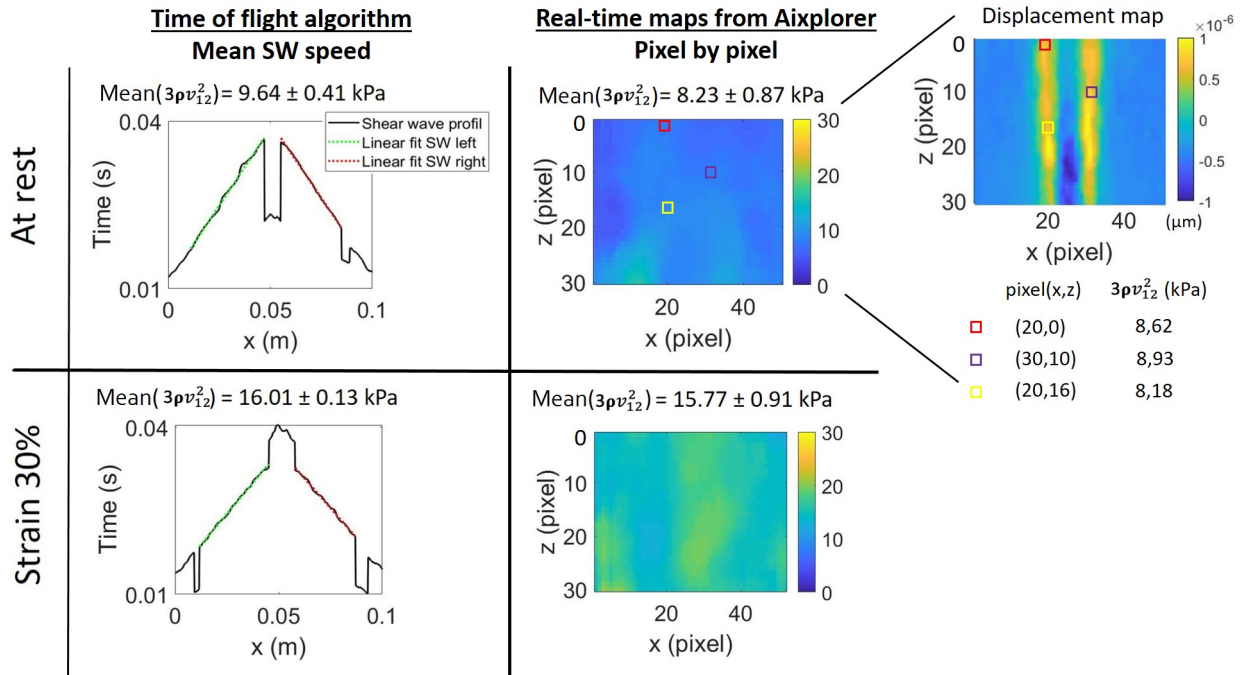


FIGURE 4.4: Comparison between two approaches on an elastic gel: Real-time maps from Aixplorer and the Time of flight method. The automatic Aixplorer code allows obtaining the local SW speed at each pixel (represented by little squares) whereas the time of flight method allows obtaining the mean SW speed. The displacement map allows seeing the shear wave which creates micrometric displacement while propagating.

The real-time maps from Aixplorer give local data of the shear wave velocity at every pixel in the window selected (Fig. 4.4). It means that  $z$  goes from the crack tip to the end of the blue window (elasticity map). Data were collected only in the region of interest chosen, depending on

the size and location of this blue window. To obtain this map, Aixplorer proceeds to time of flight measurements between the surrounding pixels and smooth the results. After these operations, the so-called "resolution" is affected and is estimated to be more than 0.2 mm. The time to extract the map from the Aixplorer is about 1 minute (while it is every second with our code).

In addition to the SW velocity map given by the Aixplorer, we also retrieved the shear wave speed with the propagation movies. Fig. 4.5 b allows determining the pixels where the crack tip is located Fig. 4.5 a. In Fig. 4.5 c and Fig. 4.5 d, we see that we can measure a local increase of the shear wave velocity in front of the crack tip. Indeed, the signal amplitude, i.e SW velocity, is shown for three different regions in Fig. 4.5 d and is represented by the colored boxes in Fig. 4.5 b. The signal is shown for  $z = 20$  (depth of the crack tip) and  $x = 60-70$ ,  $70-80$  (right before the crack tip) and  $x = 80-90$  (where the crack tip is).

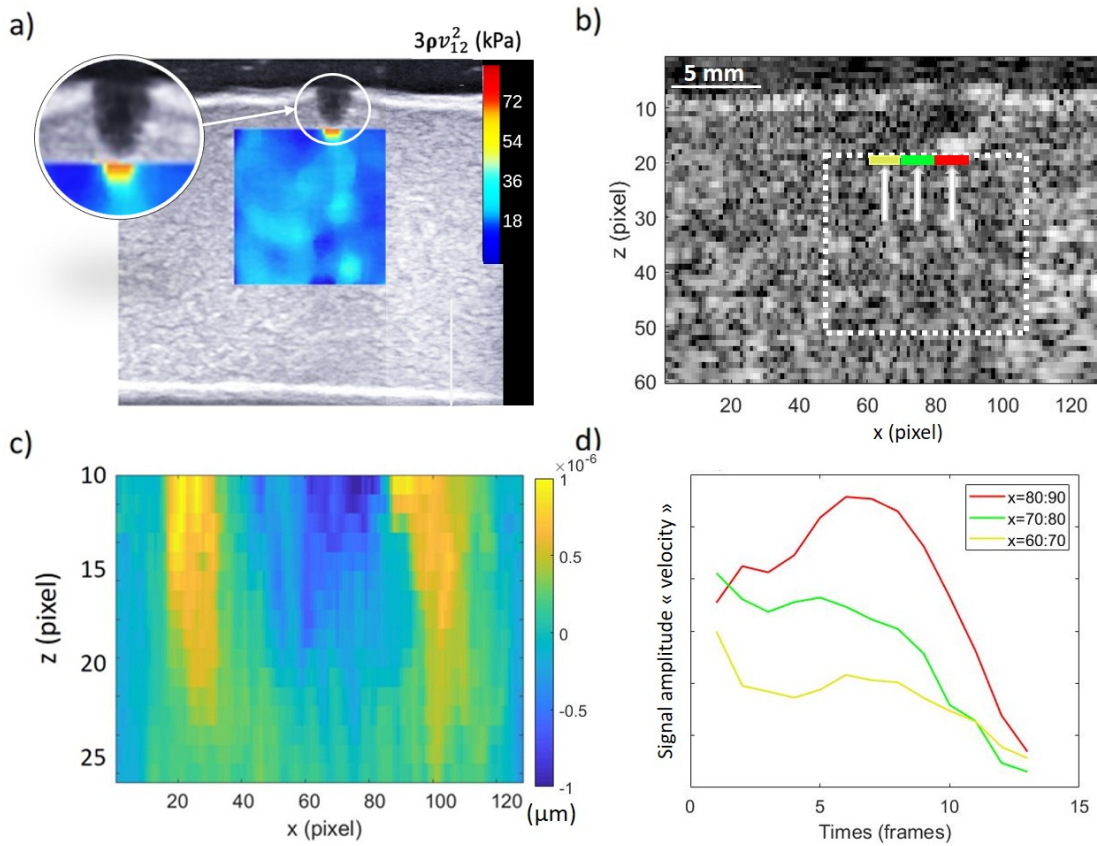


FIGURE 4.5: a) Bmode image with the elasticity map in front of the crack tip of an elastic gel SP0. A singularity is visible in red. b) Ultrasound image of the notched gel. The crack tip is located at  $z = 20$  pixel and  $x = 80-90$  pixel approximately. The white dotted box represents the elasticity map visible on a). The three colored boxes correspond to the curves of d). c) Two shear wave fronts are created by the radiation force. The right front from 80 to 100 pixels is accelerated (closed to the crack tip). d) Increase of the signal amplitude at the exact place of the crack tip ( $x = 80-90 - z = 20$  - red box).

Finally, a simple experiment was done to recreate an opening notch but with no force applied ( $\sigma_\infty = 0$ ) to be sure that the signal at the crack tip was not an artifact due to the interface oil-gel. An opening notch is created with the scalpel by cutting a triangle instead of a line. The gel was imaged without any tension, i.e at rest. In Fig. 4.6, the red spot at the crack tip is missing. This confirms that the red spot is not an artifact but represents a true physical phenomenon.

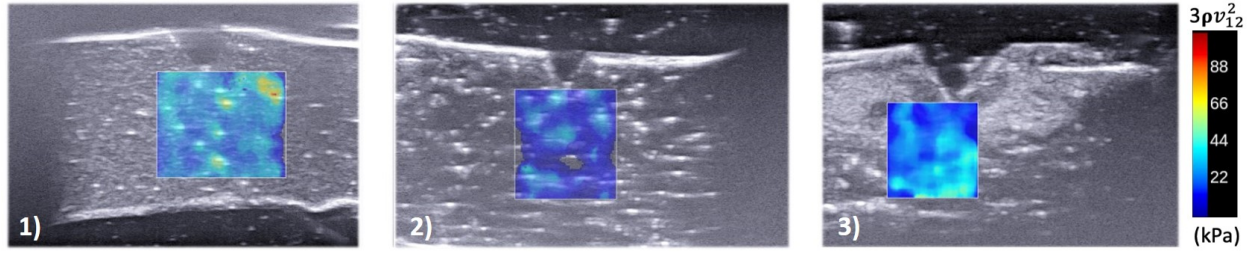


FIGURE 4.6: Three different notched SP0 gels with a triangle shape to recreate the notch under tension. In this particular case, the gel is at rest. At the crack tip, the red spot is missing, confirming the idea that the signal at the crack tip is not an artifact when the gel is submitted to a stress.

Fig. 4.7 shows the elasticity map all around the crack tip. In this study, we decided to focus on the window ahead of the crack tip, where the singularity is present and not around the crack tip lips.

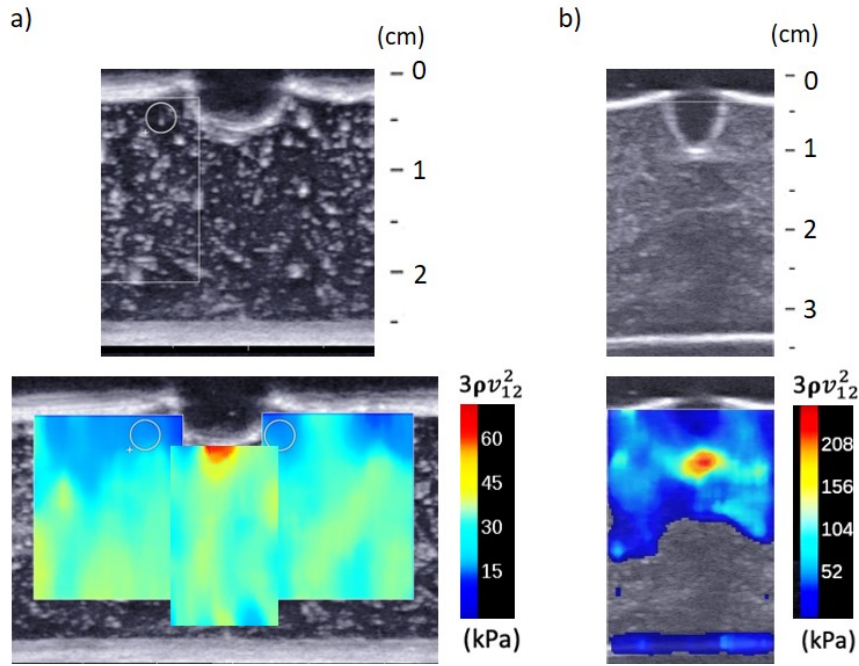


FIGURE 4.7: a) SP2 gel with a reconstructed elasticity map all around the crack tip. b) SP3.5 gel with an elasticity map surrounding the crack tip. In both cases, the gels appear to be soft near the crack tip lips whereas a singularity is found ahead of the crack tip.

#### 4.1.3 From local shear wave speed to local stress

The singularity at the crack tip, represented by an increase of the shear wave speed at this exact location, will be intensively studied in the following part for all gels (from elastic SP0 to viscoelastic SP2 and SP3.5 at preparation state  $Q_0$  and at equilibrium swollen state  $Q_e$ ). Since all Landau coefficient's gels have been determined (see Table 3.6 and 3.7 at the end of Chapter 3) through coupled experiments of mechanical testing and SWE, why not use acoustoelasticity to recover a local stress from the local SW speed extracted in the Aixplorer maps (Fig. 4.8)?

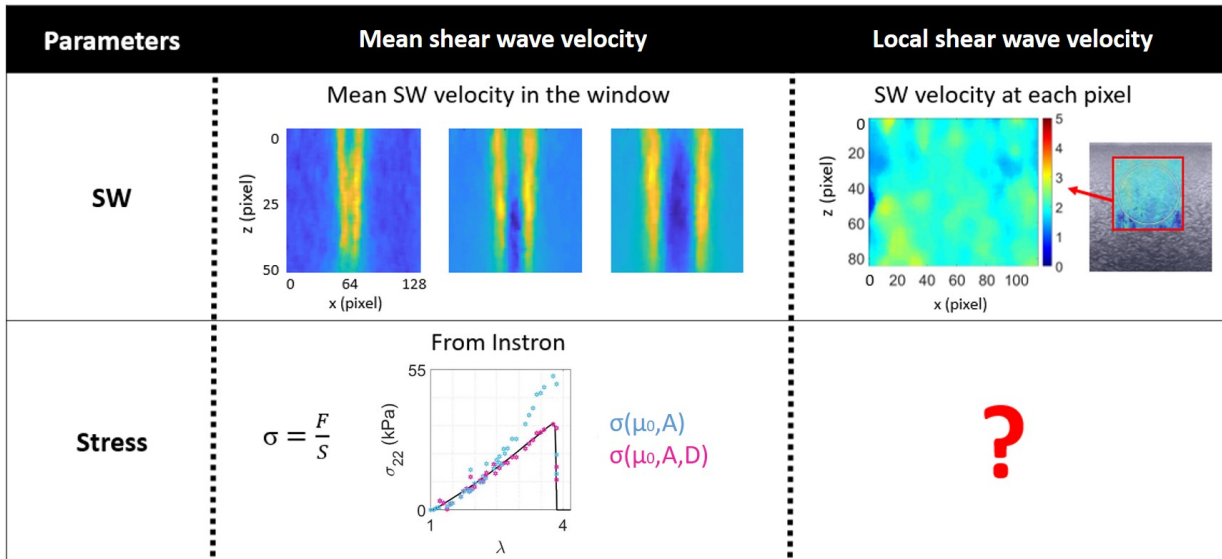


FIGURE 4.8: The most important parameters in this study are presented here: the shear wave velocity and the stress. They are linked together through the acoustoelasticity theory. As a simple cross product, it appears that knowing the Landau coefficients (through the calculation of the macroscopic terms), it is possible to calculate the local stress with the local shear wave velocity.

Fig. 4.8 shows that elastography allowed getting a macroscopic (mean) as well as a local shear wave velocity (i.e a global and local stiffness). Since acoustoelasticity links the SW velocity to the stress, it could also link the local SW velocity to the local stress.

Stress measure at local scale is not so straightforward. The measure of the local stress is very appealing in mechanics since this is a key-point to better understand fracture modelling and because stress cannot be obtained experimentally. The through-thickness stress obtained by shear wave velocity is the originality of this study. Usually, the stress is calculated through the deformation and verified by simulation. A commonly used method to determine stress is Finite Element Method (FEM) for dimensioning and validating industrial structures (see part 4.4).

## 4.2 Temporal mapping of the stress concentration around the crack tip

As seen in methodology, in Fig. 4.5, a stress singularity appears at the crack tip. How the stress field is impacted by viscoelasticity (NP content) and swelling state? How does this singularity evolve with time? In this part, the scale represented next to the elasticity map will be  $3\rho v^2$ , as it is given by the Aixplorer. Also, Aixplorer gives the shear wave speed pixel by pixel, the first one being at 0.2 mm in front of the crack tip.

### 4.2.1 Elastic gels: No temporal evolution of local stresses

As expected from the macroscopic study (Fig. 3.20), elastic gels show no stress relaxation even at the crack tip (see Fig. 4.9). This can also be seen on the ultrasound images: one hour after, the singularity was still present.

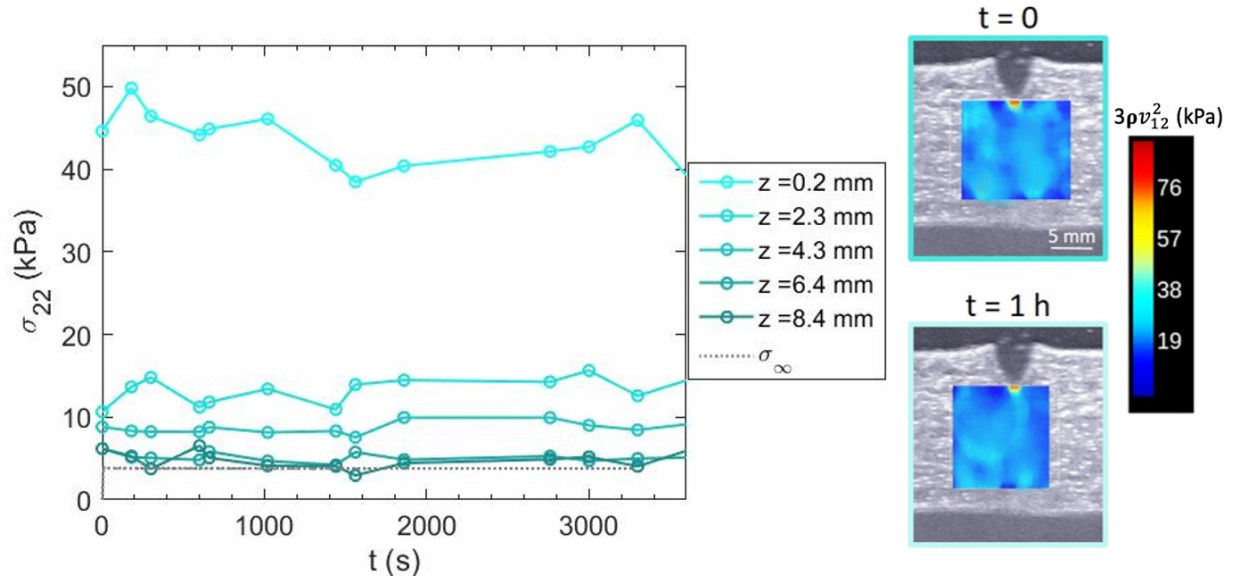


FIGURE 4.9: Local stress measured by Shear Wave Elastography at different depth in front of the crack tip and at different times for the SP0 gel with COD = 5.5 mm -  $a/W = 0.23$ . Macroscopic mechanical response recorded by the load cell,  $\sigma_\infty$ , is given as a guideline. No relaxation is observed either locally or macroscopically.

There is no relaxation anywhere in the gel neither macroscopic. The macroscopic stress,  $\sigma_\infty$  ( $F/S_0 \times \lambda$ ), is represented in black dotted lines. It is comforting to see that the stress far from the crack tip meets the macroscopic stress measured by the load cell ( $\approx 5$  kPa). Approaching the crack tip, stress concentration operates.

#### 4.2.2 Viscoelastic gels: Dynamic reorganization of the network

We observe in Chapter 3 that viscoelastic gels relax under stress (Fig. 3.27) due to the addition of the silica NPs inside the matrix that interact with the polymer chains. How can we quantify this macroscopic relaxation time and is it comparable to local processes?

##### Macroscopic relaxation processes

Stress-strain curves of Fig. 4.10 demonstrate an important amplitude of stress relaxation process within the first seconds of testing. The relaxation process is directly related to the amount of silica NPs. Note that at  $t \rightarrow \infty$ , all curves overlapped on the purely elastic gel response (polymer network) Focusing typically on the first tens seconds, which corresponds to the SP2 and SP3.5 half-life stress relaxation, we have considered an exponential decay of the stress relaxation with the general form:

$$\sigma(t) = \sigma_0 \exp\left(-\frac{t}{\tau}\right) + \sigma|_{t=\infty} \quad (4.1)$$

with  $\tau$  (s) a characteristic time of relaxation process,  $t$  (s) the time and  $\sigma_0$  (kPa) the stress at  $t = 0$  resulting from the polymer network and the transient silica crosslinks. a fitting parameter to adjust the vertical position of the curve (see Fig.4.10).

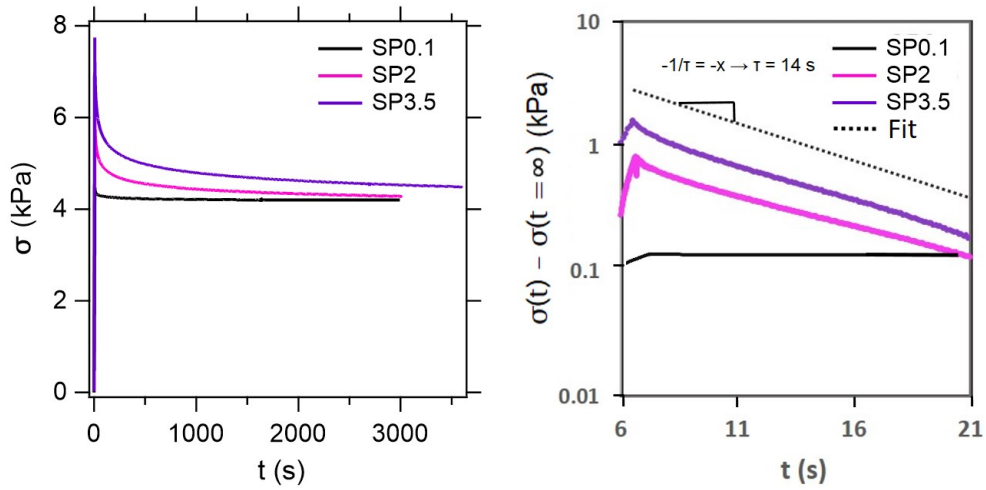


FIGURE 4.10: Relaxation experiments on SP0.1, SP2 and SP3.5 hydrogels with an initial strain of 50 % for SP0.1 and SP2 and 30% for SP3.5, all at a strain rate of 0.06 Hz. The true stress is shown as a function of time. The right graphic focuses on the first seconds of stress relaxation with a logarithmic representation of the true stress compared to an exponential fit with a characteristic time equals to 14 seconds, as a guideline.

A characteristic time of relaxation processes is found to be around 14 seconds. Previous studies (Rose, 2013, Petit et al., 2014) found the same characteristic time of relaxation on small samples of volume equals to  $\approx 0,2 \text{ cm}^3$  whatever the strain induced (between 2 and 160%). This relaxation time is confirmed with the geometry of this study with a volume of  $V \approx 10 \text{ cm}^3$ . Compression tests were performed on a SP3.5 sample (volume equals to  $\approx 343 \text{ cm}^3$ ) to confirm that geometry is independent of the relaxation processes (Fig. 4.11).

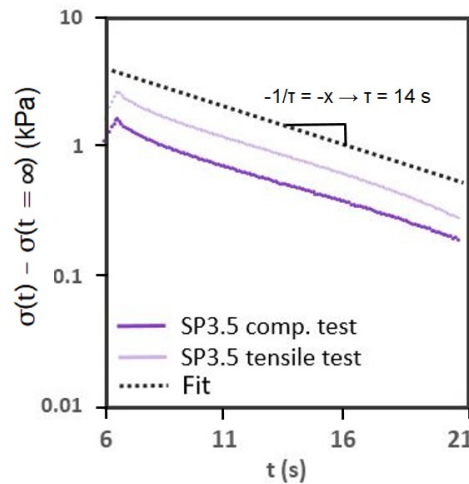


FIGURE 4.11: Relaxation experiments on SP3.5 hydrogels with an initial strain of 30 % at a strain rate of 0.06 Hz for a compression and a tensile test. The true stress is represented as a function of time for the first seconds of stress relaxation through a logarithmic representation compared to an exponential fit with a characteristic time equal to 14 seconds, as a guideline.

As demonstrated, the size of the sample does not impact the characteristic relaxation time  $\tau$ . This characteristic time,  $\tau$ , around 14 seconds, should be related to the kinetics of exchange processes of the PDMA chains at the silica surface. Indeed, the same value was found for three different volumes (from 0.2 to 343 cm<sup>3</sup>), different strains (30 and 50%) and different amounts of NPs (SP2 and SP3.5).

### Local relaxation processes at the crack tip

Local relaxation processes have been studied on SP2 and SP3.5 gels. During these local studies, the data from the load cell, i.e macroscopic, were presented in Fig. 4.10. SP0 gels already demonstrated no relaxation either macroscopic or local (see Fig. 4.9). The nanocomposites gels show a great macroscopic relaxation capacity in Fig. 4.10.

In Fig. 4.12, the local study starts with a SP2 gel studying the evolution of the stress field around the crack tip for one hour. By simply taking a look at the ultrasound images, it clearly appears that relaxation takes place at the crack tip due to the disappearance of the stiff spot, corresponding to a decrease of the shear wave velocity near this crack tip. This change at the crack tip is illustrated graphically with a significant decrease of the stress appearing in the first twenty minutes. The stress decreases from approximately 90 kPa to 45 kPa (the mean local stress at the crack tip of elastic gels (see Fig. 4.9)).

To proceed to a local study, we have first delimited study areas every 0.6 mm. Strong relaxations are observed and happen in the first two millimeters (Fig. 4.12, blue, orange, yellow). From this result, we will focus on the 2 first millimeters ahead of the crack tip. Qualitatively experimental curves are well ordered as a function of the distance from the crack tip. Interestingly, the closer to the crack tip, the higher the relaxation amplitude (see Figure 4.13) and conversely when  $z$  increases, the local stress and the amplitude relaxation decrease.

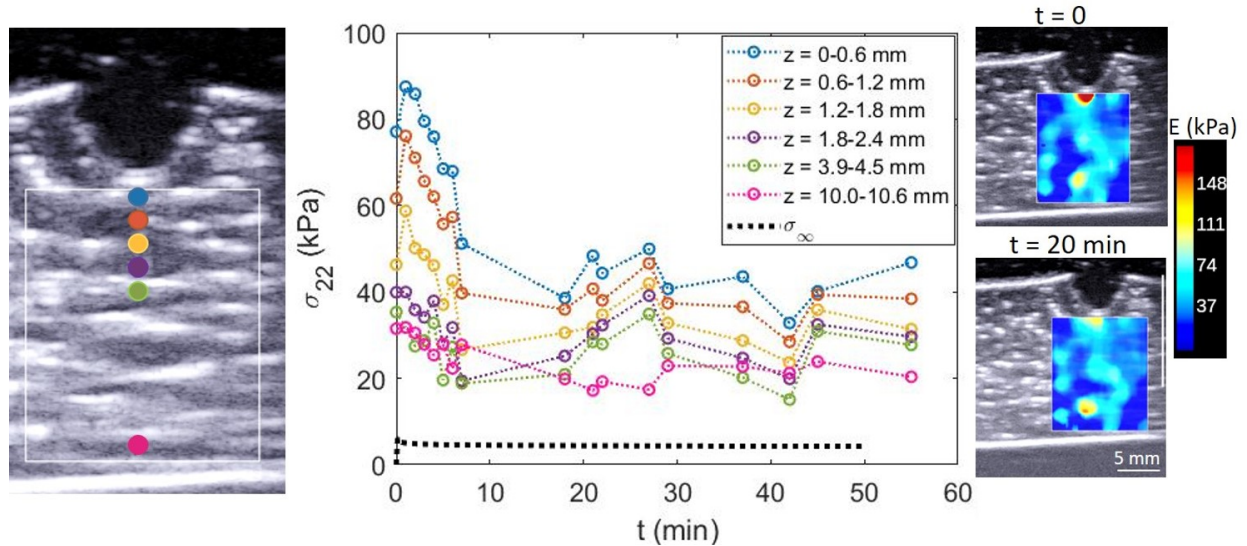


FIGURE 4.12: Local evolution of the stress relaxation measured by Shear Wave Elastography during a tensile test until 50% strain for a SP2 gel. The strain is fixed for almost one hour. After 20 minutes, it appears that the singularity at the crack tip is erased. The local relaxation is studied at different depths ahead of the crack tip. Note that the contrast in the ultrasound image is given by the heterogeneities which appear distorted by the strain imposed. COD = 6.5 mm -  $a/W = 0.21$ .

Local stress relaxation curves of Fig. 4.13 demonstrate an important stress relaxation process within the first five minutes of testing. Note that far from the crack tip ( $z = 13.1$  mm), the local stress measured by SWE is in rather good agreement with the macroscopic measure (load cell).

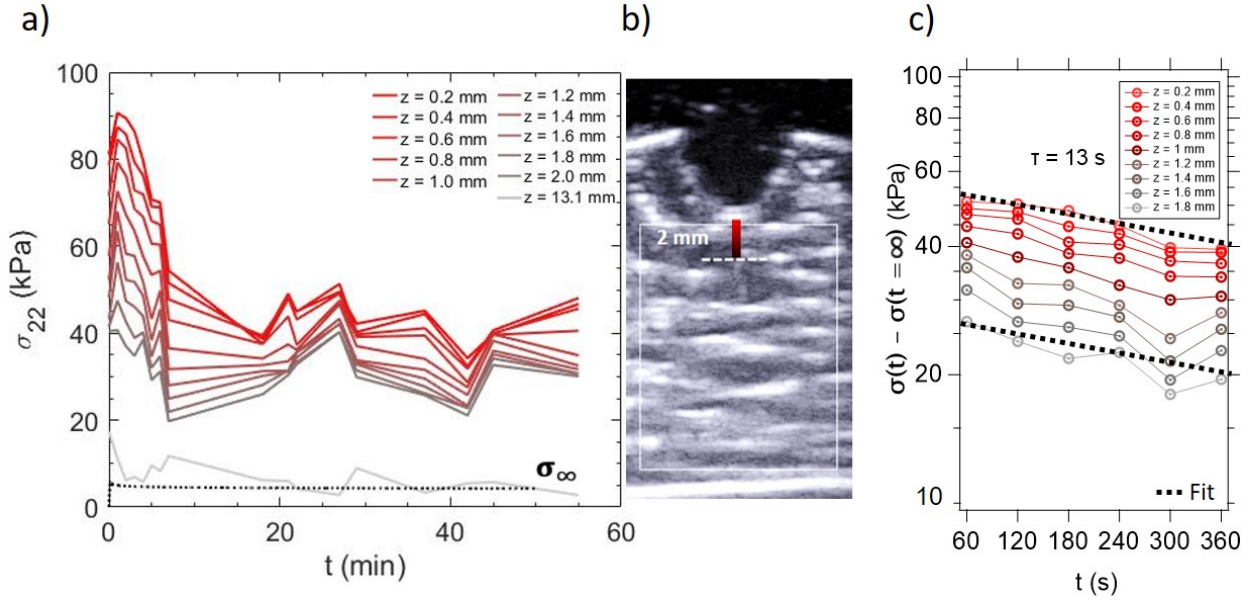


FIGURE 4.13: a) The experiment is the same as Fig. 4.12 but this time, we focus on the first 2 mm where we observe a decrease of the relaxation amplitude as we move away from the crack tip  $z = 0$ . Macroscopic mechanical response recorded by the load cell,  $\sigma_\infty$ , is given as a guideline. b) Bmode image of the gel and illustration of the first 2 mm. c) Logarithmic representation of the true stress over the maximum true stress of each curve as a function of time compared to an exponential fit with a characteristic time of about 13 seconds, as a guideline.

An exponential decay of the stress relaxation (see Eq. 4.1) is represented in Fig. 4.13.c) for the first five minutes of relaxation (which also represents the half-life stress relaxation of the gel). The half stress relaxation is around 67.5 kPa which is reached approximately 300 seconds. We evidenced a common characteristic time of the relaxation process. This characteristic time is about 13 seconds between  $z = 0.2$  mm and  $z = 2$  mm. As previously showed, the same estimation of characteristic time is found independently of the level of applied strain (the deformation is less pronounced as one moves away from the crack tip).

The same test was performed on SP3.5 gels. These gels, with about 16% of  $\text{SiO}_2$ , are more difficult to study due to their high stiffness. In Fig. 4.14, we can observe in the ultrasound images that the signal is not as good as SP2. At the bottom of the elasticity maps, there is a lack of signal. Nevertheless, we still observe a singularity at the crack tip at  $t = 0$ . After 1 hour, the singularity is erased but another one is created about 6 mm ahead of the crack tip. This is discussed in the Annex B. The true stress estimated from the load cell is represented in gray dotted lines. The mean stress away from the crack tip calculated by elastography is not shown since the material shows too many heterogeneities and a lack of signal.

Once again, to extract a characteristic time of relaxation, a focus is done on the two first millimeters. The half-life stress relaxation is closed to 300 seconds and the same characteristic time of about  $\tau = 13$  s is found as SP2 gels.

This value is close to the one found in macroscopic tensile/compression tests. The slight difference between the macroscopic and the local relaxation time is negligible due to the fact that we get data every minute for the local  $\tau$ , thus less precision on the half-life stress relaxation.

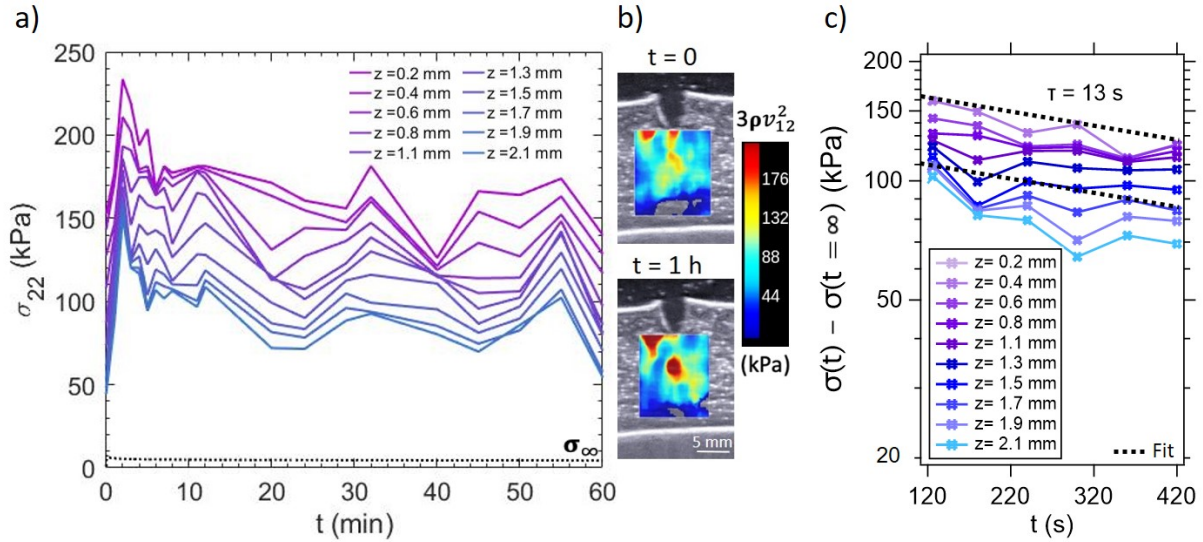


FIGURE 4.14: a) Local evolution of the stress relaxation measured by Shear Wave Elastography during a tensile test until 30% strain for a SP3.5 hydrogel. The true stress  $\sigma(t)$  as a function of time is represented. b) Ultrasound images are shown at  $t = 0$  and  $t = 1$  h. c) Zoom on the first 300 seconds of stress relaxation: logarithmic representation of the true stress  $\sigma(t)$  as a function of time compared to an exponential fit with a characteristic time of about 13 seconds, as a guideline. COD = 4.9 mm -  $a/W = 0.26$ .

To conclude on viscoelastic gels studied at preparation state  $Q_0$ , we were able to extract a characteristic time of macroscopic and local relaxation processes. We found the same value around  $\tau \approx 13$ -14 seconds. This proves the fact that the characteristic time  $\tau$  makes sense and is related to the kinetics of interaction between the polymer chains and the nanoparticles.

### 4.2.3 Role of swelling state

#### Swollen elastic gels at maximum swelling degree

As shown in Chapter 2, swollen elastic gels display softer behavior (Fig. 3.8). Here, locally, no relaxation is observed either macroscopic or local (see Fig. 4.15). Since the material is full of water, thus softer, the shear wave speed is slower and the signal is better. A singularity is still observed at the crack tip and does not change after one hour. The signal is homogeneous anywhere else, it was then easy to extract the mean stress from  $z = 2$  mm to the end of the blue box,  $z = 10.6$  mm. It is close to the one recorded by the load cell.

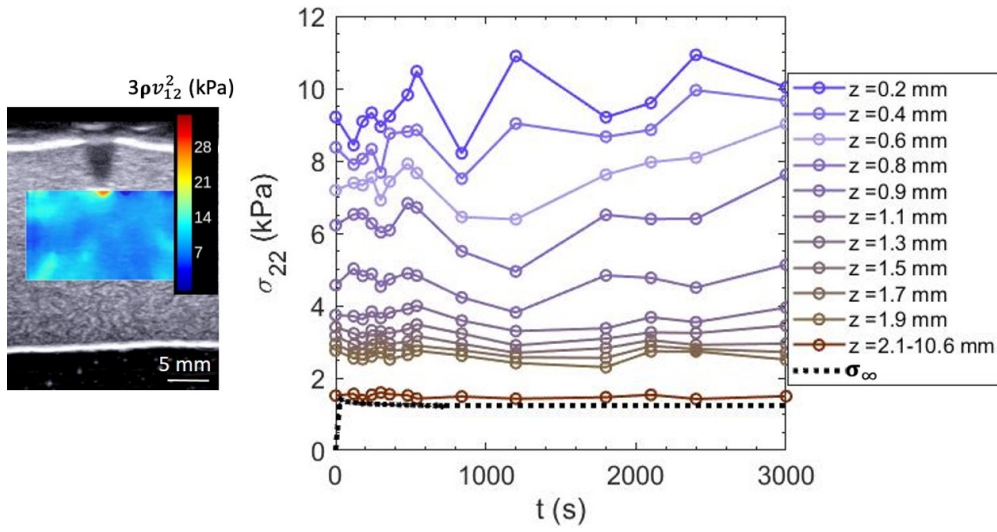


FIGURE 4.15: Local evolution of the stress measured by Shear Wave Elastography ahead of the crack tip for SP0 Qe gel with an initial strain of 30% at 0.01 Hz and comparison with the macroscopic stress calculated from the load cell. COD = 4.3 mm /  $a/W = 0.26$ .

### Macroscopic relaxation behavior of swollen viscoelastic gels

Interestingly, mechanical properties of viscoelastic gels are also drastically reduced by swelling (as observed with rheology in Fig. 3.8). The behavior remains viscoelastic but the amplitude of relaxation is smaller than  $Q_0$  gels. In Fig. 4.16, during a tensile test with a fixed 30% strain, one can observe a relaxation of about 0.5 kPa for SP3.5 in one hour whereas the decrease in stress is about 3 kPa for the SP3.5 at  $Q_0$ . The gel is also softer since the stress is decreased by two for the same 30% strain.

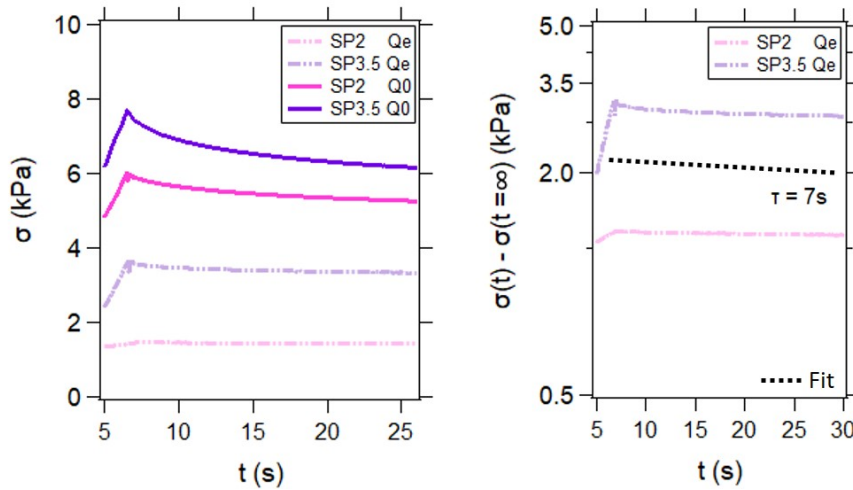


FIGURE 4.16: Relaxation experiments on SP2 Qe and SP3.5 Qe hydrogels with an initial strain of 30%, at a strain rate of  $10^{-2}$  Hz. Left: The true stress is shown as a function of time and gels at  $Q_0$  and at Qe are compared. The right graphic shows a logarithmic representation of the true stress of SP2 and SP3.5 gels at Qe compared to an exponential fit with a characteristic time equals to 7 seconds, as a guideline.

We can extract a relaxation time based on the same concept as Eq. 4.1. Here, we found a notably reduced characteristic time with  $\tau \approx 7$  seconds suggesting that the kinetics processes or

rearrangement between NPs and the polymers chains is speeded up in these conditions due to competing effects of chain solvation and adsorption.

### Local relaxation behavior of swollen viscoelastic gels

Local stress relaxation processes have been studied for SP2 and SP3.5 gels at swelling equilibrium state  $Q_e$ . Let us start with SP2  $Q_e$  gels (Fig. 4.17). We notice first a clear stress amplification effect near the crack tip (as observed in SP2 and SP3.5 at preparation state  $Q_0$ ). Surprisingly, focusing on dynamics, within the timescale investigated, non-monotonic effects are observed near the crack tip: a first increase of the stress during the first two minutes, then followed by a decrease of the stress and an increase again. If we focus on the decrease (2 mm away from the crack tip), it is possible to extract a characteristic time  $\tau$  (from 120 s to 300 s), being  $\tau \approx 7$  seconds. The half-life stress is not known due to the increase that follows. Then, the increasing stress indicates that the crack tip stiffened after having relaxed. It goes back to the value of 7 kPa, the same before the relaxation of the polymer chains onto the silica NPs happens.

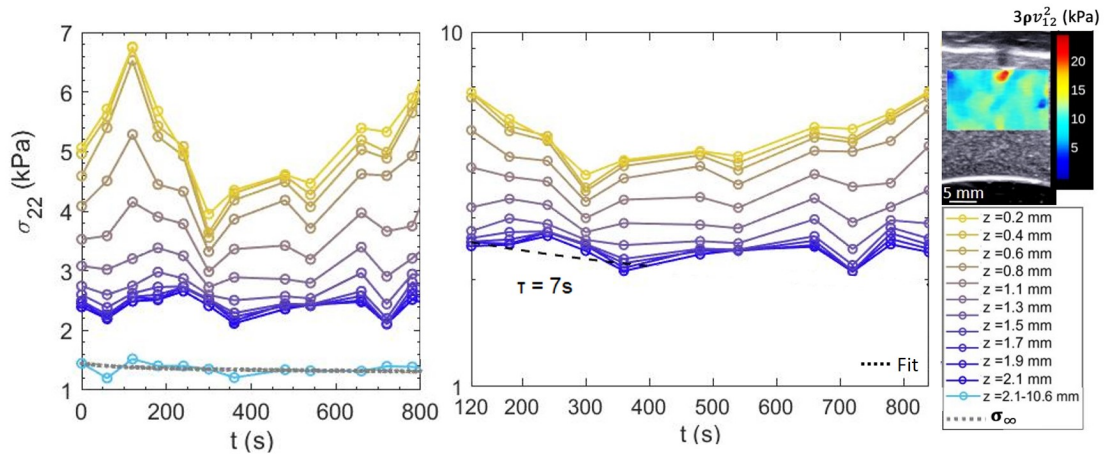


FIGURE 4.17: Local evolution of the stress ahead of the crack tip for 30% strain and comparison with the macroscopic stress calculated from the load cell on SP2  $Q_e$  gels immersed in oil.  $L_0 = 25$  mm, COD = 3.0 mm /  $a/W = 0.14$ .

The same test was performed on SP3.5  $Q_e$  gels (see Fig. 4.18). Once again, a stress relaxation is observed followed by an increase of the stress. A characteristic time  $\tau$  of about 7 seconds is calculated away from the crack tip which seems to interact with its environment (oil) when the gel is swollen, modifying the kinetic of relaxation at the crack tip.

From ultrasound images, one can notice that the geometry of the crack tip is quite different between SP2 and SP3.5 despite the same 30% applied. This is due to the difference in  $L_0$ . Nevertheless, despite the different crack geometry, a close characteristic time  $\tau$  is observed and allows to deduce the kinetic of exchanges processes in swollen viscoelastic gels (around  $\approx 7$  seconds). Also, both gels present an increase of the stress. This stiffening over time may seem surprising. Indeed, this phenomenon was not observed on gels at their preparation state ( $Q_0$ ) and on SP0  $Q_e$  gels either. It is noticed for the first 1.5 mm ahead of the crack tip. That's why the characteristic time of relaxation processes was calculated away from the crack tip (at  $z = 2$  mm).

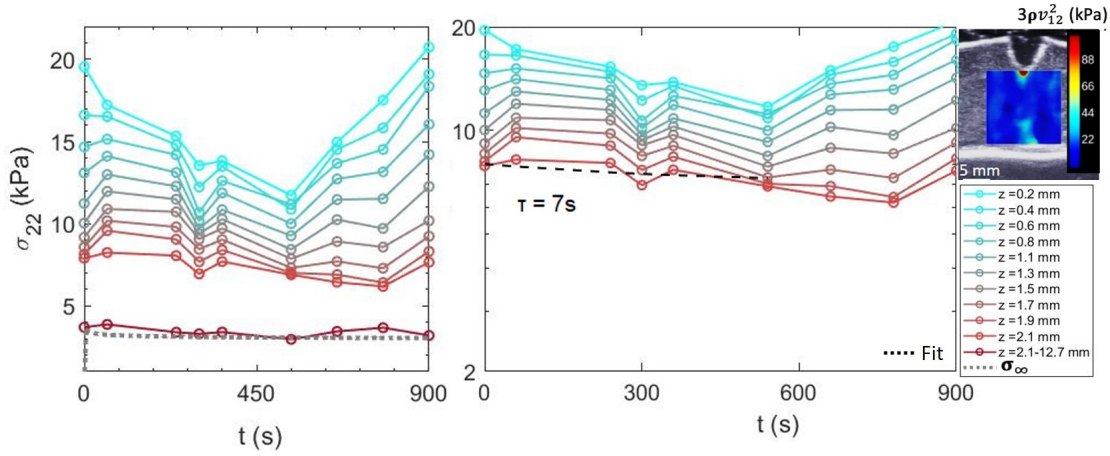


FIGURE 4.18: Local evolution of the stress ahead of the crack tip for 30% strain and comparison with the macroscopic stress calculated from the load cell on SP3.5  $Q_e$  gels immersed in oil.  $L_0 = 64$  mm, COD = 6.7 mm /  $a/W = 0.31$ .

To verify the impact of geometrical effects and especially surface effects, relaxation tests were performed on 2 mm thick samples ( $V \approx 0.2$  cm<sup>3</sup>) with 0 vol.% (SP0) and 20 vol.% of SiO<sub>2</sub> (SP5) at  $Q_e$ . The relaxation experiments were carried out in oil, in water and in air (see Fig. 4.19). It appears that after one hour immersed in oil, the gel with 20 vol.% of SiO<sub>2</sub> exhibits an increase of stress after having relaxed. This increase is far to be negligible. In elastic gels SP0, we also observe a slight increase but less important suggesting an interaction between the NPs and the oil when the gel is swollen at equilibrium state  $Q_e$ .

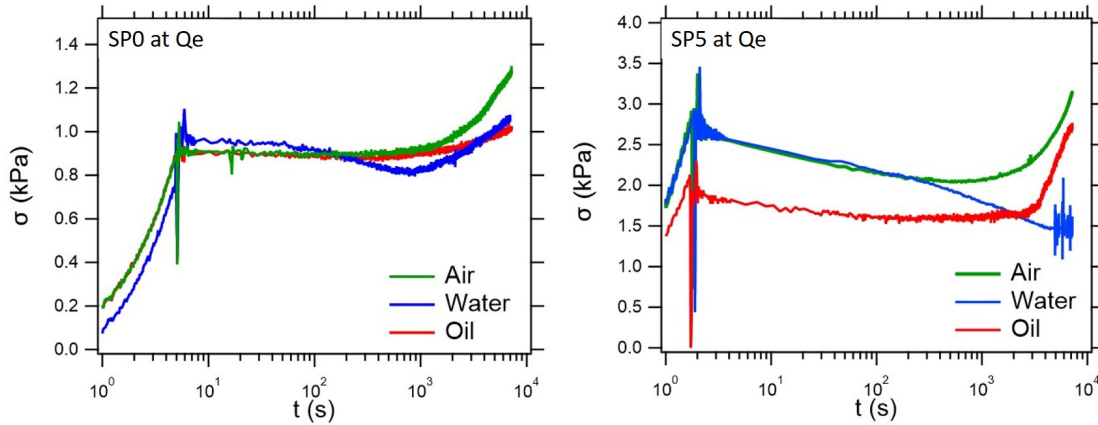


FIGURE 4.19: Tensile tests with 20% strain at a strain rate of 0.1 Hz followed by relaxation experiments for 2 hours on SP0 and SP5 gels swollen at equilibrium state  $Q_e$ . Tests are performed in air, oil and water. The immersion medium has great importance on the stress relaxation of the gel. These experiments were carried out by Camille Rei during an internship.

Concerning the experiment conducted in air, it is expected that gels dry, i.e stiffens, thus the stress increases after some time (in green in Fig. 4.19). Indeed, this phenomenon has been observed on both gels. This non monotonic effect was not noticed at preparation state  $Q_0$ . However, at  $Q_e$ , when the hydrogel is fully swollen and stretched, some drying occurred in air, but also in oil as demonstrated by these control experiments.

Our sample being much bigger ( $V \approx 10$  cm<sup>3</sup>), this local effect of drying was not recorded by the

load cell (macroscopic). Nevertheless, the area around the crack tip targeted by the US probe is really close to the gel/oil interface. To determine this volume, we consider  $x$  (width) and  $z$  (depth) resolution to be around 0.2 mm and  $y$ , the elevational resolution near the probe being around 5 mm (in the gel thickness). We obtain a volume close to  $V \approx 0.0002 \text{ cm}^3$ . Therefore, it is very likely that the same phenomenon happens locally around the crack tip. When the sample is stretched, the notch opens and the oil interacts with the interface. The shorter the distance between the gel and the oil, the faster the drying of the gel.

A simple way to verify this hypothesis is to perform the local experiment in water. We conducted this experiment on a SP3.5  $Q_e$  gel (see Fig. 4.20).

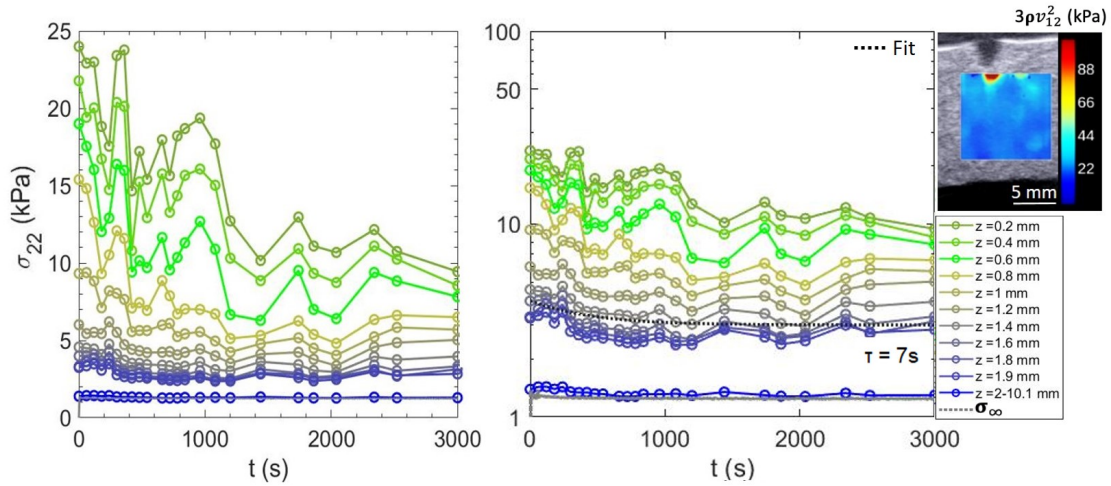


FIGURE 4.20: Local evolution of the stress ahead of the crack tip for 30% strain and comparison with the macroscopic stress calculated from the load cell on SP3.5  $Q_e$  gels immersed in water.  $L_0 = 26 \text{ mm}$ ,  $\text{COD} = 3.5 \text{ mm}$  /  $a/W = 0.20$ .

Immersed in water, the stress at the crack tip decreases. Being composed of almost 16% of silica NP, the nanoparticles prevent the gel to swell more, i.e the polymer chains can not fully extend. These experiments demonstrate that oil interacts with the gel at the crack tip when this one is fully swollen. We also calculated the characteristic time  $\tau$  considering the same time  $t$  of SP3.5  $Q_e$  immersed in oil (440 seconds). A value around  $\tau \approx 7$  seconds is found, the same characteristic time of relaxation processes of swollen viscoelastic gels SP2 and SP3.5 immersed in oil.

To conclude, viscoelastic swollen gels relax in a macroscopic and local way with a characteristic time  $\tau$  around 7 seconds.

These experiments also highlight the fact that paraffin oil interacts with swollen viscoelastic gels at large deformations which is, in this particular case, around the crack tip.

#### 4.2.4 Separating macroscopic from local relaxation processes

##### Creep test on viscoelastic gel

Is local relaxation driven by macroscopic relaxation? To verify if local processes still happen without macroscopic effects, a creep test was performed. This time, the gel was stretched until a certain force which was then fixed. This experiment was conducted on a SP2 viscoelastic gel at  $Q_0$  and compared with the relaxation experiment of part 4.2.2. The force was fixed to 0.9 N (force reached by the gel at 50% strain), corresponding to a stress of 6 kPa (see Fig. 4.21).

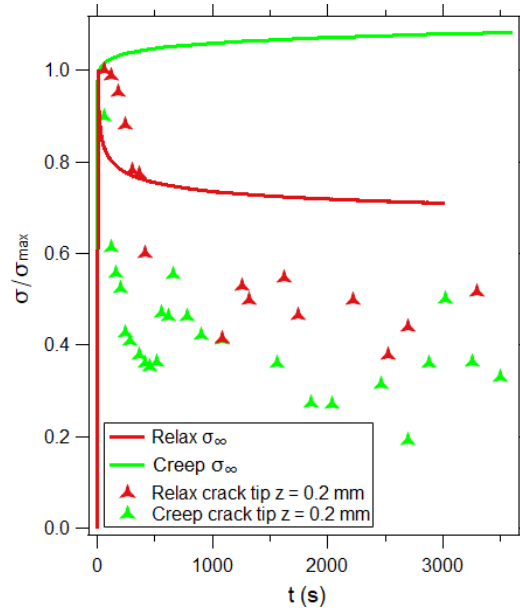


FIGURE 4.21: Creep test on a SP2 gel at  $Q_0$  in green compared to a relaxation test in red. Both experiments show a local relaxation at the crack tip. Relaxation test: COD = 6.5 mm -  $a/W = 0.21$ , Creep test: COD = 5.6 mm -  $a/W = 0.21$ .

During the creep experiment, in order to maintain the force constant, the displacement was automatically adjusted by the load cell to counterbalance the macroscopic relaxation processes and thus,  $\lambda$  increases. This is visible in Fig. 4.21 (increase of  $\sigma_\infty \propto \lambda$ ) and on the ultrasound images with the increased COD from 5.6 mm to 8.3 mm of Fig. 4.22.

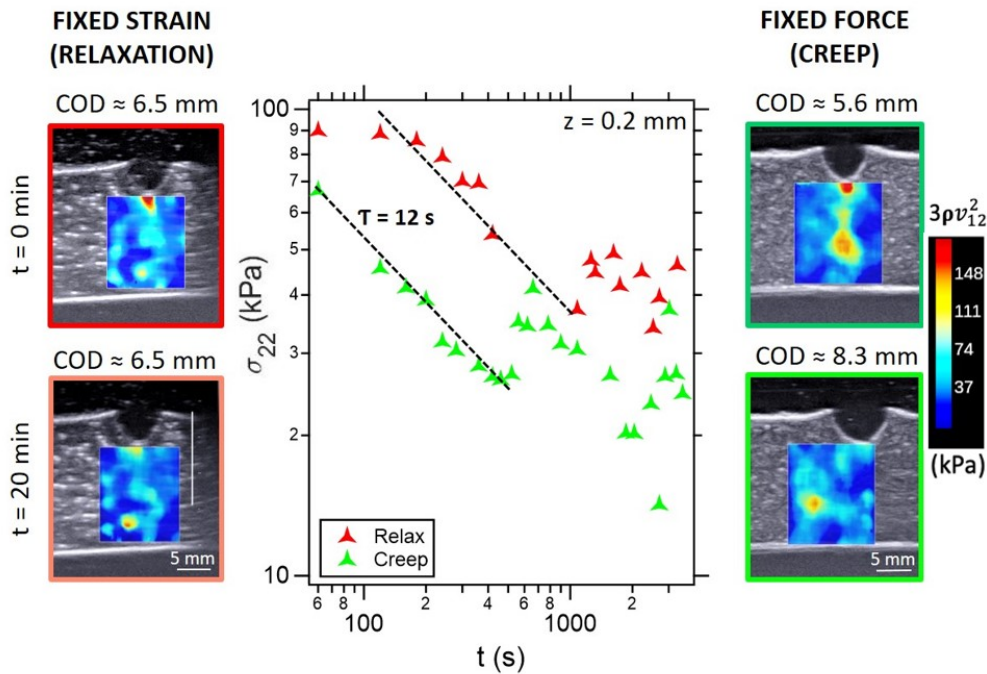


FIGURE 4.22: Creep test on a SP2 hydrogel at  $Q_0$  in green compared to a relaxation test in red. Both experiments show a local relaxation at the crack tip (graph and ultrasound images). The crack depth ratio is the same for both gels:  $a/W = 0.21$ .

In these experiments, the length between the clamps ( $L_0$ ) was not strictly equal (42 mm in the

relaxation test against 52 mm in the creep test). Thus, it is normal to not find the same stress value at the crack tip. Nevertheless, it is undeniable that the stress around the crack tip relaxed even though the macroscopic stress did not in the creep experiment.

This shows the feasibility of studying stress relaxation locally in a small volume. Again, a characteristic relaxation time was calculated and was found to be around  $\tau = 12$  seconds, which is in good agreement with the previous results.

### 4.3 Spatial mapping of the stress concentration around the crack tip

Chapter 3 highlighted the non-linearity of the hybrid gels under homogeneous stress. In large deformations, typically around the crack tip, non-linear effects are not negligible. How does the stress field ahead of the crack tip evolve with  $z$ ? LEFM (Linear Elastic Fracture Mechanics) theory predicts that the stress decreases as the inverse square root of  $z$  in elastic materials. Is it the case for the experimental stress field of the elastic PDMA hydrogel and what is the stress field for the viscoelastic gels and swollen gels?

#### 4.3.1 Effect of crack tip geometry on stress field: case of elastic gels

##### Increasing COD with fixed crack depth ratio $a/W$

The two parameters that govern the crack tip geometry are the COD and the crack tip ratio  $a/W$ . A simple experiment at a crack depth ratio fixed ( $a/W = 0.23$ ) and different COD is presented Fig. 4.23. When the gel is at rest, i.e COD = 0, the stress is equal to zero along  $z$ . When we open the notch, the COD increases, the singularity appears and the stress at the crack tip increases with the COD.

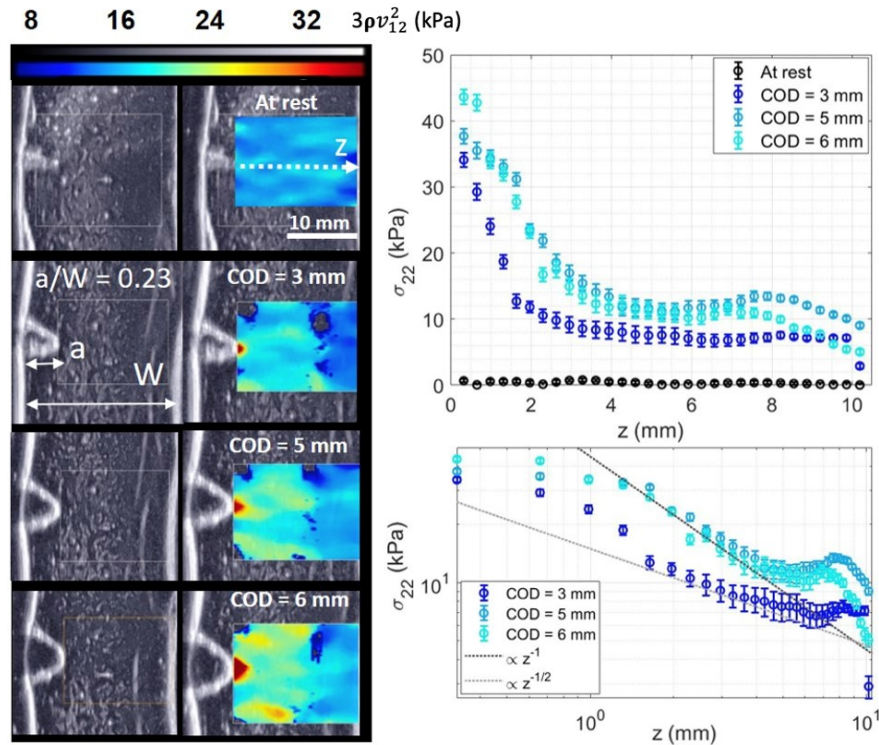


FIGURE 4.23: Local stress as a function of  $z$  in elastic gels for different COD with  $a/W$  ratio fixed at 0.23. Linear and logarithmic scales are represented. Two different trends are represented:  $z^{-1/2}$  and  $z^{-1}$  as a guideline.

We observe different stress evolution as a function of  $z$  from  $z^{-1/2}$  to  $z^{-1}$  when the COD increases. The other parameter ( $a/W$ ) is also important. For  $a/W \sim 0.45$ , we obtain Fig. 4.24.

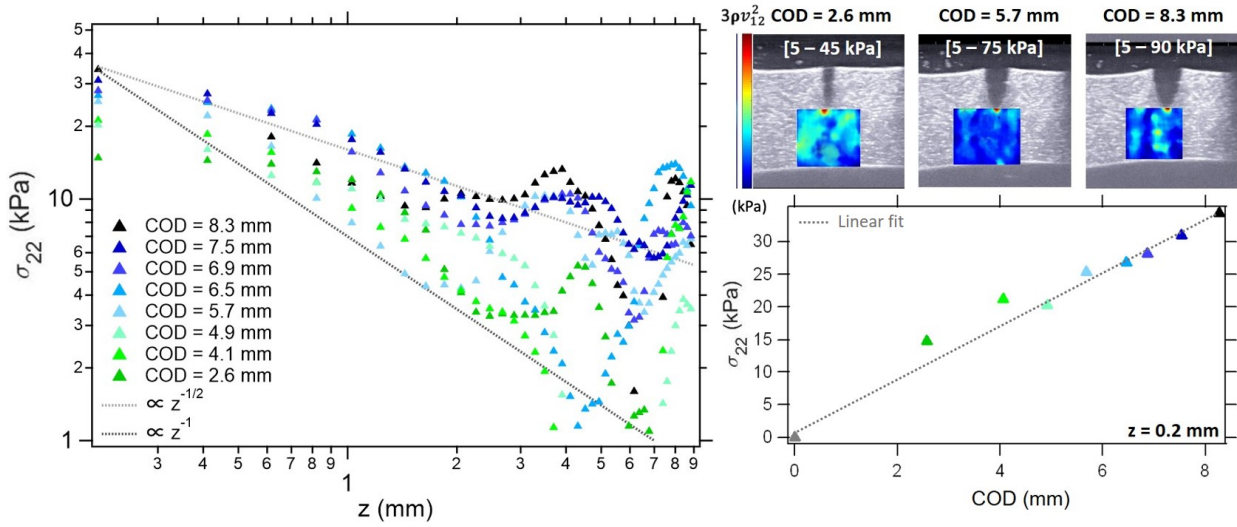


FIGURE 4.24: Left: Local stress as a function of  $z$  in elastic gels for different COD with  $a/W$  ratio fixed at 0.45. Logarithmic scale is represented. Two different trends are represented:  $z^{-1/2}$  and  $z^{-1}$  as a guideline. Right: Three ultrasound images are represented at three different COD and with a different scale in the color bar. Below these images is represented the stress at the crack tip as a function of the COD with the colors corresponding to the curves of the graphic on the left.

The stress at the crack tip ( $z = 0.2$  mm) is also represented as a function of the COD, taking the first point of each curve accounting for this geometry ( $a/W = 0.45$ ). When the COD increases, the stress at the crack tip increases as well. Concerning the stress as a function of  $z$ , the COD has an impact but we can not deduce a clear trend. For example, for large COD (as 8.3 mm), the stress seems to scale with  $z^{-1/2}$  up to about 2 mm whereas the stress seems to decrease as  $z^{-1}$  for a COD of 4.1 mm (from  $z = 0.6$  mm to 3 mm). By opening the notch, thus increasing the stress at the crack tip, the slope of the stress as a function of  $z$  is not steeper (Fig. 4.24) as it is the case in Fig. 4.23 with  $a/W = 0.13$ . To conclude, we can deduce that increasing the COD enhances the stress at the crack tip and changes the trend of the stress field. The shape of the stress field can not be deduced but seems to range between  $z^{-1/2}$  and  $z^{-1}$ . Note that passed 3-4 mm, probably due to geometrical effect, the stress does not show a clear trend but up and downs.

### Effect of COD and crack depth ratio $a/W$ variations

The COD and  $a/W$  parameters are both changed and presented in Fig. 4.25. As one can expect, they both affect the evolution of the stress along  $z$ .

We can notice that the stress with the highest  $a/W$  shows a lowest stress at  $z = 0.2$  mm. Indeed, intuitively, it is easier to open a notch when the crack length  $a$ , thus  $a/W$ , is big (pink). This intuition is confirmed in Fig. 4.26 where the force is plotted as a function of the COD for three elastic gels with different crack depth ratios. The bigger stress at the crack tip is assigned by the dark blue curve with a COD of 6.2 and  $a/W = 0.22$ . If we compare these two curves where the COD is comparable, we notice that the crack depth ratio is important to define the maximum stress at the crack tip. In any case, in Fig. 4.25, we found a singularity at the crack tip varying between  $\sigma \approx 30$  kPa and  $\sigma \approx 60$  kPa in elastic gels. The stress decreases as  $z^{-1/2}$ ,  $z^{-1}$  or  $z^{-3/2}$  depending on the crack tip depth ratio and COD. It seems that the closer configuration to LEFM is the one with the higher crack depth ratio  $a/W \sim 0.45$ .

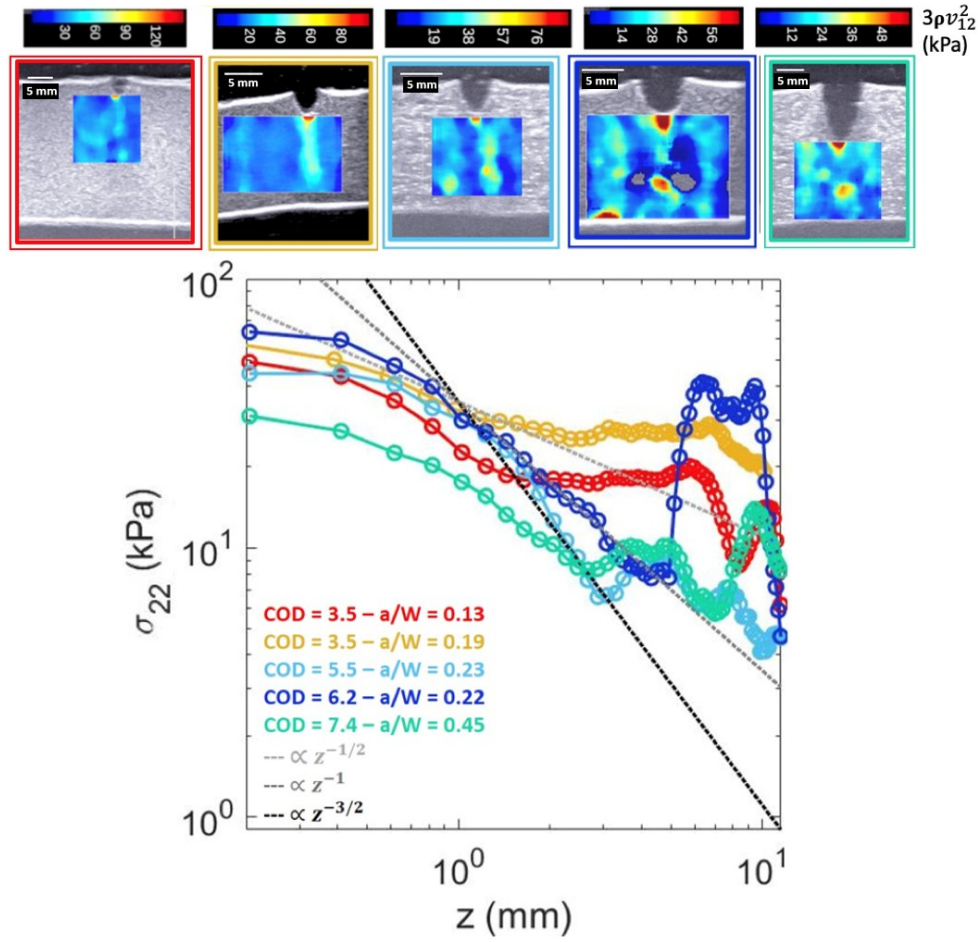


FIGURE 4.25: Local stress as a function of  $z$  for elastic gels for different COD (mm) and  $a/W$  ratio. Three different trends are represented:  $z^{-1/2}$ ,  $z^{-1}$  or  $z^{-3/2}$ .

In Fig. 4.26, the force was recorded at different strains and the COD was measured with ultrasound images. An uncertainty of 0.01 N was chosen for the force and approximately fixed to 0.3 mm for the COD (operator dependent).

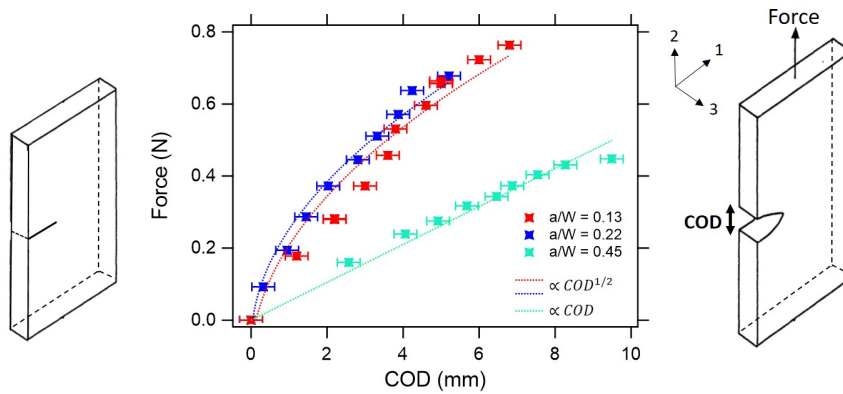


FIGURE 4.26: Force as a function of the COD. Two schemes are represented to illustrate the graphic. The left scheme represents the beginning of the experiment with a force and COD equal to zero.

For  $a/W \sim 0.45$ , the stress evolves linearly until COD = 8 mm whereas it seems to increase with the square root of the COD for  $a/W = 0.22$  and  $a/W = 0.13$  highlighting the gel non-linearity. This

non linearity could explain the difference in the stress spatial mapping which goes from  $z^{-1/2}$  ( $a/W = 0.45$ ) to  $z^{-1}$  ( $a/W = 0.22$  and  $a/W = 0.13$ ) (Fig. 4.25).

### Absence of temporal evolution of the spatial mapping for elastic gels

Elastic gels do not relax and the stress remains unchanged over time (Fig. 4.27).

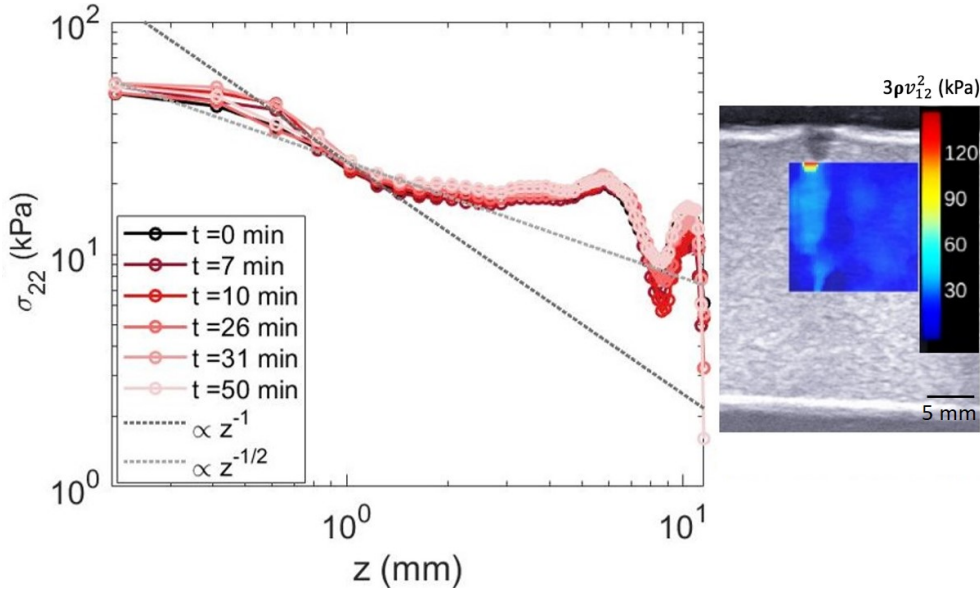


FIGURE 4.27: Local stress as a function of  $z$  in elastic gels. Logarithmic scale is represented. Two different trends are shown:  $z^{-1/2}$  and  $z^{-1}$  as a guideline. COD = 3.5 mm -  $a/W = 0.13$ .

As demonstrated in Fig. 4.9, the stress at the crack tip does not change over time. The same conclusion is made for a chosen  $z$  from 0.2 to 10 mm (Fig. 4.27). This has been verified for all elastic gels tested in Fig. 4.25.

To conclude on elastic gels, there is no relaxation of the stress either locally or macroscopically. The stress does not evolve with time. Concerning the spatial decrease of the stress ahead of the crack tip, hydrogels are too complex to be reduced to LEFM theory. As a reminder, this theory was developed on glass, far different from our soft material. It appears that the stress field strongly depends on the COD (opening of the crack) and  $a/W$  (crack depth ratio). From these parameters, the stress decreases as  $z^{-1/2}$ ,  $z^{-1}$ ,  $z^{-3/2}$  or a combination of all and remains difficult to predict. Nevertheless, with a large crack depth ratio ( $\approx 0.5$ ), nonlinear effects seem avoided reducing the stress at the crack tip and reconciling the stress trend of  $z^{-1/2}$ .

### 4.3.2 Stress field impacted by the presence of NPs in viscoelastic gels

#### COD and crack depth ratio $a/W$

In Fig. 4.28, we present the results for three different viscoelastic gels superimposed on the previous results of elastic gels. Two viscoelastic gels with  $a/W = 0.52$  have been tested and they are in good agreement, i.e they share the same trend of the force versus COD. Whatever the crack depth ratio for viscoelastic gels, i.e  $a/W = 0.22$  or  $0.52$ , the force increases as the square root of the COD.

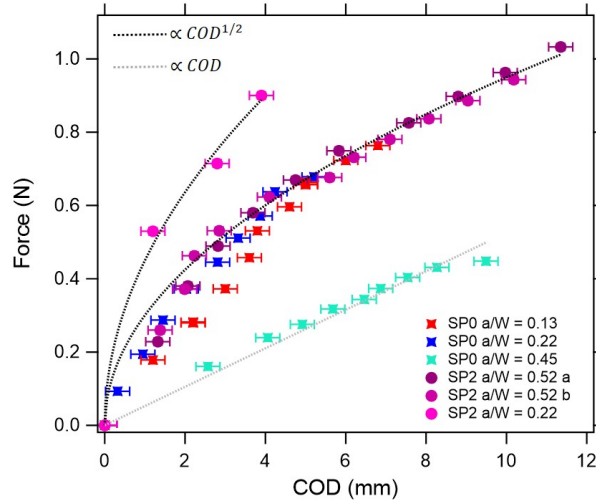


FIGURE 4.28: Force as a function of the COD for elastic and viscoelastic gels with different crack depth ratios.

Note that elastic gels with a small crack depth ratio, i.e  $a/W = 0.22$  and  $a/W = 0.13$ , show great similarities with viscoelastic gels with a crack depth ratio of  $a/W \approx 0.5$ . This suggests that these elastic gels share a common behavior with viscoelastic gels around the crack tip (according to the geometry of the crack). This similarity can be explained by non linear effects that are exacerbated in large deformation which is the case around a crack tip. Intuitively, for viscoelastic gels with small  $a/W$ , i.e 0.22, this effect should be bigger. Indeed, we find a result even further from the linear fit (with a bigger amplitude of the square root of the COD).

For gels that show the same behavior of the force evolution according to the COD, do they also show an equivalent spatial mapping of the stress ahead of the crack tip? The four gels that display non-linearity in the evolution of the force according to the COD in Fig. 4.28 are represented in Fig. 4.29 to see how the stress field evolve with  $z$ .

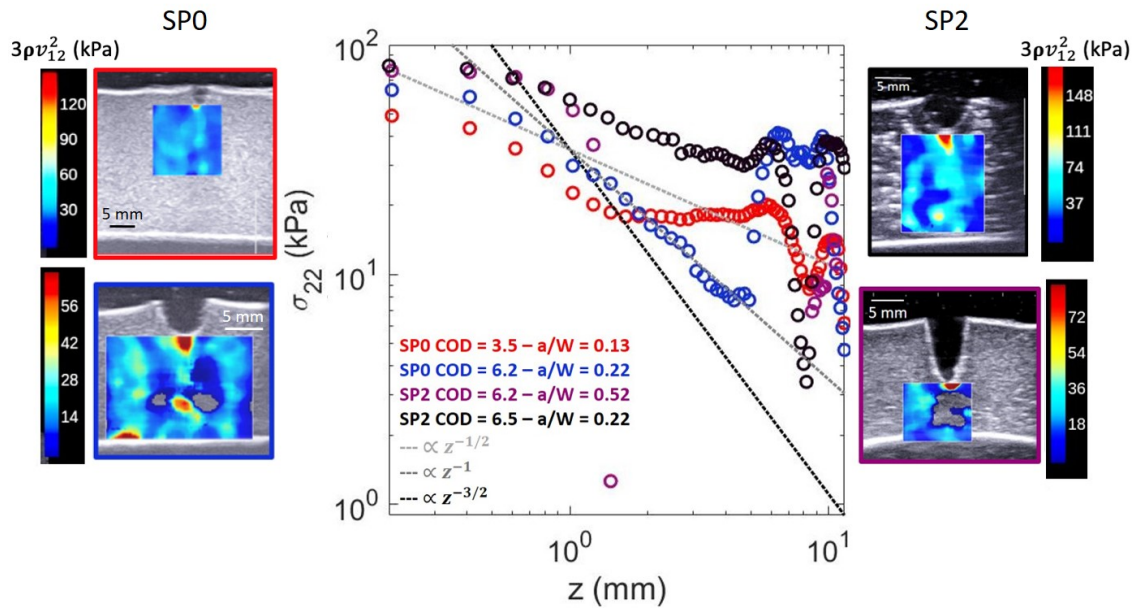


FIGURE 4.29: Local stress as a function of  $z$  for two elastic gels and two viscoelastic gels at different COD and  $a/W$  ratios. Logarithmic scale is represented. Three different trends are shown:  $z^{-1/2}$ ,  $z^{-1}$ , and  $z^{-3/2}$  as a guideline.

For the two elastic gels, Fig. 4.29 shows that from 0.2 to 2 mm, the decrease of the stress versus  $z$  is the same: red curve (COD = 3.5 mm and  $a/W = 0.13$ ) and dark blue curve (COD = 6.2 mm and  $a/W = 0.22$ ). As observed in Fig. 4.26, these two gels show the same force for the same COD. Concerning the decrease of the stress along  $z$  for SP2 gel with  $a/W = 0.52$ , we only have access to few data due to a lack of signal (from 1 mm to about 9 mm ahead of the crack tip) (see Fig. 4.29, right). We can only trust the five first points since, as explained in part. 4.1.2, the automatic code proceeds a lot of cross-correlations with the surrounding pixels and smooth the results. If we stick to the first points of the purple curve, we observe that it matches the dark curve (SP2 gel with  $a/W = 0.22$ ). The decay seems analogous for the two hybrid gels. Even if SP2 gel  $a/W = 0.52$  share the same non linear force-COD curve than the two SP0 gels, it does not mean that their stress gradient will be identical.

The gels that share the same Force-COD curve do not necessarily share the same spatial stress field ahead of the crack tip due to local interactions brought by NPs in the case of SP2. Simple scaling laws do not allow to reflect the stress field.

### Temporal evolution of the spatial stress mapping of SP2

For the spatio-temporal evolution of SP2 viscoelastic gels, we study the gel with the crack tip depth ratio  $a/W \approx 0.22$ . We already saw in the previous part that viscoelastic gels relax (macroscopically in Fig. 4.10 and locally in Fig. 4.12). The local relaxation is also visible for a given  $z$  of Fig. 4.30.

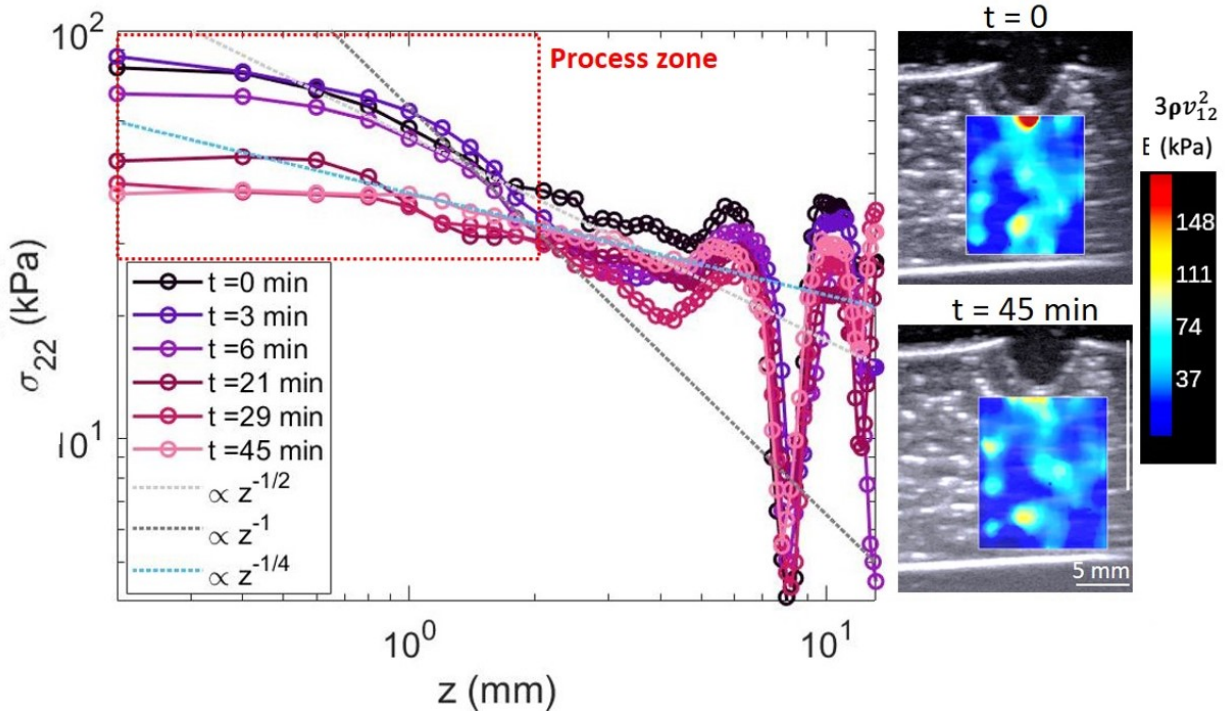


FIGURE 4.30: Local stress distribution as a function of  $z$  on SP2 gels for different times.  $z^{-1}$ ,  $z^{-1/2}$  and  $z^{-1/4}$  are shown as a guideline. The dotted red rectangle represents the process zone that we defined between 0 to 2 mm. COD = 6.5 mm -  $a/W = 0.21$ .

Through the physical interactions between the polymer chains and the silica NPs, we highlight a local stress reorganization inside the gel and especially at the crack tip since we measure a great amplitude relaxation (about 50%: from 90 to 45 kPa, approximately). We can define a process

zone of 2 mm. Indeed, after 2 mm, the curves overlap each other. This process zone indicates that viscoelasticity and nonlinearity are strong in this zone. NPs are able to shield the crack tip singularity through topological rearrangements.

### 4.3.3 Influence of swelling on the local stress field

It is expected that LEFM works better for swollen elastic gels. Indeed, these gels at  $Q_e$  are more elastic than at their preparation state  $Q_0$  since dangling chains are not contributing to viscoelastic losses of polymer strands.

In Fig. 4.31, the stress as a function of  $z$  is represented at  $t = 0$  for the three different gels SP0, SP2 and SP3.5 at  $Q_e$ . We focus at short time to avoid any interactions between the NPs and the oil.

In the first millimeter, the three curves overlap each other. Then, SP0 gel shows a steeper stress decay than the two others (close to  $z^{-3/2}$ ) followed by a stress gradient close to  $z^{-1/2}$ .

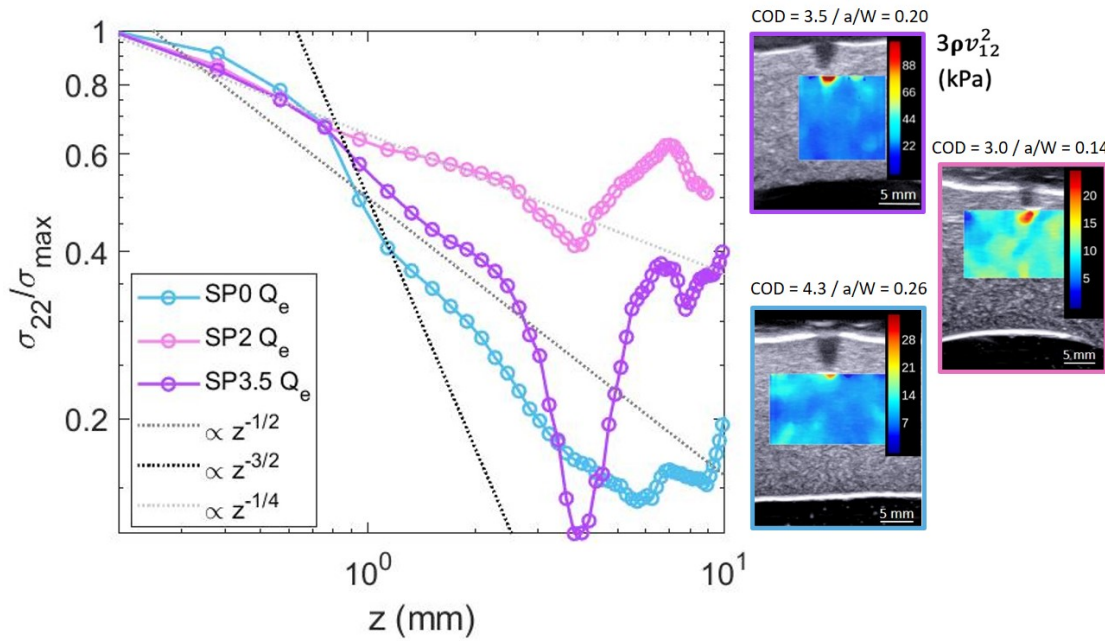


FIGURE 4.31: Local stress at  $t = 0$  as a function of  $z$  during a tensile test performed in oil fixed at 30% strain for SP0, SP2 and SP3.5 gels at  $Q_e$ .  $\sigma/\sigma_{max}$  is shown to compare the three gels. The steeper stress gradient is reached for SP0 gels.

In SP2 swollen viscoelastic gels, the stress decreases as  $z^{-1/4}$  reminding the one of SP2 gels at  $Q_0$  after 45 minutes of 50% strain (see Fig. 4.32). It would mean that the configuration adopted by the polymer network and the NPs at  $Q_e$  at  $t = 0$  is already relaxed and analogous to SP2 at  $Q_0$  after 45 minutes. This phenomenon is not observed in SP3.5 gels where the stress field shows the same gradient decay over  $z$  (close to  $z^{-1/2}$ ). Nevertheless, SP3.5 gels had an unexpected behavior at  $Q_0$  (see annex B) where an aggregation was highlighted ahead of the crack tip.

In Chapter 3, it has been shown that swollen elastic gels, SP0 at  $Q_e$ , are inherently more fragile than any other model gels of this study. They have a poor fracture stress and strain (Fig. 3.7). Their mechanical fragility can be caused by two intrinsic properties: stress concentration/stress gradient around defects that are too high and the lacking of dissipation mechanisms.

Fig. 4.32 shows that the gradient of the stress field is the same for swollen gels  $Q_e$  at  $t = 0$  compared to their analogues at preparation state  $Q_0$  at  $t = \infty$ .

Concerning elastic gels, we can therefore conclude that if these gels are more brittle, it is not a question of stress gradient at the crack tip but rather a question of dissipation which is suppressed at equilibrium state.

Concerning viscoelastic gels swollen at equilibrium state  $Q_e$ , the mechanical tests revealed that they have higher fracture stress and strain than a chemical gel in the as-prepared state  $Q_0$  (Fig. 3.7). Here, this last result makes it possible to deduce that these gels have a lower stress gradient, with a gradient half as steep, compared to the SP0 gel at  $Q_0$ . Therefore, in the presence of NPs, not only they are able to bring dissipation into the gel but also to lower the stress gradient.

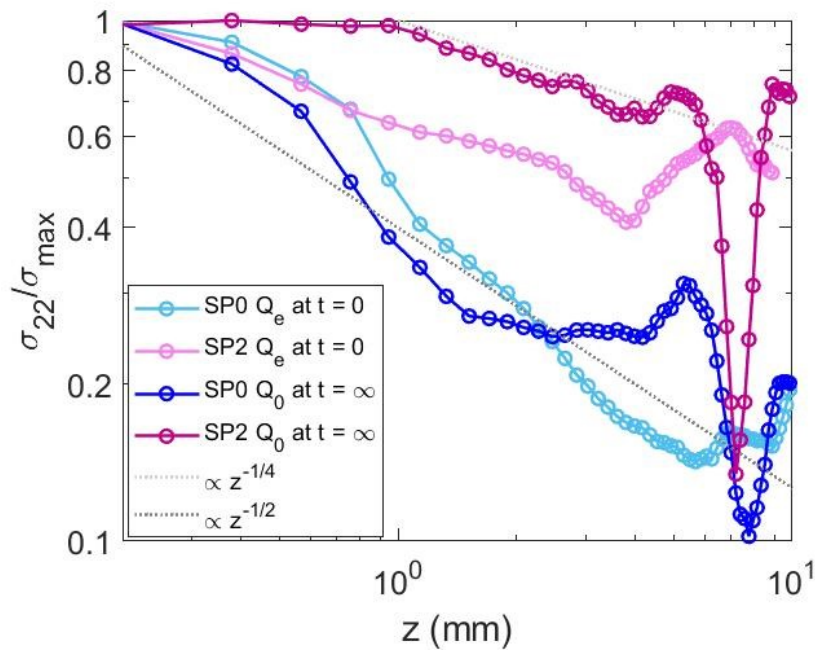


FIGURE 4.32: Local stress as a function of  $z$  during a tensile test performed in oil fixed at 30% strain for SP0 and SP2 at  $Q_e$  at  $t = 0$  and SP0 and SP2 at  $Q_0$  at  $t = \infty$ .  $\sigma / \sigma_{max}$  is shown to compare the three gels. The steeper stress gradient is reached for SP0 gels.

## 4.4 Finite Element Method (FEM)

### 4.4.1 Introduction to FEM

There are a lot of different analytical methods that engineers can use to solve structural mechanics problems, whether it is to calculate the deflection of a beam or the stresses in a flat plate. Engineers often encounter problems that can't be solved through experimental or analytical methods, typically because the geometry is too complex. Finite Element Method (FEM) is a powerful numerical technique that uses computational power to calculate approximate solutions to these types of problems. It is widely used in all major engineering industries. For example, it is used to check that satellite components survive the launch conditions or to optimize the design of automotive components, like the lower control arm of a car suspension system. Finite element analysis software can be used to analyze a wide range of solid mechanics problems, including static, dynamic,

buckling, and modal analyses.

In this thesis, FEM will be applied to static linear-elastic stress analysis. Finite element simulations were carried out so as to assess the true stress field at the local scale ahead of the crack tip. Z-set software<sup>1</sup> (Besson et al., 1997) was utilized. The software is edited by Mines Paris, the ONERA and SAFRAN Tech. The general presentation of a Finite Element code consists of introducing three main components: discretization, boundary conditions and constitutive models.

#### 4.4.2 Discretization

This first process is called discretization and the collection of nodes and elements is called the mesh. Discretization is useful because it allows dissociating finite numbers of discrete elements instead of studying the entire body.

To determine the stress field in the hydrogel, especially near the crack tip, the SENT (Single Edge Notch Tensile) geometry was created using Abaqus (see the mesh Fig. 4.33).

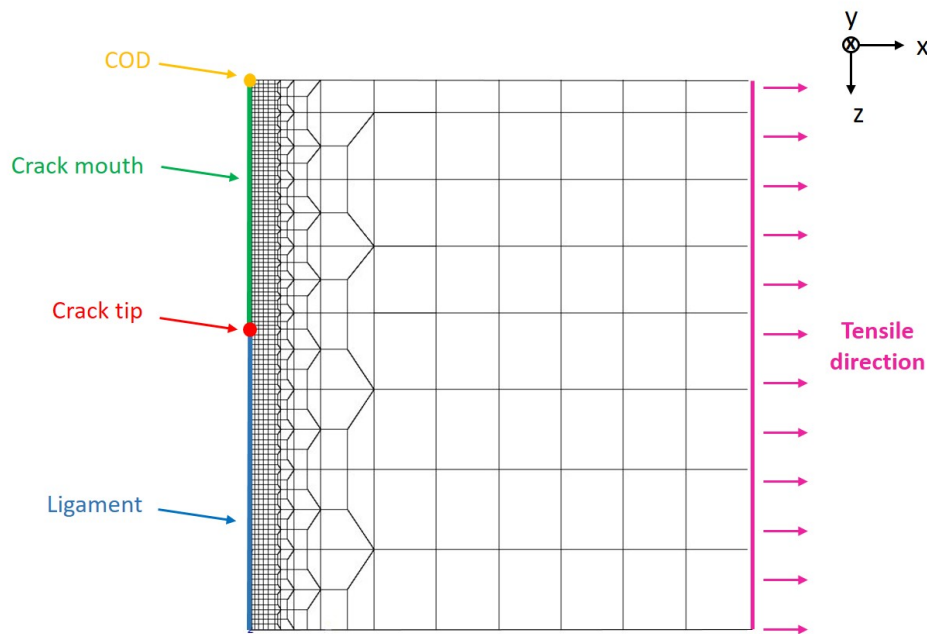


FIGURE 4.33: Meshing of the SENT specimen indicating the crack tip, the crack opening displacement (COD), the crack mouth (also called crack lips), the ligament, and the tensile direction. Boundary conditions and symmetry were applied on the node sets.

The present SENT like specimen were meshed by using quadratic with full integration elements. Half of the SENT specimen was meshed using 2D plane strain under finite strain updated lagrangian formulation. So as to account for the incompressibility constraint, hybrid elements with mixed displacement-pressure at the nodes were associated with Rivlin strain energy whereas regular elements were selected for Mooney compressible deformation energy. The mesh size ahead of the crack tip was about 200  $\mu\text{m}$ .

<sup>1</sup><http://www.zset-software.com/>

#### 4.4.3 Boundary conditions

The second process is the boundary conditions related to what is applied on the body at the macroscopic scale: either the nodal reaction forces or the nodal displacements (or both in the case of mixed mode loadings).

Due to symmetry, only half of the specimen was meshed. Therefore the “ligament” was blocked horizontally. The right node set was blocked in the vertical direction and the prescribed displacement was applied on this node set, letting the crack opening displacement increase with respect to the applied displacement.

#### 4.4.4 Constitutive models

The model is implemented directly in tensorial forms i.e. fully 3D. The computation of the stresses and strains in the 3 axes of the space is carried out by the software according to the boundary conditions and the meshing.

##### Particular case of uniaxial tension

This subsection should be included in the constitutive models parts. The uniaxial case can be handled either by analytical (formal maths), developed in the following, or by numerical using a representative volume element (RVE) like the model gel without a crack. RVE is defined as a "structure" where the stress and strain are homogeneous. That is why this case can be handled (analytical method).

The direction of uniaxial tension is assumed to be in the direction 2 and the elongation along this direction is called  $\lambda = \lambda_2$ .

Then, assuming isotropy or at least transverse isotropy, we will consider that  $\lambda_1 = \lambda_3 = \lambda_T$  (T stands for Transverse). The deformation gradient tensor is then written :

$$\mathbf{F} = \begin{pmatrix} \lambda_T & 0 & 0 \\ 0 & \lambda & 0 \\ 0 & 0 & \lambda_T \end{pmatrix} \quad (4.2)$$

If the material is considered as quasi-incompressible  $\lambda_T = 1/\sqrt{\lambda}$  since  $J = \det(\mathbf{F}) = 1$ .

The right Cauchy-Green tensor  $\mathbf{C} = \mathbf{F}^T \mathbf{F}$  is written:

$$\mathbf{C} = \mathbf{F}^T \mathbf{F} = \begin{pmatrix} \lambda_T^2 & 0 & 0 \\ 0 & \lambda^2 & 0 \\ 0 & 0 & \lambda_T^2 \end{pmatrix} \quad (4.3)$$

The three invariants  $I_1$ ,  $I_2$  and  $I_3$  of  $\mathbf{C}$  are:

$$\begin{aligned} I_1 &= \text{trace}(\mathbf{C}) = \lambda^2 + 2\lambda_T^2 \\ I_2 &= \frac{1}{2} [(\text{trace}(\mathbf{C}))^2 - \text{trace}(\mathbf{C}\mathbf{C})] = \lambda_T^2 (2\lambda^2 + \lambda_T^2) \\ I_3 &= \det(\mathbf{C}) = \lambda^2 \lambda_T^4 \end{aligned} \quad (4.4)$$

Preliminary results on the characteristic polynomials give the derivatives of the invariants with respect to the  $\mathbf{C}$  tensor following:

$$\frac{\partial I_1}{\partial \mathbf{C}} = \mathbf{I} \quad \frac{\partial I_2}{\partial \mathbf{C}} = I_1 \mathbf{I} - \mathbf{C} \quad \frac{\partial I_3}{\partial \mathbf{C}} = I_3 \mathbf{C}^{-1} \quad (4.5)$$

with  $\mathbf{I}$ , identity tensor. Thus:

$$\begin{aligned} \frac{\partial I_1}{\partial \mathbf{C}} &= \begin{pmatrix} 1 & 0 & 0 \\ 0 & 1 & 0 \\ 0 & 0 & 1 \end{pmatrix} \\ \frac{\partial I_2}{\partial \mathbf{C}} &= \begin{pmatrix} \lambda^2 + \lambda_T^2 & 0 & 0 \\ 0 & 2\lambda_T^2 & 0 \\ 0 & 0 & \lambda^2 + \lambda_T^2 \end{pmatrix} \\ \frac{\partial I_3}{\partial \mathbf{C}} &= \begin{pmatrix} \lambda^2 \lambda_T^2 & 0 & 0 \\ 0 & \lambda_T^4 & 0 \\ 0 & 0 & \lambda^2 \lambda_T^2 \end{pmatrix} \end{aligned} \quad (4.6)$$

Considering a strain energy  $W$ , the second Piola-Kirchhoff stress tensor used in the numerical calculations, is obtained as follows:

$$\mathbf{S} = 2 \frac{\partial W}{\partial \mathbf{C}} = 2 \left[ \frac{\partial W}{\partial I_1} \frac{\partial I_1}{\partial \mathbf{C}} + \frac{\partial W}{\partial I_2} \frac{\partial I_2}{\partial \mathbf{C}} + \frac{\partial W}{\partial I_3} \frac{\partial I_3}{\partial \mathbf{C}} \right] \quad (4.7)$$

So:

$$\mathbf{S} = 2 \left[ \frac{\partial W}{\partial I_1} \mathbf{I} + \frac{\partial W}{\partial I_2} (I_1 \mathbf{I} - \mathbf{C}) + \frac{\partial W}{\partial I_3} I_3 \mathbf{C}^{-1} \right] \quad (4.8)$$

This stress tensor is decomposed into a deviatoric part ( $S_d$ , terms in  $I_1$  and  $I_2$ ) and a spherical part or iso-static part ( $S_s$ , term in  $I_3$ ).

#### Quasi-incompressible hyperelastic behavior (Rivlin)

The incompressible constraints makes analytical development easy since the spherical terms ( $I_3$ ) vanishes. But it brings difficulty in the FE methods because it needs specific elements (called hybrid or mixed) due to the fact that the bulk modulus is supposed to be infinity. The hydrostatic pressure ( $p+p_0$ ) is then defined by the boundary conditions.

The material is considered as quasi-incompressible, so  $\lambda_T = 1/\sqrt{\lambda}$ .

$$I_1 = \lambda^2 + \frac{2}{\lambda} \quad I_2 = 2\lambda + \frac{1}{\lambda^2} \quad I_3 = 1 \quad (4.9)$$

with:

$$\frac{\partial I_2}{\partial \mathbf{C}} = \begin{pmatrix} \lambda^2 + \frac{1}{\lambda} & 0 & 0 \\ 0 & \frac{2}{\lambda} & 0 \\ 0 & 0 & \lambda^2 + \frac{1}{\lambda} \end{pmatrix} \quad (4.10)$$

In the case of quasi-incompressibility,  $\sigma_s$  is treated in a special way by using hybrid or mixed elements. The Lagrange multiplier  $p$  ensures the incompressibility condition  $\det \mathbf{F} = 1$  and is fixed by the boundary conditions.  $p_0$  is the offset of the hydrostatic pressure justified by the fact that without deformation, the stress tensor is zero.

$$\mathbf{S} = 2 \left[ \frac{\partial W}{\partial I_1} \mathbf{I} + \frac{\partial W}{\partial I_2} (I_1 \mathbf{I} - \mathbf{C}) \right] - (p + p_0) I_3 \mathbf{C}^{-1} \quad (4.11)$$

simplified by:

$$\mathbf{S} = 2 \left[ \left( \frac{\partial W}{\partial I_1} + I_1 \frac{\partial W}{\partial I_2} \right) \mathbf{I} - \frac{\partial W}{\partial I_2} \mathbf{C} \right] - (p + p_0) \mathbf{C}^{-1} \quad (4.12)$$

For  $\mathbf{F} = \mathbf{C} = \mathbf{I}$ ,  $p = 0 \rightarrow \mathbf{S} = 0$ .

$$\mathbf{0} = 2 \left[ \left( \frac{\partial W}{\partial I_1} + 3 \frac{\partial W}{\partial I_2} \right) \mathbf{I} - \frac{\partial W}{\partial I_2} \mathbf{I} \right] - p_0 \mathbf{I} \Rightarrow p_0 = 2 \left[ \frac{\partial W}{\partial I_1} + 2 \frac{\partial W}{\partial I_2} \right] \quad (4.13)$$

The traction being uniaxial:  $S_{11} = S_{33} = 0$

$$p + p_0 = \frac{2}{\lambda} \left[ \frac{\partial W}{\partial I_1} + \left( \lambda^2 + \frac{1}{\lambda} \right) \frac{\partial W}{\partial I_2} \right] \quad (4.14)$$

Replacing  $p$  by its expression, we get :

$$S_{22} = 2 \left( 1 - \frac{1}{\lambda^3} \right) \left( \frac{\partial W}{\partial I_1} + \frac{1}{\lambda} \frac{\partial W}{\partial I_2} \right) \quad (4.15)$$

The Cauchy stress  $\sigma$  can be obtained from  $\mathbf{S}$  as follows:

$$\sigma = \frac{1}{J} \mathbf{F} \mathbf{S} \mathbf{F}^T \quad (4.16)$$

with  $J = \sqrt{I_3}$ . The Cauchy stress obtained is:

$$\sigma_{22} = 2 \left( \lambda^2 - \frac{1}{\lambda} \right) \left( \frac{\partial W}{\partial I_1} + \frac{1}{\lambda} \frac{\partial W}{\partial I_2} \right) \quad (4.17)$$

For a Rivlin strain energy of order 1 :

$$W = c_{10} (I_1 - 3) + c_{01} (I_2 - 3) \quad (4.18)$$

The Cauchy stress in the direction of traction is written :

$$\sigma_{22} = 2 \left( \lambda^2 - \frac{1}{\lambda} \right) \left( c_{10} + \frac{c_{01}}{\lambda} \right) \quad (4.19)$$

In the study,  $c_{10}$  and  $c_{01}$  are empirically determined material constants.  $c_{10}$  equals to  $c_{10} = \frac{\delta W}{\delta I_1} = 0.00155$  MPa and  $c_{01} = \frac{\delta W}{\delta I_2} = 0$ . The shear modulus is equal to  $\mu = (c_{10} + c_{01}) \times 2 = 3.1$  kPa.

Considering  $c_{01} = 0$ , the Cauchy stress in the incompressible case is equal to :

$$\sigma_{22} = 2c_{10} \left( \lambda^2 - \frac{1}{\lambda} \right) \quad (4.20)$$

### Compressible hyperelastic behavior (Mooney)

We thus return to the gradient tensors of deformation of the general (isotropic) case.  $\lambda_T$  is part of the measurable variables, not necessarily measured due to technical limitation with the setup. The invariants and their derivatives have already been explained in part. 4.4.4.

Equation 4.8 is used again:

$$\mathbf{S} = 2 \left[ \frac{\partial W}{\partial I_1} \mathbf{I} + \frac{\partial W}{\partial I_2} (I_1 \mathbf{I} - \mathbf{C}) + \frac{\partial W}{\partial I_3} I_3 \mathbf{C}^{-1} \right] \quad (4.21)$$

For the second Piola-Kirchhoff tensor  $\mathbf{S} = \mathbf{S}_d + \mathbf{S}_s$ , the calculation of the deviatoric part is similar to that of the incompressible case. It is thus necessary here to calculate  $\mathbf{S}_s$ , the last term in  $I_3$ :

$$\mathbf{S}_s = 2 \left[ \frac{\partial W}{\partial I_3} I_3 \mathbf{C}^{-1} \right] \quad (4.22)$$

The Mooney deformation energy considered in the method is written as :

$$W = c_{10} (I_1 - 3) + c_{01} (I_2 - 3) + m \frac{c_{10} + c_{01}}{2} (I_3 - 1)^2 \quad (4.23)$$

where  $c_{10}$ ,  $c_{01}$ ,  $m$  are the material parameters:  $c_{10}$ ,  $c_{01}$  are common to Mooney and Rivlin and  $m$  is specific to Mooney, similar to a compressibility modulus weighted by the average of  $c_{10}$ ,  $c_{01}$ . This reduces the large discrepancy between the values of the shear modulus and the compressibility modulus.

$$\begin{aligned} \frac{\partial W}{\partial I_3} &= -\frac{m(c_{10} + c_{01})}{2} (\sqrt{I_3} - 1) I_3^{-3/2} \\ \mathbf{S}_s &= -\frac{m(c_{10} + c_{01})}{2} (\sqrt{I_3} - 1) \frac{1}{\sqrt{I_3}} \mathbf{C}^{-1} \end{aligned} \quad (4.24)$$

For the component along the tensile direction of the stress  $S_s$ , we write:

$$S_s^{22} = -\frac{m(c_{10} + c_{01})}{2\lambda^3\lambda_T^2} (\lambda\lambda_T^2 - 1) \quad (4.25)$$

The Cauchy stress  $\sigma$  (using Eq. 4.16) is equal to:

$$\sigma_s^{22} = \frac{\lambda}{\lambda_T^2} S_s^{22} = -\frac{m(c_{10} + c_{01})}{2\lambda^2\lambda_T^4} (\lambda\lambda_T^2 - 1) \quad (4.26)$$

Finally, for the compressible hyperelastic model:

$$\sigma_{22} = 2c_{10} \left( \lambda^2 - \frac{1}{\lambda} \right) - \frac{m(c_{10} + c_{01})}{2\lambda^2\lambda_T^4} (\lambda\lambda_T^2 - 1) \quad (4.27)$$

Since  $c_{01} = 0$  and  $m = 1$  MPa:

$$\sigma_{22} = 2c_{10} \left( \lambda^2 - \frac{1}{\lambda} \right) - \frac{mc_{10}}{2\lambda^2\lambda_T^4} (\lambda\lambda_T^2 - 1) \quad (4.28)$$

To calculate  $\sigma_{22}$ , it is needed to measure  $\lambda_T$  as well as  $\lambda$ .

Finally, to verify the incompressibility, one can compare  $\lambda_T$  to  $1/\sqrt{\lambda}$ .

Plane strain is assumed meaning the study is done at a half thickness in the bulk, as elastography with the ultrasound probe. The material parameters were changed until a good match with both the experimental force and COD was obtained. The optimization is directly done on the notched gel.

## 4.5 Stress field and comparison with simulation

### 4.5.1 Unnotched elastic gel

The two models, Rivlin (incompressible) and Mooney (compressible) are tested on an unnotched gel during a tensile test until fracture (Fig. 4.34). The models fit well the experimental curve until about  $\lambda = 2$  where the models increase compared to the data and follow the third order of AE theory. It gives us insight into the limitation of simulation. FE model is only a first-order approximation.

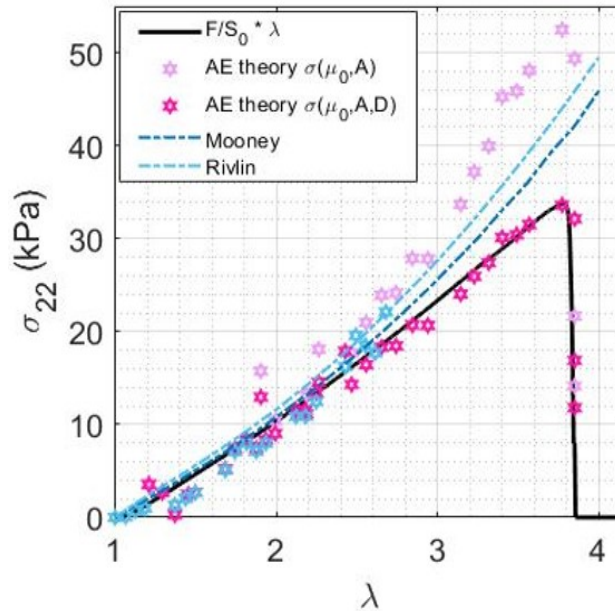


FIGURE 4.34: Stress as a function of  $\lambda$  for a tensile test until fracture for SP0 elastic gel. The experimental stress is represented in black. Acoustoelasticity at 3<sup>rd</sup> and 4<sup>th</sup> order and the Mooney and Rivlin models from FEM are presented.

This consists of the stress-strain curve within a representative volume element (homogeneous stress/strain state). Rivlin model is plotted thanks to analytical approach using Eq. 4.20 whereas Mooney were computed by Zset software. Indeed, as explained in the previous part, the setup was limited and transverse elongation were not measured.

### 4.5.2 Crack tip stress field elaborated by Finite Element Method

FEM was performed on an elastic gel SP0 with  $a/W = 0.45$ . For this purpose, the force, COD and gel geometry were given (Fig. 4.35.a).

The analytical model of acoustoelasticity theory is confronted with two numerical models from the finite element method (FEM), incompressible (Rivlin) and compressible (Mooney). The opening of the crack is shown for different COD in ultrasound images (Fig. 4.35.a). During the test, the crack opening is continuously increasing and the crack mouth shape evolves. FEM adjusted its parameters to find the best match possible in the evolution of the force with the COD (Fig. 4.35.b).

Except for the last diverging point at COD = 9.5 cm, the evolution of the force vs COD is linear. The shear wave speed is no more constant in the elasticity map and its velocity increases at the crack tip (visible in red on the elastic maps of Fig. 4.35.d). Through calculations based on AE theory, we managed to obtain a spatial stress field (represented in Fig. 4.35.c along  $z$ ). A stress singularity is well present at the crack tip of stressed notched gel as expected by Fracture Mechanics theory.

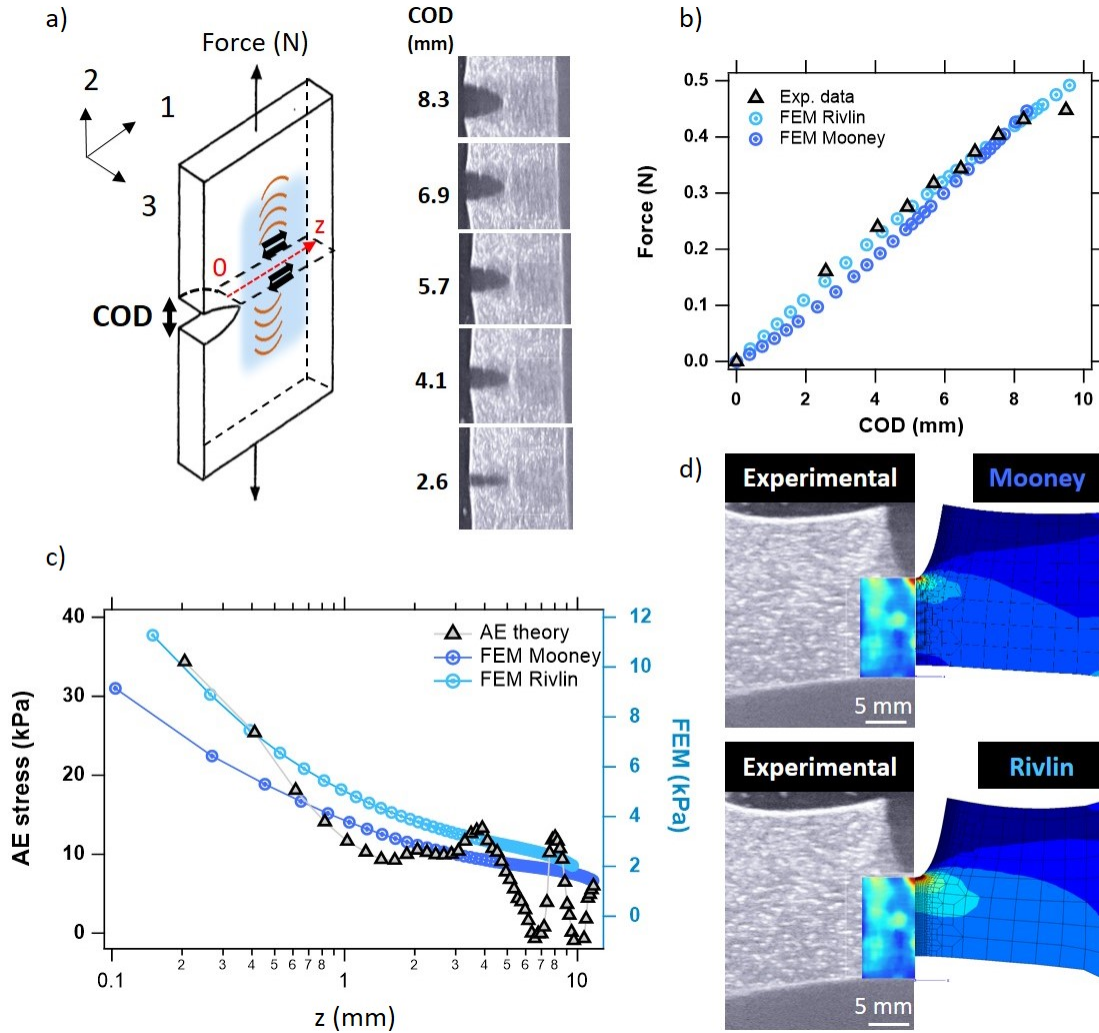


FIGURE 4.35: a) Scheme of the single edge notched gel at a certain strain  $\lambda$ . The notch opens and the COD (crack opening displacement) can be extracted as a function of the force  $F$  imposed. The imaging plane is represented in blue. The dark arrows represent the shear wave polarization and the orange semi-circles represent the shear wave propagation. Ultrasound images are illustrated on the right for five different COD. The COD of 8.3 mm corresponds to a 35% strain.  $a/W$  is equal to 0.5. b) Force as a function of the COD for a strain rate of  $f = 0.06$  Hz. Experimental data and simulations are represented. c) Local stress field ahead of the crack tip, along  $z$ . LEFM and Neo-Hookean solutions are presented as a guideline. d) Experimental map given by Aixplorer (shear wave velocity) compared to the two models given by FEM (Cauchy stress). The compressible model, Mooney, fits better the experimental image given by elastography in terms of geometry. c) and d) represent the COD = 8.3 (penultimate point in the Force-COD) curve.

In Fig. 4.35.c, the stress levels of AE theory (first y-axis, left) were about a factor 3 of that of the FE simulations (second y-axis right). A scale factor for the stress level from the two methodologies

should be studied from these results. However, the stress gradients obtained by the two methods are in good agreement.

Fig. 4.35.d allows the comparison between the deformed image at the same COD for experimental and FE simulations using nearly incompressible (Rivlin) model and compressible (Mooney) model. Although both models were in good agreement with the crack mouth shape, it was observed that the transverse contraction (negative strain) was more pronounced for Rivlin model than for Mooney model. This can be attributed to the “Poisson’s ratio effects” for which the transverse strain is half of the longitudinal one for isochoric (incompressible) deformation ( $\nu = 0.5$ ). For compressible model, the Poisson’s ratio is lower than 0.5, so is the transverse strain. It can clearly be seen in Fig. 4.35.d that the deformed remaining ligament is closer to the experiment for Mooney model than for Rivlin model. As a consequence, the stress level is more “relaxed” for Mooney model (Fig. 4.35.c) in comparison with the Rivlin one.

Given the small difference between simulations and experimental data, the results obtained are really encouraging and support the possibility of measuring a local stress by shear wave elastography.

## 4.6 Key results

This chapter reports what we believe to be the first measurements of the 2D crack tip stress field using shear wave elastography. With this technique, the through-thickness stress is accessible and takes into account non linear effects.

The major results presented in this chapter are:

- The temporal stress mapping of SP0 (elastic) and SP2 (viscoelastic) gel (Fig. 4.36) allows highlighting a mirror effect between the macroscopic and the local stress relaxation. Indeed, the stress at the crack tip of viscoelastic gels meets the one of elastic gels ( $\approx 50$  kPa) about 45 minutes after the beginning of the experiment which is also the case for the macroscopic relaxation of SP2.

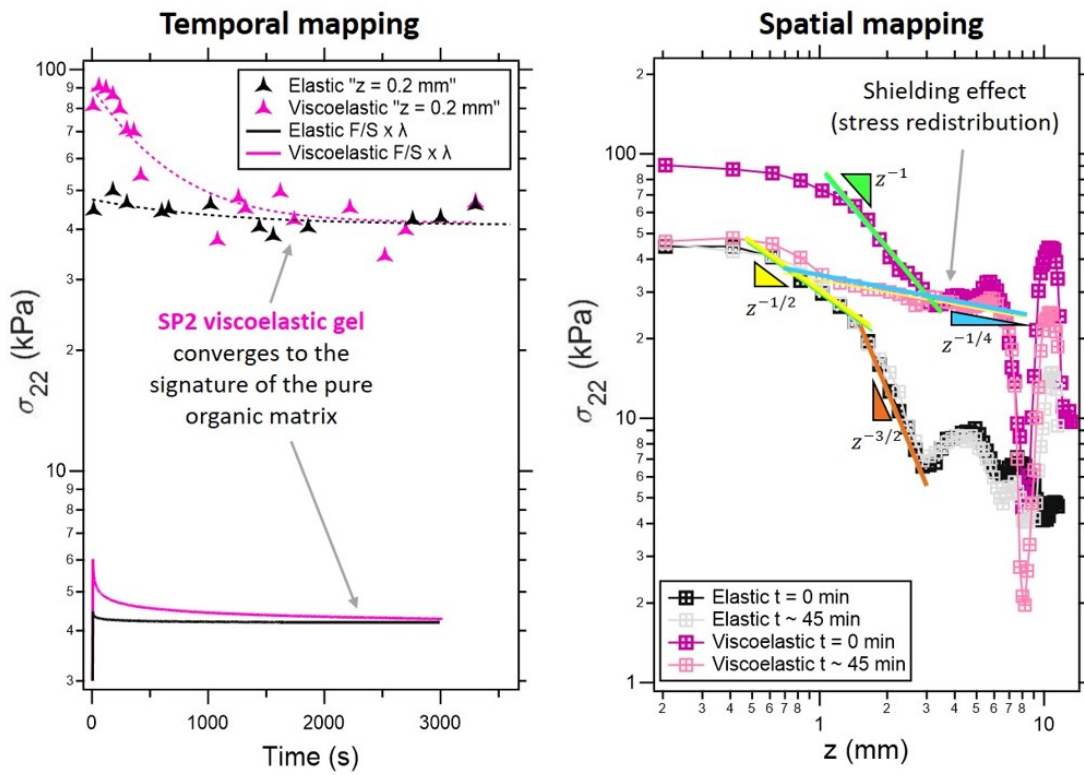


FIGURE 4.36: Comparison between SP0 (elastic) and SP2 (viscoelastic) gel. Tensile test on notched gels fixed at 50% for one hour. Left: Macroscopic and local stress relaxation at the crack tip. Right: Spatial stress evolution according to  $z$  ahead of the crack tip.

- The spatial mapping of SP0 (elastic) and SP2 (viscoelastic) gel (Fig. 4.36) allows visualizing the stress evolution according to  $z$  at  $t = 0$  and  $t = 45$  min. As observed with the temporal mapping, the local stress at the crack tip is the same for both gels after 45 minutes. The stress gradient is completely different between these two gels since the singularity disappeared in the case of viscoelastic gel. Indeed, in SP2 gel, the local relaxation leads to a stress homogenization that is visible at  $t = 45$  min. A shielding effect is observed: the stress at that time decreases as  $z^{-1/4}$ . This homogenization is an important process since it avoids a singularity, thus stress concentration. Since fracture generally starts from the stress concentration

around a defect (here a notch), the NPs allow a rearrangement of the all matrix in the first millimeters in front of the crack tip to avoid fracture propagation.

- Local relaxations at the crack tip happen even when the macroscopic force is maintained, preventing any macroscopic relaxation. The same stress gradient as a function of  $z$  is observed in SP2 gel whether during a relaxation test or during a creep test (see Fig. 4.37). The stress gradient as a function of  $z$  is the same in the process zone, i.e in the 2 first millimeters ahead of the crack tip (see Fig. 4.37). This means that the local processes take place in the same way in the relaxation and creep test: the rearrangement of NPs and polymer chains is still very active in the process zone despite the forbidden macroscopic relaxation.

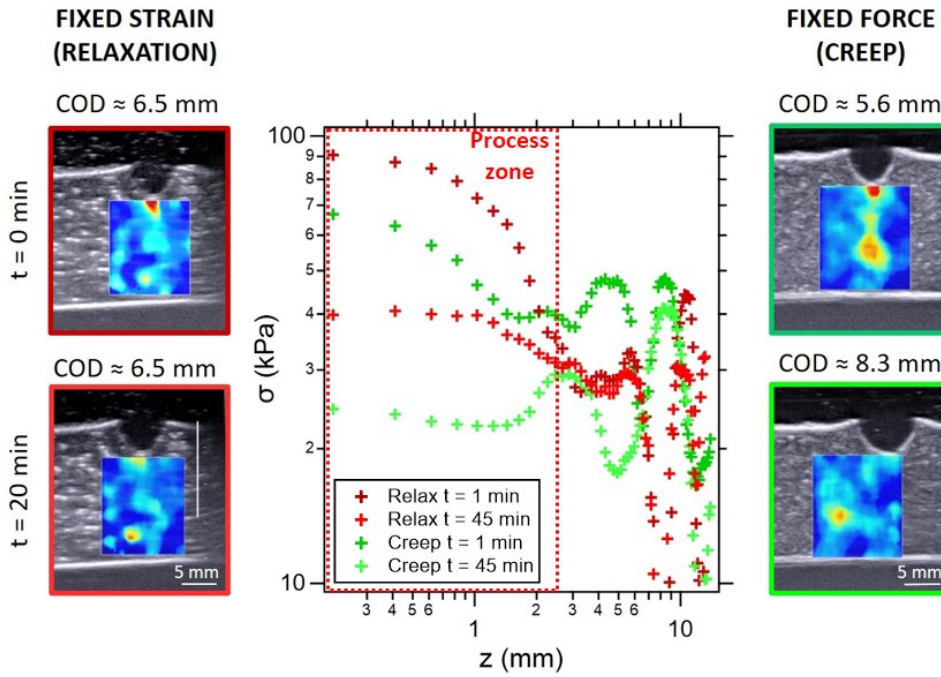


FIGURE 4.37: Spatial stress evolution of SP2 during a relaxation/creep test as a function of  $z$  at  $t = 1$  min and  $t = 45$  min. The crack depth ratio is the same for both gels:  $a/W = 0.21$

- The local characteristic time of relaxation in the creep test is  $\tau \approx 12$  seconds (Fig. 4.22), really close to the macroscopic relaxation. This means that local relaxations are not driven by macroscopic ones. We could have found a different characteristic time under creep tests since the all-matrix was resisting the macroscopic relaxation by maintaining the force constant, i.e increasing the displacement. This supports the fact that  $\tau$  is related to the kinetics of local interactions between the polymer chains and the nanoparticles.
- Between SP0 gel at  $Q_0$  and its analogue swollen at equilibrium state, the stress gradient is the same, despite a more brittle material in the case of the swollen gel. Thus, the brittleness of swollen elastic gels lies in the lack of dissipation, notably the dangling chains that are useless in this configuration.
- Silica nanoparticles play an important role even when the gel is filled with water (already demonstrated in Chapter 3, in Fig. 3.7). For SP2 gel, the configuration adopted by the polymer network and the NPs at  $Q_e$  at  $t = 0$  is already relaxed and analogous to SP2 at  $Q_0$  after 45 minutes. In swollen nanocomposite gels, the relaxation processes seem to be faster ( $\tau \sim 7$  seconds) with fewer configuration possibilities due to the stretching of the polymer

chains. The functionality of the polymer and silica network is increased locally in swollen viscoelastic gels. Viscoelastic gels at preparation state tends to this configuration at long time scale.

- Finite Element Model results are in rather good agreement with our experimental data. FEM, being considered as a gold standard for assessing fracture in materials, supports the measure of a stress through a shear wave velocity.
-



## Chapter 5

# Dynamic Fracture Mechanics

### Content

In this chapter, we will study the fracture propagation. When a fracture propagates and one material fails into two (or more) pieces (see Fig. 5.1), a huge strain energy liberation operates. The main question that arises is how this energy is transferred out of the material?

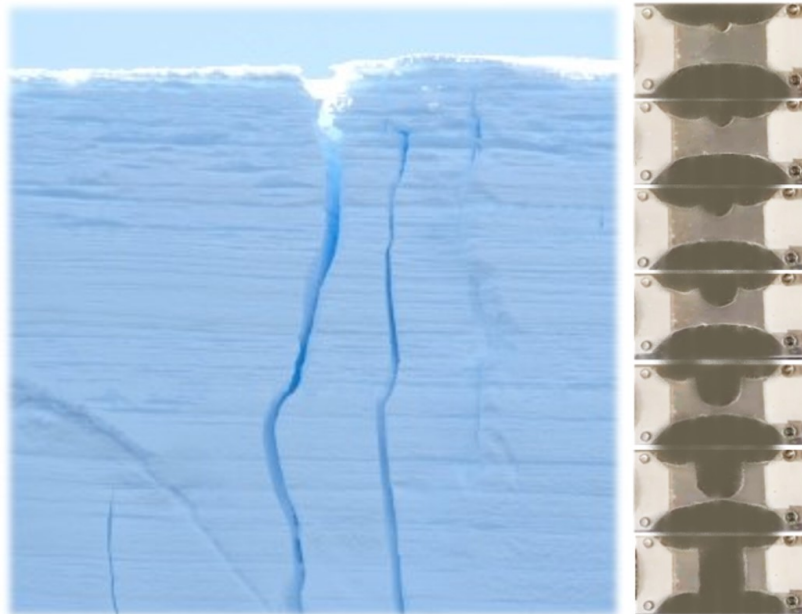


FIGURE 5.1: Left: Detail of an iceberg fracture, in Commonwealth Bay, east of Terre Adélie<sup>1</sup>. Right: Fracture propagation of a PDMA gel (SP0) at  $Q_0$ .

Through the use of ultrafast imaging, fracture propagation will be observed every millisecond through ultrasound images in different gels: elastic, viscoelastic and swollen. In this section, shear waves will not be created, but only ultrafast plane waves to capture the crack process. A fracture toughness,  $G_{IC}$  (value at which the crack propagates), will be calculated and the crack velocity extracted. Interesting physical phenomena will be recorded at the crack tip during the fracture propagation. Finally, double-network gels provided by Gong's group (Gong et al., 2003) will be tested in ultrafast imaging with the idea to detect the rupture events of the sacrificial network.

<sup>1</sup>[https://images.cnrs.fr/photo/20160071\\_0393](https://images.cnrs.fr/photo/20160071_0393)

## 5.1 Fracture propagation in SENT

### 5.1.1 Methodology

#### Ultrafast imaging

For this experiment, the single edge notched specimen will be used as illustrated in Fig. 4.2. The shear waves won't be created through the radiation force (see Fig. 5.2). Only the ultrafast scanner will be used to capture the fracture propagation events. The principle has been explained in part. 2.2.5. To record event during fracture propagation, the axial tissue velocity field  $U_z$  is estimated by calculating the correlation between two successive images. In the mean time, the mechanical testing tool will also record the time, force and displacement caused by this fracture propagation.

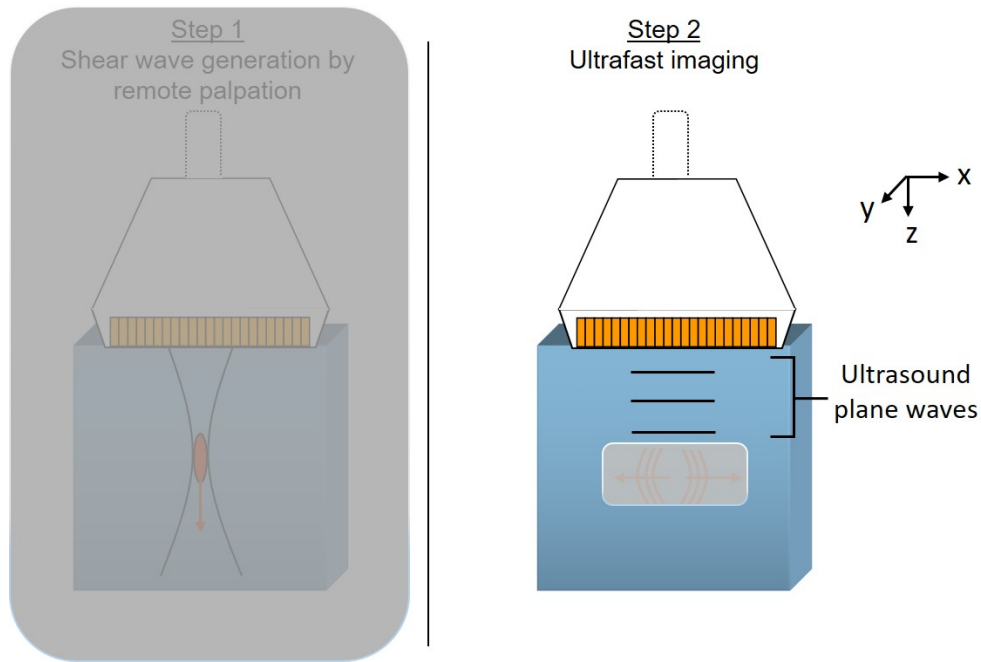


FIGURE 5.2: In fracture dynamics experiment, the radiation force is not used (left, step 1), thus the shear wave are not created (right, grey rectangle). Only ultrafast ultrasound plane waves (step 2) are sent and received to image the gel (from Bercoff, 2004).

The emission frequency of the ultrafast plane waves is typically about 6.4 MHz. An acquisition sequence has been created with plane waves at a framerate of 1000 frames/second and three different angles:  $[-2^\circ, 0^\circ, 2^\circ]$ . The sequence was repeated 10 times. Some of the experiments were conducted on a small prototype tensile setup without force measurements. In this case, another ultrasound probe was used: SLH 20-6 with a higher frequency band (6-20 MHz) and a better resolution of  $140 \mu\text{m}$ . For this configuration, the emission frequency of plane waves was changed to 11.25 MHz.

## 5.2 Physical parameters

### 5.2.1 Fracture toughness

The fracture toughness  $G_{IC}$  estimate is based on Greensmith equation (Eq. 5.1) dedicated to rubbery materials (see part 1.2.2). It depends on the length of the cut  $a$  and the stored-energy density  $W_c$  appropriate to the extension ratio  $\lambda_c$  until fracture:

$$G_{IC} = \frac{6aW_a}{\sqrt{\lambda_a}} \quad (5.1)$$

The fracture toughness of the three different gels SP0, SP2 and SP3.5 has been estimated from Eq. 5.1. The experiment was done on a un-notched sample ( $a = 0$ ) and a notched sample with the exact same width and  $L_0$  (length between the two clamps). A tensile test is performed at a strain rate of  $0.06 \text{ s}^{-1}$  until fracture (Fig. 5.3). Here, the stress is defined as the force measured during the test, normalized by the initial cross-section area of the un-notched part of the sample ( $\sigma_N = F/S_0$ ). As expected in Fig. 5.3, the curves between the notched and unnotched sample almost overlap. The notched sample will break before the intact sample since the fracture propagation will start sooner from the defect (notch). Some discrepancies in stiffness are observed (SP0) and can be explained by a slightly change in the geometry or in the tightening screws of the clamps.

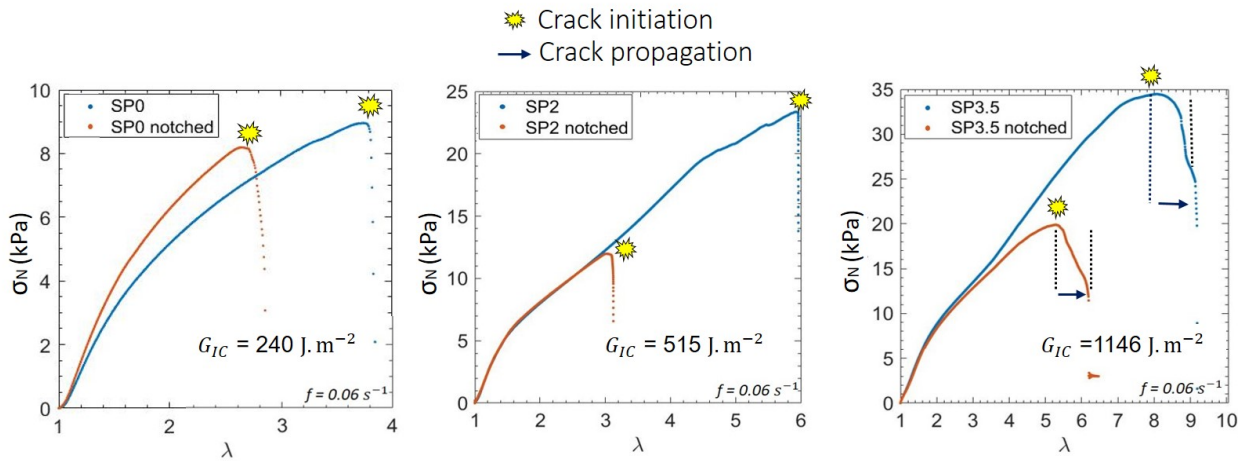


FIGURE 5.3: Stress/strain curves of tensile test until fracture of a un-notched and a notched SP0.1, SP2 and SP3.5 gel. Calculation of their fracture toughness. Geometry size is  $L_0 = 42$ ,  $W = 24$  cm,  $e = 10$  cm with a length notch  $a = 5$  cm. Thus,  $a/W = 0.21$ .

As explained through the lecture of this manuscript, the addition of NPs inside the gel matrix enhance the mechanical properties of the gel. When the amount of NPs increases, the fracture toughness increases as well. Note that the fracture toughness of SP3.5 is more than  $1 \text{ kJ.m}^{-2}$  which is the value for unfilled rubber (Lake et al., 1967). Also, it is visible on the stress-strain curve that the increase of NPs slows down the crack propagation. This quantitative analysis of the fracture experiments proves that NPs highly toughens the hydrogel. The silica nanoparticles interact efficiently with the PDMA matrix since the crack propagation is delayed. Previous colleagues showed that the level of energy release rates increases with higher strain rates (Le Gulluche, 2019). They also find the same results of an increased toughness with an increased amount of silica NPs (Rose, 2013, Le Gulluche, 2019) but different  $G_{IC}$  values due to the difference in the geometry (small size sample). The comparison is presented in Table 5.1.

$G_{IC}$ ( $J \cdot m^{-2}$ ) $a/W \sim 0.2$	Small size $\sim 5 \times 2 \times 20 \text{ mm}^3$	Big size ( $n = 1$ ) $\sim 25 \times 10 \times 23 \text{ mm}^3$
SP0	$10.2 \pm 1.2$	$240 \pm 4$
SP2	$130.2 \pm 6.0$	$515 \pm 13$
SP3.5	$249.1 \pm 3.5$	$1146 \pm 21$

TABLE 5.1: Comparison between small samples (Rose, 2013) and big samples for fracture toughness. Sample size being width  $\times$  thickness  $\times$  length between clamps ( $L_0$ ). The same crack depth ratio  $a/W = 0.2$  is used.

To verify if the difference in values was due to geometrical effects or changes in the synthesis, the tests were performed with the same geometry used by Rose (Rose, 2013). Two SP2 parallelepipedic samples of size  $W = 5 \text{ mm}$ ,  $e = 2 \text{ mm}$ , and  $L_0 = 15 \text{ mm}$  were tested. The results are presented in Fig. 5.4. The strain at failure for the small size sample is around  $\lambda \approx 7$  (un-notched sample) and  $\lambda \approx 4$  (notched sample) whereas for the big size sample, it is  $\lambda \approx 6$  and  $\lambda \approx 3$ , respectively. Concerning the stress, for the same strain, the stress is almost multiplied by two in the small samples. Nevertheless, from the two tests, a mean value of  $G_{IC} = 143 \text{ J/m}^2$  was found. A similar value was found in the work of previous colleagues ( $130 \text{ J/m}^2$ ) (Rose, 2013).

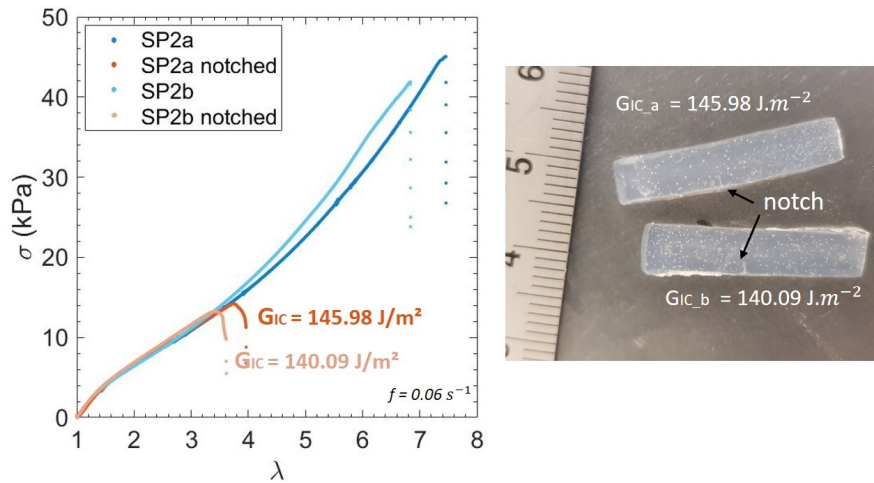


FIGURE 5.4: Left: Stress/strain curves of a tensile test until fracture of a un-notched and a notched SP2 sample. Right: Picture of the two notched SP2 small samples. Geometry size is  $W = 5 \text{ mm}$ ,  $e = 2 \text{ mm}$  and the length notch  $a = 1 \text{ mm}$ . Thus  $a/W = 0.2$ .

Again, geometry has an important impact on mechanics as observed in Part. 3.2.3.

### 5.2.2 Crack opening displacement (COD) and crack length ( $a$ )

Through ultrasound Bmode images, the fracture propagation is presented in Fig. 5.5 for a swollen elastic gel ( $Q_e$ ). The scale corresponding to the Bmode images is the brightness and is conventionally not illustrated. Fig. 5.6 presents the corresponding mechanical test. This gel is elastic and very brittle. Then, it is expected that this gel has a fast fracture propagation and a small fracture toughness.

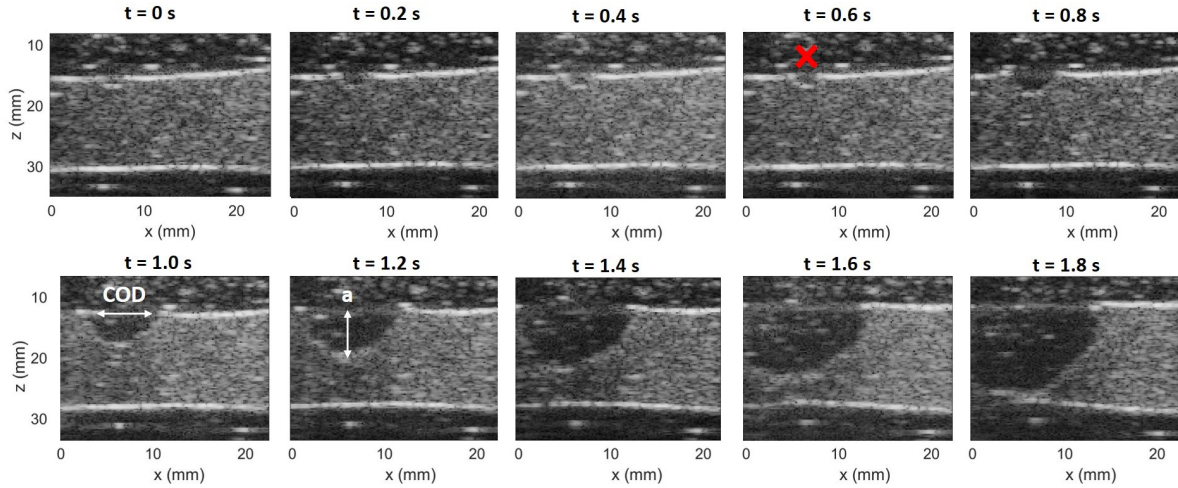


FIGURE 5.5: Screenshot of Bmode ultrasound images of a SP0 gel at  $Q_e$  taken every 0.2 s. The fracture starts around 0.6 s and ends right after  $t = 1.8$  s. The red cross indicates the initiation of the crack propagation. Geometry size is  $L_0 = 15$  mm,  $W = 18$  mm,  $e = 5$  mm, with a length notch  $a = 2$  mm. Thus  $a/W = 0.1$ . Video following this link: <https://mycore.core-cloud.net/index.php/s/WkqJl4GCvZP4EYB>

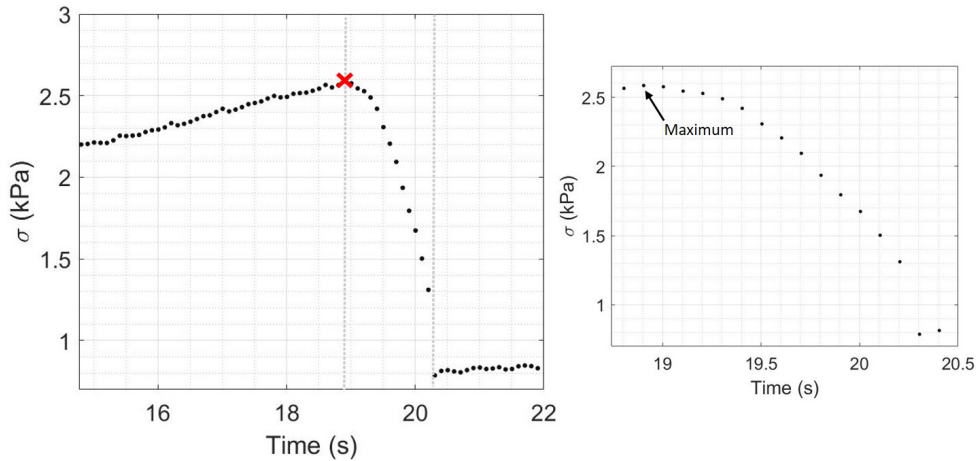


FIGURE 5.6: Nominal stress vs time curve from the load cell during a tensile test until fracture at 0.06 Hz on a swollen elastic gel  $Q_e$  corresponding to Fig. 5.5. The fracture propagation lasts 1.3 s. It starts at the maximum stress corresponding to  $t = 18.9$  s, and ends at  $t = 20.2$  s. The red cross indicates the initiation of the crack propagation.

The times of both techniques do not correspond since the imaging tool considers  $t = 0$  as the beginning of the imaging sequence acquisition (operator dependent and right before the crack propagation) while the mechanical testing machine considers  $t = 0$  as the beginning of the tensile test.

After calculation based on the stress/strain curve of Fig. 5.6 and Eq. 5.1, the fracture toughness of SP0 gel at  $Q_e$  is  $19.0 \text{ J.m}^{-2}$ . This value is really low compared to its analogue SP0 at preparation state ( $Q_0$ ),  $240.4 \text{ J.m}^{-2}$ . This confirms that swelling an elastic gel enhances its brittleness by reducing viscoelastic losses.

From the load cell data (see Fig. 5.6) and image analysis (Fig. 5.5), it is possible to deduce the duration of the crack propagation: about 1.3 seconds. In the stress/time curve, the crack propagation starts right after the maximum stress (red cross) and finishes when the stress is stabilized to the weight of the half part of the sample.

From Fig. 5.5, it is possible to extract the COD and the length of the crack " $a$ " during a crack propagation at different time (see Fig. 5.7). Thus, it is also possible to estimate a crack propagation velocity from the slope  $a/t$ . The crack length  $a$  increases linearly with time. The crack propagation velocity is around  $11.6 \text{ mm.s}^{-1}$ . On the contrary, the COD does not seem to evolve linearly but more with a trend of the square root of  $t$ .

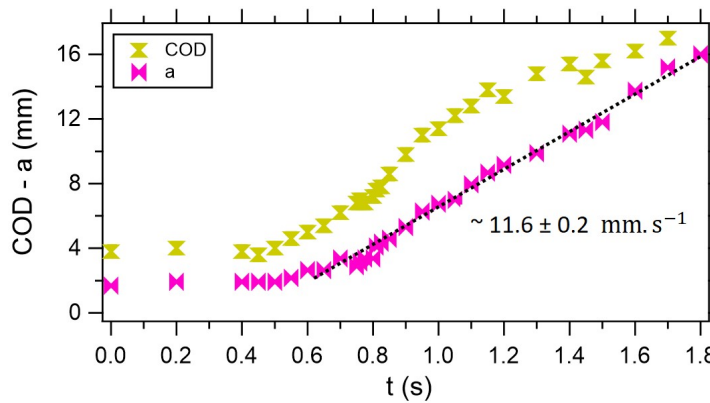


FIGURE 5.7: COD and crack length  $a$  as a function of time corresponding to Fig. 5.5 for SP0 at  $Q_e$ .

It is also possible to plot the evolution of the COD versus  $a$ . LEFM theory predicts that the COD increases with the square root of  $a$ :  $COD \approx a^{1/2}$ . This trend (LEFM fit) was plotted in Fig. 5.8 and matches quite well with the experimental data. It has been found by Long (Long et al., 2016) that for small applied displacements (i.e. slow crack propagation), the COD is asymptotically consistent with the LEFM prediction whereas LEFM breaks down for fast crack propagation (comparison done between  $v = 3 \mu\text{m.s}^{-1}$  and  $v = 10 \text{ mm.s}^{-1}$ ). This is due to the effect of nonlinear elasticity and viscoelasticity which is confined to a region very close to the crack tip in slow crack propagation and not detected by the measurements. Nevertheless, in this case, the velocity is considered fast, being around  $v = 10 \text{ mm.s}^{-1}$ , and LEFM seems consistent with the results.

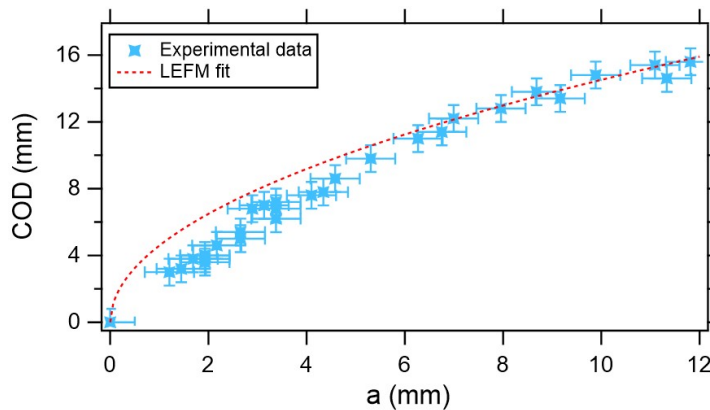


FIGURE 5.8: Evolution of the COD according to  $a$  corresponding to Fig. 5.5 for SP0 at  $Q_e$ . LEFM fit is plotted as a guideline. The crack propagation velocity was found to be around  $11.6 \text{ mm.s}^{-1}$ .

### 5.3 Crack tip during fracture propagation: Source of shear wave

The ultrafast ultrasound scanner allows to record the crack propagation and visualize it in slow motion. During a typical test, 10 000 frames are recorded at a framerate of 1 000 images/second, meaning that the test duration is 10 seconds. In other words, a screenshot is taken every millisecond during the crack propagation.

#### 5.3.1 Brittle fracture of swollen elastic gel (at maximum swelling degree)

During the fracture propagation of the elastic swollen gel (see Fig. 5.5), it is possible to extract the profile in depth ( $z$ ) and in the probe width ( $x$ ) according to the time (see Fig. 5.9). The displacement map  $x$ - $t$  is averaged over the values of  $z$  while the displacement map  $z$ - $t$  is averaged over the values of  $x$ . An US probe is illustrated schematically (not to scale).

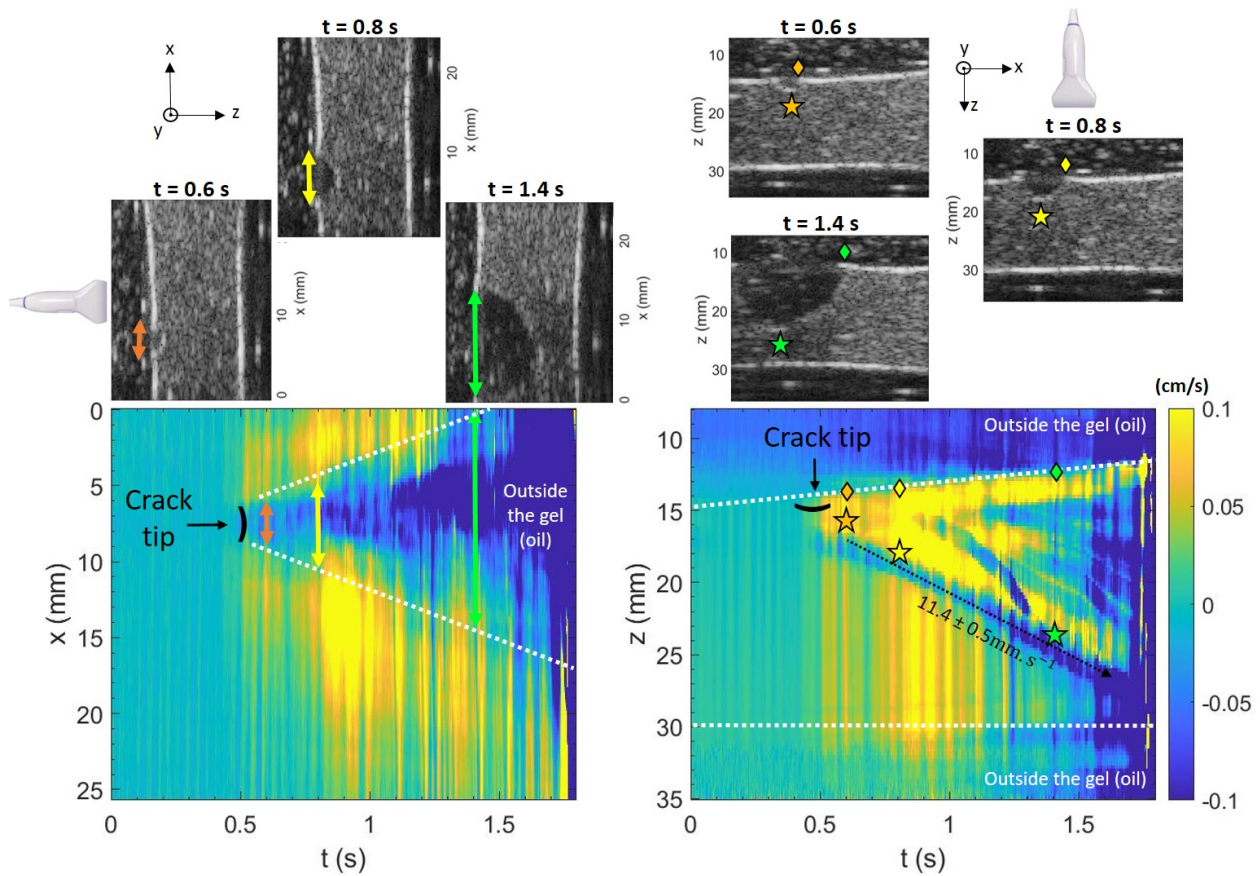


FIGURE 5.9: Profile of the crack propagation for SP0 at  $Q_e$ . Left:  $x$ - $t$  profile; Right:  $z$ - $t$  profile. The scale of the displacement maps informs on the velocity of the displacements that occur inside the material.

The depth acquisition was delimited from  $z = 8$  to  $z = 35$  mm since only oil was present from  $z = 0$  to  $z = 8$  mm. The profile in  $z$  is easy to follow and to understand: the fracture starts around  $z = 15$  and ends around  $z = 25$  mm. The  $z$ - $t$  displacement map also clearly shows the beginning of the fracture propagation. Indeed, from  $t = 0.5$  s, the crack tip, located at  $z = 15$  mm, starts to move at a velocity of  $0.1 \text{ cm.s}^{-1}$  but it only starts to propagate in the  $z$  direction only from  $t = 0.6$  seconds. From  $t = 0.5$  s to  $t = 0.6$  s, the crack tip oscillates around  $z = 15$  mm. The  $z$ - $t$  map allows to extract the crack velocity and the same value of about  $11 \text{ mm.s}^{-1}$  was found (as Fig. 5.7).

Concerning the  $x$  profile, it allows to visualize the opening of the crack (COD) but also a lot of displacements on each side of the crack tip (inside the gel).

The scale of the displacement map ranging from  $[-0.1 \ 0.1]$  ( $\text{cm.s}^{-1}$ ) describes the velocity and the direction of the displacement: a positive value in the  $z$ - $t$  profile means that the displacement is oriented towards the direction of the probe while a negative value informs on a displacement that goes in the opposite way.

If a zoom is made in the  $x$ - $t$  profile during the crack propagation, for example around 0.6 seconds, it is possible to detect a slope and extract a velocity of a fast displacement in the  $x$  direction (see Fig. 5.10). The displacement is generated from the crack tip and is visualized into the all gel width. By looking into the Bmodes images, a simple screenshot of what happens inside the gel, nothing is detectable. On the contrary, taking the displacement map  $x$ - $z$  allows to see the displacements that occur inside the gel.

It appears that all these displacements detected from the crack tip and propagating correspond to shear waves generation. In Fig. 5.10, the local displacement generated by the shear wave has a velocity of about  $0.2 \text{ cm.s}^{-1}$  whereas the shear wave velocity is about  $1.2 \text{ m.s}^{-1}$ , consistent with the stiffness of the material. It is important not to confuse the shear wave velocity with the local velocity of the micrometric displacement induced by the shear wave.

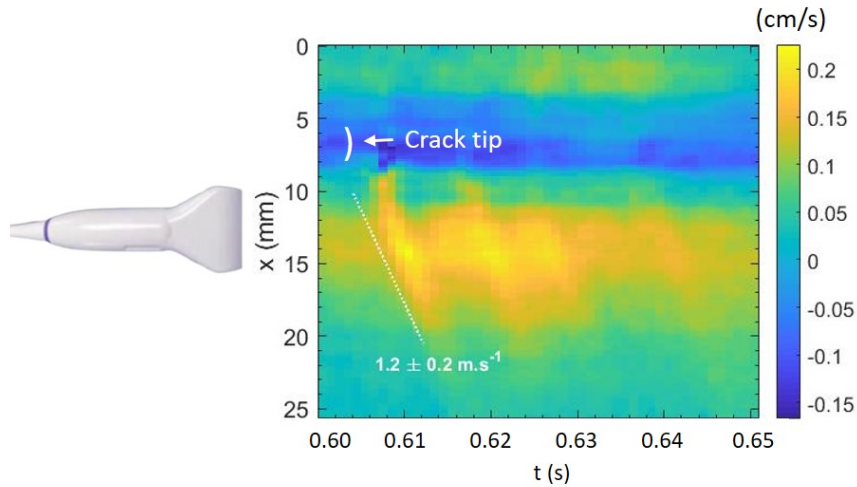


FIGURE 5.10: Zoom of the  $x$ - $t$  profile of SP0  $Q_e$  gel around 0.6 seconds. Estimation of the shear wave velocity created from the crack tip. This velocity is in good concordance with the material stiffness.

If no displacement occurs inside the gel, the displacement map shows no change between one image and the following (Fig. 5.11). A white arrow indicates the crack tip. It is moving (indicated in white in the displacement map) since the fracture is propagating. No other movement is visualised inside the gel.

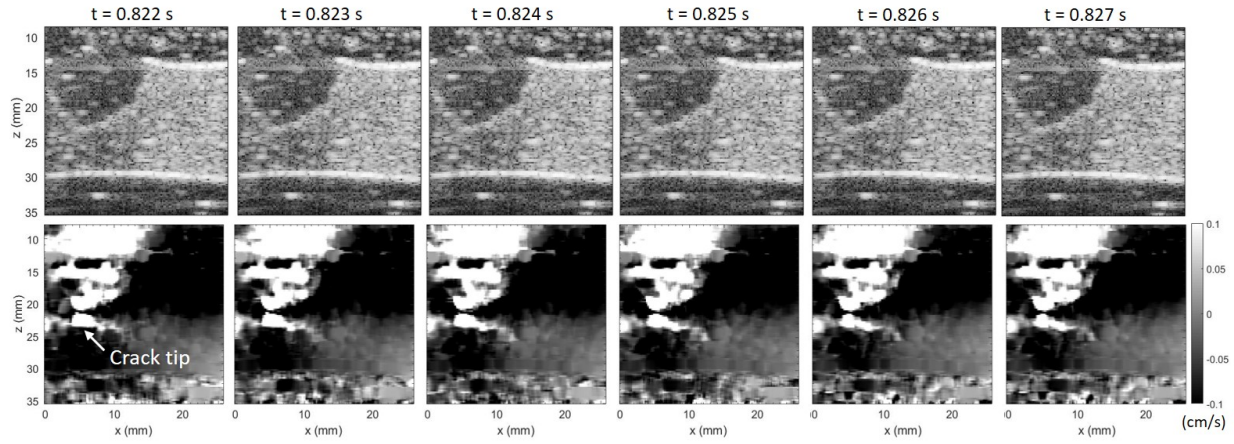


FIGURE 5.11: Top: Bmode image of SP0 at  $Q_e$ . No evolution is seen during 5 ms. Bottom: Displacement map (difference in the phase signal between one image and the following). Nothing happens inside the gel except at the crack tip which is in movement, since propagating. Video following this link: <https://mycore.core-cloud.net/index.php/s/g31BU8Adv0kGAiv>

Fig. 5.12 shows an example of a shear wave created at 0.839 seconds. To visualised this shear wave propagating through the material, the Bmode images are shown during 5 milliseconds (Fig. 5.12, top) as well as the displacement map corresponding (Fig. 5.12, bottom). To recall, the displacement map is the difference in the phase signal between the image  $n$  and the image  $n+1$ . It allows to see the changes between one image and the following, thus detect movements. The Bmode images only represent a screenshot of the gel at that time  $t$  and it is impossible to detect changes by eyes. Nevertheless, changes occur since the displacement map (Fig. 5.12, bottom) clearly shows a shear wave propagating from the crack tip to the end of the gel width (indicated by a black arrow).

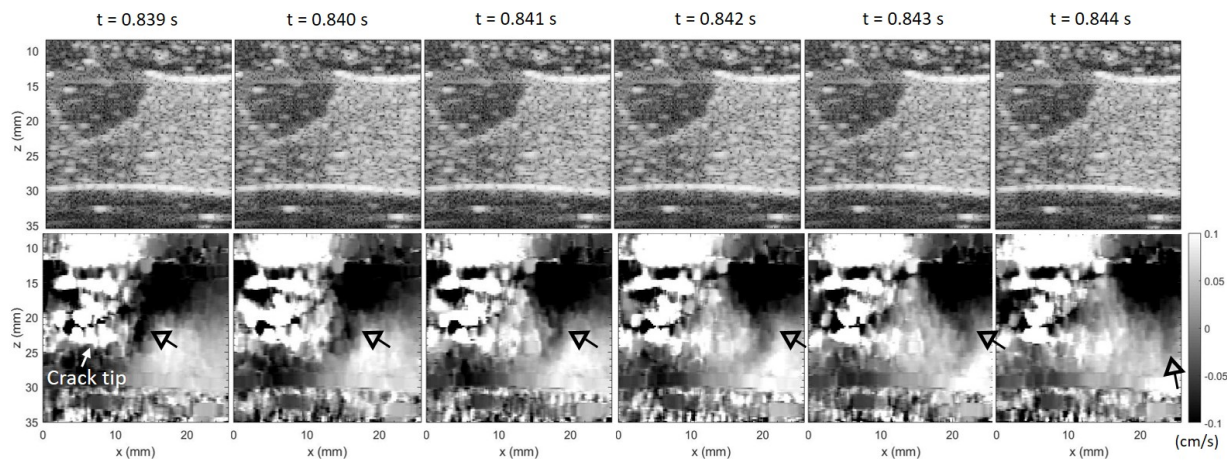


FIGURE 5.12: Top: Bmode image of SP0 at  $Q_e$ . Bottom: Displacement map. Visualisation of a shear wave created at the crack tip source and propagating through the right direction (from  $x \approx 10$  to  $x \approx 25$ ). Black arrows help the reader to follow the shear wave propagation inside the gel. Video following this link: <https://mycore.core-cloud.net/index.php/s/g31BU8Adv0kGAiv>

By comparing Fig. 5.11 and Fig. 5.12, it is clear that shear wave events occur inside the gel in a short amount of time (for example from  $t = 0.839$  to  $t = 0.844$  s) and not every time (example given

from  $t = 0.830$  to  $t = 0.835$  s). A shear wave, created at the crack tip, can be seen propagating to the right direction. Due to the framerate of 1000 images/seconds, the shear wave can only be caught in 5 ms (from  $t = 0.839$  to  $t = 0.844$  s). This is enough to extract the shear wave velocity. The shear wave was created at the crack tip ( $x \approx 10$  mm) and transferred out of the gel ( $x \approx 25$  mm) (Fig. 5.13).

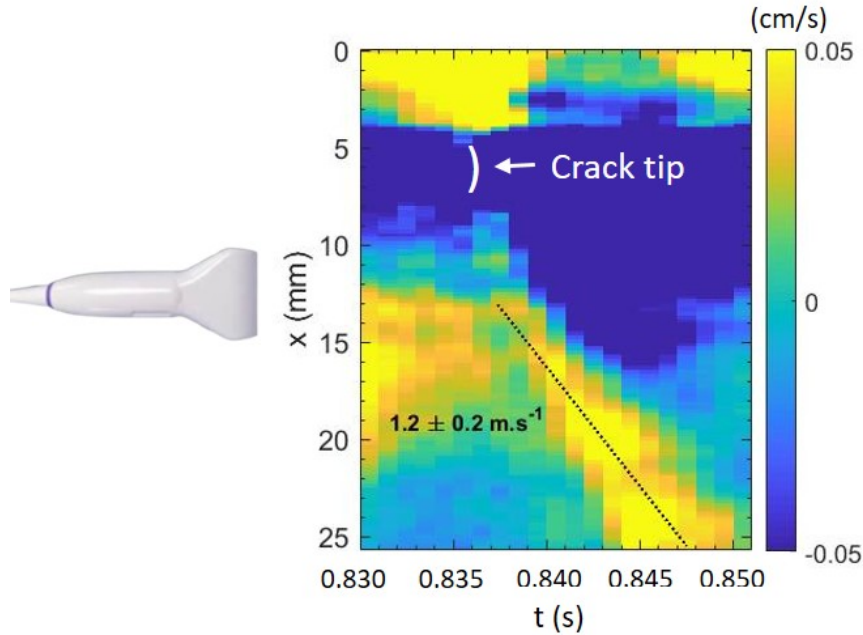


FIGURE 5.13: Calculation of the shear wave velocity corresponding to the event at 1840 ms in the SP0  $Q_e$  gel. A velocity of about  $1.2 \text{ m.s}^{-1}$  is found. This shear wave creates displacement into the gel with a corresponding velocity of  $0.05 \text{ cm.s}^{-1}$ .

Again, searching in the  $x$ - $t$  profile the time wanted (around 0.830 and 0.850 s), it is possible to extract the shear wave velocity:  $1.2 \pm 0.2 \text{ m.s}^{-1}$ .

Since the swollen elastic gel is the most elastic material in this study, this is the one with the bigger number of shear waves created during a crack propagation (see video following this link: <https://mycore.core-cloud.net/index.php/s/6G9H9sc8M0zG9mX>). Indeed, there is no energy dissipation, thus the gel breaks suddenly without any viscoelastic stress relaxation. The gel breaks when the energy inside the material reached  $19.04 \text{ J.m}^{-2}$  and the fracture propagates at a velocity of about  $11 \text{ mm.s}^{-1}$ .

The next experiments presented for elastic and viscoelastic gels at preparation state  $Q_0$  won't be linked to the mechanical testing machine. These tests were performed on the prototype setup with the SLH 20-6 probe.

### 5.3.2 Fracture of elastic gels

For this experiment, the crack propagation was progressing toward the ultrasound probe as it can be seen in Fig. 5.14. The fracture starts at  $t = 0.8$  seconds and ends at  $t = 3$  seconds. For the SP0 at  $Q_0$ , fracture propagation lasts 2.2 seconds. Due to the width of the probe (smaller for SLH 20-6), it was not possible to get the COD during the all experiment. The imaged width is 18 mm with SLH 20-6 while it is  $x = 25$  mm with SL 10-2. Thus, from  $t = 1.2$  s, the COD can not be extracted. This is also due to the gel that blunts at the crack tip caused by strong non linear effects that seem to be reduced in SP0 gel at  $Q_e$ .

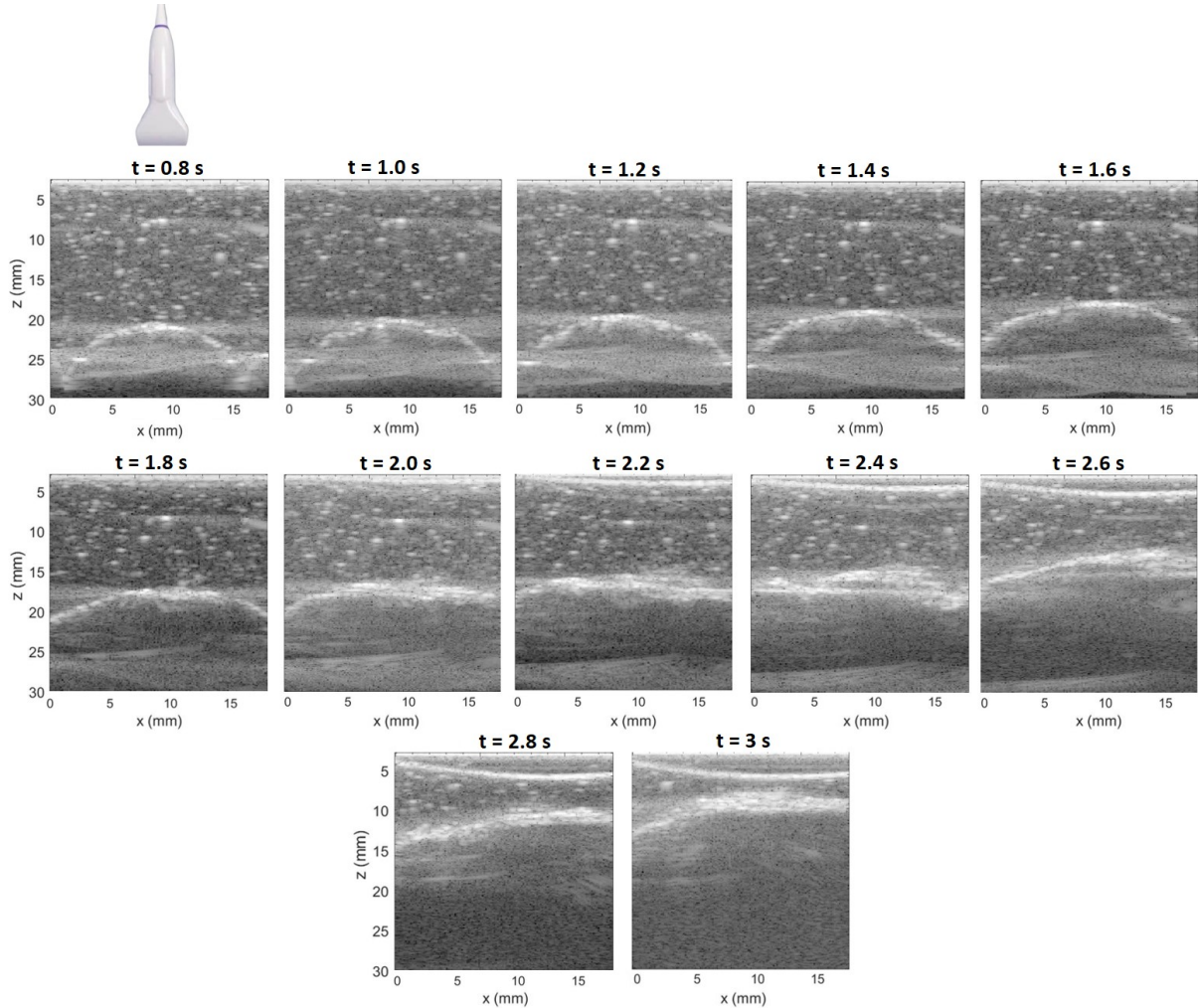


FIGURE 5.14: Screenshot of Bmode ultrasound images of an SP0 gel at  $Q_0$  taken every 0.2 s. The fracture starts at 0.8 s and lasts for 2.2 seconds and it propagates toward the probe. Geometry size is  $L_0 = 42$  mm,  $W = 20$  mm,  $e = 10$  mm,  $a = 5$  mm. Thus,  $a/W = 0.25$ . Video following this link: <https://mycore.core-cloud.net/index.php/s/5T51NanIu24cW2c>

The crack propagation profile in time is shown according to  $x$  and  $z$  in Fig. 5.15. The  $x$ - $t$  profile is less clear than SP0 at  $Q_e$  due to a lack of speckle. Indeed, this experiment corresponds to the first preliminary tests and at this time, agar was not present inside the gel, making it more difficult to detect movements that arise inside the gel.

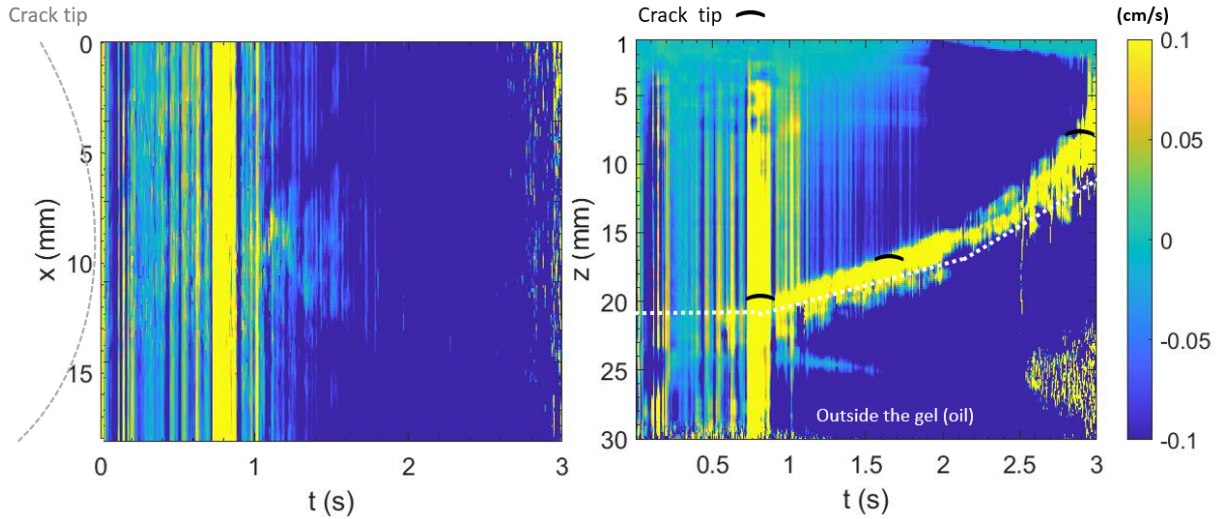


FIGURE 5.15: Profile of the crack propagation for SP0 at  $Q_0$ . Left: x-t profile; Right: z-t profile. The scale informs on the displacements that occur inside the material. The yellow band before  $t = 1$  second is due to an operator displacement to open more the gel since the fracture had not started at  $t = 0$ .

Due to the material stiffness that is higher for SP0 at  $Q_0$  ( $E \approx 10.5$  kPa) than SP0 at  $Q_e$  ( $E \approx 5.4$  kPa), and to the difference of speckle between these two gels, it is more difficult to catch the shear waves created in SP0 at  $Q_0$ . Nevertheless, lots of shear waves are created at the crack tip. An example is shown Fig. 5.16 with the displacement maps. The corresponding Bmode images are not shown since it has been understood that the small displacements created by the shear waves can not be visualized by eyes. Also, the Bmode images corresponding to each displacement map are the same in the small range of time observed (some milliseconds) (see Fig. 5.12). To have the Bmode image corresponding to Fig. 5.16, one can refer to Fig. 5.15 at 1.8 seconds.

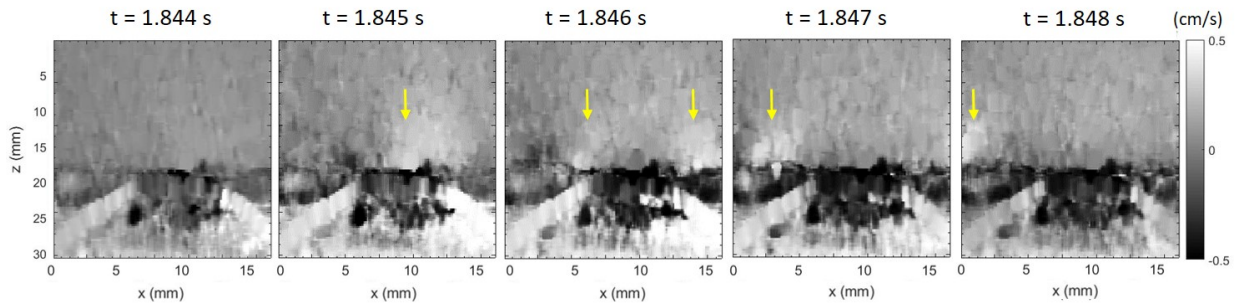


FIGURE 5.16: Displacement map for SP0 gel at  $Q_0$ . Visualisation of two shear wave fronts created at the crack tip source and propagating in both direction. Yellow arrows help the reader to follow the shear wave propagation inside the gel. Video following this link: <https://mycore.core-cloud.net/index.php/s/GlkboYUPr0Q4KOW>

The SW propagates in 4 ms. It is possible to extract a shear wave velocity through a zoom of the x-t profile between  $t = 1.844$  s and  $t = 1850$  s (Fig. 5.17). The velocity is found to be around  $2.5 \text{ m.s}^{-1}$ , in agreement with the stiffness of material.

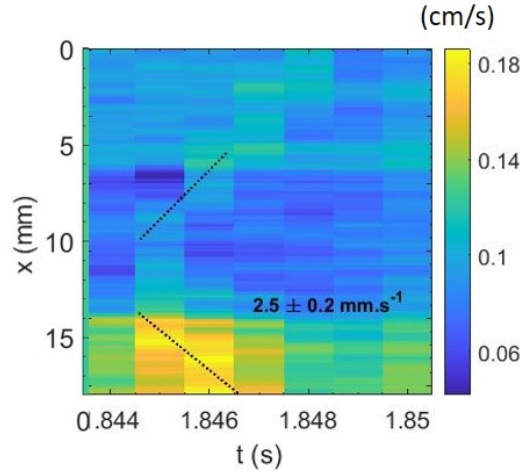


FIGURE 5.17: Shear wave speed corresponding to an event happening at 1840 ms in the SP0 gel at  $Q_0$ . A velocity of about  $2.5 \text{ m.s}^{-1}$  is found.

### 5.3.3 Fracture propagation of viscoelastic gels

#### First case of viscoelastic gel SP1

A first try of fracture propagation with viscoelastic gels was done with a gel with 5 vol.% of  $\text{SiO}_2$  (SP1), gel comprises between the SP0 and SP2. The acquisition has recorded 10 seconds of fracture propagation. The fracture lasts for more than 10 seconds but the acquisition was limited to only 10 seconds. At  $t = 0 \text{ s}$ , the propagation has already started and the blunting is clearly visible. The first second is shown through Bmode images in Fig. 5.18 followed by the last 9 seconds in Fig. 5.19.

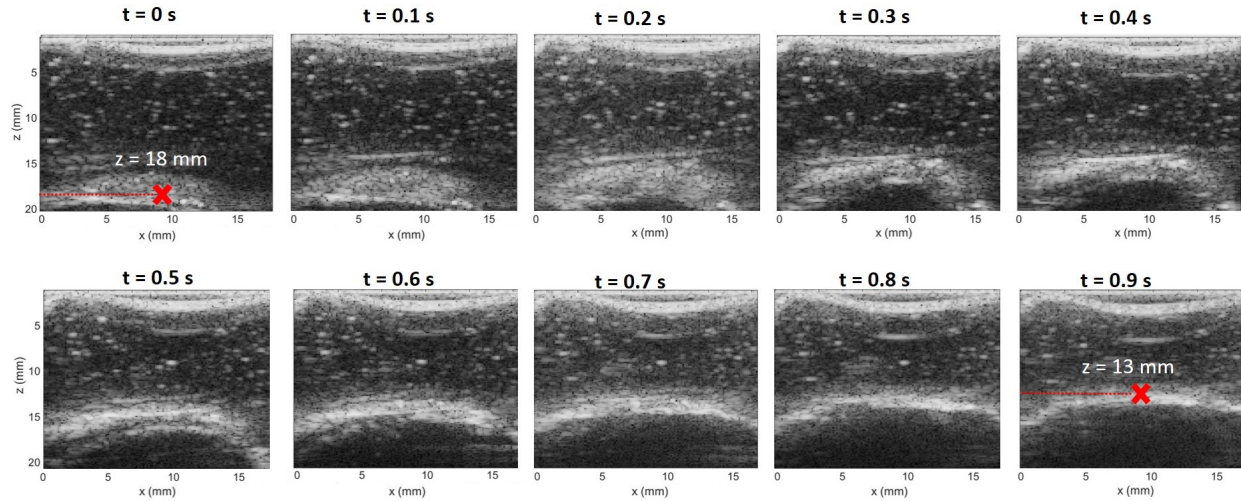


FIGURE 5.18: Screenshot of Bmode ultrasound images of SP1 (5 vol.% of  $\text{SiO}_2$ ) gel at  $Q_0$  taken every 0.1 second. The first second of fracture propagation is shown here. The red cross is placed approximately at the location of the crack tip. The crack tip evolves from  $z \approx 18 \text{ mm}$  to  $z \approx 13 \text{ mm}$ . Geometry size is  $L_0 = 45 \text{ mm}$ ,  $W = 20 \text{ mm}$ ,  $e = 11 \text{ mm}$ ,  $a = 5 \text{ mm}$ . Thus,  $a/W = 0.20$ . Video following this link: <https://mycore.core-cloud.net/index.php/s/vA1qyb0QSOMUqNf>

During the first second, the crack tip evolves approximately from  $z \approx 18$  mm to  $z \approx 13$  mm having a velocity of about  $6 \text{ mm.s}^{-1}$ . From 1 to 10 seconds, the crack evolves differently, it slows down and stabilizes. The crack tip moved from  $z = 13$  mm to  $z = 9$  mm approximately for 9 seconds with a velocity of about  $0.4 \text{ mm.s}^{-1}$ . The crack tip is difficult to determine exactly due to the strong blunting effect.

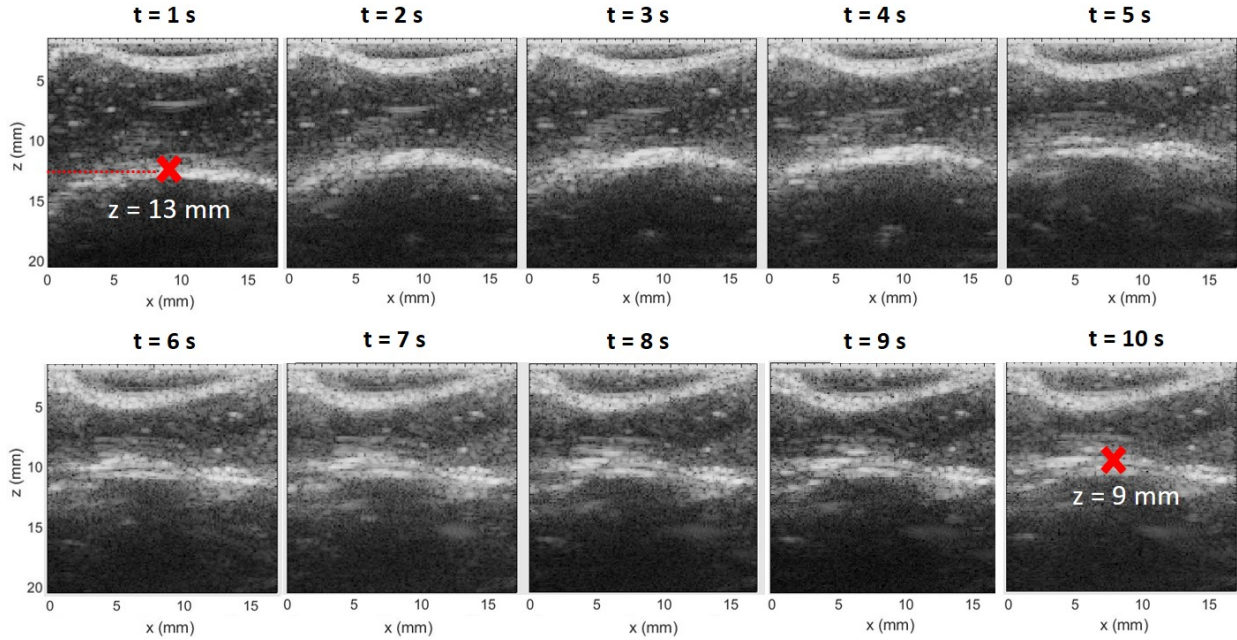


FIGURE 5.19: Screenshot of Bmode ultrasound images of SP1 (5 vol.% of  $\text{SiO}_2$ ) gel at  $Q_0$  taken every second. The red cross is placed approximately at the location of the crack tip. In 9 seconds, the crack tip evolves from  $z \approx 13$  mm to  $z \approx 9$  mm. Video following this link: <https://mycore.core-cloud.net/index.php/s/vA1qybOQSOMUqNf>

The displacement maps corresponding to Fig. 5.18 and Fig. 5.19 are shown Fig. 5.20.

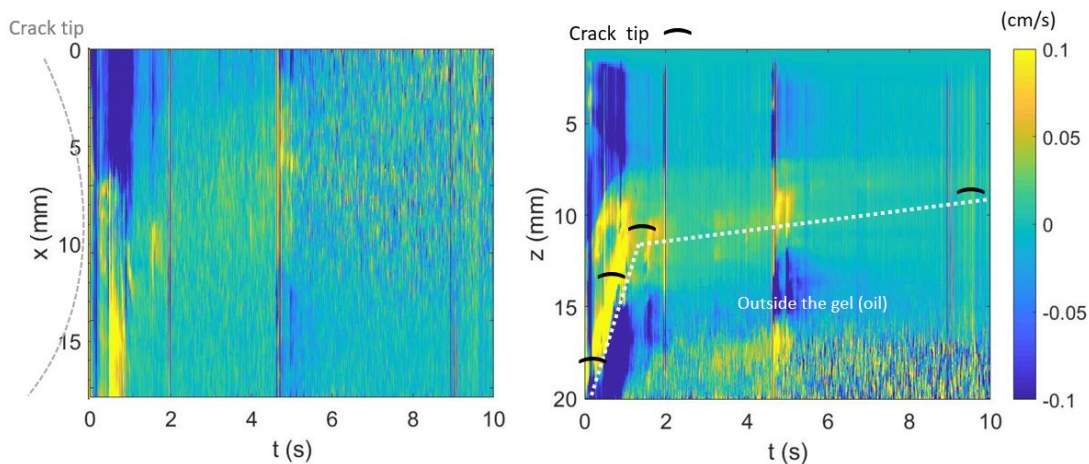


FIGURE 5.20: Profile of the crack propagation for SP1 at  $Q_0$ . Left:  $x$ - $t$  profile; Right:  $z$ - $t$  profile. The scale informs on the displacements that occur inside the material.

It is interesting to notice in the  $z$ - $t$  profile map another trajectory ahead of the one of the crack tip (starting at approximately  $z = 12$  mm). It looks like there is a displacement evolving at the

same velocity than the crack tip, inside the gel, until it merges with it (around  $z = 9$  mm) at approximately  $t = 1$  second.

Again, a lot of events occur during the crack propagation and it is possible to visualize shear waves created at the crack tip (Fig. 5.21. Right after the creation of a shear wave at  $t = 473$  ms, another one follows at  $t = 490$  ms.

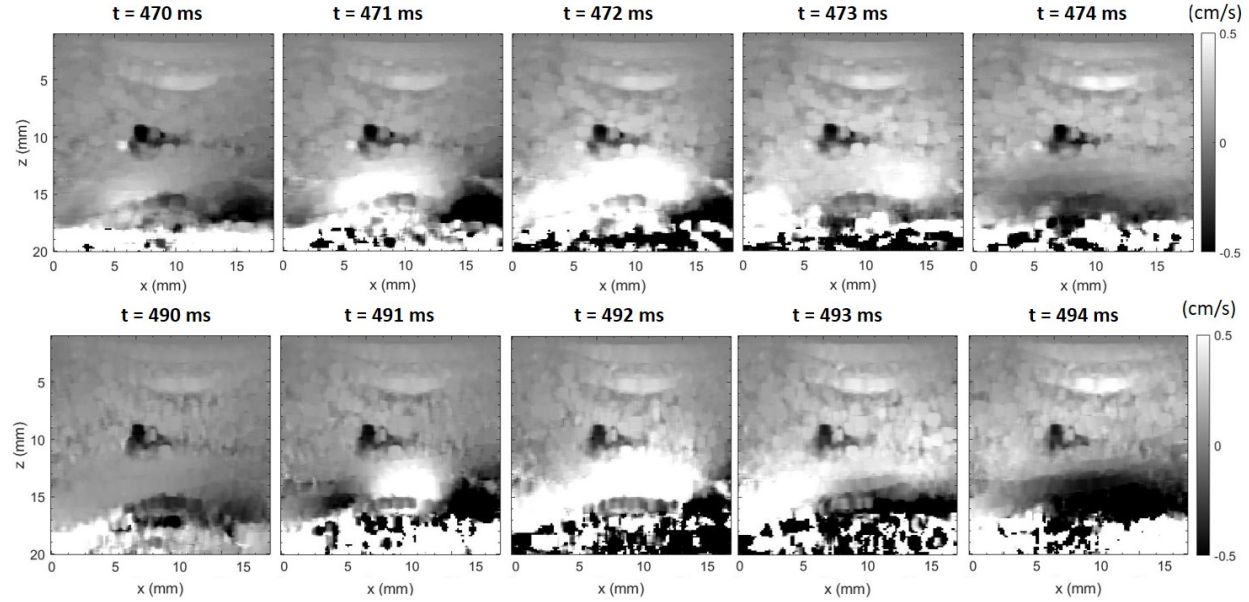


FIGURE 5.21: Top: Displacement map of SP1 at  $Q_0$  between  $t = 471$  and  $t = 475$  ms. Shear wave created at the crack tip at  $t = 473$  ms and propagating for 2 ms. Bottom: Displacement map of SP1 at  $Q_0$  between  $t = 490$  and  $t = 494$  ms. Shear wave created at the crack tip at  $t = 491$  ms and propagating for 3 ms in a SP1 gel. Video following this link: <https://mycore.core-cloud.net/index.php/s/SH6MrBOZZKCHWmc>

In Fig. 5.21, the shear waves are only visible in two or three images, thus it propagates in 2 - 3 ms. Their velocity, estimated in Fig. 5.22, is equal to about  $3.3 \text{ m.s}^{-1}$ . Both shear waves propagate at the same velocity and the same displacement is created from their propagation ( $\sim 0.5 \text{ cm.s}^{-1}$ ).

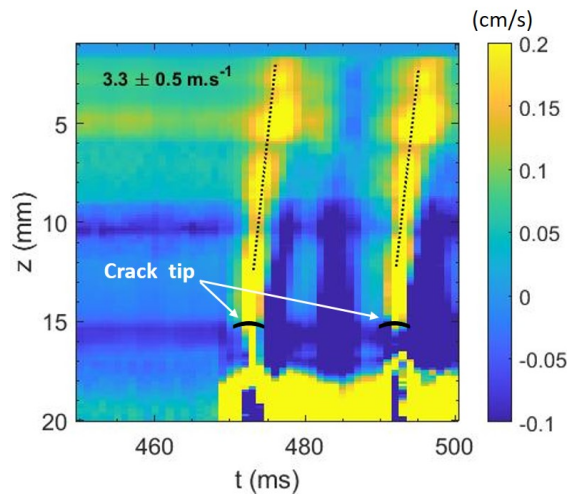


FIGURE 5.22: Calculation of shear wave velocity created around 473 ms and 492 ms in SP1 gel. Their velocity is the same.

The stiffer the material, the faster the shear wave. Indeed if we compare the gels, it becomes more and more difficult to see the displacements inside the gel since its stiffness increases.

### Second case of viscoelastic gel with a higher amount of NPs

Another viscoelastic gel, SP2, has been studied for fracture propagation. The Bmode images are shown from  $t = 6$  seconds since the fracture starts at this moment. Fracture ends at  $t = 9.4$  seconds.

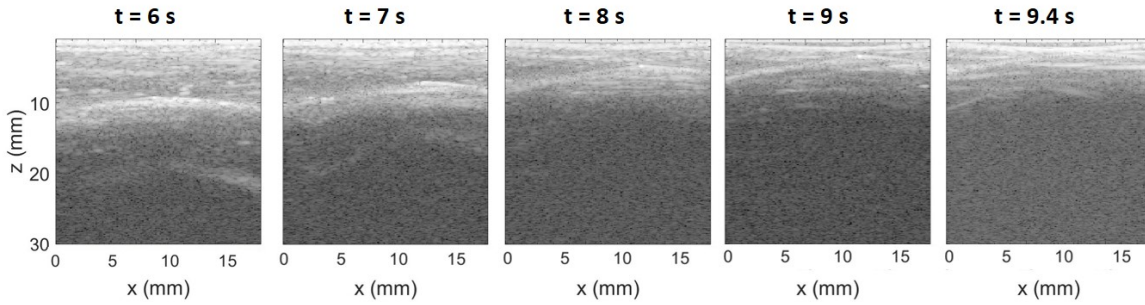


FIGURE 5.23: Screenshot of Bmode ultrasound images of a SP2 gel at  $Q_0$  taken every second. The fracture lasts 3.4 seconds. Here the fracture was recorded until the total breaking of the gel. Geometry size is  $L_0 = 40$  mm,  $W = 25$  mm,  $e = 10$  mm,  $a = 5$  mm. Thus,  $a/W = 0.2$ . Video following this link: <https://mycore.core-cloud.net/index.php/s/btnN520tqHQyW0i>

The profile of the crack propagation according to  $x$  and  $z$  is visible in Fig. 5.24. As shown with SP1 gel, the fracture velocity tends to decelerate at some points. This result will be discussed in next part (part 5.4).

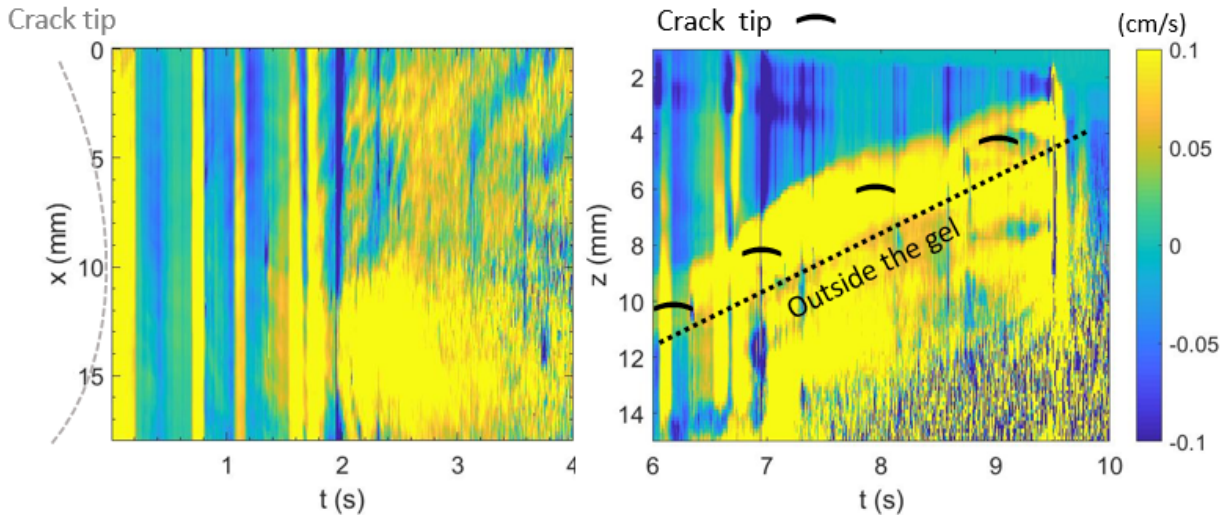


FIGURE 5.24: Profile of the crack propagation for SP2 at  $Q_0$ . Left:  $x$ - $t$  profile; Right:  $z$ - $t$  profile. Zoom between  $z = 1$  to  $z = 15$  mm. From  $z = 15$  to  $z = 30$  mm, only noise is present due to the oil. The scale informs on the displacements that occur inside the material.

Again, the crack tip is a source of shear waves. One event is shown around  $t = 6.9$  seconds in Fig. 5.25. It is interesting to notice that the shear wave is less visible in this viscoelastic gels.

Indeed, it is stiffer than SP1, thus it is complicated to see the shear wave propagation due to its high velocity. In fact, the source is well visible at  $t = 6.942$  s but the shear wave created is almost invisible.

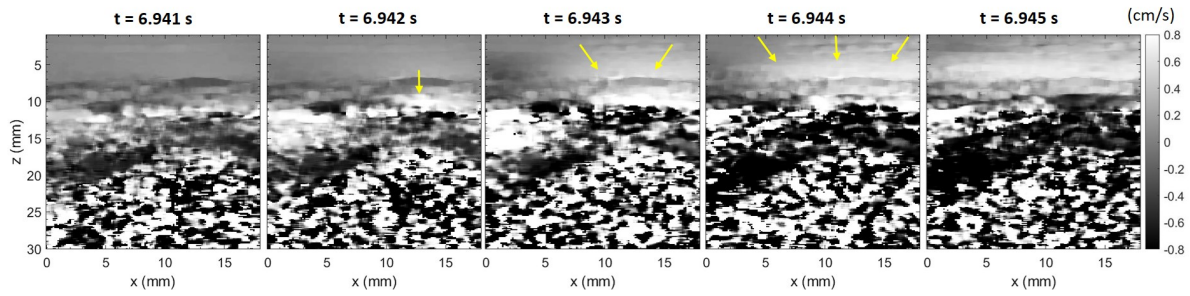


FIGURE 5.25: Displacement map of SP2 gel. Shear wave created at the crack tip. The yellow arrows indicate the location of the shear wave source. From  $z = 10$  to  $z = 30$  mm, ultrasound propagated in oil. Video following this link: <https://mycore.core-cloud.net/index.php/s/o8EKskRruc6vHqF>

The shear wave speed corresponding to Fig. 5.25 is estimated in the  $z$ - $t$  profile of Fig. 5.26.

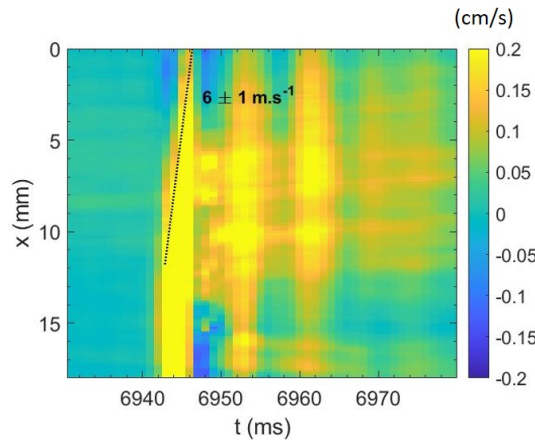


FIGURE 5.26: Calculation of the shear wave speed created at the crack tip of a SP2 gel around  $t = 6.9$  s.

The shear wave created at the crack tip during a fracture propagation in SP2 gel is really fast. It propagates at about  $6 \text{ m.s}^{-1}$ .

## 5.4 Crack propagation analysis

### 5.4.1 Effect of NPs on crack propagation velocity

In this section, the crack profile of SP0 and SP2 gel at preparation state  $Q_0$  (Fig. 5.27), already presented in the previous part, is discussed here. As a reminder, these experiments were not linked to the mechanical testing machine. Manually, the gel were stretched until the beginning of the crack propagation and the crack were spontaneously evolving at fixed length.

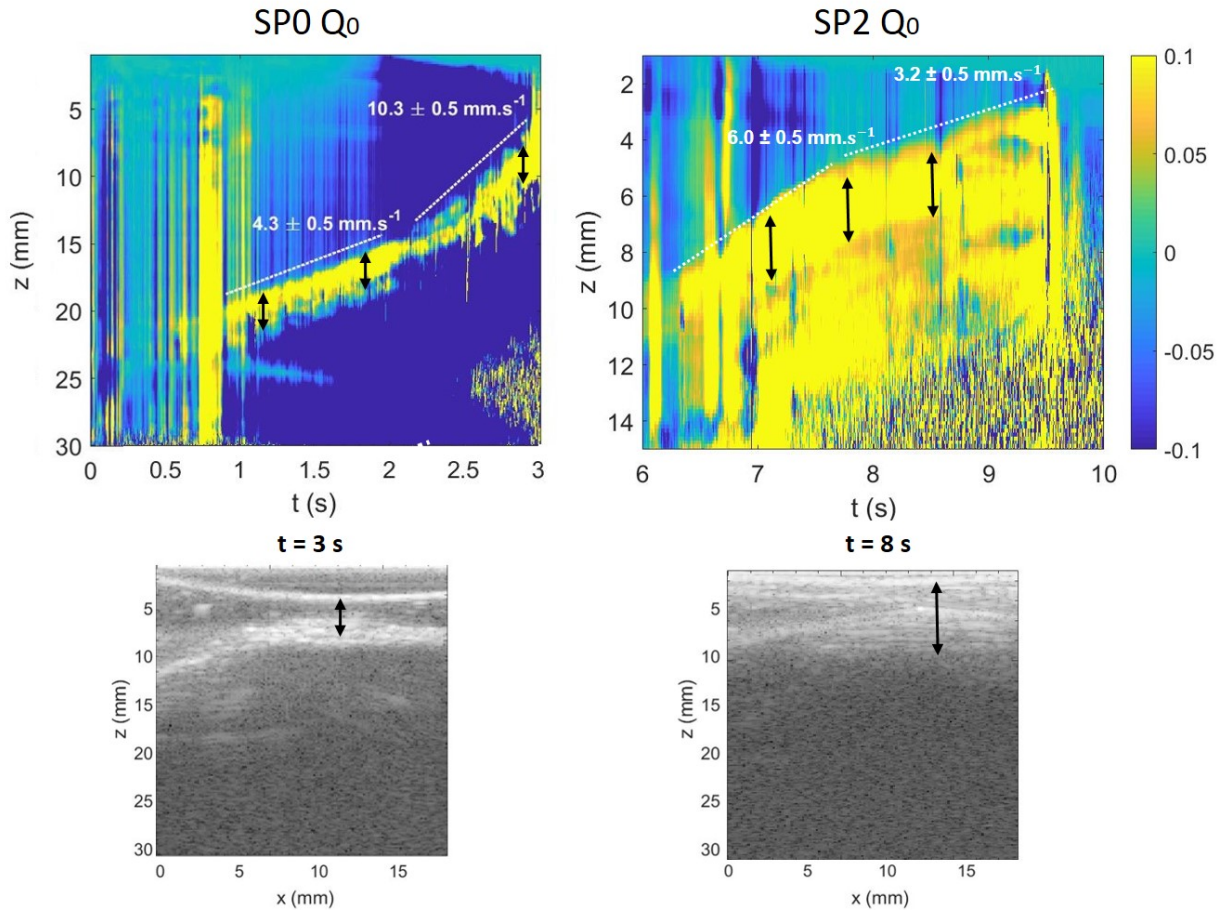


FIGURE 5.27: Top: Displacement maps of SP0 and SP2 gel at  $Q_0$  during a free crack propagation, i.e no forces are involved during the crack propagation. The displacement was maintained fixed. The black arrows show the thickness of the crack trajectory, bigger for SP2. Bottom: Bmode images corresponding and chosen at a time  $t$  to illustrate the enlargement in  $z$  of the crack tip.

The speed at which the crack propagates is a relevant parameter since it gives an idea of how fast the energy is transferred from one broken zone to its unbroken neighbor in the polymer network. By comparing chemical network to a network with silica nanoparticles, it helps to understand the transfer of energy when the NPs are present. Through this manuscript, it has been demonstrated that NPs enhance the mechanical properties of the gels, delaying its fracture due its high fracture toughness. How the velocity of the crack is impacted with the presence of NPs? Fig. 5.27 shows the profile of fracture propagation of SP0 and SP2. The profile of the crack propagation is different between the chemical gel and the gel with silica nanoparticles. On the contrary to the chemical gel swollen at equilibrium state ( $Q_e$ ) (Fig. 5.9), SP0 and SP2 at  $Q_0$  present two different stages of the crack propagation velocity. This is probably due to the testing machine in the case of SP0 at  $Q_e$  that was stretching the gel at a constant velocity, helping the crack to propagate uniformly.

When a constant displacement is applied, both gels, SP0 and SP2, react differently. The crack propagation velocity of SP0 seems to increase from  $4.3$  to  $10.3 \text{ mm.s}^{-1}$  presumably due to an increase of the applied energy release rate  $G_{IC}$  induced by the increase of the crack length  $a$ . In contrast, the crack propagation velocity decreases from  $6.0$  to  $3.2 \text{ mm.s}^{-1}$  for viscoelastic gels. The

crack propagation slowing down was also visible by eyes during the experiment. This deceleration is due to the reduction of energy released during the crack propagation through strong energy dissipation. By increasing the amount of silica NP in the gel, one can even assume to stop crack propagation (Ronsin et al., 2019).

For elastic materials, after the onset of unstable crack growth, the crack generally accelerates to a high velocity. A central prediction of this theory is that straight cracks smoothly accelerate to the Rayleigh wave speed (the velocity of surface acoustic waves) in large enough systems (Livne et al., 2007). LEFM has been experimentally validated for accelerating cracks that follow straight trajectories, prior to the onset of instabilities (Bouchbinder et al., 2009). It can follow complex paths for reasons that are not fundamentally understood (Chen et al., 2017).

### 5.4.2 Multiple crack propagation in hybrid gels

In Fig. 5.27, the enlargement of the crack trajectory in SP2 compared to SP0 (thinner) is due to the presence of NPs since they have the same thickness,  $e = 10$  mm. This enlargement is explained by the fact that the fracture is not sudden throughout the thickness as it is for elastic material. In the viscoelastic material, the fracture operates at different height in the thickness creating a large crack tip zone in the  $z$  direction. If one compare the Bmode images of SP0  $Q_0$  (Fig. 5.14) and SP2  $Q_0$  (Fig. 5.23), it appears that the crack tip of SP2 gel is not clearly defined in  $z$ .

A movie of the fracture propagation of SP2 has been recorded and some screenshots are presented in Fig. 5.29. It is clearly visible that at the end of the fracture propagation, when the blunting is really strong, another fracture operates through the thickness of the gel (and not in the width as usual). An explanatory scheme is available in Fig. 5.28 and the corresponding video is available in the legend of Fig. 5.29.

A first crack propagates in the direction 1 as usual. A second crack operates at the very end of the crack tip in the direction 3.

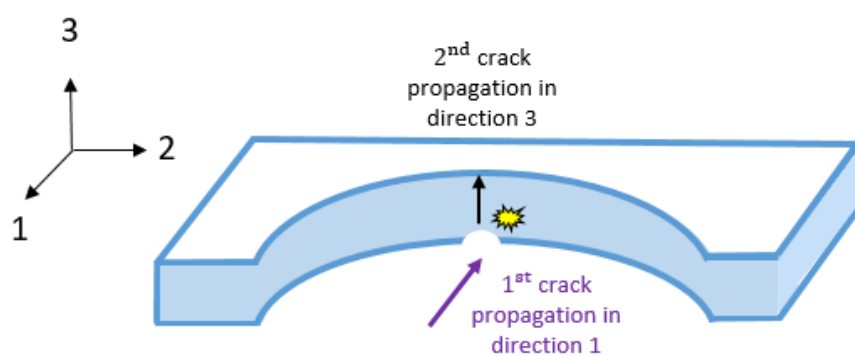


FIGURE 5.28: Scheme of the two propagation arising in the viscoelastic gel SP2. The first propagation is in direction 1 as observed in this manuscript. Another one arises in SP2 viscoelastic gel at the end of fracture propagation in direction 3.

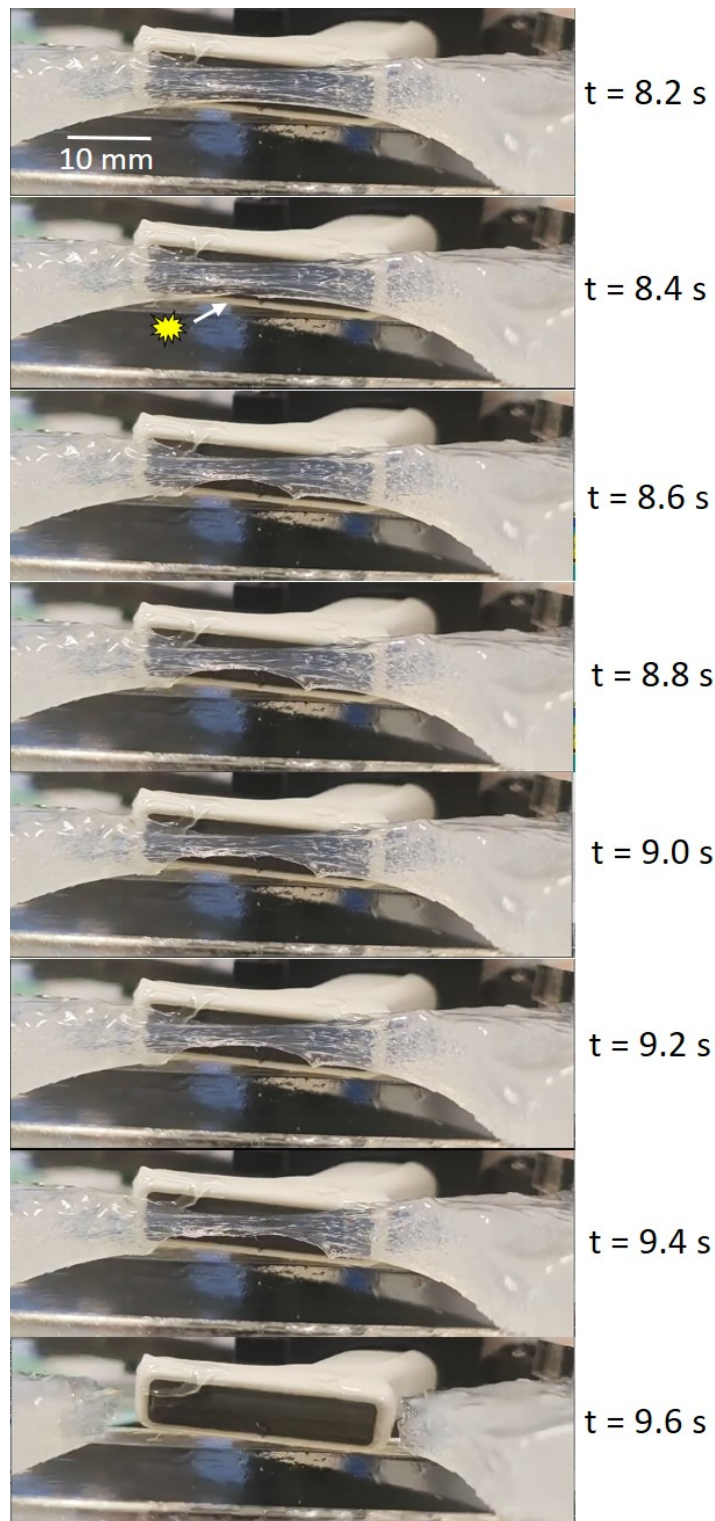


FIGURE 5.29: End of crack propagation in SP2 gel on the prototype setup with the SLH20-6 probe. From  $t = 8.4 \text{ s}$ , another fracture propagation starts transversely to the probe. Video following this link: <https://mycore.core-cloud.net/index.php/s/gn5eJnk9VcZHRM3>

## 5.5 Key results

Ultrafast imaging is able to detect the fracture propagation with a precision of milliseconds. Some very interesting events were highlighted:

- The crack tip is a source of shear waves. For elastic gels that do not dissipate energy, a lot of shear waves were created at the crack tip due to the release of energy when the crack breaks and propagates. For viscoelastic gels, less shear waves were created. Right before the shear wave propagates, a clear concentration of the stress is visible at the crack tip before the crack bursts and releases the strain energy. Since the fracture toughness  $G_{IC}$  is much higher for viscoelastic gels (Table 5.1), these shear waves contain more energy than the ones of elastic gels.

The shear wave velocity produced at the crack tip was calculated for each kind of gels. It increases with the stiffness of the gel and with the fracture toughness (see Table 5.2).

Gels (n = 1)	Shear wave velocity (m. s <sup>-1</sup> )	Frame visibility	$G_{IC}$ (J. m <sup>-2</sup> )
SP0 at $Q_e$	$1.2 \pm 0.2$	6	$19 \pm 1$
SP0 at $Q_0$	$2.5 \pm 0.2$	4	$240 \pm 4$
SP1 at $Q_0$	$3.3 \pm 0.5$	3	$515 \pm 13$
SP2 at $Q_0$	$6.0 \pm 1.0$	2-3	$1146 \pm 21$

TABLE 5.2: Shear wave velocity created from the crack tip depending on the gel. The shear wave speed increases with the gel's stiffness and with the fracture toughness. Thus, the shear waves visibility in the frames is reduced.

The energy dissipation associated with the formation and propagation of shear waves is typically referred to as acoustic emission (Achenbach, 2012). The generation of acoustic emission from the fracture process has been described based on the different types of produced waves. For example, in semi-infinite media, Rayleigh waves (surface waves) have been estimated to carry about 67 % of the energy radiated from the damage source in perfectly isotropic materials, while the shear and longitudinal waves contain 26 % and 7 %, respectively (Achenbach, 2012).

In the light of geophysical observations made at the scale of the Earth, during an earthquake, the sudden rupture of a fault causes vibrations that propagate in the rocks: these are the seismic waves. Acoustic emission is a low energy seismic event. A seismic event may be induced by fracture initiation, fracture propagation, or a sudden movement of existing fractures. During fracture, gels undergo a seismic event at small scale.

- The more viscoelastic the gel, the slower the propagation of the crack. Indeed, from a very schematic viewpoint, in a pure chemical network, once the critical energy release rate is reached, the energy is transferred from one broken polymer strand to its unbroken neighbor and the fracture propagation tends to accelerate under monotonic loading. When physical interactions are coupled to the elastic matrix, the network is more complex. The viscoelastic gel dissipates energy through large scale reorganization in order to relax the internal stresses (as seen in Chapter 4 in Fig. 4.36).

Also, extremely large blunting is clearly visible in viscoelasticity gels. The crack tip is almost unrecognizable since large remodelling of the initial crack tip are taking place. It is no more

a sharp crack tip as it was at the beginning of the test. Polymer segments exchanges operating at NP surface enhances the resistance to crack propagation by shielding the crack tip singularity through unusual crack blunting.

- Our results are similar to those of Catheline's team who built an efficient tool to study rupture dynamics friction between a gel and a sandpaper (Latour et al., 2011). They used ultrafast ultrasonic speckle interferometry based on the same method used in Chapter 5 to follow the dynamic of the interface failure in a friction experiment. They also highlighted the supershear rupture regime associated with the emission of waves created during the friction that they called Mach waves fronts. Notably, ultrafast scanners provide a small-scale laboratory setup for making novel geophysical observations that can be translated to the level of the Earth (e.g., slip dynamics in active faults).
-

## 5.6 Ultrafast imaging in double network (DN) gels

### 5.6.1 Materials

In this part, ultrafast imaging is used to visualize the fracture propagation of Double Network (DN) gels. The idea was to experience our methodology and observations on another type of gels. DN gels, presented in Chapter 1, part 1.1.3 stand for a reference in the world of gel toughening strategy. Gels display high composition in water (90 wt.%) coupled to extraordinary mechanical performances close to rubbers ( $E \approx 1$  MPa). Double network gels are known for their sacrificial network, able to dissipate energy by bond breaking combined with a supporting network to resist to the macroscopic fracture. DN gels with their significant energy dissipation capacities exhibit high fracture resistance ( $G_{IC} \approx 1$  kJ.m<sup>-2</sup>). The breaking of the first network appears close to the crack tip in a region called the damage zone (Gong, 2010) (Fig. 5.30). Brown (Brown, 2007) propose a simple model accounting for the very high toughness of double network gels based on the assumption that the first, stiff network will break up forming multiple cracks when the stress is above a defined value.

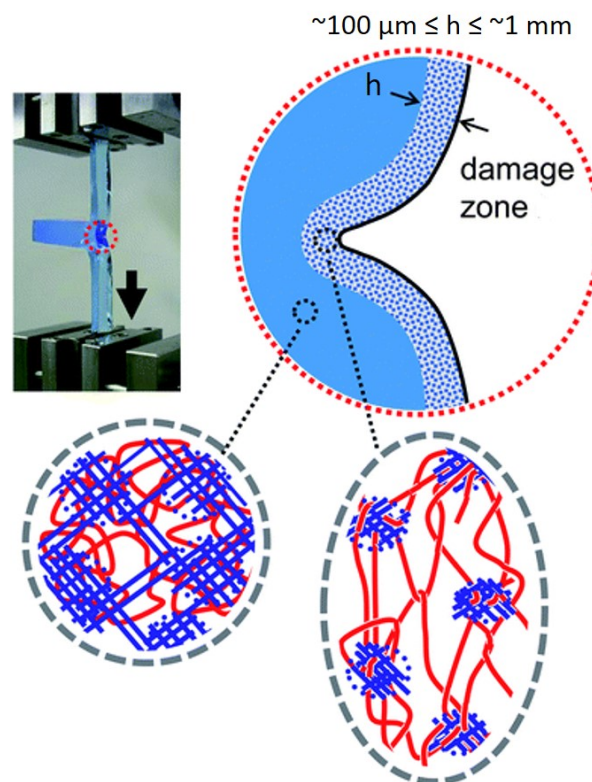


FIGURE 5.30: Illustration of local damage zone at the crack front of DN gels. (from Gong, 2010).

In part 5.6.4, the thickness  $h$  of the process zone will be discussed. It is not clearly defined since it depends on the sample geometry, sample synthesis, and the technique used to characterize the process zone. Nevertheless  $h$  seems to be comprises between  $100\ \mu\text{m}$  and  $1\ \text{mm}$  coupling theoretical models and experimental attempts (Brown, 2007, Yu et al., 2009, Liang et al., 2011 and Matsuda et al., 2020).

Gels were received as usually prepared directly from the Laboratory of Soft and Wet Matter, Hokkaido University (Sapporo, Hokkaido, Japan) from Professor Gong. During the first try, the lack of speckle rapidly aborts the study (Fig. 5.31).

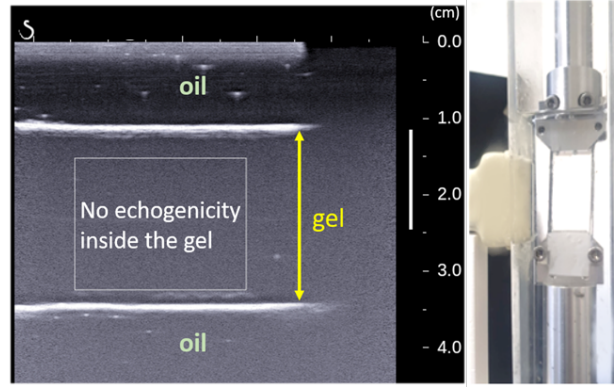
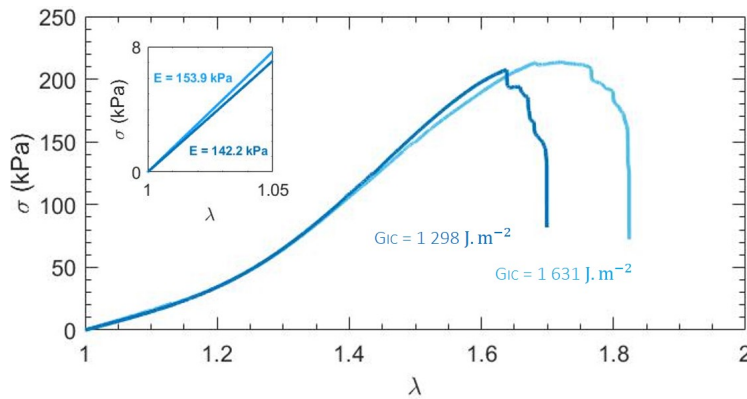


FIGURE 5.31: Lack of speckle in traditional DN gels.

Even with agar (1 wt%), the gel was transparent to ultrasounds. The synthesis had to be changed. Agar quantity was increased to 2 wt%. To prevent melting of agar, the first monomer species AMPS (acid) was changed to NaAMPS (neutral). Also, to anticipate possible agar precipitation, strong UV intensity was used to shorten the gelation time. This works perfectly and it can be seen in the following Bmode images that the obtained speckle was great. The sample preparation plan was elaborated and synthesized by Hane Yukiko and Ryuji Kiyama. Gel geometry is  $W = 20\text{--}25\text{ mm}$ ,  $e = 10\text{ mm}$  and  $a = 5\text{ mm}$ .

### Mechanical response of DN gels

The stiffness of the DN gel has been drastically decreased from 1 MPa to about 150 kPa to optimize the imaging conditions. DN gels were tested in our laboratory with the tensile testing machine at a strain rate of  $0.01\text{ s}^{-1}$  linked to the imaging technique as shown in Fig. 5.31, right. A notch of  $a/W = 0.2$  is created inside the DN gel. The stress strain curves obtained are illustrated Fig. 5.32.

FIGURE 5.32: Stress strain curves of DN gels at a strain rate of  $f = 0.01\text{ s}^{-1}$ . Calculation of the Young's modulus and the fracture energy of DN gels.

Due to the high stiffness of double network gel, the framerate was increased from 1000 to 2000 Hz meaning that two images were obtained every millisecond. The memory capacity of the machine being 10 000 images, the corresponding time of acquisition was 5 seconds.

A lot of movements inside the gel were captured during the crack propagation. In contrast to hybrid gels that showed events occurring only at the crack tip. That's why, the results will be presented by superimposing the Bmode image with the corresponding displacement map recorded between the  $n-1$  image and the  $n$  image. Furthermore, additional colour (blue and red) will be

used as in Doppler techniques to help to see the movements inside the gel. The direction of velocity is assigned the color red or blue, indicating direction toward or away from the ultrasound probe respectively.

### 5.6.2 Fracture of DN gels dissected every millisecond

#### Beginning of DN gels fracture propagation

The fracture propagation of DN gel is really slow. Fig. 5.33 shows that the fracture lasts about 16 seconds. Only 5 seconds can be recorded by ultrafast ultrasounds during this fracture propagation.

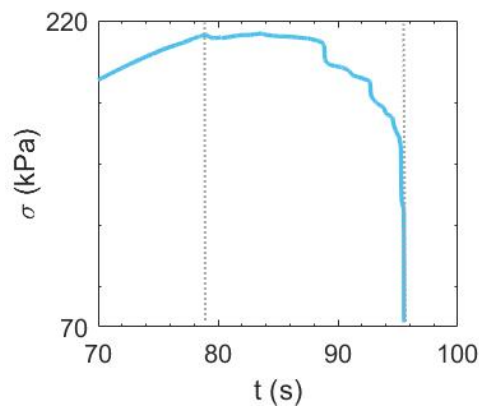


FIGURE 5.33: Fracture propagation of the DN gels visualized by the stress time curve. The fracture starts at  $t = 79$  s and ends at  $t = 95$  s.

In 5 seconds, it is difficult to see by eyes the change between  $t = 0$  and  $t = 5$  s in Fig. 5.34. The movements detected in blue at a velocity of  $0.05 \text{ cm.s}^{-1}$  represent the oil displacement probably due to bubble that are detected and pushed by the ultrafast ultrasound plane waves.

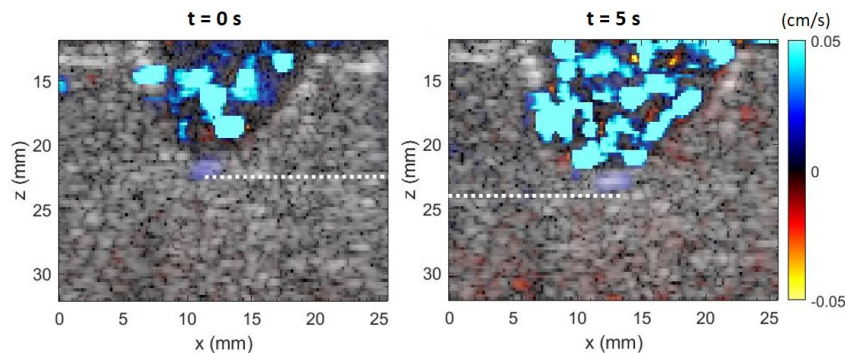


FIGURE 5.34: Bmode images corresponding to a fracture propagation in DN gels at  $t = 0$  and  $t = 5$  seconds. The fracture propagates really slowly as almost no changes are visible by eyes. The white dotted line shows the location of the crack tip.

The  $x$ - $t$  and  $z$ - $t$  profile allow to see displacements that occur inside the DN gel during these 5 seconds. In fig. 5.35 top, at a scale of  $[-0.5 \text{ } 0.5] \text{ (cm.s}^{-1}\text{)}$ , it is too fast to detect the crack tip advancing. Nevertheless, movements are observed ahead of the crack tip corresponding to paraffin bubble trajectory in oil. They have the same trajectory and velocity. In Fig. 5.35 bottom, by reducing the scale by ten, the evolution of the crack tip according to  $z$  is visible.

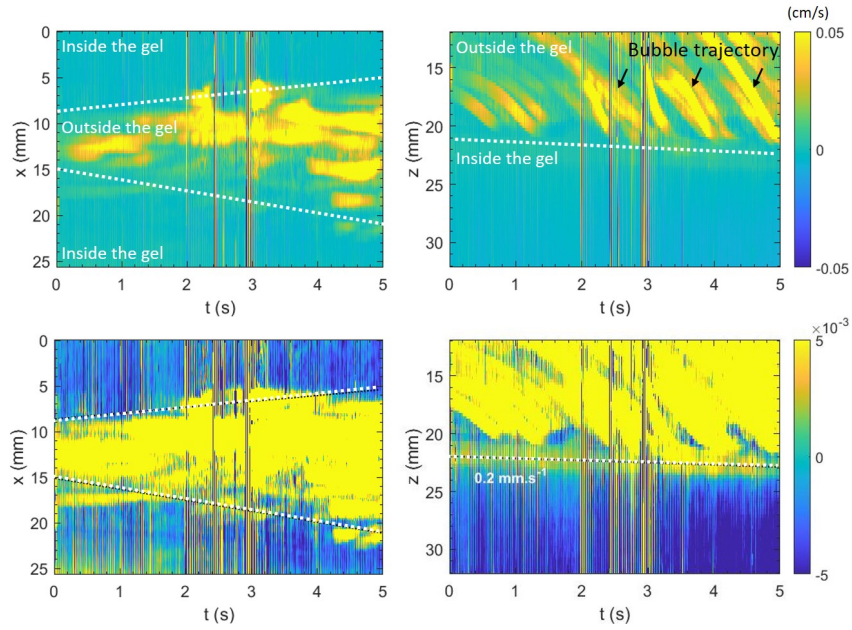


FIGURE 5.35: Profile of the fracture propagation. x-t and z-t profile of the beginning of fracture propagation in DN gels presented with two different scale.

The crack evolves linearly according to  $z$  (from  $z = 21$  to  $z = 23$  mm approximately) at a constant velocity of  $0.2 \text{ mm.s}^{-1}$ . The yellow part in the x-t profile represents the crack opening displacement (COD) which becomes bigger with time, as expected since the crack is advancing. During these five seconds of acquisition, a lot of displacements are detected inside the gel. For example, a shear wave is created from the bottom right of the gel (see Fig. 5.36). This has never been observed in our model gels since shear waves were only created from the crack tip.

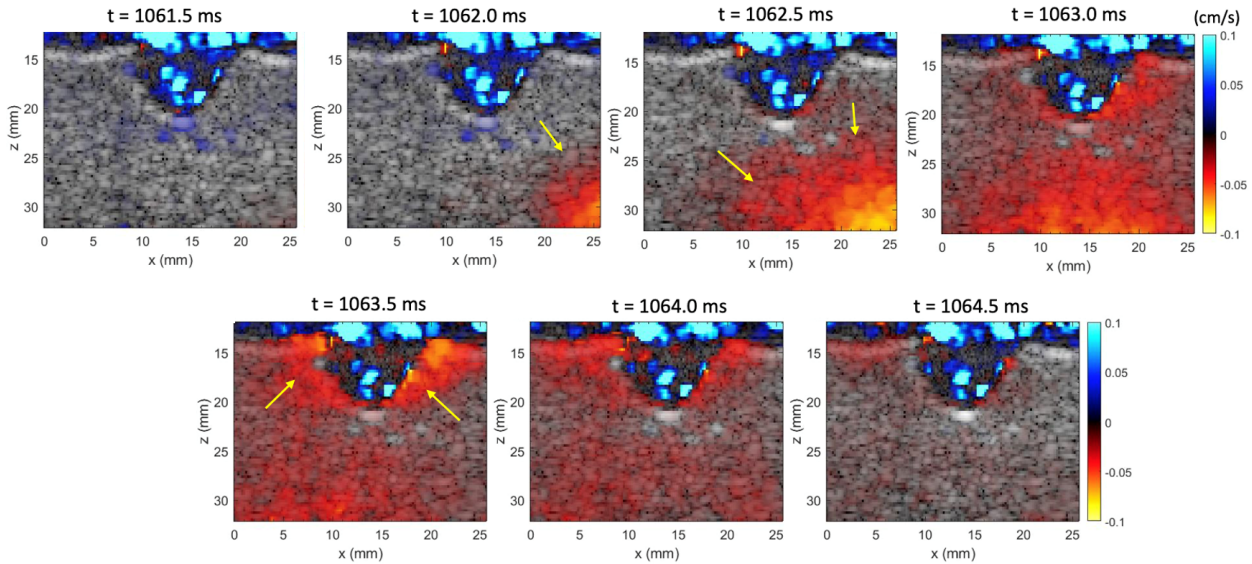


FIGURE 5.36: Displacement visualized from the bottom of the gel to the crack tip lips. The displacements disappear at  $t = 1064.5 \text{ ms}$ . The yellow arrows help the reader to see the shear wave source (bottom right) and the concentration of this shear wave around the crack tip. Video following this link: <https://mycore.core-cloud.net/index.php/s/WKY9ggmdSLth91c>

As already noticed in hybrid gel, displacements can be detected from the crack tip (see Fig. 5.37, Fig. 5.38 and Fig. 5.39) where we observed two waves front propagating in opposite directions.

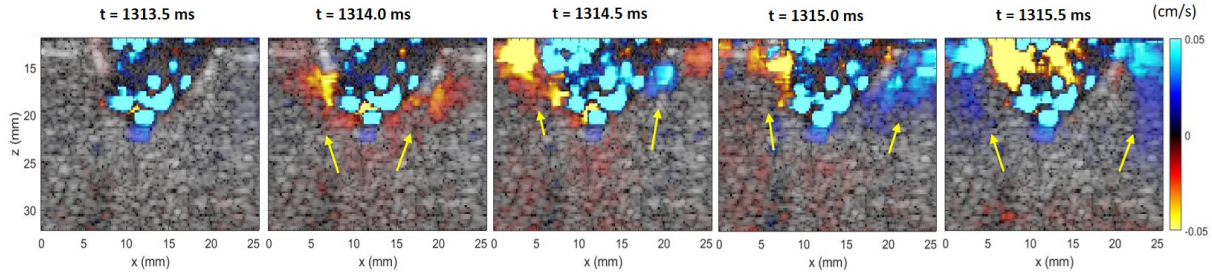


FIGURE 5.37: Displacement visualized from the crack tip of DN gels. Two waves front of shear waves are observed, created at  $t = 1314$  ms. Yellow arrows help the reader to visualize the shear wave. Video following this link: <https://mycore.core-cloud.net/index.php/s/hjT6YMz1K0b9VRF>

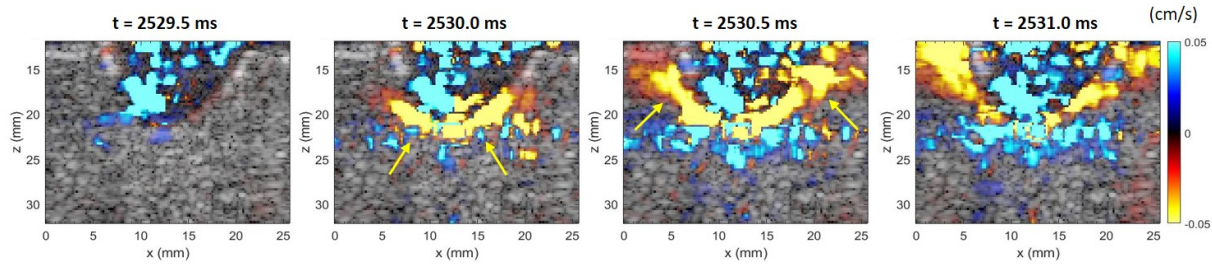


FIGURE 5.38: Displacement visualized from the crack tip lips of DN gels. The shear wave is created at  $t = 2530$  ms. Video following this link: <https://mycore.core-cloud.net/index.php/s/sqFnxWyOr0Afx0G>

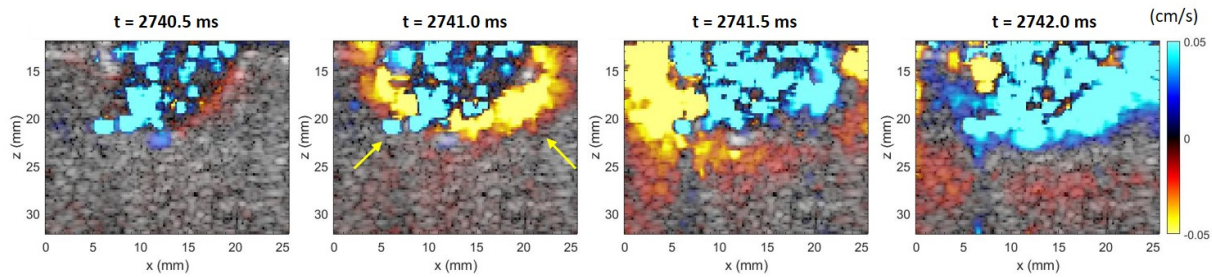


FIGURE 5.39: Displacement visualized from the crack tip lips of DN gels. The shear wave is created at  $t = 2741$  ms. Video following this link: <https://mycore.core-cloud.net/index.php/s/j8fe543MyDwrC7H>

It looks like the shear wave is created from all around the crack tip lips and not from the crack tip source as it was observed in our model gels. Indeed, in SP1 and SP2 gels, right before the shear wave propagates, the source was well visible and concentrated at the crack tip (Fig. 5.25 and Fig. 5.21). It is also possible that the source is not visible appearing too quickly to be catch by a framerate of 2000 frames/s.

Some events also occur ahead of the crack tip which might correspond to the process zone (Fig. 5.40). This event can not be due to bubble passing ahead of the gel, otherwise, the movement will be followed until it gets out of the image. Here, the movement is detected at one point and disappeared few milliseconds after like a quick internal fracture.

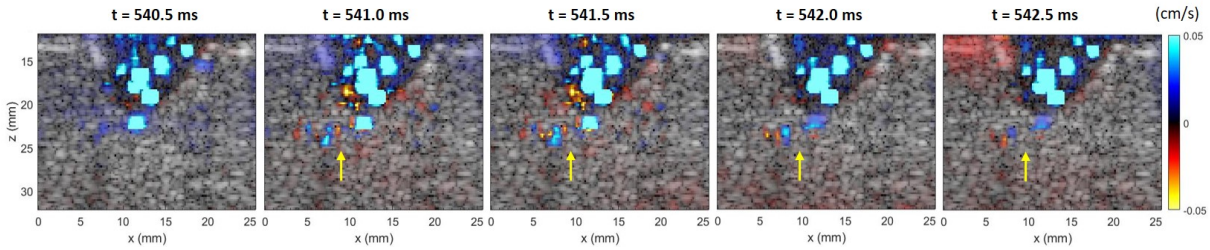


FIGURE 5.40: Displacement visualized near the process zone of DN gels. Yellow arrows help the reader to detect the internal movements inside the gel. Video following this link: <https://mycore.core-cloud.net/index.php/s/uNim07uDss4vqAh>

Due to technical limitations, the end of the fracture propagation were not recorded. In the next part, another DN gel was studied and imaged during the end of fracture propagation.

### End of the DN gel fracture propagation

In another sample, fracture propagation were recorded at the end of the propagation. The fracture lasts only 4 seconds (see stress/time curve of Fig. 5.41). On the contrary to Fig. 5.33 that shows a plateau for almost 10 seconds, this gel shows a sudden stress decrease. The sequence acquisition recorded the last two seconds of fracture propagation. Bmode images corresponding to the time in the stress/strain curve are presented.

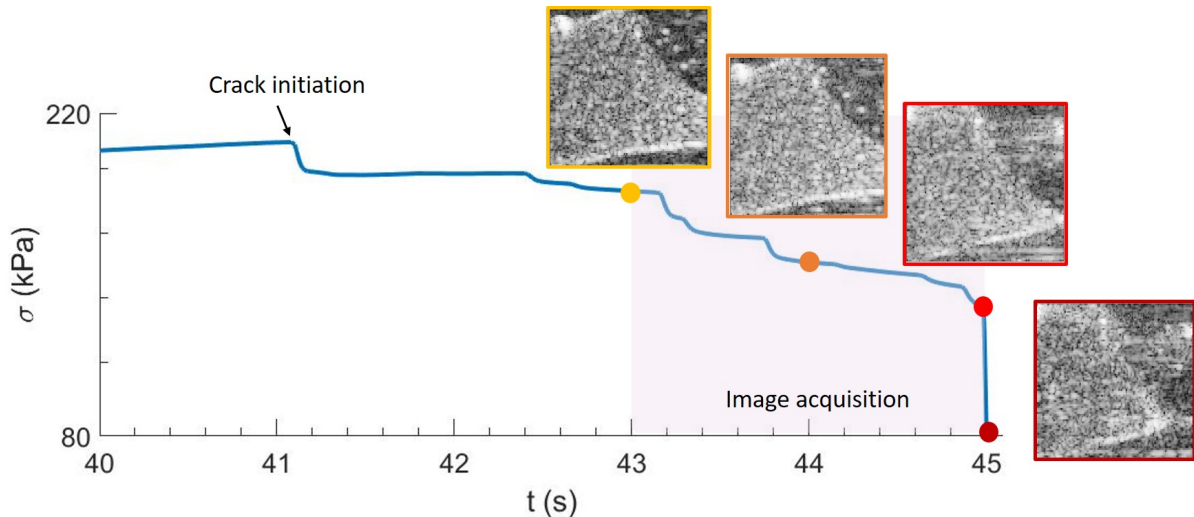


FIGURE 5.41: Fracture propagation of the DN gels visualized by the stress time curve. The fracture starts at  $t = 41$  s and ends at  $t = 45$  s. Bmode images corresponding are shown.

In the imaging sequence acquisition,  $t = 0$  corresponds to  $t = 43$  seconds in the stress/strain curve. Internal movements are visible at different time in Fig. 5.42 suggesting a possible local fracture at this place.

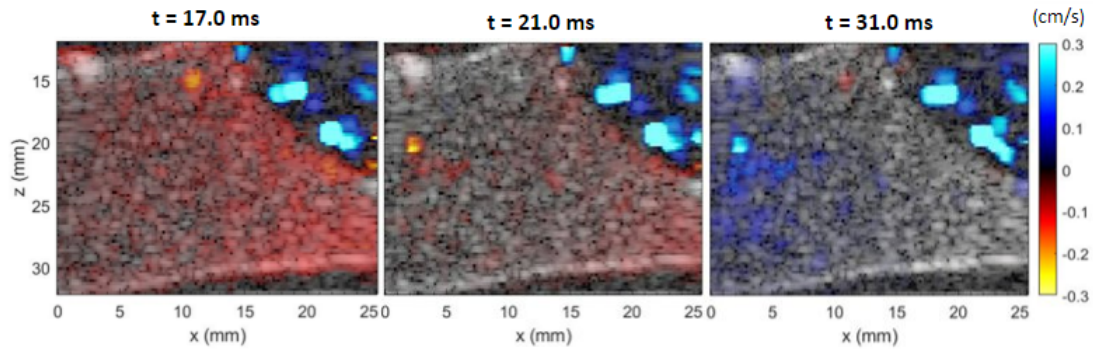


FIGURE 5.42: Map displacement superimposed to Bmode images in a DN gel. Movements occur inside the gel away of the crack tip. They appear and suddenly disappear. It could correspond to a fracture event happening inside the gel. Video following this link: <https://mycore.core-cloud.net/index.php/s/02HyCNVZgFP3KIC>

Then, by looking at the displacement maps during the 2 seconds of fracture propagation, a lot of events happen. For example, Fig. 5.43 highlights the displacements that occur at the crack tip lips. In this particular case, a wave is created at the crack tip ( $t = 235.0$  ms) and propagates through the crack tip lips. The crack tip source disappears around  $t = 244.5$  ms replaced by an internal movement going in the opposite direction (blue), away from the probe.

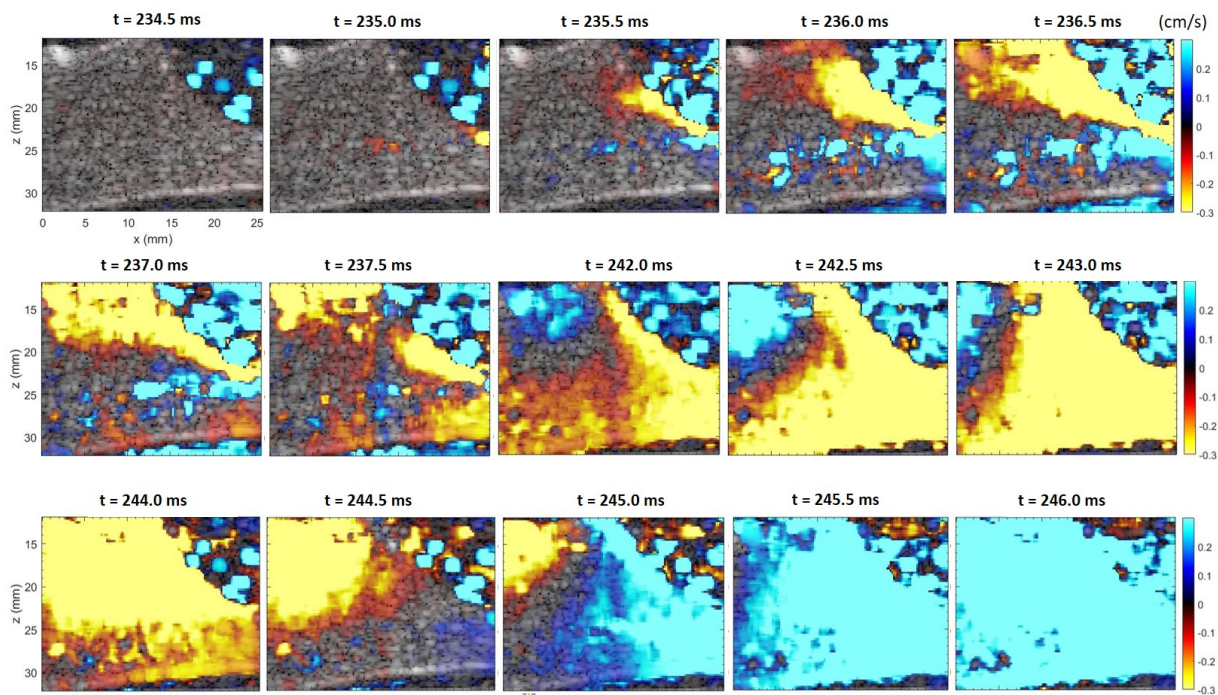


FIGURE 5.43: A shear wave is created from the crack tip generating plenty of displacement in the DN gel. Video following this link: <https://mycore.core-cloud.net/index.php/s/EENbNL0Lc1SFxU9>

In Fig. 5.44, near the crack tip lips, a movement appears at  $t = 834.5$  ms and a wave is created from this source propagating around at  $t = 835$  ms and  $t = 835.5$  ms and disappearing at  $t = 836$  ms. It might represent the breaking of the sacrificial network.

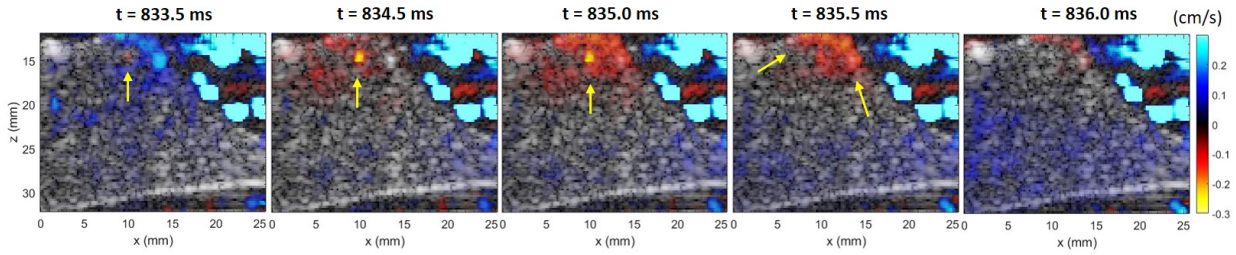


FIGURE 5.44: Detection of a displacement inside the DN gel near the crack tip lip. The illuminating point represents a movement that occurs inside the gel. It looks like a shear wave is created from this source and propagates outside the gel. Video following this link: <https://mycore.core-cloud.net/index.php/s/Rdlzpo3NThEy2xs>

What is observed in Fig. 5.44 could be the breaking of the sacrificial network located in the process zone as exposed in Fig. 5.30. A shear wave is created from this fracture event suggesting that, when the first network breaks, energy is dissipated through shear waves.

### 5.6.3 Stretching of an intact DN gel

The experiments have also been performed on an un-notched gel. The gel was imaged during the beginning of a tensile test at a strain rate of  $0.01 \text{ s}^{-1}$  until  $\lambda = 1.8$ . Due to technical limitations, it was not possible to stretch the intact gel until fracture. Displacements are seen in Fig. 5.45 at different places inside the gel. This, again, suggests an internal and local fracture that could reflect the breaking of the sacrificial network.

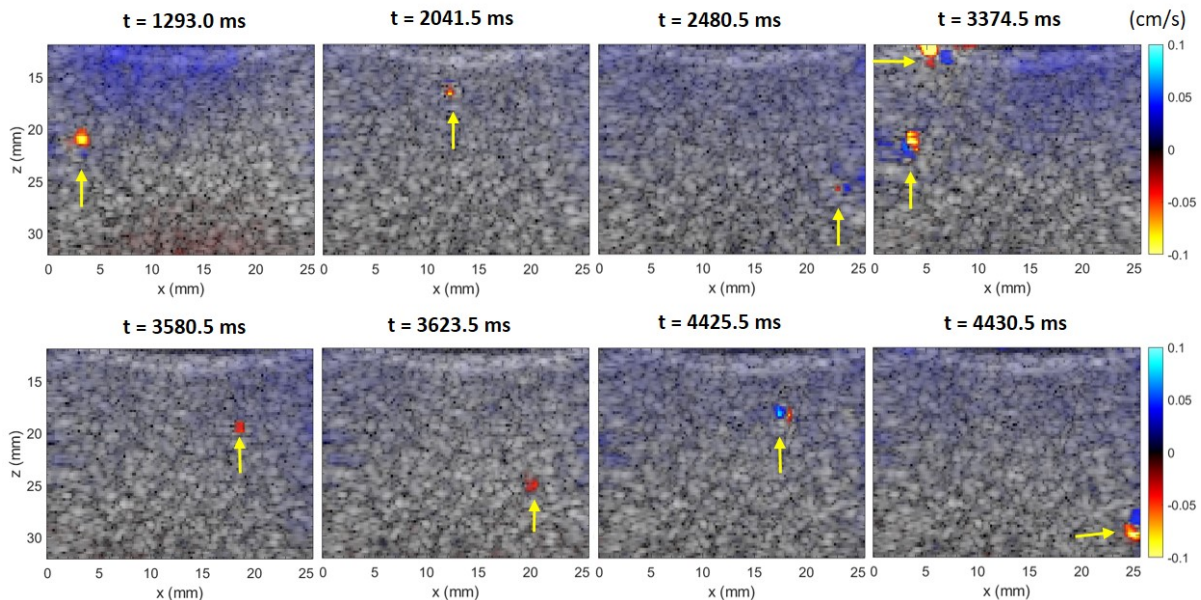


FIGURE 5.45: Stretching of an intact DN gel at a strain rate of  $0.01 \text{ s}^{-1}$ . Different events corresponding to internal displacements are caught at different times of the stretching. Yellow arrows help the reader visualize the displacements detected inside the gel.

### 5.6.4 Key results and discussion

- On the contrary to our model gels, DN gels show multiple events that occur at different places in the gel: at the crack tip, but also at the crack tip lips, or even far away from the crack tip. Tensile tests were also performed on un-notched DN gels, and still, displacements were detected inside the gel at different locations. This suggests that the events observed are due to the breaking of the sacrificial network. The breaking of the sacrificial network is smaller (local, at a molecular scale) than the "breaking" of the crack tip, visible by eyes through the crack propagation. The shear wave created generates smaller displacements more difficult to catch by ultrafast ultrasounds. The displacements detected are in the order of the micrometer and their velocity is around  $1 \text{ mm.s}^{-1}$ .

This source of fracture events could be related to the existence of submicrometer-scale voids in the first network as it was shown by dynamic light scattering (Na et al., 2004, Tsukeshiba et al., 2005) or *in situ* small-angle X-ray scattering (Fukao et al., 2020). Fukao *et al.* (Fukao et al., 2020) found that the mechanical balance between the two networks determines the internal fracturing process in DN gels. For the DN gel with significant differences in moduli between the two networks, internal fracturing is initiated near the voids in the lateral direction, propagates along the stretching direction, and percolation of the fracture in lateral direction triggers necking of the sample. For the DN gel with relatively fewer differences in moduli between the two networks, internal fracturing occurs dispersedly over the sample, irrespective of the presence of voids, and necking is not observed.

Here, there are no clear necking points in the stress/strain curve (Fig. 5.32). Internal fracturing spotted by ultrafast ultrasounds occurs in the direction vertical to the stretching and seems to happen everywhere in the sample.

- US imaging readily allows the definition of a process zone. Recently, the size of the DN gel damage zone has been estimated by mechanochemical technique (Matsuda et al., 2020) (Fig. 5.46).

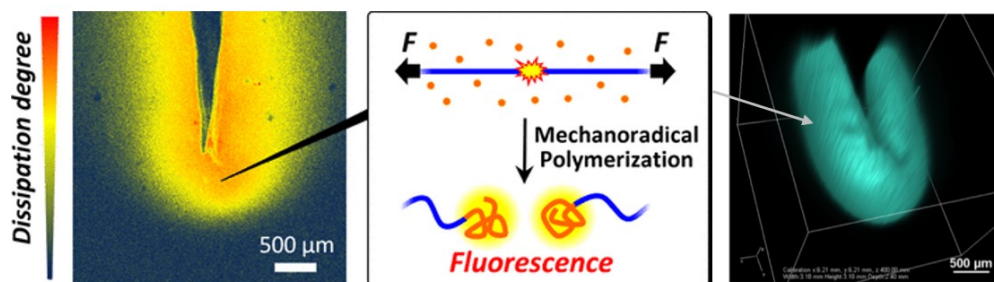


FIGURE 5.46: Mechanochemical technique to visualize the bond scission of the first network in the damage zone of tough double-network hydrogels. Left: 2D fluorescence images and Right: 3D fluorescence images obtained using a laser scanning confocal microscope around the crack tip of a torn DN gel fed with mechanoradicals and fluorescent molecules (from Matsuda et al., 2020).

In the experiment of Fig. 5.46, mechanoradical polymerization was performed via tearing or stretching the DN gel. The DN gel was first cut, then immersed in a solution to supply the gel with mechanoradicals and fluorescent molecules. Afterward, the gels were torn. Finally, the sample were stored in a glovebox to allow for mechanoradical polymerization. Fluorescence images were then performed as the last step of the experiment. The results clearly indicate that internal fracturing occurred around the crack tip during the tearing or

stretching of the sample. The damage zone from the fractured surface to the bulk is several millimeters thick (Fig. 5.46, right).

Mechanoradicals allow detecting displacements at a molecular scale (polymer chain scission) with a technique resolution of about  $50\ \mu\text{m}$  (Matsuda et al., 2020). This allows quantifying a process zone size around  $500\ \mu\text{m}$  (for a DN gel with a COD of  $300\ \mu\text{m}$  and a crack length of  $a = 1.5\ \text{mm}$ ). Ultrasounds confirmed these results and allow the detection of internal fractures with a resolution of about  $200\ \mu\text{m}$ . With ultrafast ultrasounds, a large crown (about  $2\ \text{mm}$  wide) of internal displacements was found around the crack tip which could be qualified as a process zone (Fig. 5.47). It seems that internal fracture happens all along the crack tip lips in a perimeter of  $2\ \text{mm}$ . Furthermore, since ultrasounds allow the detection of internal fracture in the bulk, this supports the results of Matsuda *et al.* (Matsuda et al., 2020), not being only at the surface. The fluorescence intensity, which reflects the degree of polymer strand scission, shows a gradient distribution in the damage zone. It maximizes near the fractured surface and decreases gradually from the surface to the bulk. The damage zone extends over approximately  $2\ \text{mm}$ . It would be interesting to study the thickness of the damage zone by sending ultrafast ultrasound plane waves through the sample thickness ( $y$  direction). In this way, internal fracturing will be seen at different depth in the bulk.

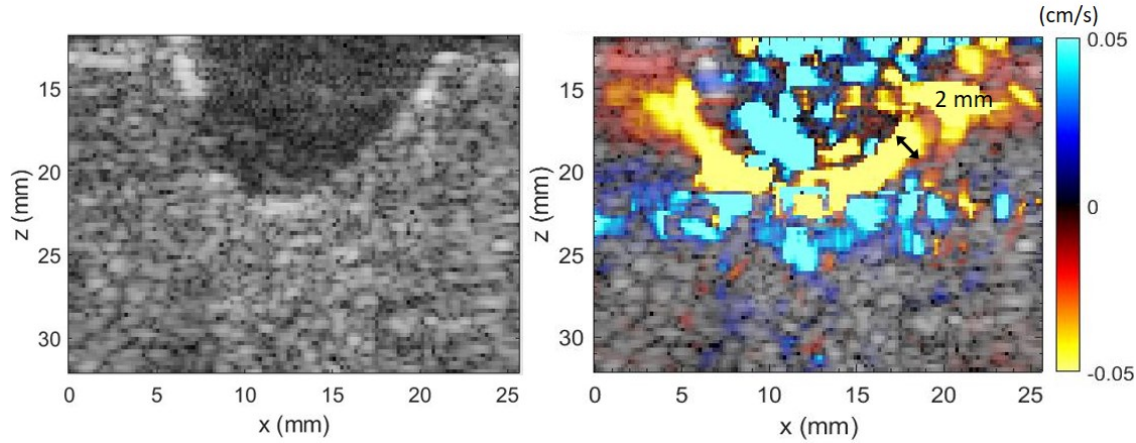


FIGURE 5.47: DN gel during a crack propagation. Left: Bmode image of the gel. Right: Velocity of the displacement field  $U_z$ . A crown of about  $2\ \text{mm}$  wide surrounds the crack tip which might correspond to the process zone where dissipation occurs through the breaking of the first network. COD of about  $16\ \text{mm}$  and a crack length  $a$  of about  $10\ \text{mm}$ )

The thickness of the whole damage zone has been estimated with some discrepancy: Matsuda *et al.* (Matsuda et al., 2020) found a value close to  $h \sim 1090\ \mu\text{m}$  (based on the combination of the mechanoradical polymerization and fluorescent microscopic technique, Fig. 5.46), Liang *et al.* (Liang et al., 2011) defined the process zone size around  $h \sim 650\ \mu\text{m}$  using optical microscopes and Yu *et al.* (Yu et al., 2009) observed the damage zone with a thickness of several hundreds  $\mu\text{m}$  using a 3D violet laser scanning microscope. They also showed that the thickness  $h$  increases with the fracture energy  $G_{IC}$ .

The difference in the damage-zone thickness  $h$  is attributed to: a small difference of gel composition and a difference of sample geometry, i.e., the thickness of the gel being around  $3\ \text{mm}$  for Matsuda (Matsuda et al., 2020) and Yu (Yu et al., 2009) and  $0.1\ \text{mm}$  for Liang (Liang et al., 2011). In our case, the gel composition was modified with the addition of agar and the decrease in modulus of the second network. Furthermore, the geometry is totally different since ultrasounds need big samples (the thickness of the gel in this study is  $10\ \text{mm}$ ). In

view of these results, it seems that the damage zone adapts its size according to the sample geometry and synthesis.

- This last study shows the feasibility of using ultrasounds and ultrafast imaging to assess the physical processes that are invisible by eyes inside the DN gel during stretching or during fracture propagation. This *in-situ* ultrafast technique possibly allows visualizing, in real-time, the sacrificial network breaking anywhere in the gel during a tensile test. It also highlights a process zone of about 2 mm around the crack tip, translated by internal displacements. This process zone size remains the one found in our model gels with silica NPs. Indeed, in SP2 gels, it has been demonstrated during a relaxation and creep test that the spatial stress field changed drastically in the first 2 mm ahead of the crack tip, meaning that dissipation effects are really strong in this zone (Fig. 4.37).
-



## Conclusions

This research work has made possible the merging of different scientific worlds from imaging, soft matter, mechanics, and chemistry. One of the goals was to develop a comprehensive picture of links between macromolecular architectures (using model systems) and their macroscopic properties. Characterizing gels by developing customized mechanical techniques is what is currently done in soft matter laboratories. Here, the characterization is pushed further with the use of an imaging technique coupled with a conventional mechanical tool. This work demonstrates the promise of shear wave elastography as a tool to study the mechanics and fracture of hydrogel due to the difference in velocity between shear and compression waves that propagate inside the material. This project participates to fill the gap on a still poorly unexplored mechanical characteristic of the gel: the fracture. Shear wave elastography and conventional mechanical testing complement each other perfectly for the study of the mechanical and fracture behavior of hybrid hydrogel. SWE allows a very high-frequency range of study, which is not common. The shear waves created through the radiation force, itself created through the focused ultrasounds, propagate at a frequency of about 200 Hz (and can reach up to a thousand Hertz with different probes). This high frequency is even more interesting when we know that similar shear waves propagate inside the human body. Indeed, aortic valve closure occurs over a time period of approximately 5 ms or less (Aase et al., 2008). Thus, the frequency range of the generated shear wave is assumed to be between around 200 and 300 Hz (Debbal et al., 2008, Reed et al., 2004). In order to understand the mechanics of biological tissues, it is important to study them with similar frequencies arising inside the body.

One insight emerging from this work is that energy dissipation is a key factor to resist fracture:

- **Before fracture propagation**, shear wave elastography allows capturing local stress changes. On one hand, we learned that viscoelastic gels dissipate energy by homogenizing the stress inside the material, creating a shielding effect, and erasing the singularity (see Fig. 5.48).

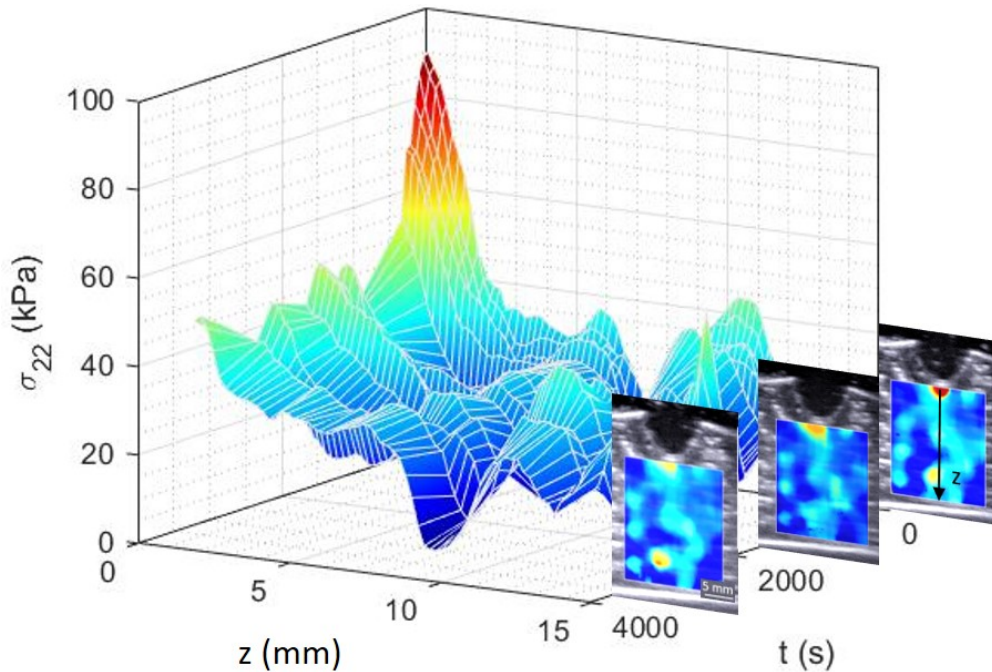


FIGURE 5.48: 3D plot for SP2 viscoelastic gel (PDMA + 10 vol.% of SiO<sub>2</sub>). Stress is dissipated inside the gel, the singularity is erased.

A singularity must be avoided since it is the starting point of a fracture propagation. On the other hand, this study confirmed that swollen elastic gels at equilibrium state are more brittle than their analogue at preparation state. Through the local study, we have learned that this is due to the suppression of dissipation mechanisms and not due to the spatial stress field, since the same stress gradient is reached for this two gels (close to LEFM prediction  $\sigma \sim z^{-1/2}$ ).

The classic approach to the fracture of elastic materials, LEFM, treats all relevant physical quantities to linear order in the elastic deformation with respect to the undeformed state of the material. In a complex and highly deformable material as hydrogel, it has been seen in this manuscript that non-linearities are important at large deformation. In LEFM, all non-linearities and dissipation are assumed to be confined to a microscopically small region near the crack tip, and are neglected. The fracture of soft materials involves large deformations and crack blunting before crack propagation occurs. Through chapter 3, it has been demonstrated with the use of acoustoelasticity that order 4 in non-linear elasticity was needed to identify the mechanical response of the material. The Landau coefficients (non linear coefficients  $A$ , 3<sup>rd</sup> order and  $D$ , 4<sup>th</sup> order) were experimentally identified and used to depict the mechanical behavior of the gel at large strain. Through coupled experiments with mechanical testing, these coefficients were calculated for each gel depending on the amount of NPs and its state ( $Q_0$  or  $Q_e$ ). Knowing these coefficients, it was possible to extract a local stress highlighting the feasibility of using shear wave elastography to study the fracture mechanics of soft matter.

- **During fracture propagation**, ultrafast ultrasounds allow the visualization of unique physical phenomena: dissipation results in the creation of shear waves being generated directly from the crack tip and traveling outside the gel (Fig. 5.49).

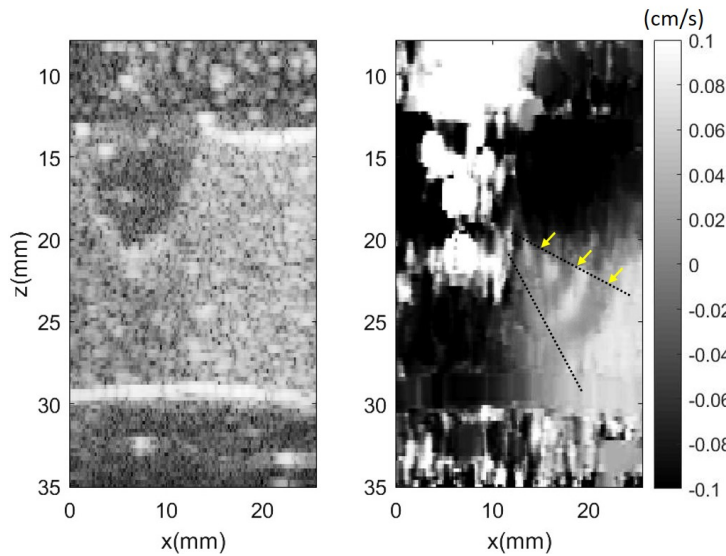


FIGURE 5.49: Visualization of shear waves created at the crack tip in a swollen elastic gel  $Q_e$ . Left: Bmode image; Right: Corresponding displacement map. Three shear waves are visible. The contrast has been intensified to better see the waves and yellow arrows help the reader to identify them.

The more elastic is the gel, the more shear waves are created during fracture propagation since energy dissipation is not possible in an elastic material. Through the addition of silica nanoparticles inside the elastic gels, the fracture is delayed, fewer shear waves are created at the crack tip and the crack propagation slows down, on the contrary to elastic gel where the crack tends to accelerate. During an earthquake, seismic waves are the translation of energy dissipation. The gel undergoes traumas quite similar to seismology during a fracture process.

The size and shape of the process zone can be experimentally defined. In our model gels, the process zone was characterized by studying the evolution of the spatial stress field ahead of the crack tip (along  $z$ ). Significant changes arise in the first 2 mm and in the first hour of relaxation test. In DN gels, the process zone was defined by capturing the internal displacement during a fracture propagation. Internal fracture occurs around the crack tip in the first 2 mm.

- **After fracture propagation**, the gel has been split in two. Putting the two pieces of the gel back together (in contact) in oil (to avoid dehydration), the gel heals, each piece sticks to the other and the gel becomes one again. This phenomenon is due to the silica nanoparticles that behave as adhesive fillers inside the PDMA network (Rose et al., 2014). If fracture occurs in biological tissues, they have the capacity of repairing. As a perspective, it would be interesting to study the local stress during a recovery process by closing the notch (inverse of what has been done in this study) to understand how works the healing process (Fig. 5.50). In the same idea, EPFL scientists have developed an injectable gel that can attach to various kinds of soft internal tissues and repair tears resulting from an accident or trauma, helping biological tissues to recover more rapidly (Karami et al., 2021).

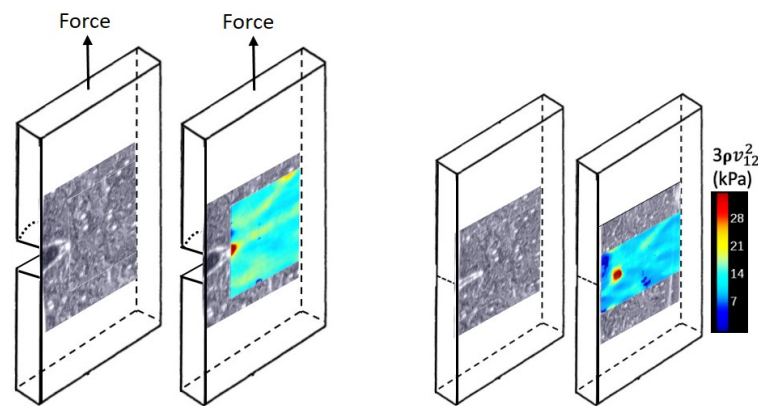


FIGURE 5.50: Left: Fracture process. The local stress is probed at the crack tip. Right: Recovery process. The notch is closed with no force applied. The NPs do their job acting as adhesive fillers inside the PDMA network to reconnect the crack tip lips together. How the stress evolves during the recovery process?

Many applications could see the day turned to the world of soft materials and fracture. Fracture propagation has been studied with ultrafast ultrasound plane waves for the first time. With the ultrafast cadence (2000 Hz) and the frame-by-frame comparison at the micrometer scale, fracture detection can be followed in gels.

In parallel, this project presents the opportunity to develop the technique of SWE to assess more accurately the mechanical properties of biological tissues and to understand precisely what parameters are measured when the tissue is under tension, under osmotic or mechanical stresses. More precision could be obtained from the diagnosis made by shear wave elastography by knowing the Landau Coefficients of biological tissues: quantify the local stress around a crack tip in soft tissues (liver, muscle, kidney...) or define the local stress caused by the growth of a tumor which presses against nearby nerves and muscles.

This project sought to develop an innovative experimental methodology to meet the next challenges in the field of gel design together with developing the description of biological tissues in terms of elastic and dissipative components and fracture processes.



# Annex

## A Stress determination with shear wave elastography on hybrid gels

Tensile tests until fracture are performed on elastic and viscoelastic gels at preparation state  $Q_0$  and swollen at equilibrium state  $Q_e$  to calibrate the AE parameters (non linear coefficients  $A$  and  $D$ ). The Landau coefficients used for AE theory are all reported in Tables 3.6 and 3.7 of Chapter 3. As already discussed through this manuscript, the interactions between PDMA and silica NPs induce not only an increase in initial stiffness but also an increase in the strain at failure. Indeed, for the high fraction of silica (SP3.5), the reinforcement is obvious (Fig. 51).

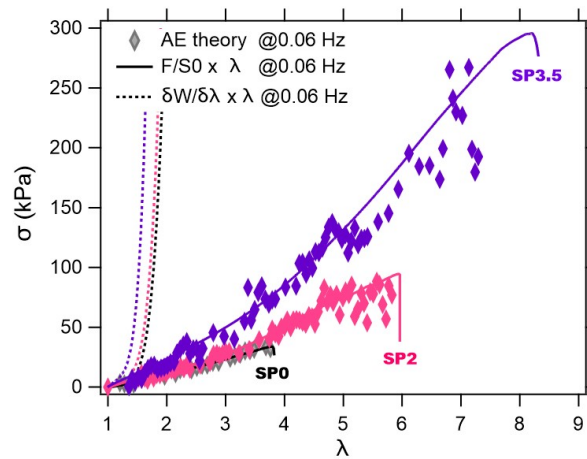


FIGURE 51: Tensile test until fracture for elastic/viscoelastic gels at preparation state  $Q_0$ . The stress/strain curves of these three different gels are shown for a strain rate of 0.06 Hz. Acoustoelasticity stress follows well the experimental stress whereas the stress calculated from the invariants deviates drastically at the beginning of the strain.

Shear wave velocity measurements represented by the diamond spots follow well the stress-strain curve given by the Instron. Nevertheless, the machine used for elastography was made for a medical purpose, i.e for soft tissues which range from 10 to 100 kPa approximately like liver ( $E \approx 10$  kPa) or breast ( $E \approx 20$  kPa) (Guimarães et al., 2020). Its precision is limited with high stiffness ( $E > 200$  kPa) since the stiffer the tissue, the faster the shear wave propagates and so it is more difficult to catch it. More advanced technology would be required with an ultrafast scanner allowed to scan with higher frequency in the range of tens of thousands of hertz. Another important parameter to have in mind is that for large strains, the sample thickness becomes thinner due to lateral contractions and it is possible that focalized ultrasound spots are not all perfectly centered inside the gel, altering the measure. For the dotted curve representing the stress calculated by the derivative of the strain energy  $W$  by  $\lambda$ , we can notice the more viscoelastic the gel, the bigger the coefficient  $\mu_0$ ,  $A$  and  $D$  (see Table 3.6 at the end of Chapter 3) and the faster the curve deviates which is expected since the strain energy density function used applies for incompressible elastic gels (Hamilton et al., 2004, Zabolotskaya et al., 2004).

### A.1 Impact of strain rate on AE theory

The typical tensile stress-strain responses are studied investigating time dependence varying the strain rates as  $0.06 \text{ s}^{-1}$ ,  $0.01 \text{ s}^{-1}$  and  $0.006 \text{ s}^{-1}$ . As shown in Fig. 3.6, the stiffness of the elastic gel has no dependence on the frequency. Nevertheless, the extensibility seems larger for higher strain rates (Fig. 52).

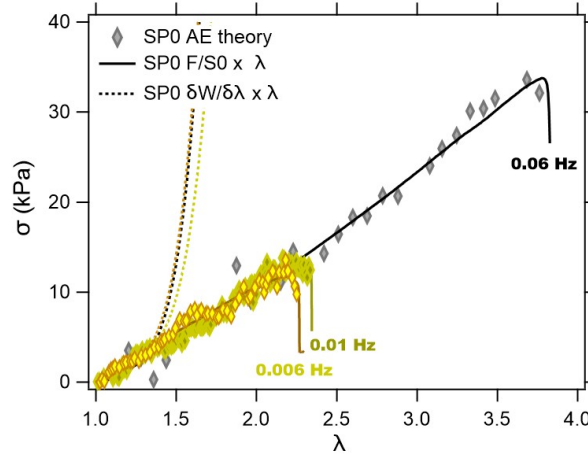


FIGURE 52: Stress-strain curve of unfilled system/elastic system for tensile tests until fracture at three different strain rates 0.006, 0.01, 0.06 Hz. AE theory works well to retrieve the stress imposed on the gel.

When the strain rate decreases, more measures can be taken from SWE due to the increased time of the experiment and so a better fit is obtained to find  $A$  and  $D$ . In dotted lines, the stress calculated from the invariants diverges around 30% strain as expected from previous results.

Concerning SP3.5 viscoelastic gels, the strong reinforcement effect of nanoparticles, observed for higher time scales, vanishes at low strain rate (Fig. 54) and at equilibrium state (Fig. 55). Indeed, by decreasing the strain rate by 6 and 10 ( $0.06 \text{ s}^{-1}$  to  $0.01 \text{ s}^{-1}$  and  $0.006 \text{ s}^{-1}$ ), the SP3.5 hybrid hydrogels are fully or partially relaxed.

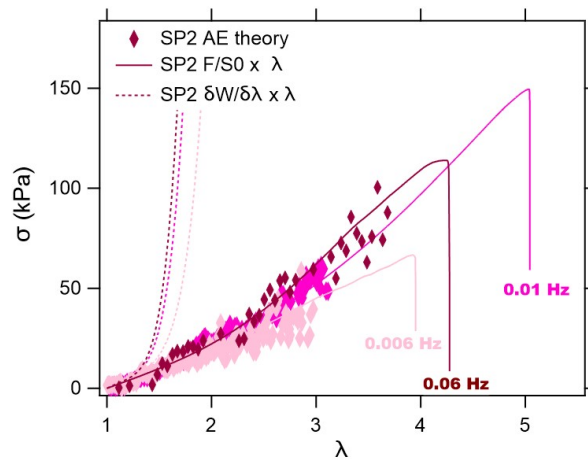


FIGURE 53: Stress-strain curve of NPs filled system with 10 vol.% of  $\text{SiO}_2$  for tensile tests until fracture at three different strain rates 0.006, 0.01, 0.06 Hz. We observe the strain rate has an impact on the extensibility at break and a slight change in the stiffness is also noticed.

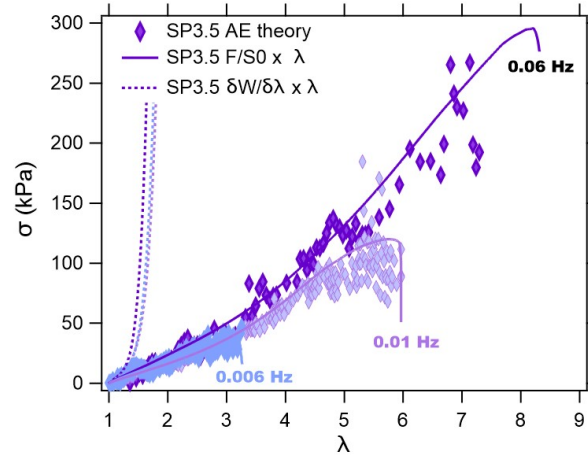


FIGURE 54: Stress-strain curve of NPs filled system with 15 vol.% of  $\text{SiO}_2$  for tensile tests until fracture at three different strain rates 0.006, 0.01, 0.06 Hz. We observe the strain rate has a significant impact on the extensibility at break and a change in the stiffness is observed.

As shown in Fig. 53 for SP2 gels, the stiffness and the extensibility do not change a lot with frequency compared to SP3.5 (Fig. 54).

The strain rate effect is also presented on swelling PDMA gel samples at equilibrium state  $Q_e$  (Fig. 55). Their mechanical properties at break are notably reduced compared to samples in the as-prepared state: the work of extension is greatly reduced especially for SP3.5: for a strain rate of 0.06 Hz,  $\lambda$  at break equals 8.2 for  $Q_0$  whereas it is equal to 2.3 for  $Q_e$ .

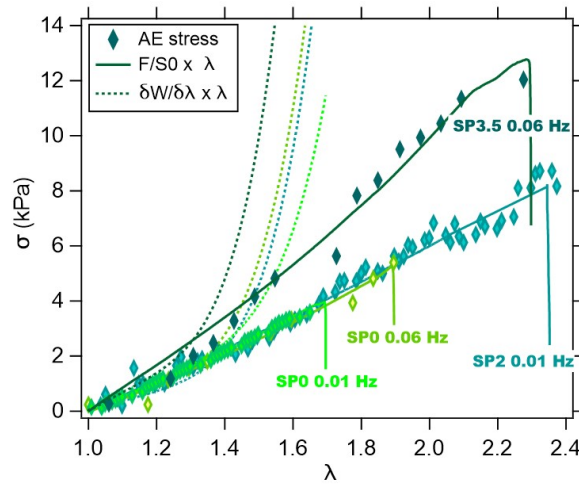


FIGURE 55: Stress VS strain curves of PDMA and nanocomposite PDMA/Silica hydrogel at maximal swelling degrees at different strain rates.

## B Local mechanical behavior of SP3.5 gels around the crack tip under tension

### B.1 Unusual stress field ahead of the crack tip

SP3.5 being composed of more NPs, they are more viscoelastic, i.e they are able to dissipate more strain energy due to topological rearrangements. It should be the same locally but it is more difficult to quantify due to the higher shear wave speed. In Fig. 56, one can observe the evolution of the local stress according to  $z$  ahead of the crack tip. At  $t = 0$ , the trend is close to  $z^{-1}$  between  $z = 0.8$  mm and  $z = 3$  mm, then the stress field seems to stabilize to a trend close to  $z^{-1/2}$  (in the  $z$  range). Then, we observe a big increase of the stress around 5 - 6 mm ahead of the crack tip. The stiffer part between 5-6 mm that appears in front of the crack tip may be an aggregation of the silica nanoparticles that was created due to the opening notch (Fig. 57). We observe that this bump intensity increases with time while the stress at the crack tip decreases. At this special location, the silica NPs are closed to each other preventing any interactions with the polymer chains. While it is relaxing in front of the crack tip, the stress is increasing at this special location due to the accumulation of polymer chains that were released at the crack tip. The stress relaxation is represented by a less steep slope of the stress as time increases (as seen in SP2 gels in Fig. 4.30 and Fig. 4.36).

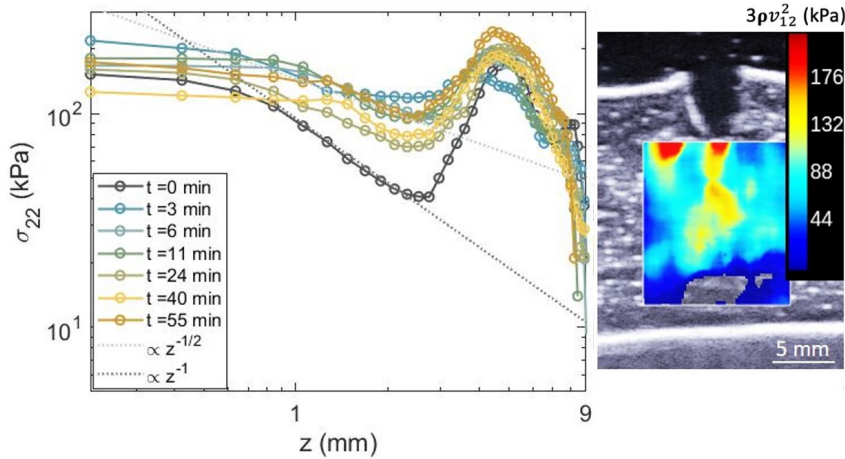


FIGURE 56: Local stress distribution as a function of  $z$  on SP3.5 gels at  $Q_0$  for different times.  $z^{-1}$  and  $z^{-1/2}$  are represented as a guideline. The process zone is less pronounced and difficult to define. COD = 4.9 -  $a/W = 0.26$ .

While we did not observe a clear evolution of the stress field according to the COD in elastic gels, and we did not see any changes in stress with time, different conclusions can be drawn for viscoelastic gels. It appears that the stress field softens with time as we notice a less steep trend from  $z^{-1}$  to  $z^{-1/4}$  in SP2 gels and from  $z^{-1}$  to  $z^{-1/2}$  in SP3.5 gels. Again, it is more difficult to conclude for SP3.5 due to the increase of the stress ahead of the crack tip (see Fig. 57).

Due to the increase of the stress between 5 and 6 mm, it is difficult to define a process zone. Concerning the "bump" that is observed in the gel, we remark that it often appears and few examples will be shown in the next part.

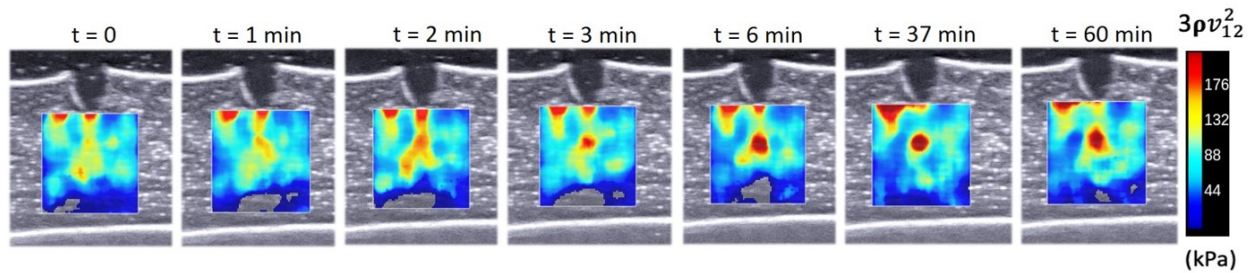


FIGURE 57: SP3.5: Evolution of the shear wave map as a function of time. A phenomenon appears about 6 mm after the crack tip.

### Spot appearing ahead of the crack tip

An increase of the stress often appears ahead of the crack tip in SP3.5 gels and sometimes SP2 gels (Fig. 58). This has never been observed on SP0 gels. It means that this phenomenon is closely linked to the silica nanoparticles. One explanation could be that the NPs aggregate at this exact location. This location remains the same, ahead of the crack tip, at the meeting of the convergence lines of the crack tip lips.

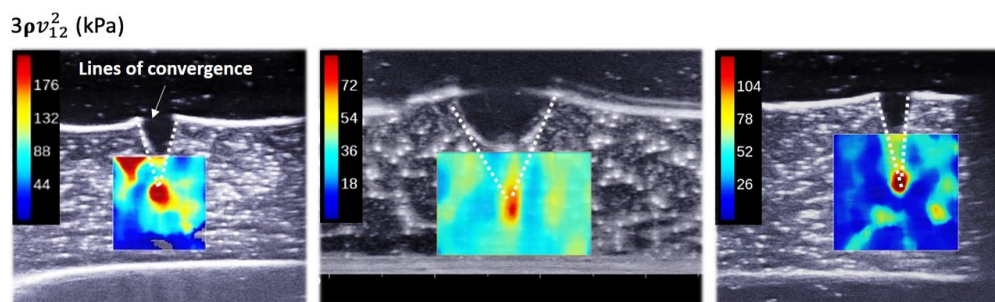


FIGURE 58: Convergence lines of the crack tip lips of SP3.5 gel (left) and SP2 gel (middle and right). A singularity is found ahead of the crack tip.

This phenomenon was not observed on swollen viscoelastic gels. This supports the hypothesis of silica aggregation (see schemes of Fig. 59). Indeed, in swollen viscoelastic gels, the NPs are stretched being attached to the polymer chains. By osmotic contribution, NPs pulled away from each other which prevents any aggregation.

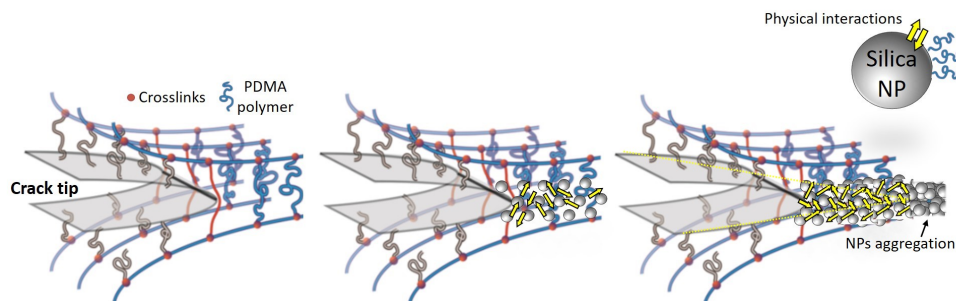


FIGURE 59: From left to right: SP0, SP2 and SP2 or SP3.5 presenting silica aggregation. The amount of  $\text{SiO}_2$  NPs increases at the crack tip which decreases the distance apart from each other. It might create aggregates in the convergence lines of the crack tip, thus prevent physical interactions to happen.



# Resumé substantiel en français

## Contexte

Un hydrogel est un matériau mou, largement gonflé d'eau, rendu élastique via un réseau de chaînes de polymère. Un gel est intrinsèquement fragile. On peut remédier à cette fragilité grâce à l'ajout de liaisons sacrificielles dynamiques. L'ingénierie macromoléculaire a permis au XXIème siècle de formuler des gels à destination de la biologie afin de proposer des matériaux de synthèse tout en remédiant aux problèmes de biocompatibilité, de compatibilité des interfaces tissu/matériau et être au plus proche des propriétés mécaniques dont le corps a besoin. Pourtant, la fracture de ces matériaux hautement déformables et parfois viscoélastiques reste un sujet mal compris et assez peu exploré expérimentalement. Le défi aujourd'hui est de mieux comprendre les mécanismes mis en jeu en pointe de fissure, mais les techniques expérimentales permettant une approche locale sont limitées. Notre travail vise à développer une méthode innovante pour sonder la fracture des gels. L'eau étant leur principal composant, ces matériaux, comme les tissus biologiques, sont une excellente plateforme pour l'étude de la propagation d'ondes acoustiques, i.e. de cisaillement (S) ou de compression (P). Dans les matériaux composés principalement d'eau, les ondes de compression, typiquement les ultrasons, se propagent à environ  $1500 \text{ m.s}^{-1}$  (vitesse des ondes P dans l'eau) alors que les ondes de cisaillement sont de l'ordre du  $\text{m.s}^{-1}$  (entre environ  $1\text{-}8 \text{ m.s}^{-1}$ ) et leur vitesse augmente avec la rigidité du matériau. Il est donc possible de suivre la propagation des ondes S. C'est le principe de l'élastographie par onde de cisaillement, technique d'imagerie utilisée dans le monde du diagnostic médical et qui sera transposé dans cette étude pour comprendre la mécanique et la fracture des hydrogels.

La fracture des gels sera étudiée localement en pointe de fissure de manière quasi-statique. Ensuite, les phénomènes physiques mis en jeu lors de la propagation d'une fissure seront investigués grâce à l'imagerie ultrarapide. Il est important de comprendre comment la fracture se propage et s'il est possible de l'éviter ou de la stopper. Le but de tout matériau est d'éviter une rupture brutale et donc de résister à la propagation de fracture.

## Principes et méthodes

### Chimie: Composition de l'hydrogel

L'hydrogel est composé d'un réseau polymérique (PDMA) maintenu par un réticulant chimique (MBA). Enchevêtrées dans ce réseau, les nanoparticules de silice (NPs) servent d'ancrage réversible du segment polymère par simple adsorption. Dans ces réseaux hybrides (interactions chimiques et physiques), les NPs sont dispersées dans la matrice de polymère chimiquement réticulée, jouant le rôle de réticulant physiques en offrant une plateforme pour l'adsorption des chaînes de PDMA sur la surface de la silice (Rose, 2013). La présence des NPs contrôle la composante viscoélastique du gel. Les capacités d'adsorption du polymère sur les NPs assurent également l'adhésion à l'interface du gel. Marcellan et Leibler (Rose et al., 2014) ont exploré une autre façon de coller les hydrogels en utilisant la solution de nanoparticules comme adhésif, sans affecter la rigidité ou la perméabilité de l'assemblage. Cette colle a également prouvé son efficacité sur les tissus biologiques.

Le gel chimique et le gel physique sont présentés Fig. 60.

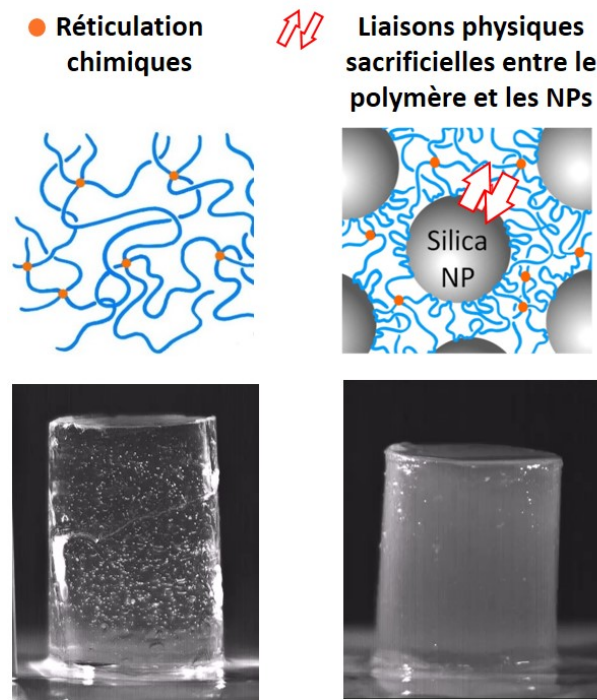


FIGURE 60: Présentation des gels. Gauche : Gel chimique composé d'un réseau de polymère (bleu) maintenu par des liaisons covalentes, interactions chimiques (orange). Droite : Gel physique grâce à l'addition des NPs. Des interactions physiques d'adsorption/désorption ont lieu entre le polymère et les NPs permettant au gel de se réarranger sous contrainte.

### Couplage test mécanique et imagerie

Les gels sont sollicités mécaniquement par une machine de traction et sont imagés par une technique d'imagerie par ultrasons (Fig. 61.a). Les gels ont été synthétisés de façon à avoir une géométrie compatible avec les sondes ultrasonores: épaisseur de 10 mm, largeur d'environ 20-25 mm et longueur comprise entre 30 et 60 mm. Une entaille d'environ 5 mm est créée dans le gel pour mimer une fissure et ce dernier est mis sous tension afin d'étudier les conditions de propagation de la fissure (Fig. 61.b). Pour l'étude de la fracture quasi-statique (étude de la pointe de fissure avant propagation), le mode SWE (élastographie) sera utilisée pour étudier la vitesse de l'onde de cisaillement en pointe de fissure. Pour ce qui est de la propagation de fissure, des ultrasons ultrarapides en onde planes seront envoyés à une cadence de 1000 Hz permettant de capturer toutes les millisecondes une image de la propagation de fracture.

### Théorie simplifiée de l'acoustoélasticité

Le principe de l'élastographie repose sur la mesure de la vitesse  $v$  de propagation d'une onde S, captée par les ultrasons ultrarapides. Dans les milieux simples (non déformés), cette vitesse donne accès au module de cisaillement  $\mu$  (en kPa) :  $\rho v^2 = \mu$ , avec  $\rho$ , la masse volumique du milieu. Lorsqu'une contrainte,  $\sigma$ , est appliquée au matériau, ce dernier devient anisotrope, polarisant l'onde S, et modifiant sa vitesse (Fig. 61.c). L'acoustoélasticité (AE), c'est à dire l'analyse de la propagation des ondes dans un milieu déformé (Landau et al., 1959), est alors indispensable à prendre en compte. La vitesse de l'onde S dépend alors de la contrainte exercée :  $\rho v^2 = \mu \pm \sigma(\mu, A) \pm \sigma^2(\mu, A, D)$ , avec A et D (en kPa), les coefficients d'élasticité non-linéaire du 3<sup>ème</sup> ordre et 4<sup>ème</sup> ordre, respectivement. Le couplage des techniques (mécanique et imagerie) permet d'obtenir la force et la vitesse de l'onde S simultanément (Fig. 61.d). Pour la première

fois, la théorie de l'AE va être utilisée expérimentalement pour estimer une contrainte imposée au matériau, en champs homogènes. De plus, les contraintes locales seront mesurées au voisinage d'une fissure après avoir identifier expérimentalement les coefficients non linéaires A et D pour diverses configurations d'essais et pour des formulations de gels élastiques et viscoélastiques.

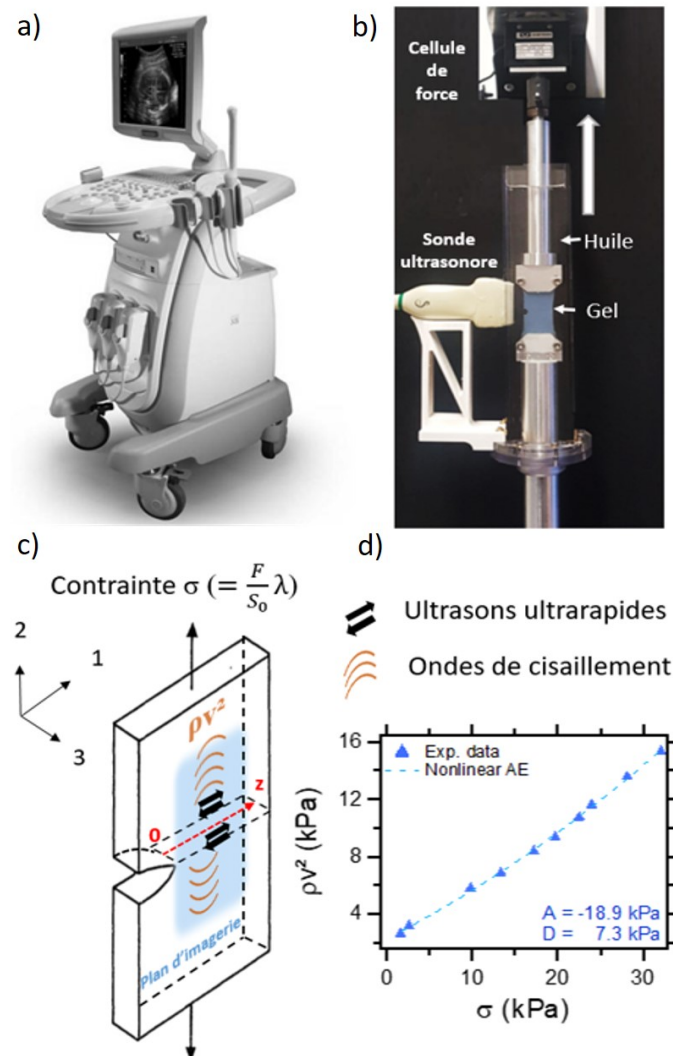


FIGURE 61: a) Machine d'élastographie: Aixplorer. b) Montage expérimental de traction couplé à l'élastographie. c) Schéma du gel fissuré mis sous tension et du plan d'imagerie (bleu) devant la pointe de fissure. d) Fit polynomial entre la vitesse de l'onde S et la contrainte  $\sigma$  pour déterminer les coefficients non-linéaire A et D.

## Résultats principaux

### Fracture statique sur gel élastiques

Après avoir identifié expérimentalement les coefficients A et D, la contrainte macroscopique est retrouvée et le modèle d'acoustoélasticité est validé pour le 4<sup>ème</sup> ordre. Les résultats sont confrontés à deux modèles de simulation. Les modèles s'adaptent bien à la courbe expérimentale jusqu'à environ  $\lambda = 2$  où les modèles de Mooney et de Rivlin révèlent un durcissement par rapport aux données expérimentales (proche du 3<sup>ème</sup> ordre de la théorie AE). Cela nous donne un aperçu des limites de la simulation.

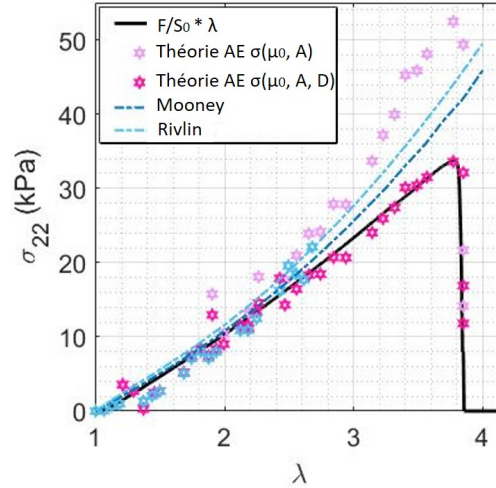


FIGURE 62: Contrainte en fonction de  $\lambda$  pour un essai de traction jusqu'à la rupture pour un gel élastique. La contrainte expérimentale est représentée en noir. L'acoustoélasticité à l'ordre 3 et 4 et les modèles de Mooney et Rivlin issus de la simulation sont présentés.

Grâce à une mesure de la vitesse de l'onde de cisaillement locale, il a été possible de remonter à une contrainte locale. Le champ de contrainte devant la pointe de fissure pour un gel élastique est ainsi comparé à une simulation par éléments finis (Fig. 63).

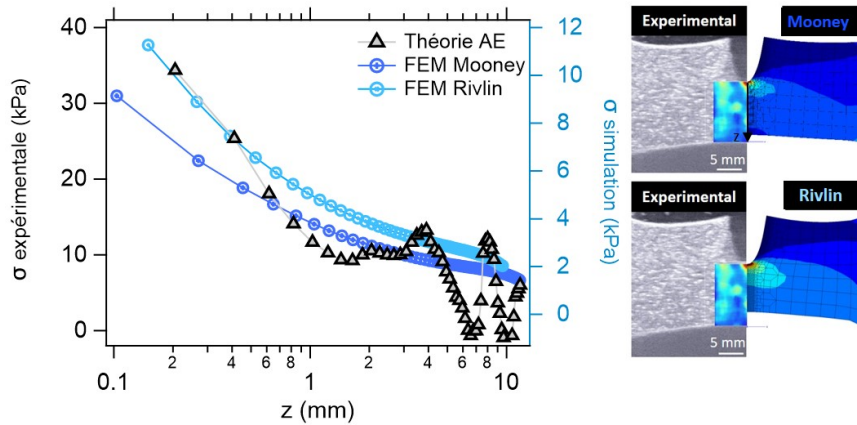


FIGURE 63: Profil spatial de la contrainte en pointe de fissure selon  $z$  pour un gel élastique. Les résultats expérimentaux (théorie AE) ont été comparés à des résultats de simulation par éléments finis. Deux modèles ont été testés: Mooney (compressible) and Rivlin (incompressible).

La différence entre la simulation et l'expérience peut être due au choix des modèles numériques utilisés, aux conditions aux limites et aussi à la différence en ordre du développement de l'énergie de déformation utilisée. La simulation utilise une énergie de déformation d'ordre 1 pour les deux modèles, tandis que la théorie AE utilise une fonction d'énergie de déformation développée au 3<sup>ème</sup> et 4<sup>ème</sup> ordre et suppose l'incompressibilité. L'idée d'essayer un modèle compressible était justifiée par la contraction latérale beaucoup plus faible dans le cas compressible que dans le cas incompressible, et donc plus proche de la réalité (carte d'élastographie/simulation, Fig. 63 droite). Les résultats obtenus sont très encourageants et valident la pertinence de nos mesures de contraintes locales par élastographie. Le profil temporelle de la contrainte sera présenté Fig. 64 en comparaison d'un gel viscoélastique. Comme attendu dans un gel élastique, sans dissipation d'énergie, la contrainte reste la même (selon  $z$  et selon le temps).

### Fracture statique sur gel viscoélastiques

Le gel avec des nanoparticules est viscoélastique grâce aux interactions physiques réversibles et relaxe considérablement les contraintes en pointe de fissure ( $z = 0$ ) (Fig. 64).

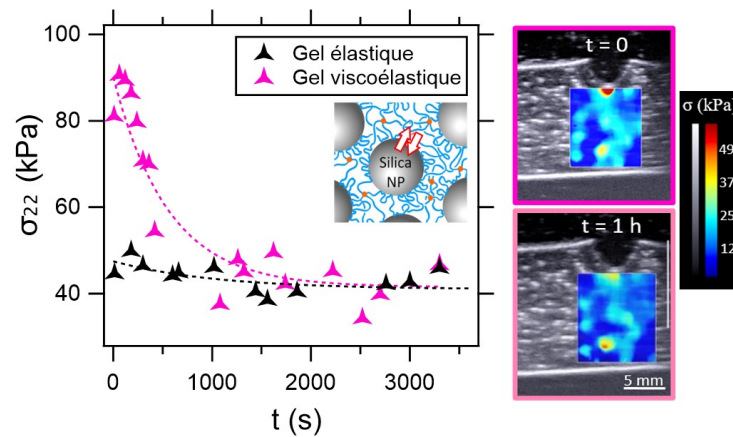


FIGURE 64: Profil temporel en pointe de fissure ( $z = 0$ ) pour un gel élastique et un gel viscoélastique. Le gel viscoélastique est capable de relaxer sa contrainte en pointe de fissure. Elle rejoint la contrainte du gel élastique après une vingtaine de minutes. Ce résultat est aussi visible sur les cartes d'élastographie présentées à droite du graphique. La singularité (point rouge) en pointe de fissure a disparu.

La relaxation des contraintes converge vers la signature d'un gel sans nanoparticules (gel élastique). Ces résultats sont aussi visibles sur les cartes d'élastographie. La singularité des contraintes en pointe de fissure est effacée grâce à la présence de nanoparticules qui permettent une répartition des efforts, à travers des processus d'échanges avec le polymère. Ce mécanisme permet de retarder la propagation de la fissure par homogénéisation de contrainte. Cet effet est bien visible sur le champ de contraintes.

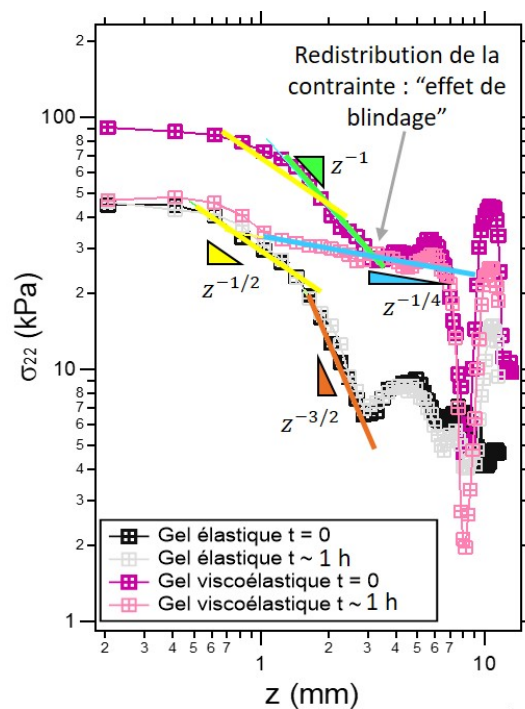


FIGURE 65: Profil spatial de la contrainte de la pointe de fissure  $z = 0$  jusqu'à  $z$  loin de la fissure pour un gel élastique et un gel viscoélastique à  $t = 0$  et  $t = 1$  h.

On remarque aussi que le gel avec NPs est capable de réduire considérablement sa contrainte proche de la fissure en fonction du temps et notamment dans les 2-3 premiers millimètres ( $\sigma_{max}$  est divisée par deux : 90 kPa à 45 kPa). Dans le gel élastique, le champ de contraintes reste la même le long de  $z$  à  $t = 0$  et  $t = 1$  h. Les NPs permettent donc un réarrangement dans les premiers millimètres devant la fissure.

### Fracture dynamique : propagation de la fissure

Lorsque la fissure se propage, le taux de restitution d'énergie élastique est maximum. L'ajout de NPs dans le gel chimique permet de retarder la fracture (c'est à dire, qu'elle est amorcée à plus grandes déformations), et lorsqu'elle est initiée, elle met plus temps à se propager.

Grâce à l'imagerie ultrarapide, il a été possible d'imager les ondes de cisaillement générées par les événements de rupture proche de la pointe de fissure. La vitesse de ces ondes est de l'ordre du  $\text{m.s}^{-1}$  et elles génèrent, sur leur passage, un déplacement micrométrique, ayant une vitesse de l'ordre du  $\text{mm.s}^{-1}$ . Le gel subit un tremblement de terre à petite échelle.

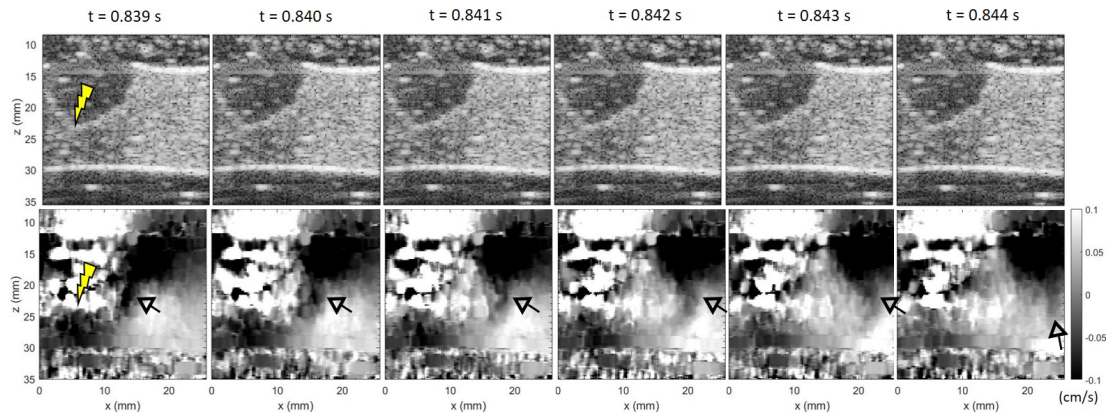


FIGURE 66: Propagation de fissure d'un gel élastique gonflé. Haut: Image Bmode. Bas: Carte de vitesse des déplacements générés dans le gel lors de la propagation de fracture. Une onde de cisaillement est créée en pointe de fissure. Les flèches noires aident à repérer l'onde et l'éclair jaune, l'endroit de la pointe de fissure.

Il est possible de retrouver l'onde de cisaillement créée dans le profil spatio-temporel. L'onde se propage suivant l'axe  $x$  principalement (Fig. 67).

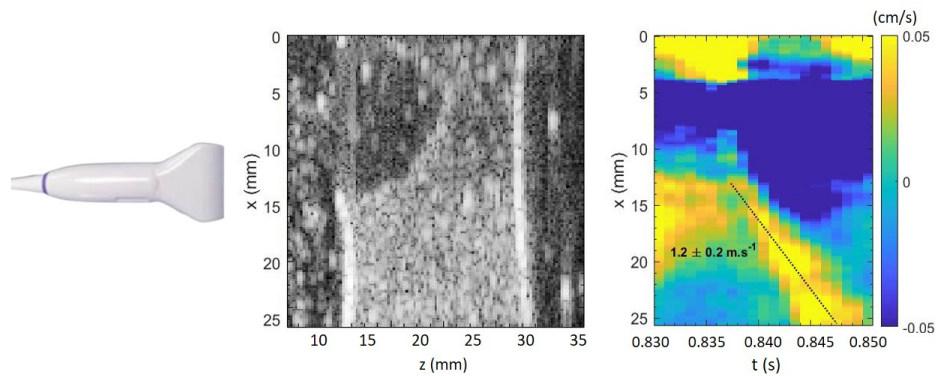


FIGURE 67: Gauche: Image Bmode du gel élastique gonflé à  $t = 0.840$  s, visualisation de l'intérieur du gel immergé dans l'huile. Droite: Carte de la vitesse des déplacements dans le gel lors de la propagation de fissure.

Sur la Fig. 67, l'image Bmode est présentée ainsi que la carte des déplacements dans la direction  $x$ , moyennée sur la direction  $z$ , en fonction du temps. L'onde est facilement repérable et sa vitesse peut être calculée grâce à la pente  $x$ - $t$ . Sa vitesse est d'environ  $1.2 \text{ m.s}^{-1}$ , cohérente avec la rigidité du gel.

### Imagerie ultrarapide sur les gels double réseaux

Pour tester les gels à double réseau (Gong et al., 2003), la cadence des ondes planes a été doublée de 1000 à 2000 Hz. En effet, le gel à double réseau est plus rigide que les gels de polymère PDMA, il faut donc augmenter la cadence si on espère enregistrer des événements de rupture.

Dans les gels à double réseau, plusieurs événements de déplacements internes ont lieu un peu partout dans le gel et surtout proche de la zone de fissure. Fig. 68 montre un exemple de déplacement interne qui a conduit à la création d'une onde de cisaillement. Il est connu que le premier réseau est fragile et casse pour promouvoir le second réseau. Il est possible qu'à  $t = 835 \text{ ms}$ , le réseau se casse localement et devienne une source d'ondes S de la même manière que la pointe de fissure génère des ondes S dans les gels de PDMA lors de la fracture (Fig. 66).

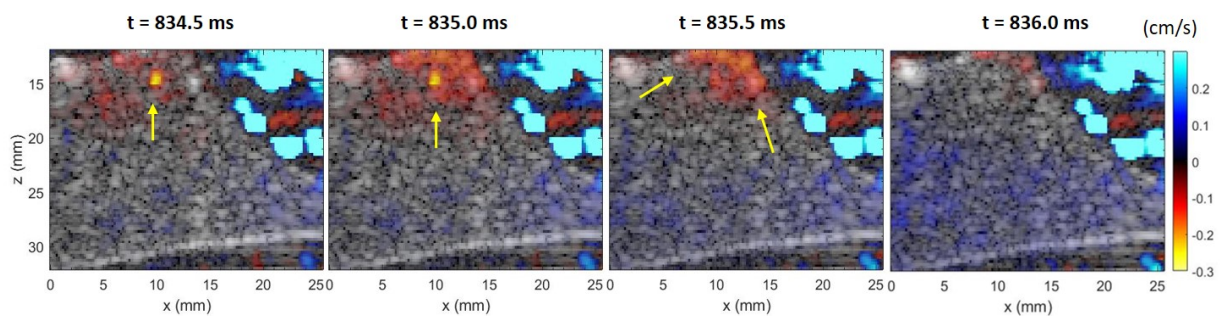


FIGURE 68: Détection d'un déplacement à l'intérieur du gel à double réseau près de la fissure. Le point lumineux représente un mouvement qui se produit à l'intérieur du gel. Il semble qu'une onde de cisaillement soit créée à partir de cette source et se propage à l'extérieur du gel.

À plusieurs reprises lors de la propagation de la fissure, des déplacements sont détectés tout le long des lèvres de la fissure. Un exemple est illustré Fig. 69 à  $t = 715 \text{ ms}$ .

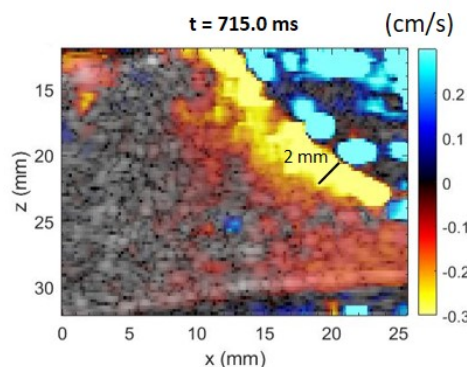


FIGURE 69: Carte de la vitesse des déplacement dans un gel à double réseau lors la propagation d'une fissure. Une zone de 2 mm environ entoure la fissure.

Les déplacements détectés dans le gel par ultrasons semblent correspondre à la rupture du réseau sacrificiel tout autour de la pointe de fissure sur un domaine d'environ deux millimètres. C'est dans cette zone, proche de la fissure, que les déformations sont les plus importantes.

## Conclusions et Perspectives

Nous avons démontré la faisabilité d'étudier la fracture des gels avec l'élastographie, technique non-invasive, in-situ, avec une bonne résolution spatiale ( $\sim \mu\text{m}$ ) et temporelle ( $\sim \text{ms}$ ). Là où, conventionnellement, la contrainte est déduite par une mesure du champ de déformation via photoélasticimétrie ou corrélation d'images, nous proposons ici une mesure de la contrainte locale par la vitesse des ondes de cisaillement, prenant en compte le comportement non-linéaire du gel. De plus, lorsque la propagation de fissure a lieu, des ondes planes d'ultrasons ultrarapides ont pu mettre en avant la dissipation d'énergie du gel sous forme d'ondes de cisaillement, créées en pointe du fissure et qui s'échappent hors du gel.

Il s'agit d'une nouvelle technique pour sonder la pointe de fissure de matériaux mous et hydratés. Ce projet a été rendu possible grâce à la collaboration entre deux laboratoires localisés à l'ESPCI. La beauté de ce travail réside en l'apport mutuel de ces deux mondes scientifiques. Lorsque le monde de l'imagerie permet une meilleure compréhension de la recherche fondamentale sur la fracture, le monde de la matière molle, par ses fortes analogies avec les tissus biologiques, sert de plateforme pour mieux appréhender la caractérisation des tissus par élastographie. En effet, cet outil va permettre aux chimistes d'adapter des stratégies de design macromoléculaire de tel sorte, par exemple, à obtenir une meilleure coopérativité du réseau en pointe de fissure. Le challenge est d'obtenir des liens sacrificiels résistants en s'inspirant de ce que la nature a déjà accompli à travers les tissus biologiques. Ces travaux pourraient aussi éclairer les médecins dans la compréhension des contraintes mécaniques complexes auxquels peuvent être sujets nos tissus biologiques et des impacts sur les processus physiologiques.

# Bibliography

- Aase, Svein A et al. (2008). "Aortic valve closure: relation to tissue velocities by Doppler and speckle tracking in normal subjects". In: *European Journal of Echocardiography* 9.4, pp. 555–559.
- Abé, Hiroyuki et al. (1996). *Data book on mechanical properties of living cells, tissues, and organs*. Springer.
- Abiza, Zaki et al. (2012). "Large acoustoelastic effect". In: *Wave Motion* 49.2, pp. 364–374.
- Achenbach, Jan (2012). *Wave propagation in elastic solids*. Elsevier.
- Anseth, Kristi S et al. (1996). "Mechanical properties of hydrogels and their experimental determination". In: *Biomaterials* 17.17, pp. 1647–1657.
- Arfken, George B et al. (1999). *Mathematical methods for physicists*.
- Azuma, Chinatsu et al. (2007). "Biodegradation of high-toughness double network hydrogels as potential materials for artificial cartilage". In: *Journal of Biomedical Materials Research Part A: An Official Journal of The Society for Biomaterials, The Japanese Society for Biomaterials, and The Australian Society for Biomaterials and the Korean Society for Biomaterials* 81.2, pp. 373–380.
- Baumberger, Tristan et al. (2006). "Solvent control of crack dynamics in a reversible hydrogel". In: *Nature materials* 5.7, pp. 552–555.
- Baumberger, Tristan et al. (2020). "Environmental control of crack propagation in polymer hydrogels". In: *Mechanics of Soft Materials* 2.1, pp. 1–38.
- Bercoff, Jeremy (2004). "L'imagerie échographique ultrarapide et son application à l'étude de la viscoélasticité du corps humain". PhD thesis. ESPCI ParisTECH.
- Bercoff, Jeremy et al. (2004). "Supersonic shear imaging: a new technique for soft tissue elasticity mapping". In: *IEEE transactions on ultrasonics, ferroelectrics, and frequency control* 51.4, pp. 396–409.
- Besson, J et al. (1997). "Large scale object-oriented finite element code design". In: *Computer methods in applied mechanics and engineering* 142.1-2, pp. 165–187.
- Bouchbinder, Eran et al. (2009). "The  $1/r$  singularity in weakly nonlinear fracture mechanics". In: *Journal of the Mechanics and Physics of Solids* 57.9, pp. 1568–1577.
- Brillouin, Léon (1925). "Les tensions de radiation; leur interprétation en mécanique classique et en relativité". In: *J. Phys. Radium* 6.11, pp. 337–353.
- Brown, Hugh R (2007). "A model of the fracture of double network gels". In: *Macromolecules* 40.10, pp. 3815–3818.
- Capadona, Jeffrey R et al. (2008). "Stimuli-responsive polymer nanocomposites inspired by the sea cucumber dermis". In: *science* 319.5868, pp. 1370–1374.
- Casciaro, Sergio et al. (2010). "Optimal enhancement configuration of silica nanoparticles for ultrasound imaging and automatic detection at conventional diagnostic frequencies". In: *Investigative radiology* 45.11, pp. 715–724.
- Castera, Laurent et al. (2008). "Non-invasive evaluation of liver fibrosis using transient elastography". In: *Journal of hepatology* 48.5, pp. 835–847.
- Catheline, S et al. (2003). "Measurement of elastic nonlinearity of soft solid with transient elastography". In: *The Journal of the Acoustical Society of America* 114.6, pp. 3087–3091.
- Catheline, Stefan (1998). "Interférométrie-Speckle ultrasonore: Application à la mesure d'élasticité". PhD thesis. Université Paris-Diderot-Paris VII.
- Céspedes, I et al. (1993). "Elastography: elasticity imaging using ultrasound with application to muscle and breast in vivo". In: *Ultrasonic imaging* 15.2, pp. 73–88.

- Chen, Chih-Hung et al. (2017). "Instability in dynamic fracture and the failure of the classical theory of cracks". In: *Nature Physics* 13.12, pp. 1186–1190.
- Chirani, Naziha et al. (2015). "History and applications of hydrogels". In: *Journal of biomedical sciences* 4.2.
- Colby, Ralph H et al. (2003). "Polymer physics". In: *New-York: Oxford University* 100, p. 274.
- Curro, John G et al. (1983). "A theoretical basis for viscoelastic relaxation of elastomers in the long-time limit". In: *Macromolecules* 16.4, pp. 559–562.
- De Gennes, Pierre-Gilles et al. (1979). *Scaling concepts in polymer physics*. Cornell university press.
- Debbal, SM et al. (2008). "Computerized heart sounds analysis". In: *Computers in biology and medicine* 38.2, pp. 263–280.
- Deffieux, Thomas (2008). "Palpation par force de radiation ultrasonore et échographie ultrarapide: Applications à la caractérisation tissulaire in vivo." PhD thesis. Université Paris-Diderot-Paris VII.
- Destrade, Michel et al. (2010). "Third-and fourth-order constants of incompressible soft solids and the acousto-elastic effect". In: *The Journal of the Acoustical Society of America* 127.5, pp. 2759–2763.
- Donald, Ian et al. (1958). "Investigation of abdominal masses by pulsed ultrasound". In: *The Lancet* 271.7032, pp. 1188–1195.
- Dyens, Ollivier (2001). *Metal and flesh: The evolution of man: Technology takes over*. Mit Press.
- Elbanna, Ahmed E et al. (2013). "Dynamics of polymer molecules with sacrificial bond and hidden length systems: towards a physically-based mesoscopic constitutive law". In: *PLOS one* 8.4, e56118.
- Fantner, Georg E et al. (2005). "Sacrificial bonds and hidden length dissipate energy as mineralized fibrils separate during bone fracture". In: *Nature materials* 4.8, pp. 612–616.
- Flory, Paul J et al. (1943). "Statistical mechanics of cross-linked polymer networks I. Rubberlike elasticity". In: *The journal of chemical physics* 11.11, pp. 512–520.
- Fukao, Kazuki et al. (2020). "Effect of relative strength of two networks on the internal fracture process of double network hydrogels as revealed by in situ small-angle X-ray scattering". In: *Macromolecules* 53.4, pp. 1154–1163.
- Gennisson, J-L et al. (2007). "Acoustoelasticity in soft solids: Assessment of the nonlinear shear modulus with the acoustic radiation force". In: *The Journal of the Acoustical Society of America* 122.6, pp. 3211–3219.
- Gennisson, J-L et al. (2013). "Ultrasound elastography: principles and techniques". In: *Diagnostic and interventional imaging* 94.5, pp. 487–495.
- Gennisson, Jean-Luc et al. (2014). "Rheology over five orders of magnitude in model hydrogels: agreement between strain-controlled rheometry, transient elastography, and supersonic shear wave imaging". In: *IEEE transactions on ultrasonics, ferroelectrics, and frequency control* 61.6, pp. 946–954.
- Gentile, Francesco et al. (2012). "Direct imaging of DNA fibers: the visage of double helix". In: *Nano letters* 12.12, pp. 6453–6458.
- Gong, Jian Ping (2010). "Why are double network hydrogels so tough?" In: *Soft Matter* 6.12, pp. 2583–2590.
- Gong, Jian Ping et al. (2003). "Double-network hydrogels with extremely high mechanical strength". In: *Advanced materials* 15.14, pp. 1155–1158.
- Greensmith, HW (1963). "Rupture of rubber. X. The change in stored energy on making a small cut in a test piece held in simple extension". In: *Journal of Applied Polymer Science* 7.3, pp. 993–1002.
- Guimarães, Carlos F et al. (2020). "The stiffness of living tissues and its implications for tissue engineering". In: *Nature Reviews Materials* 5.5, pp. 351–370.
- Guo, Hui et al. (2016). "Thermoresponsive Toughening with Crack Bifurcation in Phase-Separated Hydrogels under Isochoric Conditions". In: *Advanced materials* 28.28, pp. 5857–5864.

- Guo, Jingyi et al. (2018). "Fracture mechanics of a self-healing hydrogel with covalent and physical crosslinks: A numerical study". In: *Journal of the Mechanics and Physics of Solids* 120, pp. 79–95.
- Guo, Mingyu et al. (2014). "Tough stimuli-responsive supramolecular hydrogels with hydrogen-bonding network junctions". In: *Journal of the American Chemical Society* 136.19, pp. 6969–6977.
- Hamilton, Mark F et al. (2004). "Separation of compressibility and shear deformation in the elastic energy density ( $L$ )". In: *The Journal of the Acoustical Society of America* 116.1, pp. 41–44.
- Haraguchi, Kazutoshi et al. (2002). "Nanocomposite hydrogels: A unique organic-inorganic network structure with extraordinary mechanical, optical, and swelling deswelling properties". In: *Advanced materials* 14.16, pp. 1120–1124.
- Henderson, Kevin J et al. (2010). "Ionically cross-linked triblock copolymer hydrogels with high strength". In: *Macromolecules* 43.14, pp. 6193–6201.
- Holdt, Susan Lovstad et al. (2011). "Bioactive compounds in seaweed: functional food applications and legislation". In: *Journal of applied phycology* 23.3, pp. 543–597.
- Hong, Yu et al. (2016). "Localized tissue surrogate deformation due to controlled single bubble cavitation". In: *Experimental Mechanics* 56.1, pp. 97–109.
- Huang, Ting et al. (2007). "A novel hydrogel with high mechanical strength: a macromolecular microsphere composite hydrogel". In: *Advanced Materials* 19.12, pp. 1622–1626.
- Hughes, Do S et al. (1953). "Second-order elastic deformation of solids". In: *Physical review* 92.5, p. 1145.
- Hui, C-Y et al. (2003). "Crack blunting and the strength of soft elastic solids". In: *Proceedings of the Royal Society of London. Series A: Mathematical, Physical and Engineering Sciences* 459.2034, pp. 1489–1516.
- Imran, Abu Bin et al. (2014). "Extremely stretchable thermosensitive hydrogels by introducing slide-ring polyrotaxane cross-linkers and ionic groups into the polymer network". In: *Nature communications* 5.1, pp. 1–8.
- Irwin, George R (1957). "Analysis of stresses and strains near the end of a crack transversing a plate". In: *Trans. ASME, Ser. E, J. Appl. Mech.* 24, pp. 361–364.
- Irwin, GR (1948). "TIFracture Dynamics, 1 Fracture of Metals (Symposium)". In: *Am. Soc. Metals, Cleveland*, pp. 147–166.
- Ito, Kohzo (2010). "Slide-ring materials using topological supramolecular architecture". In: *Current Opinion in Solid State and Materials Science* 14.2, pp. 28–34.
- Jamshidi, Fatemeh et al. (2020). "Synthesis of magnetic poly (acrylic acid-menthol deep eutectic solvent) hydrogel: Application for extraction of pesticides". In: *Journal of Molecular Liquids* 318, p. 114073.
- Jen, Anna C et al. (1996). "Hydrogels for cell immobilization". In: *Biotechnology and bioengineering* 50.4, pp. 357–364.
- Karami, Peyman et al. (2021). "An Intrinsically-Adhesive Family of Injectable and Photo-Curable Hydrogels with Functional Physicochemical Performance for Regenerative Medicine". In: *Macromolecular Rapid Communications* 42.10, p. 2000660.
- Kong, Hyun Joon et al. (2003). "Independent control of rigidity and toughness of polymeric hydrogels". In: *Macromolecules* 36.12, pp. 4582–4588.
- Kraissl, Cornelius J (1951). "The selection of appropriate lines for elective surgical incisions". In: *Plastic and Reconstructive Surgery* 8.1, pp. 1–28.
- Krouskop, Thomas A et al. (1998). "Elastic moduli of breast and prostate tissues under compression". In: *Ultrasonic imaging* 20.4, pp. 260–274.
- Kwon, Hyock-Ju et al. (2010). "Application of digital image correlation method to biogel". In: *Polymer Engineering & Science* 50.8, pp. 1585–1593.
- Lake, GJ et al. (1967). "The strength of highly elastic materials". In: *Proceedings of the Royal Society of London. Series A. Mathematical and Physical Sciences* 300.1460, pp. 108–119.
- Landau, Lev Davidovich et al. (1959). *Course of Theoretical Physics Vol 7: Theory and Elasticity*. Pergamon press.

- Landel, Robert F et al. (1993). *Mechanical properties of polymers and composites*. CRC press.
- Langer, Karl (1861). "Zur Anatomie und Physiologie der Haut". In: *Sitzungsbericht der mathematisch-naturwissenschaftlichen Classe der Kaiserlichen Academie der Wissenschaften* 44, pp. 19–48.
- Latour, Soumaya et al. (2011). "Ultrafast ultrasonic imaging of dynamic sliding friction in soft solids: The slow slip and the super-shear regimes". In: *EPL (Europhysics Letters)* 96.5, p. 59003.
- Launey, Maximilien E et al. (2010). "On the mechanistic origins of toughness in bone". In: *Annual review of materials research* 40, pp. 25–53.
- Le Gulluche, Anne-Charlotte (2019). "Hybrid hydrogels as model nanocomposites: reinforcement mechanisms by analogy with filled rubbers". PhD thesis. Université de Lyon.
- Lee, Kuen Yong et al. (2001). "Hydrogels for tissue engineering". In: *Chemical reviews* 101.7, pp. 1869–1880.
- Lefranc, Maxime et al. (2014). "Mode I fracture of a biopolymer gel: Rate-dependent dissipation and large deformations disentangled". In: *Extreme Mechanics Letters* 1, pp. 97–103.
- Leibinger, Alexander et al. (2016). "Soft tissue phantoms for realistic needle insertion: a comparative study". In: *Annals of biomedical engineering* 44.8, pp. 2442–2452.
- Li, Jianyu et al. (2014). "Hybrid hydrogels with extremely high stiffness and toughness". In: *ACS Macro Letters* 3.6, pp. 520–523.
- Liang, Songmiao et al. (2011). "Direct observation on the surface fracture of ultrathin film double-network hydrogels". In: *Macromolecules* 44.8, pp. 3016–3020.
- Lin, Wei-Chun et al. (2010). "Large strain and fracture properties of poly (dimethylacrylamide)/silica hybrid hydrogels". In: *Macromolecules* 43.5, pp. 2554–2563.
- Lindley, PB (1972). "Energy for crack growth in model rubber components". In: *Journal of Strain Analysis* 7.2, pp. 132–140.
- Liu, Chang et al. (2019a). "Crack propagation resistance of slide-ring gels". In: *Polymer* 181, p. 121782.
- Liu, Chang et al. (2019b). "Direct Observation of Large Deformation and Fracture Behavior at the Crack Tip of Slide-Ring Gel". In: *Journal of The Electrochemical Society* 166.9, B3143.
- Liu, Xinyue et al. (2019c). "Ingestible hydrogel device". In: *Nature communications* 10.1, pp. 1–10.
- Livne, Ariel et al. (2007). "Oscillations in rapid fracture". In: *Physical review letters* 98.12, p. 124301.
- Livne, Ariel et al. (2008). "Breakdown of linear elastic fracture mechanics near the tip of a rapid crack". In: *Physical review letters* 101.26, p. 264301.
- Long, Rong et al. (2016). "Large deformation effect in Mode I crack opening displacement of an Agar gel: A comparison of experiment and theory". In: *Extreme Mechanics Letters* 9, pp. 66–73.
- Long, Rong et al. (2020). "The fracture of highly deformable soft materials: A tale of two length scales". In: *Annual Review of Condensed Matter Physics* 12.
- Lowndes, AG (1942). "Percentage of water in jelly-fish". In: *Nature* 150.3799, pp. 234–235.
- Luo, Feng et al. (2014). "Crack blunting and advancing behaviors of tough and self-healing polyampholyte hydrogel". In: *Macromolecules* 47.17, pp. 6037–6046.
- Marcellan, Alba et al. (2006). "A multi-scale analysis of the microstructure and the tensile mechanical behaviour of polyamide 66 fibre". In: *Polymer* 47.1, pp. 367–378.
- Matsuda, Takahiro et al. (2020). "Crack tip field of a double-network gel: Visualization of covalent bond scission through mechanoradical polymerization". In: *Macromolecules* 53.20, pp. 8787–8795.
- Mayumi, Koichi et al. (2010). "Structure and dynamics of polyrotaxane and slide-ring materials". In: *Polymer* 51.4, pp. 959–967.
- Mayumi, Koichi et al. (2013). "Stress-strain relationship of highly stretchable dual cross-link gels: separability of strain and time effect". In: *ACS Macro Letters* 2.12, pp. 1065–1068.
- Meddahi-Pellé, Anne et al. (2014). "Organ repair, hemostasis, and in vivo bonding of medical devices by aqueous solutions of nanoparticles". In: *Angewandte Chemie International Edition* 53.25, pp. 6369–6373.
- Mihajlovic, Marko et al. (2017). "Tough supramolecular hydrogel based on strong hydrophobic interactions in a multiblock segmented copolymer". In: *Macromolecules* 50.8, pp. 3333–3346.

- Mihranyan, Albert (2011). "Cellulose from cladophorales green algae: From environmental problem to high-tech composite materials". In: *Journal of Applied Polymer Science* 119.4, pp. 2449–2460.
- Montaldo, Gabriel et al. (2009). "Coherent plane-wave compounding for very high frame rate ultrasonography and transient elastography". In: *IEEE transactions on ultrasonics, ferroelectrics, and frequency control* 56.3, pp. 489–506.
- Murnaghan, Francis Dominic (1937). "Finite deformations of an elastic solid". In: *American Journal of Mathematics* 59.2, pp. 235–260.
- Na, Yang-Ho et al. (2004). "Structural characteristics of double network gels with extremely high mechanical strength". In: *Macromolecules* 37.14, pp. 5370–5374.
- Oedjoe, M Dj R (2017). "Composition of Nutritional Content of Sea Cucumbers (Holothuroidea) in Mania Waters, Sabu Raijua Regency, East Nusa Tenggara". In: *Journal of Aquaculture Research Development* 8.7, p. 1000502.
- Okumura, Yasushi et al. (2001). "The polyrotaxane gel: A topological gel by figure-of-eight cross-links". In: *Advanced materials* 13.7, pp. 485–487.
- Ophir, J et al. (1991). "Elastography: a quantitative method for imaging the elasticity of biological tissues". In: *Ultrasonic imaging* 13.2, pp. 111–134.
- Ophir, J et al. (1994). "Elastography of beef muscle". In: *Meat science* 36.1-2, pp. 239–250.
- Orowan, Egon (1949). "Fracture and strength of solids". In: *Reports on progress in physics* 12.1, p. 185.
- Park, Sung Il et al. (2015). "Soft, stretchable, fully implantable miniaturized optoelectronic systems for wireless optogenetics". In: *Nature biotechnology* 33.12, pp. 1280–1286.
- Peng, Na et al. (2016). "Biocompatible cellulose-based superabsorbent hydrogels with antimicrobial activity". In: *Carbohydrate polymers* 137, pp. 59–64.
- Petit, Laurence et al. (2014). "Design and Viscoelastic Properties of PDMA/S ilica Assemblies in Aqueous Media". In: *Macromolecular Symposia*. Vol. 337. 1. Wiley Online Library, pp. 58–73.
- Reed, Todd R et al. (2004). "Heart sound analysis for symptom detection and computer-aided diagnosis". In: *Simulation Modelling Practice and Theory* 12.2, pp. 129–146.
- Rivlin, RS et al. (1953). "Rupture of rubber. I. Characteristic energy for tearing". In: *Journal of polymer science* 10.3, pp. 291–318.
- Ronsin, O et al. (2019). "Environmental Nanoparticle-Induced Toughening and Pinning of a Growing Crack in a Biopolymer Hydrogel". In: *Physical review letters* 123.15, p. 158002.
- Rose, Séverine (2013). "Interactions polymère/silice: de la structure locale au renforcement mécanique d'hydrogels hybrides". PhD thesis. Université Pierre et Marie Curie-Paris VI.
- Rose, Severine et al. (2013). "Time dependence of dissipative and recovery processes in nanohybrid hydrogels". In: *Macromolecules* 46.10, pp. 4095–4104.
- Rose, Séverine et al. (2014). "Nanoparticle solutions as adhesives for gels and biological tissues". In: *Nature* 505.7483, pp. 382–385.
- Rubinstein, Michael et al. (1999). "Associations leading to formation of reversible networks and gels". In: *Current opinion in colloid & interface science* 4.1, pp. 83–87.
- Rudzinski, W E et al. (2002). "Hydrogels as controlled release devices in agriculture". In: *Designed monomers and polymers* 5.1, pp. 39–65.
- Sandrin, Laurent et al. (2002). "Shear modulus imaging with 2-D transient elastography". In: *IEEE transactions on ultrasonics, ferroelectrics, and frequency control* 49.4, pp. 426–435.
- Sandrin, Laurent et al. (2003). "Transient elastography: a new noninvasive method for assessment of hepatic fibrosis". In: *Ultrasound in medicine & biology* 29.12, pp. 1705–1713.
- Sarvazyan, Armen P et al. (1998). "Shear wave elasticity imaging: a new ultrasonic technology of medical diagnostics". In: *Ultrasound in medicine & biology* 24.9, pp. 1419–1435.
- Sasson, Aviad et al. (2012). "Hyperelastic mechanical behavior of chitosan hydrogels for nucleus pulposus replacement—Experimental testing and constitutive modeling". In: *Journal of the mechanical behavior of biomedical materials* 8, pp. 143–153.

- Shattuck, David P et al. (1984). "Explososcan: A parallel processing technique for high speed ultrasound imaging with linear phased arrays". In: *The Journal of the Acoustical Society of America* 75.4, pp. 1273–1282.
- Sigrist, Rosa MS et al. (2017). "Ultrasound elastography: review of techniques and clinical applications". In: *Theranostics* 7.5, p. 1303.
- Simha, NK et al. (2004). "Evaluation of fracture toughness of cartilage by micropenetration". In: *Journal of Materials Science: Materials in Medicine* 15.5, pp. 631–639.
- Sun, Jeong-Yun et al. (2012). "Highly stretchable and tough hydrogels". In: *Nature* 489.7414, pp. 133–136.
- Sun, Tao Lin et al. (2013). "Physical hydrogels composed of polyampholytes demonstrate high toughness and viscoelasticity". In: *Nature materials* 12.10, pp. 932–937.
- Syed, Sana et al. (2015). "Simple polyacrylamide-based multiwell stiffness assay for the study of stiffness-dependent cell responses". In: *Journal of visualized experiments: JoVE* 97.
- Szulgit, G K et al. (2000). "Dynamic Characterization of Sea Cucumber Dermis". In: p. 12.
- Tanter, Mickaël et al. (2002). "Ultrafast compound imaging for 2-D motion vector estimation: Application to transient elastography". In: *IEEE transactions on ultrasonics, ferroelectrics, and frequency control* 49.10, pp. 1363–1374.
- Tanter, Mickael et al. (2008). "Quantitative assessment of breast lesion viscoelasticity: initial clinical results using supersonic shear imaging". In: *Ultrasound in medicine & biology* 34.9, pp. 1373–1386.
- Tanter, Mickael et al. (2014). "Ultrafast imaging in biomedical ultrasound". In: *IEEE transactions on ultrasonics, ferroelectrics, and frequency control* 61.1, pp. 102–119.
- Taylor, Brian J et al. (2014). "A lab-on-chip for malaria diagnosis and surveillance". In: *Malaria journal* 13.1, pp. 1–11.
- Thomas, Jeanette A et al. (2004). *Echolocation in bats and dolphins*. University of Chicago Press.
- Tominaga, Taiki et al. (2007). "The molecular origin of enhanced toughness in double-network hydrogels: A neutron scattering study". In: *Polymer* 48.26, pp. 7449–7454.
- Trotter, JA et al. (2000). "Towards a fibrous composite with dynamically controlled stiffness: lessons from echinoderms". In: *Biochemical Society Transactions* 28.4, pp. 357–362.
- Trotter, John A et al. (1999). "Collagen fibril aggregation-inhibitor from sea cucumber dermis". In: *Matrix Biology* 18.6, pp. 569–578.
- Tsukeshiba, Hiroyuki et al. (2005). "Effect of polymer entanglement on the toughening of double network hydrogels". In: *The Journal of Physical Chemistry B* 109.34, pp. 16304–16309.
- Tuncaboylu, Deniz C et al. (2011). "Tough and self-healing hydrogels formed via hydrophobic interactions". In: *Macromolecules* 44.12, pp. 4997–5005.
- Van Bemmelen, JM (1894). "L'hydrogel et l'hydrate cristallin de l'oxyde de cuivre". In: *Recueil des Travaux Chimiques des Pays-Bas* 13.8, pp. 271–274.
- Van Veen, Barry D et al. (1988). "Beamforming: A versatile approach to spatial filtering". In: *IEEE assp magazine* 5.2, pp. 4–24.
- Voldřich, Z et al. (1975). "Long-term experience with poly (glycol monomethacrylate) gel in plastic operations of the nose". In: *Journal of biomedical materials research* 9.6, pp. 675–685.
- Wang, Qigang et al. (2010). "High-water-content mouldable hydrogels by mixing clay and a dendritic molecular binder". In: *Nature* 463.7279, pp. 339–343.
- Wang, Xuezheng et al. (2011). "Jellyfish gel and its hybrid hydrogels with high mechanical strength". In: *Soft Matter* 7.1, pp. 211–219.
- Wehner, Michael et al. (2016). "An integrated design and fabrication strategy for entirely soft, autonomous robots". In: *Nature* 536.7617, pp. 451–455.
- Wichterle, O et al. (1960). "Hydrophilic gels for biological use". In: *Nature* 185.4706, pp. 117–118.
- Wöll, Dominik (2016). "Fluorescence Correlation Spectroscopy Studies of Polymer Systems". In: *Fluorescence Studies of Polymer Containing Systems*. Springer, pp. 255–297.

- Woo, Joseph (2002). "A short history of the development of ultrasound in obstetrics and gynecology". In: *History of Ultrasound in Obstetrics and Gynecology* 3, pp. 1–25.
- Yang, Feichen et al. (2020). "A synthetic hydrogel composite with the mechanical behavior and durability of cartilage". In: *Advanced Functional Materials* 30.36, p. 2003451.
- Yang, Jun et al. (2019). "Strain Rate-Dependent Viscoelasticity and Fracture Mechanics of Cellulose Nanofibril Composite Hydrogels". In: *Langmuir* 35.32, pp. 10542–10550.
- Yu, Qiu Ming et al. (2009). "Direct observation of damage zone around crack tips in double-network gels". In: *Macromolecules* 42.12, pp. 3852–3855.
- Yuk, Hyunwoo et al. (2019). "Hydrogel bioelectronics". In: *Chemical Society Reviews* 48.6, pp. 1642–1667.
- Zabolotskaya, Evgenia A et al. (2004). "Modeling of nonlinear shear waves in soft solids". In: *The Journal of the Acoustical Society of America* 116.5, pp. 2807–2813.
- Zhang, Teng et al. (2015). "Predicting fracture energies and crack-tip fields of soft tough materials". In: *Extreme Mechanics Letters* 4, pp. 1–8.
- Zhu, Jintang et al. (2012). "Mechanical properties, anisotropic swelling behaviours and structures of jellyfish mesogloea". In: *Journal of the Mechanical Behavior of Biomedical Materials* 6, pp. 63–73.
- Zohdi, Rozaini Mohd et al. (2011). "Sea cucumber (*Stichopus hermannii*) based hydrogel to treat burn wounds in rats". In: *Journal of Biomedical Materials Research Part B: Applied Biomaterials* 98.1, pp. 30–37.

## RÉSUMÉ

---

Les hydrogels sont des matériaux fascinants. Emblématiques de la matière molle, ces solides mous essentiellement composés d'eau sont très sensibles à leur environnement ; ils peuvent changer drastiquement de volume ou de propriétés via un stimulus externe tel que la température, le pH, ou l'humidité. Ces matériaux sont devenus essentiels dans l'ingénierie tissulaire, la robotique molle ou l'électronique. Les gels modèles que nous utilisons ont démontré des propriétés remarquables en terme de résistance, d'autoréparation et d'adhésion. Comprendre les processus d'endommagement est essentiel pour développer des stratégies efficaces de renforcement mécanique, pourtant, l'exploration des mécanismes mis en jeu, localement en pointe de fissure, sur ces matériaux mous reste très insuffisante. Nous proposons donc de développer un outil d'imagerie ultrasonore, l'élastographie, qui révolutionne le diagnostic médical par la mesure quantitative d'un module d'élasticité. En couplant cette méthode à des tests mécaniques, nous avons démontré qu'il est possible dans des gels extrêmement déformés de remonter à une contrainte locale. La nature de cette information est unique dans le monde de la mécanique des matériaux. De plus, grâce à l'imagerie ultrarapide, il a été possible de détecter des phénomènes de libération d'énergie sous forme d'ondes créées en pointe de fissure lors de la propagation d'une fracture. Si ce projet éclaire sur la rupture des matériaux mous, il pourrait aussi apporter aux cliniciens une réelle valeur ajoutée dans le diagnostic médical afin d'affiner la description des tissus biologiques soumis à des contraintes complexes.

## MOTS CLÉS

---

Hydrogels - fracture - mécanique - élasticité non linéaire - imagerie - élastographie

## ABSTRACT

---

Hydrogels are fascinating materials. Emblematic of soft matter, these soft solids mainly composed of water are very sensitive to their environment; they can drastically change their volume or properties via an external stimulus such as temperature, pH, or humidity. These materials have become essential in tissue engineering, soft robotics, or electronics. The model gels we use have already demonstrated remarkable properties in terms of strength, self-repair, and adhesion. Understanding the damage processes is essential to develop efficient mechanical reinforcement strategies, yet the exploration of the mechanisms involved, locally at the crack tip, in these soft materials remains very insufficient. Therefore, we propose to develop an ultrasound imaging tool, elastography, which revolutionizes medical diagnosis through the quantitative measurement of an elastic modulus. By coupling this method to mechanical tests, we have demonstrated that it is possible to calculate a local stress. The nature of this information is unique in the world of mechanics of materials. Moreover, through ultrafast imaging, it was possible to detect energy release phenomena in the form of waves created at the crack tip during the propagation of a fracture. If this project sheds light on the failure of soft materials, it could also bring to clinicians a real added value in medical diagnosis to refine the description of biological tissues subjected to complex stresses.

## KEYWORDS

---

Hydrogels - fracture - mechanics - non linear elasticity - imaging - elastography